Finite Element and Monte Carlo Simulations Accompanying the SOX Experiment

Dissertation

der Mathematisch-Naturwissenschaftlichen Fakultät
der Eberhard Karls Universität Tübingen
zur Erlangung des Grades eines
Doktors der Naturwissenschaften
(Dr. rer. nat.)

vorgelegt von
Michael Gschwender
aus Ellwangen

Tübingen
2019

Gedruckt mit Genehmigung der Mathematisch-Naturwissenschaftlichen
Fakultät der Eberhard Karls Universität Tübingen.

Tag der mündlichen Qualifikation:	25.04.2019
Dekan:	Prof. Dr. Wolfgang Rosenstiel
1. Berichterstatter:	Prof. Dr. Tobias Lachenmaier
2. Berichterstatter:	Prof. Dr. Josef Jochum

The time will come when diligent research over long periods will bring to light things that now lie hidden. A single life time, even though entirely devoted to research, would not be enough for the investigation of so vast a subject. . . . And so this knowledge will be unfolded through long successive ages. There will come a time when our descendants will be amazed that we did not know things that are so plain to them. . . . Many discoveries are reserved for ages still to come, when memory of us will have been effaced. Our universe is a sorry little affair unless it has in it something for every age to investigate . . . . Nature does not reveal her mysteries once and for all.

— Lucius Annaeus Seneca (c. 4 BC – AD 65), naturales quaestiones

Abstract

In recent years several anomalies and deviations from the established three-flavor neutrino oscillation model surfaced. These were reported from beam and reactor experiments alike and could provide hints for the existence of a fourth, sterile neutrino flavor. With the use of Borexino, a liquid scintillator solar neutrino detector, the SOX experiment (**S**hort distance neutrino **O**scillation with Bore**X**ino) aimed to investigate these anomalies by using a strong radioactive β-source. This neutrino source would have been placed in a calorimeter to precisely determine the neutrino flux via the radioactive self-heating and then deployed in a tunnel below Borexino. The thesis at hand details the work related to the calibration for this calorimeter and its accompanying thermal simulations in the first part. The second part describes the additional external gamma background and dedicated Monte Carlo simulations for SOX. As the neutrinos from the source should have been detected in a different energy window and a larger part of the fiducial detector volume used than in previous Borexino analyses, new demands on background handling arise. The gamma background, mainly in the MeV range, is attributable to radioactive decays from the uranium and thorium chain as well as naturally present potassium-40. Due to the presence of Borexino's buffer liquid these γ-particles are heavily suppressed, which is why a dedicated biasing approach to reduce computation times enough for these simulations to be made possible is crucial. This approach was validated and the impact of the gamma background for different fiducial detector volumes was investigated.

Deutsche Zusammenfassung

In den vergangenen Jahren wurden diverse Anomalien und Abweichungen vom gängigen Neutrinomodell beobachtet. Ausgehend von sowohl beam-, als auch reaktorgestützten Experimenten könnten diese als erste Hinweise auf die mögliche Existenz eines vierten, sterilen Neutrinos verstanden werden. Das geplante SOX Experiment (**S**hort distance neutrino **O**scillation with Bore**X**ino) sollte als Erweiterung des bereits etablierten Flüssigszintillator-Neutrinodetektors Borexino Klarheit schaffen. Zu diesem Zweck wurde geplant, eine Neutrinoquelle in einem Tunnel unter Borexino zu platzieren, deren Fluss über eine kalorimetrische Messung bestimmt werden sollte, da sich die stark radioaktive Quelle selbst erhitzt.
Die vorliegende Arbeit beschreibt im ersten Teil die Beiträge im Bereich der Kalibration dieses Kalorimeters und die einhergehenden thermischen Simulationen. Durch den unterschiedlichen Energiebereich im Vergleich zur Messung solarer Neutrinos, sowie des größeren zur Analyse herangezogenen Detektorvolumens erhöht sich der Beitrag des externen Untergrundes. Dieser Untergrund, bestehend aus Gammastrahlung im MeV-Bereich, entsteht aus Zerfällen der Uran- und Thorium-Reihe sowie von Kalium-40. Im zweiten Teil dieser Arbeit werden dieser zusätzliche Untergrund und die zugehörigen Monte-Carlo-Simulationen beschrieben. Hierfür wurde ein bereits bestehender Ansatz (Biasing) zur Reduktion von Rechenzeit in den Simulationen weiterentwickelt und validiert, um der Unterdrückung dieses Gamma-Untergrundes durch die Bufferschicht von Borexino Rechnung zu tragen und dadurch diese Simulationen überhaupt zu ermöglichen.

Contents

General Audience Introduction

Neutrinos are elusive particles known to pass through matter, barely interacting, which earned them their initial title as the *ghost particles* of particle physics. As they are neutral, only weakly interacting particles, they can penetrate matter easily and open an observational window hidden by only observing other particles. It is this very nature that makes them notoriously hard to detect, but on the other hand makes them ideal candidates to observe processes like, for example, the nuclear fusion in the sun's core. Photons take several thousand years to escape the layers of the sun, whereas neutrinos pass from the interior through to the outer layers, within seconds, carrying information on the nuclear fusion inside and allowing to distinguish between solar models. This behavior makes neutrinos very versatile and highly interesting for a number of hard to observe events, ranging from radioactive decays in the Earth's mantle (geo-neutrinos) to cosmological sources (neutrino astronomy) and the most cataclysmic stellar explosions. In these core collapse supernova, approximately 99% of the energy is released in short bursts of neutrinos, leaving the neutrino as the most relevant particle to observe, in order to expand understanding on the underlaying physics.

Even though the first detection of the neutrino is now half a century old, a lot of unanswered fundamental questions still remain. These concern their masses, oscillation properties and their place in the Standard Model of particle physics. A three-flavor oscillation theory was successful for many decades to predict fluxes of neutrinos from various sources. However, in recent years deviations and anomalies not easily explained by this model have surfaced. Some of these might be resolved by a fourth neutrino flavor, which does not take part in weak interactions and is therefore called sterile. As most of these anomalies were observed on smaller (less than 5 km) distances from detection to source and the potential parameters of this fourth neutrino would influence the oscillation on this scale, an experimental answer has to be sought in the short baseline regime. In this scope, the SOX experiment (**S**hort distance neutrino **O**scillation with Bore**X**ino) was proposed. It was planned to place a neutrino source in a tunnel under the Borexino detector at a distance of around 8 m from the detector's center. This strong β-emitter would have been placed in a calorimeter, where its neutrino flux could be obtained by a calorimetric measurement tied to the source activity. By comparing this flux to the measured one in Borexino, a deviation from the expected flux or even a potential oscillation signal could then point to the existence of such a sterile neutrino. Borexino is already a well-established liquid scintillator neutrino detector, successful in measuring solar

neutrinos and an ideal candidate for such an endeavor, due to its high radio-purity and overall low background.

For SOX to successfully observe a missing neutrino flux from the source (or even a potential oscillation pattern), the initial flux must be very well known, to achieve this, a dedicated calibration of the calorimeter at the 1% error level was required. This could be attained via the development of an electric calibration source (mockup). The mockup aided in the calibration efforts by mimicking the source geometry and was able to release a known amount of heat into the calorimeter. Thermal simulations of the mockup, calorimeter and cerium source further assisted during the calibration/development phase. On the neutrino detector's side, good knowledge on the expected background was required and dedicated simulations in Borexino's own simulation environment were performed. Due to the change in the energy window and the fiducial detector volume, compared to previous solar measurements of Borexino, external gamma background was expected to play a bigger role. Because most of these γ-particles are suppressed by a buffer liquid, the simulation of these events is not possible without a special *biasing* approach. Unfortunately due to technical difficulties in the production of the needed neutrino source, the SOX experiment was canceled in February 2018.

Contributions to the experiment from this work can be grouped in a source related part (calorimeter plus mockup) and a detector part (Borexino) concerning the external background. This thesis is structured as follows:
Chapter 1 serves as a general introduction to neutrino physics and discusses the deviations from the three-flavor model. Chapter 2 introduces the Borexino detector and its relevant properties, while Chapter 3 discusses the SOX experiment, the mockup and the calorimetric setup. Chapter 4 details the thermal simulations which were developed in parallel to the mockup and calorimeter and shows the mockup-calorimeter thermal model. Chapter 5 starts the detector part by introducing the external background and the dedicated calibration campaign. In Chapter 6 the biasing approach, Borexino framework and Monte Carlo simulations are detailed and an analysis of the impact of the fiducial detector volume on this background is performed. Finally, Chapter 7 summarizes this work and highlights the contributions from this thesis and gives a short outlook on the current state of the field.

Chapter 1

Introduction

This chapter will give a historical overview and a brief introduction over the neutrino, its discovery and cover some milestones of the field along the way, starting with the first detection of neutrinos (Section 1.2) and the experiment that enabled it. Then followed by the first observation of solar neutrinos and the discovery of neutrino oscillations and thus ultimately resulting in the well established standard three-flavor oscillation model, described in Section 1.3. Potential experimentally observed deviations from this model will be covered in Section 1.5. These hints served as the initial motivation for the proposal of a fourth neutrino flavor, a so called light sterile neutrino. Sterile neutrinos would not partake in weak interactions, instead they would only interact gravitationally (Section 1.4). The SOX[1] experiment (Chapter 3) was proposed in order to investigate possible deviations from the three neutrino oscillation case at short baselines (a few meters up to a few kilometers from a neutrino source).
In the course of this chapter it will become clear that the basic mechanisms, as well as the experimental detection principles and technical ideas, used in the early neutrino experiments are still valid and in use to some degree today. Liquid scintillators, photomultiplier tubes, an observed signal from the inverse beta decay as a detection principle are commonly shared from the first ever experiment to today's modern neutrino detectors like Borexino (Chapter 2) and many others. Shielding, background understanding and reduction, although evolved in technical and computational aspects, still play the same key role they did since the beginning, due to the sensitivity needed to observe the elusive neutrino.

1.1 The Proposal of the Neutrino

In the 1920s the beta decay was known as the process in which a decaying nucleus sends out an electron, whilst increasing its atomic number Z by 1. Physics models from the time period of 1920 - 1930 imagined the nucleus to consist of a bound state of protons and electrons, with other electrons outside on shells of discrete energy. The observed spectrum of the emitted electron from the β^- decay was found to be continuous. This was in direct contrast to the α-decay and the emissions of γ-rays,

[1] Short distance neutrino Oscillations with BoreXino

where discrete energy levels were seen.
The rapid success of quantum mechanics in the '30s was able to correctly predict, and to some degree understand α- and γ-radiation, but failed in the case of the β-decay. There were serious issues with the electron-proton nucleus model, such as the magnetic moment of the electron or violations of the uncertainty principle. It was not understood at this point how the electrons/protons could be confined to a small section in the nucleus and how the magnetic forces could be kept at bay. A good recollection and state of this particular period in physics can be found in an article by M. Brown [25].
A possible explanation for the observed β^--spectrum was, that energy in the decay process was only statistically preserved, but could be broken for a single decay, an argument prominently made by Niels Bohr. Quantum theorists like Heisenberg, and to some degree also Bohr, considered the possibility of new physics involving new space-time metrics on the scale of the nucleus. Additionally, favored by Lise Meitner, it was often pointed out that also secondary effects could play a role in this, assuming that the electron has a fixed energy immediately after its emission and then suffers energy loss due to interactions in the nucleus itself and to a minor degree in the detector material. This specific question was experimentally tested by Ellis and Wooster [50] in 1927. They constructed a calorimetric measurement for an Radon -E source, a β^- emitter, better known as Bismuth (^{210}Bi) and still observed a continuous spectrum. By ruling out these secondary effects it was shown that the electron spectrum is indeed continuous and it contributed only to the doubts already piling up on the old electron-proton nucleus model. Meitner and Orthmann [82] confirmed the results of Ellis and Wooster in their own experiment three years later.
In this environment of troubling issues with the nucleus model and the β^--decay spectrum, Pauli wrote to his colleagues ("radioactive society") attending a congress in Tübingen in December 1930 (Figure 1.1). He remarked on the problematic understanding of the β^--decay and also the issue of spins. Of course in the β^--decay the spin is also violated, but given the many questions on this topic at the time and the possibility of new physics in the nucleus or even non conservation of energy in a single decay, the spin seemed like a minor issue, in this particular case. Pauli stated another problem connected to the spins of nitrogen and lithium however, which he refers to as the problem of spin statistics. As Pauli mentioned, it was clear from molecular band spectrum of N_2, that nitrogen possesses a spin of 1. In the electron-proton model however the mass number A, in the case of nitrogen would be 14 and the element number Z = 7. In a bound state the spin would be the added sum of 14 protons and 7 electrons. As both are spin 1/2 particles this would not add up to the observed and known value of 1 in the case of nitrogen.

Pauli proceeds to propose a new particle, which he assumes to be present in the β^--decay as well as in the nucleus itself, aiming to solve the most troublesome issues at once. In order to be congruent within already established experiments this particle must have very low cross section and interaction in order to have avoided detection so far. By being an elementary particle inside the nucleus as well as being emitted

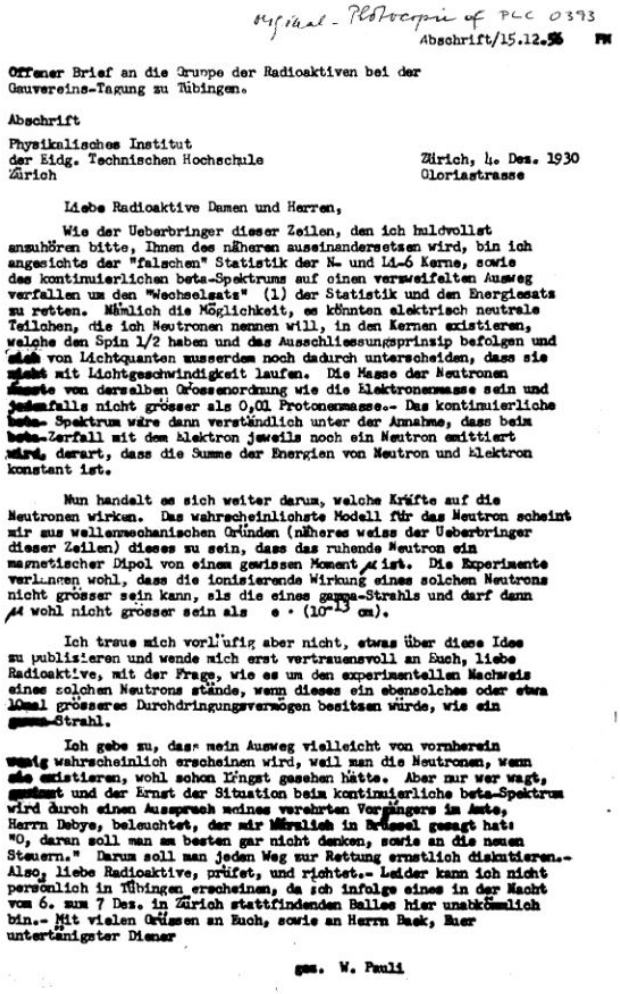

Original - Photocopie of PLC 0393

Abschrift/15.12.30 PM

Offener Brief an die Gruppe der Radioaktiven bei der Gauvereins-Tagung zu Tübingen.

Abschrift

Physikalisches Institut
der Eidg. Technischen Hochschule
Zürich

Zürich, 4. Dez. 1930
Gloriastrasse

Liebe Radioaktive Damen und Herren,

Wie der Ueberbringer dieser Zeilen, den ich huldvollst anzuhören bitte, Ihnen des näheren auseinandersetzen wird, bin ich angesichts der "falschen" Statistik der N- und Li-6 Kerne, sowie des kontinuierlichen beta-Spektrums auf einen verzweifelten Ausweg verfallen um den "Wechselsatz" (1) der Statistik und den Energiesatz zu retten. Nämlich die Möglichkeit, es könnten elektrisch neutrale Teilchen, die ich Neutronen nennen will, in den Kernen existieren, welche den Spin 1/2 haben und das Ausschliessungsprinzip befolgen und sich von Lichtquanten ausserdem noch dadurch unterscheiden, dass sie nicht mit Lichtgeschwindigkeit laufen. Die Masse der Neutronen müsste von derselben Grössenordnung wie die Elektronenmasse sein und jedenfalls nicht grösser als 0,01 Protonenmasse.- Das kontinuierliche beta- Spektrum wäre dann verständlich unter der Annahme, dass beim beta-Zerfall mit dem Elektron jeweils noch ein Neutron emittiert wird, derart, dass die Summe der Energien von Neutron und Elektron konstant ist.

Nun handelt es sich weiter darum, welche Kräfte auf die Neutronen wirken. Das wahrscheinlichste Modell für das Neutron scheint mir aus wellenmechanischen Gründen (näheres weiss der Ueberbringer dieser Zeilen) dieses zu sein, dass das ruhende Neutron ein magnetischer Dipol von einem gewissen Moment μ ist. Die Experimente verlangen wohl, dass die ionisierende Wirkung eines solchen Neutrons nicht grösser sein kann, als die eines gamma-Strahls und darf dann μ wohl nicht grösser sein als $e \cdot (10^{-13}$ cm).

Ich traue mich vorläufig aber nicht, etwas über diese Idee zu publizieren und wende mich erst vertrauensvoll an Euch, liebe Radioaktive, mit der Frage, wie es um den experimentellen Nachweis eines solchen Neutrons stände, wenn dieses ein ebensolches oder etwa 10mal grösseres Durchdringungsvermögen besitzen würde, wie ein gamma-Strahl.

Ich gebe zu, dass mein Ausweg vielleicht von vornherein wenig wahrscheinlich erscheinen wird, weil man die Neutronen, wenn sie existieren, wohl schon längst gesehen hätte. Aber nur wer wagt, gewinnt und der Ernst der Situation beim kontinuierliche beta-Spektrum wird durch einen Ausspruch meines verehrten Vorgängers im Amte, Herrn Debye, beleuchtet, der mir kürzlich in Brüssel gesagt hat: "O, daran soll man am besten gar nicht denken, sowie an die neuen Steuern." Darum soll man jeden Weg zur Rettung ernstlich diskutieren.- Also, liebe Radioaktive, prüfet, und richtet.- Leider kann ich nicht persönlich in Tübingen erscheinen, da ich infolge eines in der Nacht vom 6. zum 7 Dez. in Zürich stattfindenden Balles hier unabkömmlich bin.- Mit vielen Grüssen an Euch, sowie an Herrn Back, Euer untertänigster Diener

gez. W. Pauli

Figure 1.1: A transcription of the letter sent by Pauli in 1930 to the radioactive society holding a congress in Tübingen. In this letter Pauli states the current problems to explain the continuous spectrum in the β^--decay and the problems concerning the spins statistics of nitrogen and lithium. He then proceeds to propose a new particle, which will later be known as the neutrino [93].

in the β^--decay, Pauli effectively proposes a particle, which from today's knowledge would have been a combination of neutron and neutrino. This Pauli neutron, assumed to be a spin 1/2 particle, would correct the spin statistics mentioned above. He estimated the mass of this particle to be smaller as 0.01 times the mass of a proton. It would also solve the continuous β^--decay spectrum, assuming it is also emitted in the process and the decay energy is shared between this neutron and the electron.
The "actual" neutron was discovered in 1932 in an experiment by Chadwick [27]. Later during the end of 1933 Enrico Fermi formulated a theory of the β-decay, now including the newly found neutron and Paulis neutron, which was now named

neutrino[2], and was still undiscovered. The β^--decay could now be understood and formulated as

$$ {}^{A}_{Z}X \rightarrow {}^{A}_{Z+1}Y + e^- + \bar{\nu}_e \tag{1.1} $$

or for the free neutron:

$$ n \rightarrow p + e^- + \bar{\nu}_e \tag{1.2} $$

Here a neutron decays into a proton and emits a positron as well as an electron anti-neutrino, which both share the energy of this decay process.
Fermi published this new theory first in Italian [55] as well as in German [54] and laid the groundwork and crucial understanding for elementary particles, neutrinos and their interactions.

1.2 Early and Current Neutrino Experiments

The inverse beta (minus) decay reaction (IBD, Equation 1.3) was used as the basic detection mechanism in the neutrino discovery by Frederick Reines and Clyde Cowan in 1956[3] [98].

$$ \bar{\nu}_e + p \rightarrow e^+ + n \tag{1.3} $$

They were able to observe an anti-neutrino flux coming from the near 700 MW Savannah River reactor. Anti-neutrinos coming from fission fragments of this nearby reactor would interact with protons (in a proton-rich liquid scintillator detector). The produced positron will annihilate with an electron and produce two γ-rays with a known energy of 511 keV each and an incident angle of 180° as well as a free neutron, thus enabling a coincidence measurement. The so called prompt signal, resulting from the annihilation of the positron with an electron in the detector could then be identified by detecting the produced photons with scintillation counters. The free neutron is absorbed by the scintillator, resulting in multiple γ-rays with a total energy of up to 9 MeV via neutron capture, known as the delayed signal, which can be observed typically a few μs later.
The whole system was located in an underground lab and shielded against neutrons from the reactor, γ-rays and cosmic rays via an enclosing paraffin and lead structure. Calibration was performed with a dedicated neutron- and γ-source in order to discriminate these potential backgrounds from the real signal. As they were looking at the anti-neutrinos from the nuclear reactors the most convincing argument for their detection could be made by observing a reactor-power dependence of their signal. In the end Cowan and Reines where able to detect an anti-neutrino signal with a signal to accidental reactor-background ratio of 20:1 [42]. They report the properties of this newly detected particle as a spin 1/2 particle, with a mass below 1/5000 of the mass of an electron and a cross section considering the IBD from Equation 1.3 as $\sigma = 10^{-43}\,\mathrm{cm}^2$ for 8 MeV reactor anti-neutrinos [99].

[2] Named neutrino, by Enrico Fermi, with the Italian -*ino* prefix as an belittlement to the discovered neutron.
[3] Unofficially referred to also as Project Poltergeist.

In the following years after Cowan and Reines experiment, further experiments contributed to the now evolving, but still relatively new field of neutrino physic. C. Wu et al. [110] reported parity violation of weak interactions in 1957 by observing an asymmetry in the angular distribution of the β-spectrum of ^{60}Co. Neutrinos were established as left handed particles by Goldhaber et. al. [60] a year later in the Brookhaven laboratory. In the same laboratory the muon neutrino was discovered in 1962 [43]. The first measurement of solar neutrinos produced by electron capture process of ^{7}Be could be achieved by Davis in 1968 [45] in the Homestake mine[4]. More on solar neutrinos can be found in Section 2.2.0.1.
The observation of these solar neutrinos was based on a radio-chemical detection method using chlorine. The reaction of Equation 1.4 was initially proposed by Pontecorvo in 1946[5] [44].

$$\nu_e + {}^{37}\mathrm{Cl} \rightarrow {}^{37}\mathrm{Ar} + e^- \tag{1.4}$$

However, the reaction can not be observed directly, but the produced argon atoms are unstable and decay to chlorine with a half-life of around 35 days. Therefore the argon was collected from the tanks and from the decay processes the flux of ^{7}Be solar neutrinos could be obtained. This was achieved by separating the argon and counting the decays in a gas counter.
In the early sixties Bahcall, Davis, Fowler and others worked on new solar models. These resulted in the Standard Solar Model (SSM) able to predict the expected neutrino flux from the fission processes [9] and could be directly compared to the outcome of Davis experiment. When the Homestake experiment concluded, from the limit on the argon produced by solar neutrinos, the flux was calculated to be $3.9 \cdot 10^9\,\mathrm{cm}^{-2}\,\mathrm{s}^{-1}$ [45].
This experimental flux was only 1/3 of the predicted value from the theoretical model, which became known as the solar neutrino problem and neutrino oscillations (Section 1.3) are needed in order to explain the missing flux.
The Kamiokande detector measured solar neutrinos from ^{8}B and was the first to confirm the missing flux. This measurement was not based on a radio-chemical method, but rather on elastic electron-scattering in a water Cherenkov detector. Kamiokande measured a flux of $0.46 \pm 0.13(stat) \pm 0.08(syst)$ for $E_e > 9.3\,\mathrm{MeV}$ [64], compared to the expected value (normalized to 1) from the SSM. The GALLEX and SAGE experiments, both using a Gallium target for the IBD channel observed a flux of $[77.5 \pm 7.7]$ SNU[6] [62] in the case of GALLEX and $70.8^{+5.3}_{-5.2}(stat)^{+3.7}_{-3.2}(syst)$ SNU, $E > 233\,\mathrm{keV}$ for SAGE [102]. The expected flux from the SSM in both experiments would be 128 SNU.
With these successfully running neutrino experiments and evolving theoretical understanding in explaining these neutrino fluxes, the next milestone was achieved when atmospheric oscillations were confirmed by Super-Kamiokande in 1998 by observing an angle dependent ν_μ flux in agreement with a two flavor $\nu_\mu \rightarrow \nu_\tau$ oscillation [58]. Finally, the tau-neutrino was discovered in 2001 by the Donot collaboration at

[4] An old gold mine in South Dakota.
[5] The original suggestion from Pontecorvo was actually classified, because it was feared that this technique could be used to measure and classify the power output of American reactors.
[6] Solar Neutrino Unit: $10^{-36}\,\mathrm{cm}^{-2}\,\mathrm{s}^{-1}$.

Fermilab [48], which then completed the three lepton flavor family.

The current state regarding neutrino oscillations can be found in [46] and [13]. The three-flavor neutrino oscillation model is well established by multiple experiments with different neutrino sources. There are solar neutrino detectors like Borexino [21] (discussed in more detail in Chapter 2) and SNO [11]. Accelerator beam experiments MINOS [52], K2K [5] and reactor-neutrino detectors like Double Chooz [34], Daya Bay [7], RENO [36] and Kamland [69], as well as observatories for cosmic neutrinos like ANTARES [107] and IceCube [67].

1.3 Neutrino Oscillations

The theory of neutrino oscillation states that the neutrino flavor and mass eigenstates are mixed. A flavor eigenstate can be written as a superposition of the mass eigenstates. Thus when propagating, neutrinos oscillate and change their flavor eigenstate.
The first idea for this oscillation behavior came from Pontecorvo as early as 1957 [96], in his idea however not the flavor eigenstates where oscillating but rather the neutrino was changing to its anti-particle. A modified approach from Maki, Nakagawa and Sakata, described these flavor oscillation with a unitary PMNS matrix[7] representing the rotation of the mass and flavor eigenstates [77].
Using this mixing matrix $U_{\alpha i}$ a flavor eigenstate $|\nu_\alpha\rangle$ can be expressed as a linear combination of mass eigenstates $|\nu_i\rangle$, for neutrinos and anti-neutrinos. The following introduction and formalism is based on [12].

$$\begin{aligned} |\nu_\alpha\rangle &= \sum_1^N U^*_{\alpha i} |\nu_i\rangle \\ |\bar{\nu}_\alpha\rangle &= \sum_1^N U_{\alpha i} |\bar{\nu}_i\rangle \end{aligned} \tag{1.5}$$

with U as the mixing matrix and $\alpha = e, \mu, \tau$ as the three neutrino flavors.

In a three neutrino case the mixing matrix contains three Φ_{ij}, namely Φ_{12}, Φ_{13}, Φ_{23}. Using an Euler Rotation in the ij-plane with $R_{ij}(\Phi_{ij})$ and $\Gamma(\delta) = diag(1, 1, e^{i\delta})$ with a dirac type CP-Phase δ, the mixing matrix in a general form is then:

$$U = R_{23}(\Phi_{23})\Gamma(\delta)R_{13}(\Phi_{13})\Gamma^\dagger(\delta)R_{12}(\Phi_{12}) \tag{1.6}$$

The mixing matrix itself, in a three neutrino case, can be parameterized as in Equation 1.7, with $c_{ij} = \cos(\Phi_{ij})$, $s_{ij} = \sin(\Phi_{ij})$, and

$$U_3 = \begin{pmatrix} c_{12}c_{13} & s_{12}c_{13} & s_{13}e^{-i\delta} \\ -s_{12}c_{23} - c_{12}s_{23}s_{13}e^{i\delta} & c_{12}c_{23} - s_{12}s_{23}s_{13}e^{i\delta} & s_{23}c_{13} \\ s_{12}s_{23} - c_{12}c_{23}s_{13}e^{i\delta} & -c_{12}s_{23} - s_{12}c_{23}s_{13}e^{i\delta} & c_{23}c_{13} \end{pmatrix} \tag{1.7}$$

[7] Called PMNS matrix to incorporate the contributions of Pontecorvo, Maki, Nakagawa and Sakata.

The ordering of the mass squared difference $\Delta m^2_{ij} = m^2_i - m^2_j$, is done in the way that $m^2_{21} << |m^2_{31}|$ and $m^2_{21} > 0$ determining the mixing angles to lay in the range of $0 < \Phi_{ij} < \frac{\pi}{2}$.
If $m^2_{31} > 0$ it is refereed as the normal mass hierarchy whereas $m^2_{31} < 0$ is the inverted.

In a two neutrino case the PMNS matrix simplifies to:

$$U_2 = \begin{pmatrix} \cos\theta & \sin\theta \\ -\sin\theta & \cos\theta \end{pmatrix} \tag{1.8}$$

With the single mixing angle θ and $\Delta m^2 = m^2_2 - m^2_1$.

Starting with a neutrino state of $|\nu(t)\rangle$ its time evolution is governed by:

$$H\,|\nu(t)\rangle = i\frac{d\,|\nu(t)\rangle}{dt} \tag{1.9}$$

where H is the Hamiltonian. In a pure vacuum case the Hamiltonian is fully determined by mass and flavor and can be expressed as

$$H^f_{vac} = U H^m_{vac} U^\dagger \tag{1.10}$$

Assuming a neutrino with flavor α is created at $t_0 = 0$ and propagates in the time t, the distance of $x \approx t$, then the evolution of the flavor state is given by:

$$\nu^f(x) = T \cdot \exp\left(-i\int_0^x dx^{'} H^f(x^{'})\right)\nu^f(0) \tag{1.11}$$

or

$$\nu^f(x) = S^f \nu^f(0) \tag{1.12}$$

Where $S^f_{\beta\alpha}$ is the evolution Operator expressed as

$$S^f = T \cdot \exp\left(-i\int_0^x dx^{'} H^f(x^{'})\right) \tag{1.13}$$

Due to neutrino mixing the Hamiltonian is not diagonal thus leading to non-vanishing $\alpha \neq \beta$ terms.

The probability to detect a ν_β neutrino at a distance of L is generally given by

$$P(\nu_\alpha \to \nu_\beta) = |S^f_{\beta\alpha}(L)|^2 \tag{1.14}$$

In a pure vacuum and two neutrino mixing case, the transition probability for $\nu_\alpha \to \nu_\beta$ is then

$$P(\nu_\alpha \to \nu_\beta) = \sin^2(2\theta)\sin^2\left(\frac{\Delta m^2 L}{4E}\right) \tag{1.15}$$

where θ is the mixing angle between mass and flavor eigenstates and $\Delta m^2 = m^2_2 - m^2_1$. The sign of Δm^2 has not impact on the two-flavor vacuum oscillation and this can

therefore not be used to probe the mass hierarchy. The survival probability is in turn given by :

$$P(\nu_\alpha \to \nu_\beta) = 1 - \sin^2(2\theta)\sin^2\left(\frac{\Delta m^2 L}{4E}\right) \tag{1.16}$$

For the three-flavor transition probabilities (Equation 1.17), a one-dominant mass scale is assumed, meaning $\Delta m^2_{21} << |\Delta m^2_{31}| \approx |\Delta m^2_{32}|$.

$$\begin{aligned} P(\nu_e \to \nu_\mu) &= s^2_{23}\sin^2(2\Phi_{13})S_{23} + c^2_{23}\sin^2(2\Phi_{12})S_{12} - P_{CP} \\ P(\nu_e \to \nu_\tau) &= c^2_{23}\sin^2(2\Phi_{13})S_{23} + s^2_{23}\sin^2(2\Phi_{12})S_{12} + P_{CP} \\ P(\nu_\mu \to \nu_\tau) &= c^4_{13}\sin^2(2\Phi_{23})S_{23} - s^2_{23}c^2_{23}\sin^2(2\Phi_{12})S_{12} - P_{CP} \end{aligned} \tag{1.17}$$

Here $S_{23} = \sin^2\left(\frac{\Delta m^2_{32}L}{4E}\right)$ and $S_{12} = \sin^2\left(\frac{\Delta m^2_{21}L}{4E}\right)$ and $\Phi_{13} = 0$ in the case of S_{12} and P_{CP} describes the CP-violating phase:

$$P_{CP} = 8J\sin\left(\frac{\Delta m^2_{21}L}{4E}\right)\sin^2\left(\frac{\Delta m^2_{31}L}{4E}\right) \tag{1.18}$$

With $J = \frac{1}{8}\sin(2\Phi_{12})\sin(2\Phi_{23})\sin(2\Phi_{13})\cos(\Phi_{23})\sin(\delta)$

When considering neutrino oscillations in matter, the Hamiltonian is non-constant, and neutrino evolution can be expressed by adding a potential V to the vacuum Hamiltonian H_{vac}.

$$i\frac{d\nu^f(x)}{dx} = \left(H^f_{vac} + V^f(x)\right)\nu^f(x) \tag{1.19}$$

In the case of electron neutrinos produced in the sun, a starting point is to diagonalize the Hamiltonian in the basis of local mass eigenstates and apply the so called adiabatic approximation. In this approximation it is assumed that the distance, in which the medium changes its density properties is larger than the scale $L_{ij} \approx \frac{4\pi E}{\Delta m^2}$, in which the phase difference equals $\Delta\Phi_{ij} = 2\pi$.
When the baseline L of the neutrino transformation probability is much larger than L_{ij}, the probability $P(\nu_e \to \nu_e)$ from the point of production x_p to the point of detection x_d is given by:

$$P(\nu_e \to \nu_e) = \sum_i |\tilde{U}_{\alpha i}(x_p)|^2 |\tilde{U}_{\beta i}(x_d)|^2 \tag{1.20}$$

In the two neutrino scenario (where only $\Phi_{12} \neq 0$), an effective matter oscillation angle can be expressed as:

$$\sin\left(2\tilde{\Phi}_{12}\right) = \frac{\sin(2\Phi_{12})}{\sqrt{\sin^2(2\Phi_{12}) + C^2}} \tag{1.21}$$

with $C(x) = \cos(2\Phi_{12}) - \frac{2\sqrt{2}G_F n_e(x)E}{\Delta m^2_{21}}$, where n_e is the electron density and an effective squared mass term:

$$\Delta\tilde{m}^2_{12} = \tilde{m}^2_2 - \tilde{m}^2_1 = \Delta m^2_{21}\sqrt{\sin^2(2\Phi_{12}) + C^2} \tag{1.22}$$

In the case of $\Delta m^2_{21} > 0$ and $\Phi_{12} < \frac{\pi}{4}$, Equation 1.23 reaches its maximum on the local mixing angle $\tilde{\Phi}_{12}$

$$\Delta m^2_{21} \cos(2\Phi_{12}) = 2\sqrt{2} G_F n_e(x) E \tag{1.23}$$

If this region, which is determined by the electron density n_e, is wide enough, all ν_e convert to a different flavor, which is refereed to as the MSW effect.

With typical solar electron density and neutrino values $n_e \approx 10^{26}\,\mathrm{cm}^3$, $E \approx 1\,\mathrm{MeV}$, $\Delta m^2_{21} \cos(2\Phi_{12}) \approx 10^{-5}\,\mathrm{eV}^2$ the survival probability for solar ν_e can be estimated as[8]

$$P(\nu_e \to \nu_e) \approx \frac{1}{2} + \frac{1}{2} \cos\left(2\tilde{\Phi}_{12}\right) \cos(2\Phi_{12}) \tag{1.24}$$

This three-flavor formalism is very capable of explaining solar/atmospheric/reactor neutrino fluxes. Recent values for the important mass squared differences and mixing angles can be found in Table 1.1.

1.4 Light Sterile Neutrinos

Besides some experimental (controversial) indication for light sterile neutrinos, discussed in Section 1.5, the theoretical question about right-handed neutrinos can also lead towards these hypothetical particles. A right-handed neutrino would be represented as a weak isospin singlet in the Standard Model. Although not able to interact via the weak force[9], mixing with the left-handed neutrinos would be possible. There could be more than one sterile neutrino, and models assuming this are typically referred to $3+1$ or $3+2$ and $3+3$ in case of multiple sterile neutrinos. Indications from cosmology however disfavor all but one additional sterile neutrino [100]. Their mass could be generated by combining majorana and dirac mass therms via the SeeSaw mechanism [1], which leads typically to heavy sterile neutrinos, but the mechanism can produce lighter ones, too. From the results of the Large Electron-Positron Collider (LEP) at CERN the number of active neutrinos that couple to $W^\pm$ or Z - bosons is $N_\nu = 2.984 \pm 0.008$ [53], it is clear that an additional neutrino can only be a sterile one. From experimental observations a squared mass difference in the range of $0.1 - 1\,\mathrm{eV}^2$ is preferred (see Figure 1.2) compared to the solar $\Delta m^2_{solar} = 7.5 \cdot 10^{-5}\,\mathrm{eV}^2$ and atmospheric $\Delta m^2_{atmo} = 2.3 \cdot 10^{-3}\,\mathrm{eV}^2$ [61] mass squared differences. Squared masses of a few eV^2 or up to keV^2 would influence the β-decay spectrum and thus, would have been detected by now. Here the electron-neutrino flavor state, mixed with the heavier sterile one, would lead to a kink in the continuous recoil spectrum, which could be be measured, possibly by the upcoming KATRIN [56] experiment.

In terms of appearance/disappearance probabilities similar steps as in Section 1.3

[8] Assuming a detection at point x_d in vacuum.
[9] Hence the sterile prefix.

Table 1.1: Overview table from multifit analyses for current (2017) neutrino mass squared and mixing angle values. This combined analysis has been performed by data obtained from anti-neutrino channels of T2K, data from NOνA, Daya Bay, RENO, Double Chooz, IceCube, ANTARES and the fourth phase of Super-Kamiokande. Table produced from [46].

Parameter	best fit $\pm 1\sigma$	2σ range	3σ
$\Delta m^2_{21}[10^{-5}\text{eV}^2]$	7.56 ± 0.19	7.20-7.95	7.05-8.14
$\Delta m^2_{31}[10^{-3}\text{eV}^2]$ (NO)	2.55 ± 0.04	2.47-2.63	2.43-2.67
$\Delta m^2_{31}[10^{-3}\text{eV}^2]$ (IO)	2.49 ± 0.04	2.41-2.57	2.37-2.61
$\sin^2(2\Phi_{12})/10^{-1}$	$3.21^{+0.18}_{-0.16}$	2.89-3.59	2.73-3.79
$\Phi_{12}/^\circ$	$34.5^{+1.1}_{-1.0}$	32.5-36.8	31.5-38.0
$\sin^2(2\Phi_{23})/10^{-1}$ (NO)	$4.30^{+0.20}_{-0.18}$	3.98-4.78& 5.60-6.17	3.84-6.35
$\Phi_{23}/^\circ$	41.0 ± 1.1	39.1-43.7 & 48.4-51.8	38.3-52.8
$\sin^2(2\Phi_{23})/10^{-1}$ (IO)	$5.96^{+0.17}_{-0.18}$	4.04-4.56 & 5.56-6.25	3.88-6.38
$\Phi_{23}/^\circ$	50.5 ± 1.0	39.5-42.5 & 48.2-52.2	38.5-53.0
$\sin^2(2\Phi_{13})/10^{-2}$ (NO)	$2.155^{+0.090}_{-0.075}$	1.98-2.31	1.89-2.39
$\Phi_{13}/^\circ$	$8.44^{+0.18}_{-0.15}$	8.1-8.7	7.9-8.9
$\sin^2(2\Phi_{13})/10^{-2}$ (IO)	$2.140^{+0.082}_{-0.0.085}$	1.97-2.30	1.89-2.39
$\Phi_{13}/^\circ$	$8.41^{+0.16}_{-0.17}$	8.0-8.7	7.9-8.9
δ/π (NO)	$1.40^{+0.31}_{-0.20}$	0.85-1.95	0.00-2.00
$\delta/^\circ$	252^{+56}_{-36}	153-351	0-360
δ/π (IO)	$1.44^{+0.26}_{-0.23}$	1.01-1.93	0.00-1.17 & 0.79-2.00
$\delta/^\circ$	259^{+47}_{-41}	182-347	0-31 & 142-360

can be taken, and a unitary mixing matrix similar to Equation 1.7 can be used:

$$U_{3+1} = \begin{pmatrix} U_{e1} & U_{e2} & U_{e3} & U_{e4} \\ \cdot & \cdot & \cdot & U_{\mu 4} \\ \cdot & \cdot & \cdot & U_{\tau 4} \\ U_{s1} & U_{s2} & U_{s3} & U_{s4} \end{pmatrix} \tag{1.25}$$

where the entries refer to electron-neutrino, muon-neutrino, tau-neutrino and sterile neutrino respectively.
At short baselines ($L < 5\,\text{km}$), the oscillations arising from Δm^2_{atmo} and Δm^2_{solar} are negligible. When deriving the appearance/disappearance probabilities, the terms referring to these two squared masses can be ignored, and the appearance/disappearance probabilities written as:

$$P(\alpha \to \beta) \approxeq 4|U_{\alpha 4}|^2|U_{\beta 4}|^2 \sin^2\left(\frac{1.27\Delta m^2_{41} L[\text{km}]}{E[\text{MeV}]}\right) \tag{1.26}$$

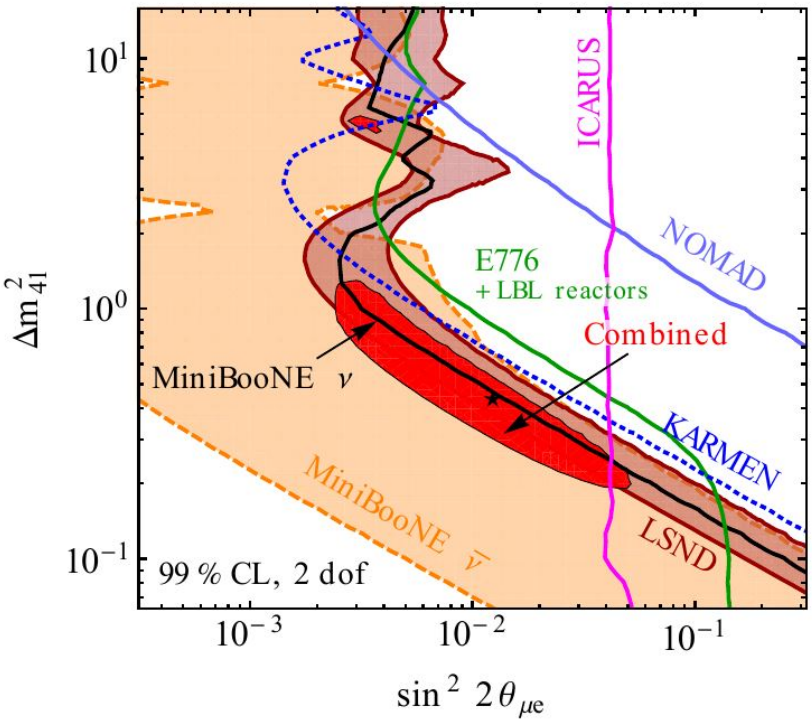

Figure 1.2: The combined data (neutrino and anti-neutrino channels) from LSND, MiniBooNE, KARMEN, NOMAD, ICARUS and E776.
It shows the upper bounds in the $3+1$ model for $\nu_\mu \to \nu_e$ and $\bar{\nu}_\mu \to \bar{\nu}_e$ appearance. Located in the red zone of combined data, is the best fit point at $\sin^2(2\Phi_{\mu e}) = 0.013$, $\Delta m^2_{41} = 0.42\,\mathrm{eV}^2$ [72].

and

$$P(\alpha \to \alpha) \approxeq 1 - 4(1 - |U_{\alpha 4}|^2)|U_{\alpha 4}|^2 \sin^2\left(\frac{1.27\Delta m^2_{41} L[\mathrm{km}]}{E[\mathrm{MeV}]}\right) \tag{1.27}$$

Using the Euler Rotation expressions similar to Section 1.3, this then exemplary leads to:

$$P(\nu_e \to \nu_e) \approxeq 1 - \sin^2(2\Phi_{14}) \sin^2\left(\frac{1.27\Delta m^2_{41} L[\mathrm{km}]}{E[\mathrm{MeV}]}\right)$$

$$P(\nu_\mu \to \nu_\mu) \approxeq 1 - \sin^2(2\Phi_{24}) \sin^2\left(\frac{1.27\Delta m^2_{41} L[\mathrm{km}]}{E[\mathrm{MeV}]}\right) \tag{1.28}$$

$$P(\nu_\mu \to \nu_e) \approxeq \frac{1}{4} \sin^2(2\Phi_{14}) \sin(2\Phi_{24}) \sin^2\left(\frac{1.27\Delta m^2_{41} L[\mathrm{km}]}{E[\mathrm{MeV}]}\right)$$

For very short baseline the remaining $P(\nu_\tau \to \nu_\tau)$, $P(\nu_\mu \to \nu_\tau)$, $P(\nu_e \to \nu_\mu)$, $P(\nu_e \to \nu_\tau)$, $P(\nu_\tau \to \nu_e)$, $P(\nu_\mu \to \nu_\tau)$ and $P(\nu_\tau \to \nu_\mu)$ can be derived similarly.

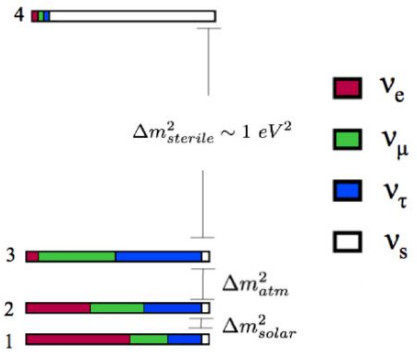

Figure 1.3: Illustration of the mass and flavor states in the $3+1$ model approach [41].

1.5 Deviation from the Three-Flavor Neutrino Model

Although the three-flavor oscillation model is overall very successful and congruent with the vast majority of experiments performed, there remain a few inconsistencies and mysteries, especially at short baselines. The two most considerable issues originate from two beam experiments and from the so called reactor anomaly.

The Liquid Scintillator Neutrino Detector (LSND), a beam experiment located at Los Alamos, was the first to report a $\bar{\nu}_e$ excess for the appearance of $\bar{\nu}_\mu \rightarrow \bar{\nu}_e$. Protons with an energy of 798 MeV are shot on a beam dumb, resulting mostly in π^+ production. These pions and resulting muons mostly (97%) decay at rest via $\pi^+ \rightarrow \mu^+\nu_\mu$ and $\mu^+ \rightarrow e^+\nu_e\bar{\nu}_\mu$. The complementary π^- and μ^- are captured in the copper and iron shielding and the contribution of $\bar{\nu}_e$ originating from them is estimated to be a total of $< 8 \cdot 10^{-4}$ of the entire flux. At a distance of 30 m from the beam, $\bar{\nu}_e$ are detected via the IBD in a cylindrically shaped detector, containing mineral oil and scintillator. In Figure 1.4 the excess of $\bar{\nu}_e$ of a total of $87.9 \pm 22.4(stat) \pm 6.0(syst)$ events leading to a significance of 3.8σ [4] over the expectation can be seen. This appearance could be due to a Δm^2 in the range of $0.2\,\mathrm{eV}^2$ - $2\,\mathrm{eV}^2$
A re-evaluation of the data on pion production used for LSND by Bolshakova et al. [15] found an underestimation in the background flux of $\bar{\nu}_e$ and therefore reduced the certainty of the excess to 2.9σ. In a follow up, done by the same group, the analysis of 2100 IBD candidate events, considering correlated and uncorrelated γ events, lowers this to 2.3σ [16] and raises more questions on this unexpected appearance behavior, but also on the LSND experiment itself.

The MiniBooNE experiment, also operating on a beam, was motivated by the LSND excess. Located 540 m from the beam target a sphere filled with 800 t mineral oil detected events by their Cerenkov light of outgoing particles [28]. In the region above 475 MeV no indication of an excess was found and that area is in full agreement with the prediction of the three-flavor oscillation model, but the region < 475 MeV did report an excess ν_e comparable to LSND. Even with the total data set corre-

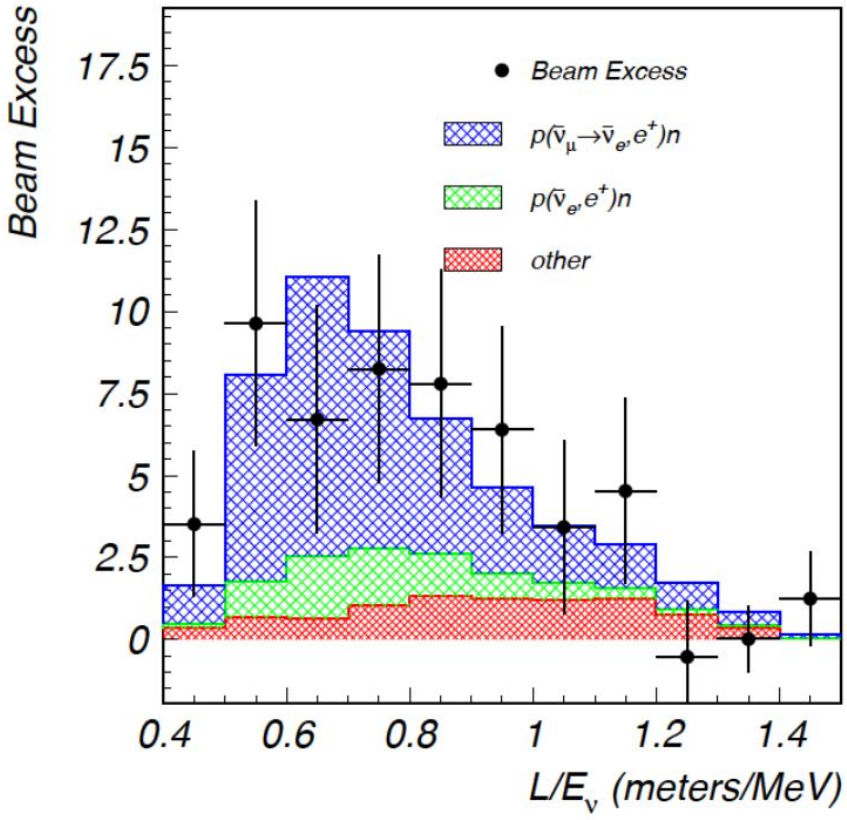

Figure 1.4: Data from the LSND experiment hinting at a possible excess in the appearance of $\bar{\nu}_\mu \to \bar{\nu}_e$. Backgrounds from the beam are shown in green, whilst other background contributions are colored red. The black data points, with quadratic statistic and systematic error bars, seem to roughly fit to the blue prediction for a signal $\bar{\nu}_\mu \to \bar{\nu}_e$ from the $3+1$ scheme [4].

sponding to $5.66 \cdot 10^{20}$ protons at a beryllium target, in the anti-neutrino channel no comparison to the LSND results could be made due to low statistics [35].

Besides these anomalies and unexpected findings from accelerator beam experiments, possible deviations from the three-flavor scenario arise also from reactor neutrino experiments. The most important ingredients for reactor neutrino flux estimation originate from the various β- decay branches of ^{235}U, ^{238}U, ^{239}Pu, ^{241}Pu and their resulting fission fragments [65]. An original measurement on the β- spectra of these isotopes was performed in the 80 s and a re-evaluation of these spectra by Mueller et al. in 2011 [85] had significant consequences on the overall expected reactor neutrino flux.
For a detector located at < 100 m from the reactor, this translates to a change in the expected event rate from 0.976 ± 0.0024 to 0.9443 ± 0.0023 [83]. This deviation of about 3% missing flux for the near distances became known as the reactor anomaly (see Figure 1.5). This anomaly also seemed compatible with an additional sterile neutrino of $\Delta m^2 > 1.5\,\mathrm{eV}^2$ [83], but could ultimately also be explained by wrong yields of ^{235}U. A recent Daya Bay paper [39] reports an energy dependent correlation

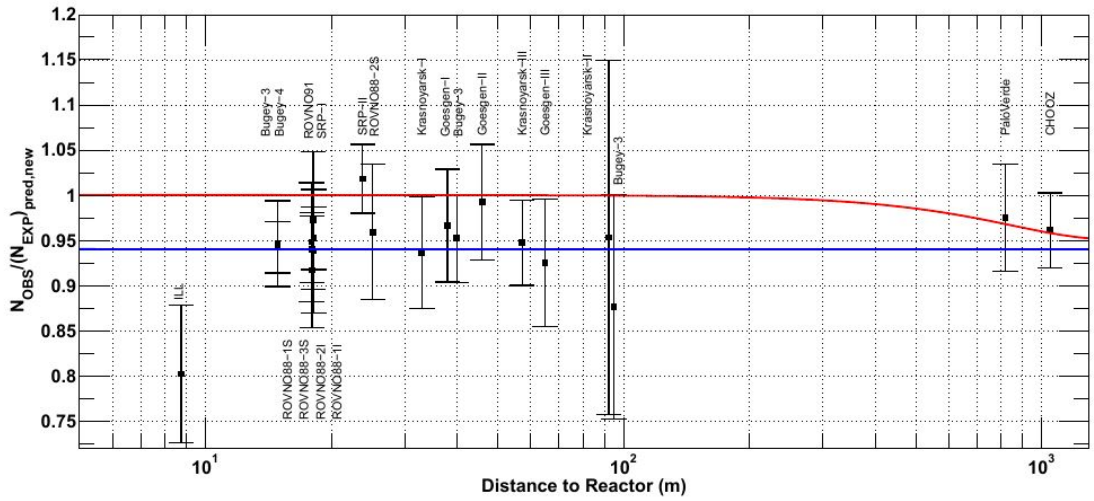

Figure 1.5: Illustration of the reactor anomaly. Errors from the experiments and the anti-neutrino spectra are in quadrature on the black data points. The three-flavor solution is shown in red, whilst the blue line corresponds to a $3+1$ model with a sterile neutrino, in this case with a mass state of $|\Delta m_{S,R}| > 1\,\mathrm{eV}^2$ and a mixing angle $\sin^2(2\Phi_{S,R}) = 0.12$ [83].

between the reactor neutrino flux and the evolution of the core fuel isotopes. With 2.2 millions IBD candidates and the calculated yields per fission, this indicates the incorrect prediction of the flux originating from ^{235}U as the main source at the core of the reactor neutrino anomaly.

The picture is all but conclusive at this point. Whatever the exact reasons for this deviations or anomalies might be, ranging from theoretical, technical or experimental issues, or even a new particle like the light sterile neutrino, these anomalies clearly show the need for a dedicated experiment in order to shine light and provide more data on the oscillation characteristics on short baselines. The SOX[10] experiment when proposed in 2013 had the goal to tackle these remaining anomalies on short distances of neutrino oscillations [20]. With the use of a strong radioactive source and an already well established detector (Borexino), it would have taken a closer look at the possible disappearance or even oscillation behavior of this anti-neutrino source in the distance of around 8 meters.
After the following introduction to the Borexino detector in Chapter 2, the SOX experiment itself will be presented in Chapter 3.

[10]Short distance neutrino Oscillations with BoreXino.

Chapter 2

The Borexino Detector

2.1 Introduction

The Borexino detector is a liquid scintillator neutrino detector, mainly designed to detect low energy solar neutrinos from the sun's core. It consists of a liquid scintillator detector volume, surrounded by a buffer layer and is encapsulated in a stainless steel sphere. The Borexino experiment, amongst others, is housed in the Hall C of the Laboratori Nazionali del Gran Sasso (LNGS), currently the world's largest underground research facility. This laboratory is under the Gran Sasso massiv[1], in the Abruzzo in central Italy, roughly 140 km from Rome (Figure 2.1).
The overburden of 1400 m corresponds to a water shielding equivalent of 3800 m and provides a good shielding for cosmic muons, resulting in a muon flux suppression by a factor of approximately 10^{-6}. Initially designed and build for the measuring of neutrinos from the electron capture of ^{7}Be, Borexino's unprecedented radio-purity enabled a broadening of the measurement capabilities.
Borexino was proposed in 1991 with the Borexino yellow book [57][2] and with the development of a first test facility, the Count Test Facility (CTF), which was constructed in order to learn about the scintillator properties, the backgrounds present and purification techniques needed to achieve a high radio-purity. The construction of Borexino itself followed and data taking started in May 2007 and is continuing successfully until today.

The ongoing operations, the good understanding of the detector, the low background and the very good radio-purity made Borexino the ideal detector for the SOX experiment. This chapter will introduce Borexino's structure, geometry and detection principle followed by a short overview of the milestones and achievements of this neutrino detector. The coming chapter follows the description of the Borexino detector found in [18] and its results obtained from measurement during 2007 to 2010 [21].

[1] Italian for Great Boulder

[2] In the first idea for a liquid scintillator neutrino experiment, trimethyl borate was favored as detector material, which is still present in the Borexino acronym, coming originally from **Bor**ate **Ex**periment combined with the italian **-ino** belittlement. This substance was then later abandoned and changed to the now used PC+PPO.

Figure 2.1: On the left, a helicopter view of the topside of the LNGS laboratory can be seen, surrounded by mountains in the Abruzzo [75]. On the right, a schematic overview of the underground Laboratory and its connection to the highway tunnel is shown. The Borexino detector itself is located in Hall C [76].

2.1.1 Overview and Geometry

Borexino makes use of an organic liquid scintillator (more in Section 2.1.3.1), which produces scintillation light by neutrino electron elastic scattering. In comparison to a radio-chemical detection method, this enables real time measurement, as well as a low enough energy threshold, especially needed for solar neutrinos from electron capture of ^{7}Be. The advantage of using an organic scintillator which is liquid at room temperatures, is its low solubility of unwanted radioactive contributors, which makes purification of the material possible. The downside is that, β- and γ-events from background sources are indistinguishable from neutrino events, leading to much stricter requirements on radio-purity on all evolved materials (as well as a very detailed background understanding).

The Borexino detector, shown in Figure 2.2 and Figure 2.3 can be grouped in two main parts, namely the Inner and Outer Detector. The Outer Detector (OD) (Section 2.1.6) serves as a muon veto (tracker) and overall buffer for the sensitive volume inside of Borexino. The OD consists of a stainless steel tank (with a diameter of 18 m) providing the structure and encapsulating Borexino and a Water Tank (WT) providing a buffer layer against radiation from the surrounding rock and operates as an Cherenkov light muon tracker. The WT is therefore equipped with 208 PMT's and the whole interior surface of both the WT and the stainless steel tanks inside are covered with a light reflective material[3] in order to maximize the Cherenkov light output. Although the depth of Borexino corresponds to a muon flux reduction of $\approx 10^{-6}$, this still results in a muon rate of ≈ 4000 per day, thus making the OD an important necessity.

The Inner Detector (ID) (discussed in Section 2.1.3) consists of the Stainless Steel Sphere (SSS), with a radius of 6.85 m and holds the buffer and scintillator liquids and the two nylon vessels. The SSS is the supporting structure on which 2212 PMTs

[3] Tyvek

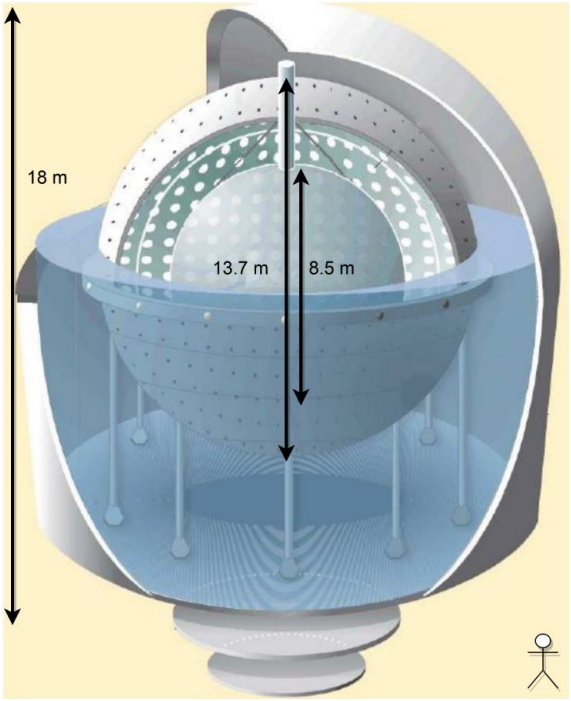

Figure 2.2: This 3D model of Borexino shows its layered sphere structure. The Outer Detector, composed of the outermost stainless steel shell and the water tank, holds the inner vessel with its stainless steel and nylon spheres, held on steel piers. Image based on [18].

(8″ E.T.L. 9357) as well as the rope structure holding the nylon vessels are mounted. The Outer Nylon Vessel (OV), with a radius of 5.50 m, holds the buffer and a light quenching liquid and shields the Inner Nylon Vessel (IV) mainly against diffusion of ^{222}Rn originating from the steel and PMT glass. Nearly all of the PMTs are equipped with light concentrators, which increase photon detection from the scintillator region. Inside the sensitive IV (r = 4.25 m) a so called Fiducial Volume (FV) is defined by a software cut/selection, to exclude background events (see Chapter 5). For the solar neutrino analyses, the FV was typically of the order of r $\approx$ 3 m, while the SOX experiment would have planned to use a FV as large as possible.

2.1.2 Detection Principle

Besides the already mentioned IBD, Borexino can detect electron neutrinos via electron elastic scattering.

$$\nu_x + e^- \rightarrow \nu_x + e^- \tag{2.1}$$

where $x = e, \mu, \tau$ as this detection process is valid for all neutrino flavors. The incoming neutrino with the energy E_ν transfers some of its energy to the electron, which in turn interacts with the scintillator, thus producing the observable signal. In this scattering process the amount of transfered energy from the neutrino to the electron is not fixed, but depends on the incident angle, which leads even for mono-energetic neutrinos, to a continuous recoil signal T_R. This spectrum extends to the

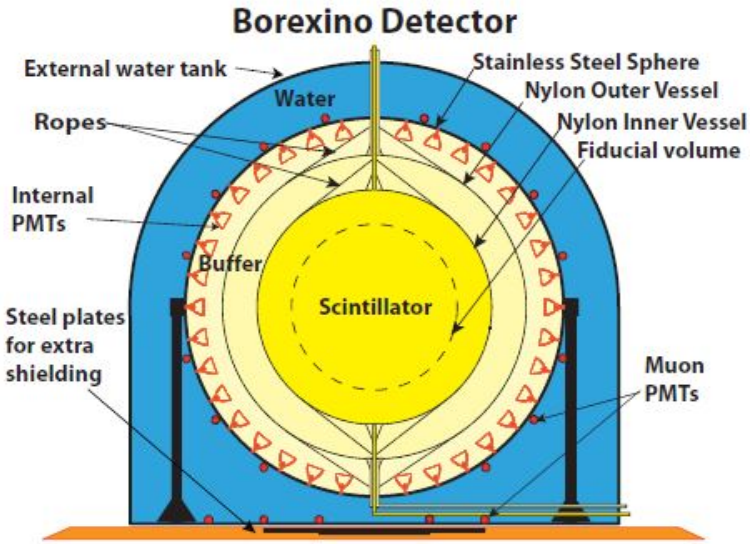

Figure 2.3: This illustration shows the layout of the Borexino detector. On the bottom, thick layers of steel provide shielding against radiation from the rock, while the blue water layer acts as a muon veto and the last shielding before the scintillator (yellow) is the buffer, shown in beige. The Outer Nylon Vessel is another thin barrier for the Inner Vessel, by protecting mostly against radon diffusion. Image from [18].

maximum energy T_R^{max}:

$$T_R^{max} = \frac{E_\nu}{1 + \frac{m_e c^2}{2E_\nu}} \tag{2.2}$$

with m_e as the electron rest mass. In the case of the mono-energetic 862 keV ^{7}Be solar neutrinos, T_R^{max} is 665 keV.

The cross section in dependence of the neutrino energy for this elastic scattering process can be seen in Figure 2.4 for σ_e and $\sigma_{\mu,\tau}$. For the recoil spectrum, radiative corrections, especially at higher electron energies become non negligible [10]. Due to the fact that ν_e react via Neutral Current (NC) and Charge Current (CC) interactions and $\nu_{\mu,\tau}$ only via NC, the energy dependent interaction probability for ν_e is approximately five times larger at 1 MeV than those for $\nu_{\mu,\tau}$.

The total rate of neutrino interactions R_ν, taking neutrino oscillations into account, is dependent on the neutrino flux Φ_ν, the density of electrons in the target volume N_e[4], the differential energy spectrum of solar neutrinos $d\lambda/dE_\nu$ and the electron-neutrino survival probability P_{ee}

$$R_\nu = N_e \Phi_\nu \int \frac{d\lambda}{dE_\nu} dE_\nu \int \left(\frac{d\sigma_e(E_\nu, T_R)}{dT_R} P_{ee}(E_\nu) + \frac{d\sigma_\mu(E_\nu, T_R)}{dT_R} [1 - P_{ee}(E_\nu)] \right) dT_R \tag{2.3}$$

[4]For Borexino, $N_e = 3.307 \pm 0.003 \cdot 10^{31}\, e^-/100\,\text{tons}$

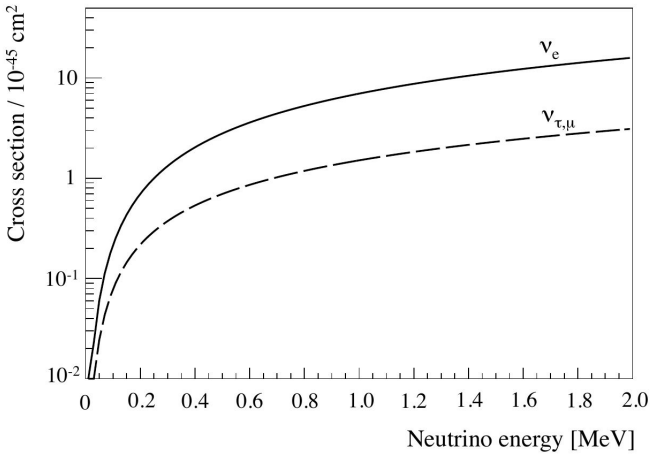

Figure 2.4: The neutrino electron elastic scattering cross section as a function of the neutrino energy. The solid line corresponds to the cross section of the ν_e, which is roughly 5 times larger at around 1 MeV than the corresponding cross section for $\nu_{\mu,\tau}$, shown with the dashed line [21].

This rate leads to a count rate of 46.48 ± 3.35 (cpd)/100 tons[5] for ^{7}Be solar neutrinos.

2.1.3 Inner Detector

Borexino's Inner Detector (ID) is supported by the 6.85 m radius stainless steel sphere (SSS), and holds two nylon vessels. The inner nylon vessel contains the PPO + PC solution, discussed in the next section. The Outer Vessel (OV) contains the PPO as a buffer liquid as well as a light quencher (DMP)[6] to reduce the scintillation yield of pure PC, which is also filled between the OV and the SSS. A short introduction and explanation of the important parts, such as the nylon vessels, scintillator, electronics and trigger chain of the ID follows in the next sections.

2.1.3.1 Scintillator

The liquid scintillator solution inside Borexino's IV is a mixture of pseudocumene (PC), 1, 2, 4-trimethylbenzene $C_6H_3(CH_3)_3$ (PC) as a solvent with 2, 5-diphenyloxatole $C_{15}H_{11}NO$ (PPO) as a solute. Essential requirements for this PC/PPO solution are a high light yield, fast decay time and a high light transparency. Four tons of this mixture where extensively studied in the CTF via a spherical arrangement with 100 PMTs. This enabled measuring and probing of the optical properties, absorption and re-emission on PPO and scattering processes, which play a key role for the precise reconstruction of the position and energy. In order to achieve a sufficient energy resolution, besides the high light yield and a low self-absorption, the emitted light spectrum and the PMTs efficiency should be aligned.
With a light yield of about 10000 photons/MeV and an emission spectrum that

[5] Calculated for a high metallicity Standard Solar Model [21].
[6] Dimethylphthalate $C_6H_4(COOCH_3)_2$, with an initial amount of 5 g/l, later reduced to 3 g/l due to an inner vessel leak.

peaks at 360 nm (as seen in Figure 2.5), these requirements are met. Combining the

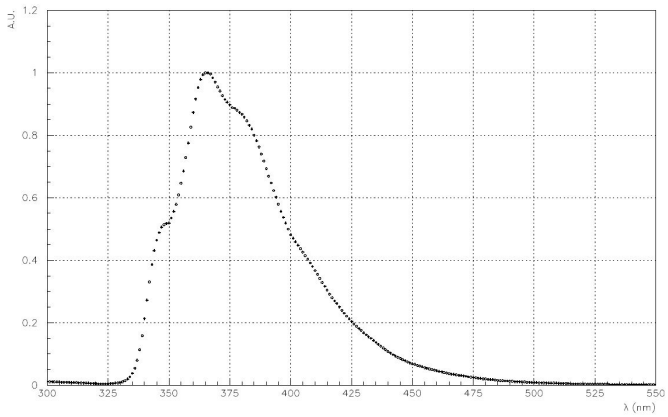

Figure 2.5: The emission spectrum of the PPO+PC solution, used as Borexino organic scintillator. With a light yield of $\approx$ 500 photons/MeV, this spectrum shows a peak at 360 nm, matching well the PMTs quantum efficiency. Image from [18].

absorption of the scintillator and the buffer fluid leads to a remaining light collection of about 500 photons/MeV, reaching the PMTs. This translates to an energy resolution of 5% at 1 MeV and at the 1σ level. Figure 2.6 shows the attenuation length, which is about 10 m at 430 nm. An absorbed photon is re-emitted with a probability of 80% by PPO with an decay time of 1.6 ns, thus leading to a low loss in photons in the scintillator medium. The exact mechanism by which an incoming

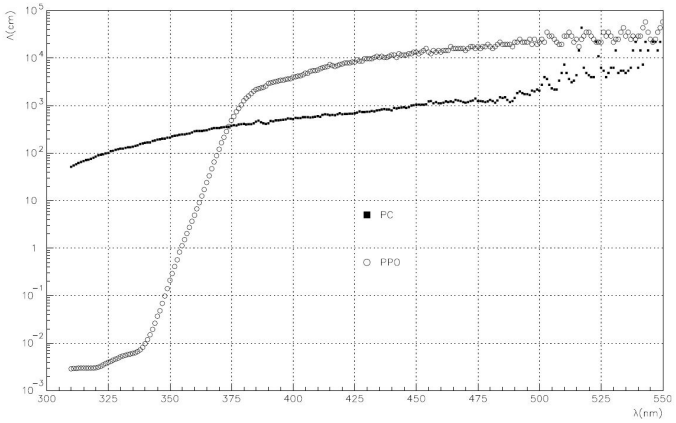

Figure 2.6: The attenuation length of PPO, shown in the empty circles and for PC, seen as the full squares [18].

particle looses its energy, excites the molecules and produces the scintillation light cannot be fully understood without the ionizing quenching effect [14]. This intrinsic effect depends on the type of particle and leads to a non-linear relation between the deposited energy and the light production. This requires a different treatment for α- , β- and γ-particles, even when they have the same energy.
Birks relation (Equation 2.4), which is used for e^- and e^+, connects the photons

emitted from the scintillation process dY^{Ph} per path length dx, to the specific energy loss dE/dx.

$$\frac{dY^{Ph}}{dx} = \frac{Y_0^{Ph} \cdot dE/dx}{1 + kB \cdot dE/dx} \tag{2.4}$$

where kB is the quenching parameter. Without quenching ($kB = 0$), the light yield would be $Y_0^{Ph} \approx 10^4$ photons/MeV. The value of kB has been obtained via a dedicated calibration with γ-sources to kB=(0.0115 ± 0.0007) cm/MeV.
The total of emitted photons dY_x^{Ph}, with $x = (\alpha, \beta, \gamma)$, regarding the particle dependence, is then given by:

$$Y_x^{Ph} = Y_0^{Ph} Q_x(E) E \tag{2.5}$$

with the quenching factor $Q_x(E) < 1$.
Using Equation 2.4 and the integration over dY^{Ph}/dx for β-particles, $Q_\beta(E)$ can be derived:

$$Q_\beta(E) = \frac{1}{E} \int_0^E \frac{dE}{1 + kB \cdot dE/dx} \tag{2.6}$$

It can be seen in Figure 2.7, that the quenching becomes more important the lower the energy, and especially so in the range of a few keV. This quenching effect has a

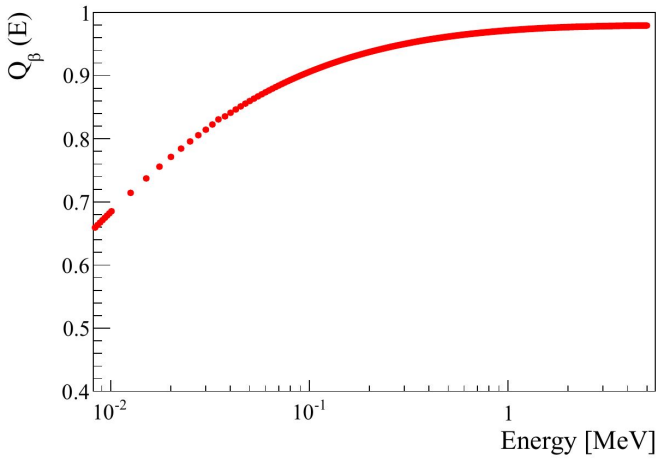

Figure 2.7: The quenching factor $Q_\beta(E)$ for β-particles, analog to Equation 2.6. This plot corresponds to kB=0.011 cm/MeV [21].

larger impact on α-particles than compared to β-particles. The resulting light yield for a α-particle with an energy of a few MeV, is about a factor of ten higher than when compared to an electron with the same energy [18].
In contrast to α- and β-particles, γ-rays are not able to easily excite the molecules directly, but can do so only via scattering or the production of secondary electrons/positrons. The amount of scintillation light for γ-rays can be calculated via the sum of all the contributions from electrons:

$$Y_\gamma^{Ph} = Y_0^{Ph} \sum_i E_i Q_\beta(E_i) = Y_0^{Ph} Q_\gamma \cdot E \tag{2.7}$$

This leads to a non-negligible γ quenching factor (for γ energies in the MeV range), since for the same energy E, $Q_\gamma(E) \leq Q_\beta(E)$.

Another relevant effect is the production of Cherenkov light created in the scintillator. This depends on the refraction index as a function of the wavelength $n(\lambda)$ and thus is introducing an energy dependency in the production of the Cherenkov photons N_C. Their amount is given by the Frank-Tamm equation [87], per wavelength and unit length:

$$\frac{d^2N_C}{dxd\lambda} = \frac{2\pi\alpha}{\lambda^2}\left(1 - \frac{c^2}{v^2n^2(\lambda)}\right) \tag{2.8}$$

where v denotes the particle velocity inside the scintillator medium, α the fine structure constant and the condition $\left(1 - \frac{c^2}{v^2n^2(\lambda)}\right) > 0$ is met.
The resulting Cherenkov photons spectrum exceeds into the ultraviolet (with a mean free wavelength in the scintillator of sub-mm) and these are thus invisible for the PMTs. But, by the absorption and re-emission behavior, these photons get wavelength-shifted to the scintillator spectrum and can therefore be observed by the PMTs. The timing of the re-emission is particle dependent and can therefore be useful for the discrimination between α- and β-particles. In fact the tail end of the pulse created by α-particles is longer compared to βs and is used as a statistical α-background subtraction tool. More detail on the Cherenkov photons production and their implementation in Borexino's simulation framework (Section 6.1) can be found in [24].

2.1.3.2 Nylon Vessels

Encapsulated within the 6.85 m SSS are the two nylon balloons, the IV and the OV, with a radius of 5.5 m and 4.25 m. It is desirable to keep the sensitive scintillator volume as far from radioactive backgrounds as possible. This also means that the nylon vessels themselves have to be as radio-pure as possible.
By working under clean conditions and with a special radon absorption system, the thin nylon sheets[7] were assembled. For the IV and OV this resulted in a very low contamination of ^{226}Ra, measured at 0.21 ± 0.3 mBq/kg of ^{226}Ra, contributing to a total of less than two decays per day with regard to the FV. After assembling, testing and cleaning, the IV and OV were shipped to Gran Sasso, where they got installed and inflated with N_2 directly inside the SSS before the filling process (see Figure 2.8).

The nylon vessels can be selected to be very thin and delicate to provide good optical transparency[8], but still have to be leak tight and chemically compatible.
Although selected to be of equal densities, there is a 0.4% density difference between buffer and scintillator liquids. To withstand the resulting buoyancy forces

[7] The material itself, used for both nylon vessels, is Nylon-6, which is a blend of ADS40T / Ultramid B4.
[8] The refractive index of Nylon-6 is 1.43, similar to PC.

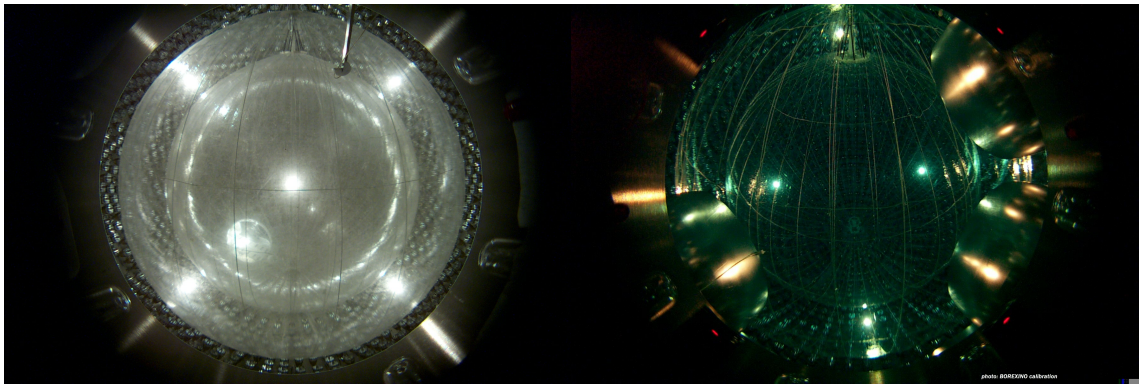

Figure 2.8: View inside Borexino, taken with a CCD camera positioned on the stainless steel sphere. The left image shows the N_2 inflated vessels before the filing with scintillator and buffer liquids whilst the right image shows the vessels after the filling. Images from [31], [32].

the nylon membranes have a sufficiently high material strength with a yield point of $20 - 70\,\mathrm{MPa}$. This material strength has to be retained while being submerged in liquids and with a possible temperature difference of up to 5°C (comparable to a 0.5% density difference), because there is a temperature gradient present in the detector from south to north. The leak tightness has been measured as $0.005\,\mathrm{cm}^3/\mathrm{s}$ for the IV and $0.1\,\mathrm{cm}^3/\mathrm{s}$ for OV at $\Delta P = 1\,\mathrm{mbar}$.
The thin (0.125 mm) nylon vessels are very flexible and are therefore hold and enforced by a tensolyn rope structure. This ultra dense polyethylene material is free of potassium, especially free of $^{40}\mathrm{K}$ a natural potassium isotope and γ emitter, which is usually found in rope materials. These tensolyn ropes hold the two nylon vessels in their spherical shape, by being looped vertically, over and under the vessels as well as horizontally around them. Ropes and nylon vessels are attached to a cast nylon and copper structure (end region/endcap region), on top and bottom of the SSS. The end region also holds the LASER calibration system, used for calibrating the event-position reconstruction, as well as temperature sensors for the buffer, and strain gauges to monitor buoyancy forces on the vessels.

2.1.3.3 Vessel Leak

In April 2008 scintillator leaked from the IV to the buffer region, by a small hole with the location $26° < \Theta < 37°$ and $225° < \Phi < 270°$. This leak was first identified when a large amount of events outside the IV were discovered during analysis in September 2008. A sample taken from the buffer then showed a high PPO concentration and confirmed the IV leak.
Seven CCD cameras mounted on the SSS were used to determine the vessel shape and derive the leak rate, estimated at approximately $1.33\,\mathrm{m}^3/\mathrm{month}$. This leak destabilized and deformed the IV. Figure 2.9 shows this deformation of the IV after the leak in January 2009 compared to the vessel shape of January 2008. To get this leakage under control, the pressure difference between the scintillator and buffer liquids was reduced, by distilling the light quencher (DMP) out of the buffer fluid.

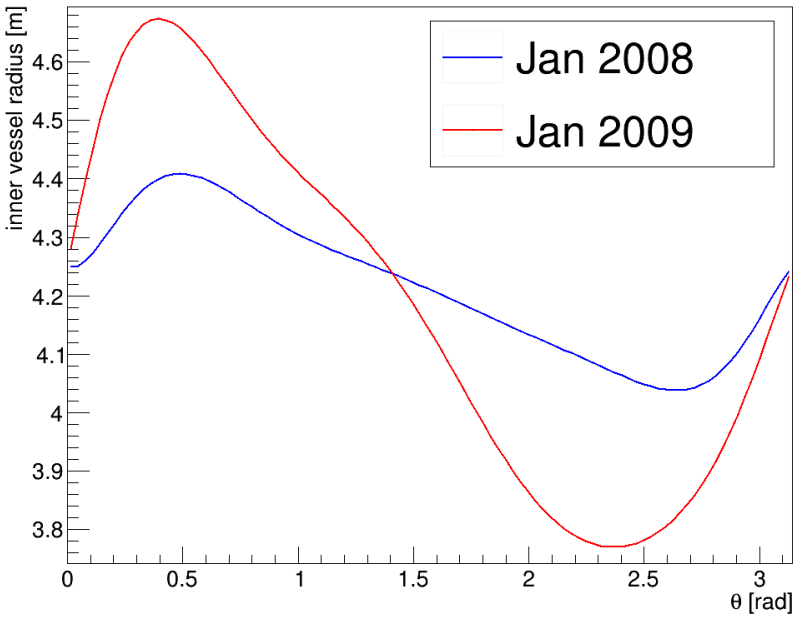

Figure 2.9: A plot showing the deformation of the inner vessel compared to before the leak from April 2008. These curves of the vessel shape are obtained by a statistical fit based on known background contributions on the IV surface. The vessel fixed with the vessel endcaps in the north and south at 4.25 m appears heavily deformed in January 2009 compared to the year before [101].

In the period of February to April 2009 a purification and distillation campaign reduced the DMP from its initial 5 g/l to 3 g/l and resulted in a lower leak rate of 0.56 m^3/month. A second distillation, starting in December 2009 and ending in January 2010 reduced the DMP further to 2 g/l, whilst refilling PC in the buffer. This lead to a successful vessel stabilization and a leak rate of $\approx 1.5\,m^3$/year. The leak, although handled, in combination with the various filling and re-filling procedures lead to a stable but slightly deformed IV, resembling more of a heart-like shape than the initial sphere (see Figure 2.10).

2.1.4 Photomultiplier Tubes

Good single electron charge resolution is a strict necessity for the PMTs installed in the Borexino detector. For an event in the energy range of $250-800$ keV the typical number of photoelectrons, seen by one PMT, lies between $0.02-2.0$ p.e[9]. A low dark count rate and an especially good timing response is also needed, as timing has a direct impact on position reconstruction. The specifications of Borexinos 8″ E.T.L 9351 PMTs are shown in Table 2.1. The PMTs have a surface curvature radius equal to 11 cm and a minimum projected surface area of 366 cm^2. While the bulb is made of Schott 8246 glass, the 12 linear focused dynodes that make the multiplier structure consist of BeCu and the cathode of CsKSb. Even though material selection was always performed with low radioactive requirements, the PMT glass has a

[9]Determined by Monte Carlo simulations

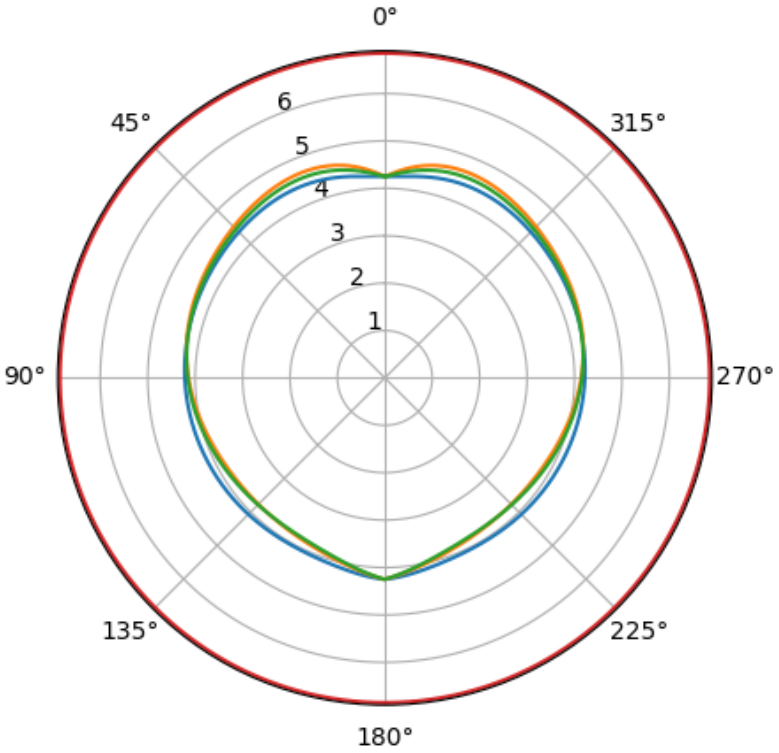

Figure 2.10: This polar plot shows the vessel evolution, before the leak from a spherical shape to its stable heart-like end position after the leak. The blue line corresponds to January 2008 (before the leak) and the orange to January 2009, the green line corresponds to the vessel shape in October 2009 [101].

low, but non-negligible contamination of uranium, thorium and potassium. These contaminations where measured to be of the order of ^{238}U: 10^{-8} g/g, ^{232}Th: 10^{-8} g/g, K_{nat} : 10^{-5} g/g and are responsible for most of the γ-particles from the inner SSS region (see also Section 5.2).

As the ID-PMTs are in contact with ultra-pure water from the outside of the SSS and also the buffer fluids from inside the IV, special care has to be taken with regards to mounting and encapsulation. All of the 2212 PMTs are mounted on the SSS, with equal distance to each other and fixed via drilled holes over the entire sphere. These holes and feedthroughs for the cabling have been helium leak tested (with a sensitivity of 10^{-9} scc/s) to ensure total separation between the water and the PC. To fix these feedthroughs and also glue the glass and housing of the tubes neck, an epoxy resign (EP45HT) has been used as the adhesive, and as a barrier against PC chemically. The base of the PMT and the neck of the tube are encapsulated by a stainless steel housing. To avoid water condensation, the inside of the cylinder is filled with mineral oil, which is not stressing the sensitive structure between the small metal pins and glass. Between the glass neck and the steel encapsulation a Teflon film is added (via a surface etching technique) as an additional barrier against the buffer liquid. As already stated, nearly all of the ID-PMTs (1800 of the 2212) are outfitted with optical light concentrators. These optical concentrators (OC) are produced

Table 2.1: The specifications for the 8″ E.T.L 9351 PMTs from the manufacturer. They have been selected for their good single charge resolution and the photocathode sensitivity matches well with the peak of the PC+PPO scintillation light between 350 − 420 nm. Table produced from [18].

Voltage for gain 10^7	1650 V	typical
Maximum voltage	2200 V	max
Maximum cathode-first anode ΔV	900 V	max
Rise time	4/6 ns	typical
Fall time	8/12 ns	typical
FWHM	7/10 ns	typical
Linearity on peak current (gain 10^6)	8 mA	typical
Linearity on peak current (gain 10^7)	10 mA	typical
Linearity on charge (gain 10^6)	80/120 pC	typical
Linearity on charge (gain 10^7)	100/150 pC	typical
SPE Peak-to-Valley ratio	2.5	typical
Photocathode sensitivity at 420 nm	26.5%	typical
Transit time spread fwhm	2.8 ns	typical
Dark current at gain 10^7	25 nA	typical
Dark counts	450 counts/s	typical

from high purity soft aluminum, via high speed material spinning processes, and then anodized to be chemically stable while submerged in water and in PC. The OCs are designed to reflect incoming photons with an incident angle $< 32.5°$, to suppress light not originating from the scintillator and were all manually cleaned and polished to achieve a reflectivity of about 90% in the relevant wavelength region of 370 − 450 nm.

A 0.5 mm thick μ-metal foil was put in place in the area of the cathode and PMT-base, as the size of the PMTs makes them susceptible to Earth's magnetic field. To avoid catalysation of this μ-metal with PC, it had to be protected with a 20 μm thick layer of phenolic paint. A sketch corresponding to the mentioned parts and structure of the ID PMTs can be found in Figure 2.11.

2.1.5 Electronics and Trigger System

The electronics chain from the PMTs is generally grouped in two parts, an analog front-end-electronic and a digital back-end-electronic, which are tasked with measuring the emitted light and its timing distribution via the photoelectrons. The system as a whole is structured into 14 identical racks, where each rack handles 160 PMTs.
In a first step, the PMT pulse is amplified by the analog electronics and the current is constantly integrated and passed to a digital board via a gate-less integrator. When a PMT creates a signal, the output of the connected integrator rises until it reaches its maximum, which is then hold for 80 ns, before decaying exponentially.

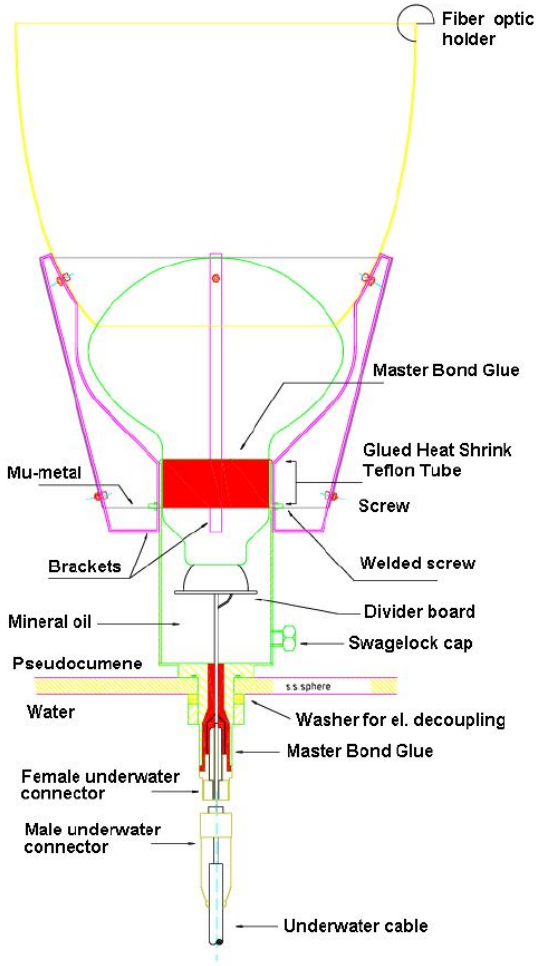

Figure 2.11: Schematic layout of an ID PMT. The yellow part in the middle is the SSS where the PMT is mounted. While its front side is in contact with the buffer, the back side and cabling is submerged in water. Special protection and adhesives had to be used to be chemically stable in the buffer liquid, as well as a μ-metal to shield against Earth's magnetic field. Image credit: [18].

This decay, with a decay constant equal to 500 ns, is due to the AC-coupling of the PMTs to their respective front-end-electronics circuits. The output of a threshold-discriminator sets the hit time t_i^j. This hit time corresponds to the PMT j, the hit i and the accumulated charge q_i^j. The charge q_i^j in combination with the detected number of hits is used to determine the released energy whilst the hit times itself are used for tagging and position reconstruction (see Section 2.1.7).
Measuring of the hit time is done via a time-to-digital converter that has a 0.5 ns resolution, significantly smaller than the 1.2 ns internal PMT jitter. An 8-bit flash-ADC samples and digitizes the threshold-discriminator's output. Processing by the digital board and software runtime leads to a dead time of 180 ns. A trigger occurs when a selected number of IV PMTs detects at least one photoelectron, in a specific time window. For most data taking during Phase-I of Borexino this number of PMT hits was set between $25 - 30$ hits, while the time window was set to 99 ns. These

values correspond to an energy threshold of $50-60$ keV. When the thresholds needed for the trigger are met, t_i^j and q_i^j of each hit are stored in a time gate of $16.5\,\mu$s. For successful operation of the electronics system, monitoring of the PMT dark count rate, as this will affect the charge q_i^j, is as crucial as timing calibration of the PMTs, because this impacts the trigger itself as well as position reconstruction. The dark count rate of $400-500$ counts/s for the internal PMTs contributes to roughly 15 random hits in the time of $16.5\,\mu$s. Figure 2.12 shows the PMTs dark count rate evolution from the beginning of data taking in May 2007.

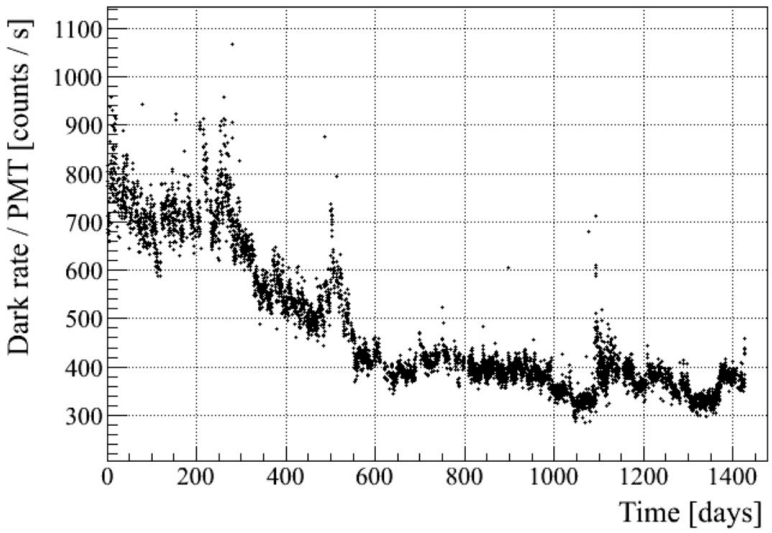

Figure 2.12: The dark count rate of the IV-PMTs, in counts per second as a function of days, starting with Day 0 as the 16.05.2007, the beginning of data taking [21].

Timing calibration is done with the laser calibration system. A 394 nm sub-ns laser pulse is sent via optical fibers to all PMTs to synchronize their timing response. This system is also applicable to validate the trigger efficiency. Therefore, 14 different laser intensities are sent to the PMTs as well as the trigger board to gain a measurement of the PMT hits depending on the laser intensity. By sending a pulse also directly to the trigger board each event is triggered even if the trigger threshold is not met. This measurement is shown in Figure 2.13 for 14 laser intensity values. In the next step, the same measurement is repeated, but this time without sending a pulse to the trigger board, but rather triggering with the used trigger threshold. The trigger efficiency can then be obtained by connecting the ratio of fired pulses to a successful trigger, for a given laser intensity. With the average number of hits per intensity, the trigger efficiency as a function of mean hits can be derived and is shown in Figure 2.14. The obtained fit value for this trigger efficiency is 25.7 hits and therefore in very good agreement with the used threshold of 25 hits. Figure 2.14 also shows that when more than 40 PMTs are hit, the trigger efficiency is close to one, thus making the trigger very effective for deposited energies > 80 keV. An extended discussion of the trigger chain including the used hardware is given in [18].

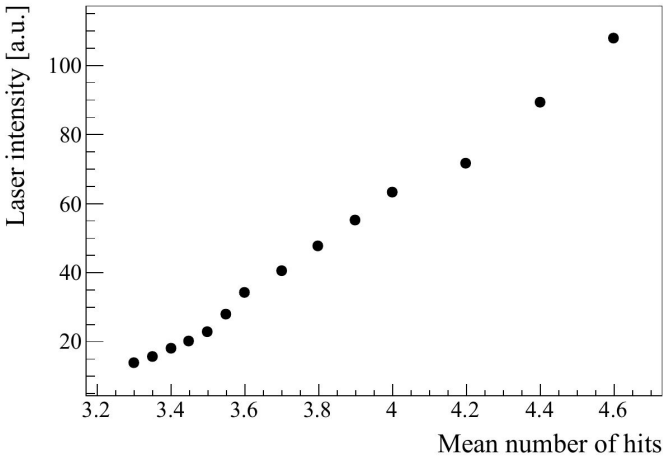

Figure 2.13: Measurement of the average number of PMT hits related to the laser intensity. The used calibration values are corresponding to an energy region of $\approx 30 - 240\,\mathrm{keV}$ [21].

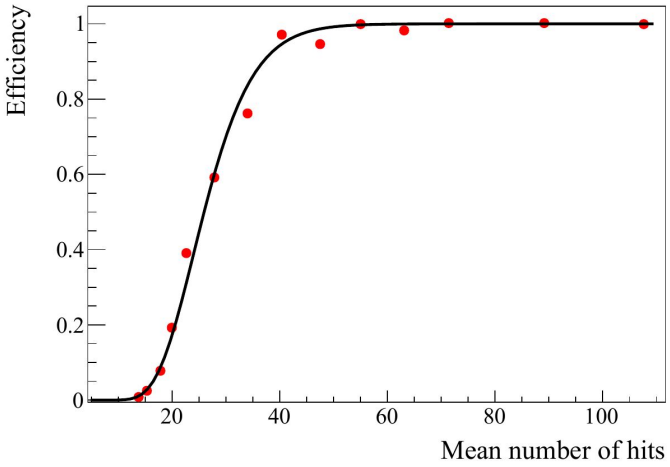

Figure 2.14: Plot of the trigger efficiency as a function of the average PMT hits. The red dots correspond to the number of hits obtained from Figure 2.13. The fit function (error function) in black, assumes Poisson statistics and the best fit value of 25.7 hits is very close to the set 25 hits threshold [21].

2.1.6 Outer Detector

The main purpose of the Outer Detector is to provide shielding and act as a muon veto for the Inner Detector. Therefore, between its massive 18 m diameter outer steel tank and the SSS, the 3.4 m radius sphere is filled with ultra pure water and instrumented with 208 PMTs, acting as a water Cherenkov detector. Although the same 8″ E.T.L 9351 PMT model as in the ID, the OD-PMTs differ mostly in terms of encapsulation.
These PMTs are not mounted in an equal distribution on the surface of the sphere like it is the case for the ID, but their layout is the result of Monte Carlo studies aimed to maximize Cherenkov light detection, whilst taking the non-spherical geometry of the steel tank into account. On the top interior half of the 590 m^2 tank surface, the PMTs are mounted in more or less equal distance (mean distance of the PMTs is 1.7 m). For shielding from the rock and structural reasons, at the bottom of the tank, there is a 1.5 m x 1.5 m stainless steel volume, where most of the south OD-PMTs are mounted with an angle of $\approx 45°$ between them and about a quarter of the remaining PMTs in the south are placed directly at the bottom of the water tank looking upwards.
At the bottom of the tank, water puts a pressure of about 2 atm on the PMTs, which are therefore encapsulated and mechanically reinforced compared to their ID counterparts (see Figure 2.15). A full readout of the ID and the OD can be triggered when at least 6 OD-PMTs are hit within the time frame of 150 ns. For muon and possible cosmogenic neutron[10] identification an acquisition time gate of 1.6 ms is read out after a muon detection. This time gate, roughly 6 times the neutron capture time, can then be used to tag and veto these events (more on muon-induced background can be found in Section 5.1.2).

[10] Neutrons produced by cosmic ray muons

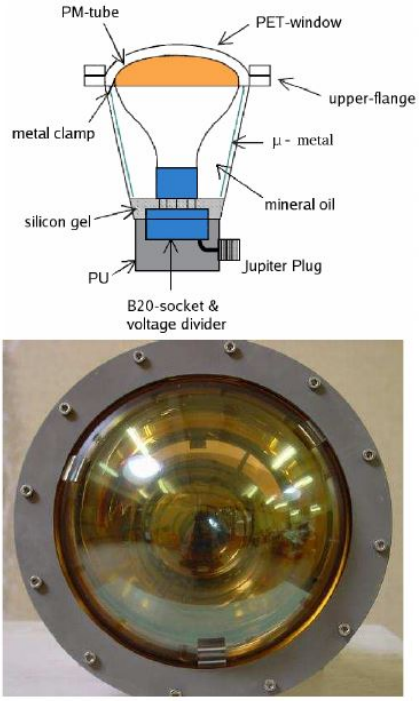

Figure 2.15: Top view: Schematic layout of an OD-PMT. The PET-foil covers the photocathode, with a transparency of $90 - 92\%$, while retaining an $\approx 180°$ acceptance angle. The μ-metal used to protect against Earth's magnetic field, the HV-connectors and the mineral oil are similar to the ID-PMTs.
Bottom view shows a front picture of an encapsulated OD-PMT, with the steel mounting ring [18].

2.1.7 Energy and Position Reconstruction

An event in Borexino is generally speaking a collection of PMT hits (above a set threshold) collected in a set time window. A typical event, which can be seen on the left in Figure 2.16, is a few tens of ns wide and has a tail of up to several hundred ns. In a trigger gate of $16.5\,\mu$s all hits are recored including the dark counts. for a signal of about 100 hits, which is occurring in less than 200 ns the dark counts amount to roughly 1 per μs. A dedicated clustering algorithm identifies the beginning of an event and accounts for the dark noise. All hits belonging to the same event are called a cluster and their position is determined within the $16.5\,\mu$s long trigger gate via the rising of the peak of the event, with a resolution of 1 ns.

Fast coincides like those from the ^{212}B -^{212}Po or the ^{85}Kr decays (discussed in Section 5.1.1) are seen as partially overlapping events on the right plot of Figure 2.16. These fast decays can be identified as two events, within a cluster as close as within 15 ns of peak-to-peak distance. The information if an event is a single or double cluster event is stored and can be used to specifically suppress events originating from fast decay coincidences.

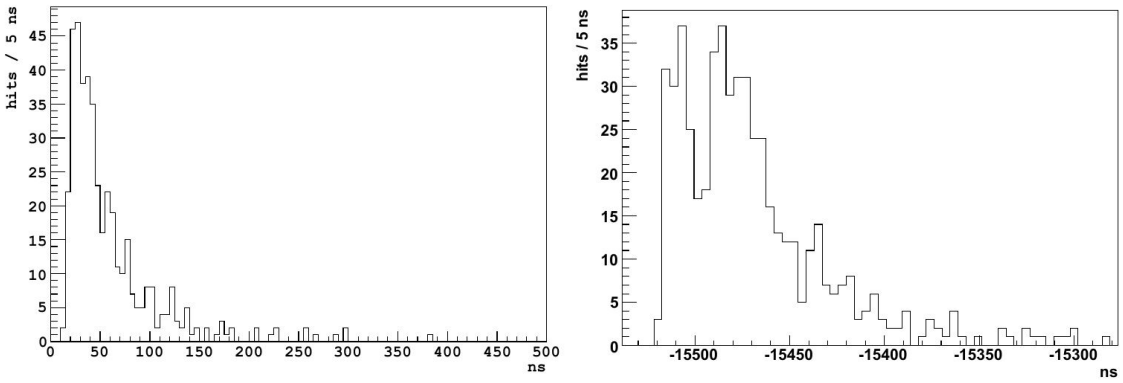

Figure 2.16: The left plot depicts an example of a single cluster event while on the right two partially overlapping events can be seen. Originating from a fast ^{212}Bi-^{212}Po decay, these clusters with a peak distance of about 25 ns can effectively be identified and distinguished from a single cluster event by the clustering algorithm [18].

The number of PMTs, which saw at least one hit N_p and the number of observed total hits N_h are obtained via the clustering algorithm and by normalizing them to the amount of working read-out channels.
These are measured as N_p^m and N_h^m, with N' operating channels by the clustering algorithm to:

$$\begin{aligned} N_p^m &= \sum_{j=1}^{N'} p^j \\ N_h^m &= \sum_{j=1}^{N'} h^j \end{aligned} \tag{2.9}$$

Where h^j=0,1,2...,n is the detected number of hits and p^j is set to 1 if one photon ore more is detected (otherwise p^j=0).
N_p and N_h are derived from the measured N_p^m and N_h^m by normalizing the working channels to the number of $N_{tot} = 2000$ total channels via:

$$N_{p,h} = \frac{N_{tot}}{N'(t)} N_{p,h}^m \tag{2.10}$$

By summing over the charge variable q_i^j (introduced in Section 2.1.5), N_{pe}^m is given as:

$$N_{pe}^m = \sum_{j=1}^{N_h^m} q^j \tag{2.11}$$

when normalizing N_{pe}^m, similar to Equation 2.10, not only working channels but rather channels (N'') with a working ADC conversion and functioning charge readout have to be used

$$N_{pe} = \frac{N_{tot}}{N''(t)} N_{pe}^m \tag{2.12}$$

The number N'' is typically a few tens of channels short compared to N'.

In Borexino's analysis and simulation framework (see Section 6.1) N_{pe} is simply referred to as the *charge* variable, while N_h is called *nhits*. Nearly all energy spectra shown in this thesis are printed in the *nhits* variable. For energies lower than approximately 1 MeV, the *nhits* multiplied by two will translate roughly to the energy in keV. For energies above 1.5 MeV the *nhits* variable is not calibrated [26].

The position reconstruction algorithm used to determine the position of an event is based on the arrival time t_i^j of the detected hits. A position depended time-of-flight T_{flight}^j function is introduced, to determine the most likely interaction in the $\vec{r}_0$ position.

$$T_{flight}^j(\vec{r}_0, \vec{r}_j) = |\vec{r}_0 - \vec{r}_j| \frac{n_{eff}}{c} \tag{2.13}$$

where $\vec{r}_j$ reefers to a PMT j, placed at the position $\vec{r}_0$.

The likelihood $L_E((\vec{r}_0, t_0)|(\vec{r}_j, t_i^j))$ is the likelihood that an event occurred at $\vec{r}_0$ at the time t_0, given the measured characteristic hit space-time pattern $(\vec{r}_j, t_i^j)$. The position is reconstructed by maximizing L_E and accounting for the number of photoelectrons per hit. More detail on this process and the position reconstruction in general is found in [8].
The effective refraction index n_{eff}, from Equation 2.13, which accounts for scattering and reflection effects, as well as considers different group velocities for photons, caused by different wavelengths, was determined to be $n_{eff} = 1.68$. This was measured during a calibration campaign with different radioactive sources[11].
Validation of this position reconstruction was possible during this calibration campaign. A calibration source emitting α-particles from ^{214}Po (from the ^{238}U chain, see Figure 5.6) was placed inside the detector, where its position could be determined by the CCD cameras mounted on the SSS and then compared to the reconstructed positions. Figure 2.17 shows the difference between reconstructed and CCD obtained positions for x- , y- and z- axis. For x and y coordinates the sigma of the distribution is in the order of 0.9 cm, whilst the z-axis is showing a shift of d = 3 cm (sigma of 1.2 cm). Events in the center of the FV are reconstructed at $\approx$ 15 cm absolute position for 300 keV and 9 cm absolute position for 1 MeV (for α-events).

[11] $n_{PC} = 1.50$ at 600 nm

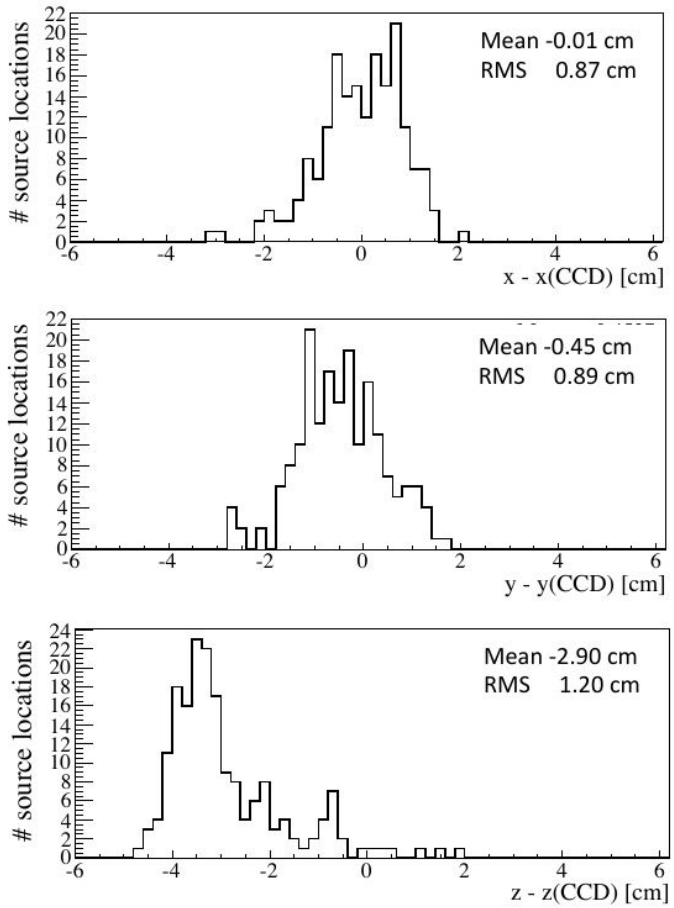

Figure 2.17: The difference between the reconstructed and CCD obtained data for 182 positions of a radon calibration source. The α-events from ^{214}Po are reconstructed and compared to the 182 different positions. The x (top), y (middle) and z (bottom) distributions are not disentangled from the CCD pictures position uncertainty [21].

2.2 Results and Physics Program

Borexinos scientific program is focused on solar neutrinos and the main results after 10 years of data taking (which can be found in [23]) are presented in this chapter, after a brief introduction on the origin of these solar neutrinos. Besides the solar program, Borexino was able to measure geo-neutrinos and also obtain other limits on neutrino parameters such as the magnetic moment.

2.2.0.1 Solar Neutrinos

Main sequence stars are kept in equilibrium by balancing gravitational forces with outwards pressure generated by nuclear fusion. The main fusion process in the case of the sun is:

$$2e^- + 4p \rightarrow {}^4\mathrm{He} + 2\nu_e + 26.79\,\mathrm{MeV} \tag{2.14}$$

This pp-chain generates about 99% of the sun's energy, the rest is due to the CNO cycle Figure 2.22, as it is the case for approximately 80% of all observed stars. Heavier stars with preexisting metals and a much higher core temperature than the sun rely on the CNO process as their means of energy production.

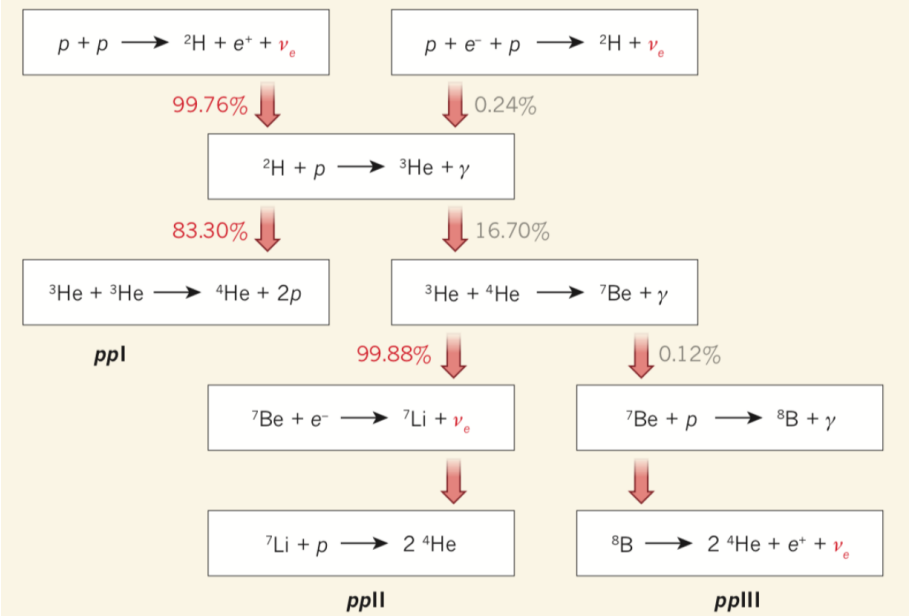

Figure 2.18: This illustration shows the three main cycles of the pp-cycle. The emitted neutrinos, marked in red, allow to observe these processes [95].

The sun's core temperature is besides others an important parameter for SSM and general understanding of main sequence stars, as is the metallicity. Observations of the neutrino flux originating from various steps in the pp-chain enable a direct probing of the sun's core, as this flux is extremely sensitive to the core temperature.

Figure 2.18 shows the three important cycles for the pp-chain, as well as the neutrinos from these fusion reactions. In Figure 2.19 the energy spectrum of the solar neutrinos originating from these processes is shown. Besides the direct access to the core temperature, the measurement of the various solar neutrinos fluxes can be used to distinguish between different SSMs in terms of metallicity and Table 2.2 shows an example with two solar models.

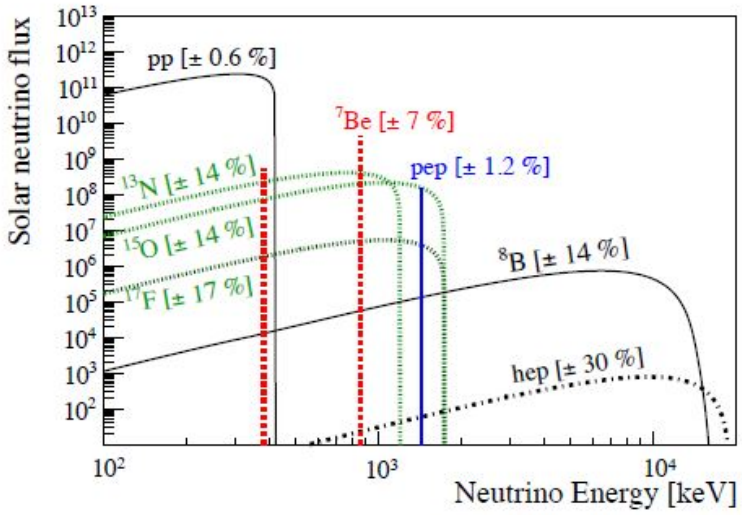

Figure 2.19: This plot shows the solar neutrino flux from the nuclear fusion, predicted by the SSM. It depicts the continuous fluxes as well as the mono-energetic neutrino flux from ^{7}Be. The uncertainties on the flux are calculated from [105] while the plot is taken from [63].

Borexino is able to detect and measure the 862 keV neutrinos, originating from the electron capture of ^{7}Be in the ppII-chain with the reaction:

$$^{7}\mathrm{Be} + e^{-} \rightarrow {}^{7}\mathrm{Li} + \nu_e \tag{2.15}$$

The measured count rate of these ^{7}Be neutrinos is R(^{7}Be)=46.0±1.5($stat$)±1.6($syst$) counts /(d· 100 t).
Furthermore, Borexino is also able to measure ^{8}B solar neutrinos with a count rate of R(^{8}B)=0.22 ± 0.04($stat$) ± 0.01($syst$) counts /(d · 100 t) [3]. A measurement of pp-neutrinos could also be achieved for the first time in a real-time detector, with a count rate of R(pp)=44 ± 13($stat$) ± 10($syst$) counts /(d · 100 t). This corresponds to a flux[12] of Φ(pp)=(6.6 ± 0.7) · $10^{10} cm^{-2} s^{-1}$, which agrees well with theoretical SSM pp-flux predictions.
Neutrinos at 1.44 MeV from the $p + p + e^{-} \rightarrow d + \nu_e$ reaction were measured at R(pep)=3.1 ± 0.6($stat$) ± 0.3($syst$) counts /(d · 100 t). With the measurements from pp-, pep-, ^{7}Be-, ^{8}B-neutrinos Borexino can test the survival probability of electron-neutrinos from the different fusion processes (see Figure 2.20) and compare them to theory.

[12] Assuming a LMA-MSW solution

Table 2.2: Comparison of the predicted solar neutrino fluxes for two different SSMs. The GS-BPS08 model assumes a higher metallicity than the AGS-BPS08 model. A high precision measurement of e.g. ^{7}Be or ^{8}B could help to rule out certain models and a limit on the CNO flux would be even better as there the models show the biggest discrepancies. The associated units to the fluxes are 10^{10} (pp), 10^{9} (^{7}Be), 10^{8} (pep, ^{13}N, ^{15}O), 10^{6} (^{8}B, ^{17}F) and 10^{3} (hep) $\mathrm{cm}^{-2}\mathrm{s}^{-1}$. Table produced from: [92].

Source	BPSO8 (GS)	BPSO8 (AGS)	Difference [%]
pp	5.97 ± 0.006	6.04 ± 0.005	1.2
pep	1.41 ± 0.011	1.45 ± 0.010	2.8
hep	7.9 ± 0.15	8.22 ± 0.15	4.1
^{7}Be	5.07 ± 0.06	4.55 ± 0.06	10
^{8}B	5.94 ± 0.11	4.72 ± 0.11	21
^{13}N	2.88 ± 0.15	1.89 ± 0.14	34
^{15}O	2.15 ± 0.17	1.34 ± 0.16	31
^{17}F	5.82 ± 0.16	3.25 ± 0.15	44

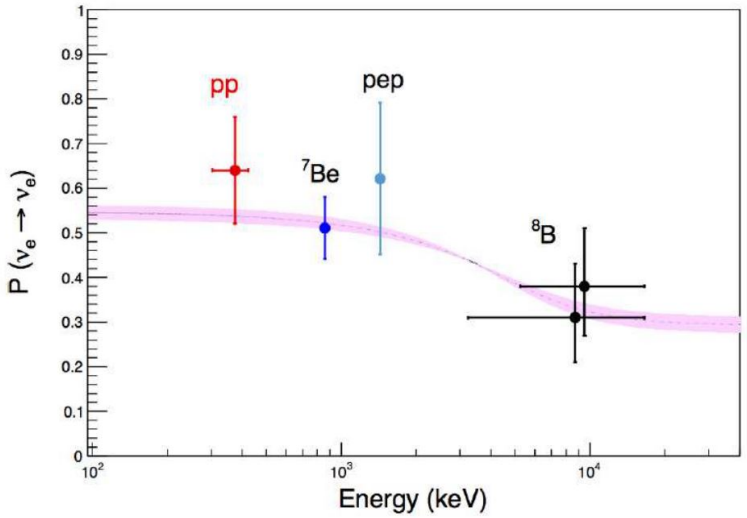

Figure 2.20: This plot shows the survival probability of the various solar neutrinos as a function of energy. The violet line shows the favored MSW-LMA solution. P_{ee} refers in the case of pp- and ^{8}B-neutrinos to the energy range from Borexinos measurement as these neutrinos are emitted in a continuous spectrum [23].

2.2.1 Geo Neutrinos and Reactor Neutrinos

Electron anti-neutrinos produced in the core, crust and mantle of the Earth by the naturally present radioactive isotopes like ^{238}U, ^{232}Th and ^{40}K are typically refereed to as geo-neutrinos. With an exposure of $(5.5 \pm 0.3) \cdot 10^{31}$ protons $\times$ yr Borexino obtained $23^{+6.5}_{-5.7}(stat)^{+0.9}_{-0.6}(syst)$ geo-neutrino events with 5.9σ, under the assumption of a chondritic Th/U mass ratio of 3.9 [22].
Figure 2.21 shows the data of the measured $\bar{\nu}_e$ candidates, where an un-binned likelihood fit of the energy spectrum with Monte Carlo generated backgrounds produces the shown geo-neutrino and reactor neutrino spectra.

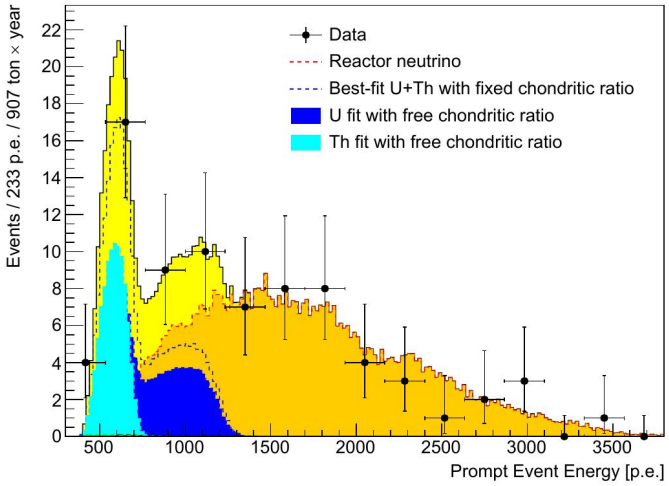

Figure 2.21: The light yield spectrum of $\bar{\nu}_e$ candidates, whose data points are plotted in black. Two fits are compared, the dotted line assumes a Th/U mass ratio of 3.9 as suggested by a chondritic model, whilst the blue/light blue colors correspond to two separate free mass parameters of ^{238}U and ^{232}Th. The reactor neutrino spectrum is plotted in dark yellow [22].

2.2.2 Other Limits

In the presence of a possible magnetic moment of the neutrino, the electron recoil spectrum would be distorted, especially at lower neutrino energies. Borexino obtained an upper limit on the effective[13] magnetic moment of $\mu_{eff} \leq 2.8 \cdot 10^{-11}\mu_B$ [29].
A paper investigating the seasonal modulation in the flux of muons reaching the LNGS is currently being submitted. This paper shows a correlation with atmospheric temperatures and derives a period for this seasonal modulation of $(366.3 \pm 0.6\,\mathrm{d})$ [30].

[13] A composition of magnetic moments from flavor and mass eigenstates

2.2.3 Future

Following the preparations, for the now discontinued SOX experiment (which will be discussed in the next Chapter 3), the Borexino collaboration plans a new calibration and re-purification campaign. After obtaining the to date strongest upper limit for neutrinos from the CNO chain (shown in Figure 2.22) at R(CNO)$\leq$ 7.9 counts/(d $\cdot$ 100 t) [23], the collaboration aims to continue its very successful solar neutrino program and even expand it, if feasible, to a potential first time direct CNO neutrino flux observation. To reach this ambitious goal, the thermal stabilization of the detector has to be improved and amongst others improvements, overall internal background has to be reduced by at least an order of magnitude.

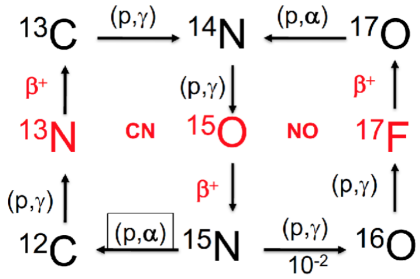

Figure 2.22: Illustration of the CNO cycle, which contributes only to about 1% to the fusion energy in main sequence stars, but is supposed to be the main energy production process for heavy metal-rich stars [95].

Chapter 3

The SOX Experiment

Motivated by the anomalies originating at short baseline neutrino oscillations discussed in Section 1.5, the **S**hort distance neutrino **O**scillations with Bore**X**ino (SOX) experiment was proposed in 2013 [20] as a dedicated experiment to precisely probe neutrino oscillation on small scales.
Together with the Borexino detector and the Borexino Collaboration, the SOX Collaboration planned to use a dedicated radioactive neutrino and/or anti-neutrino source and deploy these in a service tunnel under the Borexino detector to observe a possible disappearance of electron-neutrinos or even an oscillation pattern, which could pinpoint to a possible sterile neutrino as discussed in Section 1.4. To achieve this measurement goal, the neutrino flux of the source has to be known with a precision of 1% and was planned to be reached by obtaining the neutrino flux via a thermal power measurement of the source, deployed in a calorimeter. For this purpose a dedicated calorimeter for this measurement was developed by the SOX Collaboration. To tune this calorimeter, usage of the actual source or sources is obviously not feasible and therefore an electrical calibration source, called the mockup, was build and integrated in the calorimeter within the scope of this theses.

This chapter will discuss the SOX experiment and its unfortunate end in February 2018 [33], as well as the radioactive source, its production and encapsulation. The calorimeter and the mockup will be presented and performance of the successfully running system will be shown. The following chapter will then focus on the thermal simulations also performed during this theses, which were a useful tool during development as well as in understanding of the calorimeter - mockup system and helped to characterize its systematic behavior and heat-losses.

3.1 Introduction

In the initial proposal for the SOX experiment [20], two sources (neutrino and anti-neutrino) deployed during three different phases were foreseen (see Figure 3.1). These phases were defined by the used sources and their position in or near Borexino. In Phase A, a ^{51}Cr source emitting neutrinos was planned to be deployed in a service tunnel under Borexino. The small pit (cubical 105 cm side) was actually designed

to hold a radiative source from the beginning and is reachable through a squared tunnel (side 95 cm). This was a major advantage as the deployment of a source in the tunnel during Phase A could have been made without interference regarding Borexino. Therefore, at a distance of 8.25 m from the center of Borexino to this pit, Phase A would have deployed a ^{51}Cr source with an activity of $200 - 400$ PBq. The chromium source, produced by irradiating ^{50}Cr via thermal neutrons in a nuclear reactor, decays via electron capture to ^{51}V and produces two mono-energetic neutrinos. One at 750 keV (90%) and the other at 430 keV (10%), which could both be detected via elastic electron scattering in Borexino.
Phase B would have consisted of a cerium - praseodymium source (^{144}Ce-^{144}Pr) deployed in the water tank at a distance of 7.15 m from the center, with an activity of $2 - 4$ PBq. This source emits anti-neutrinos with an energy end-point of about 3 MeV from the β-decay and could therefore be detected via IBD[1].

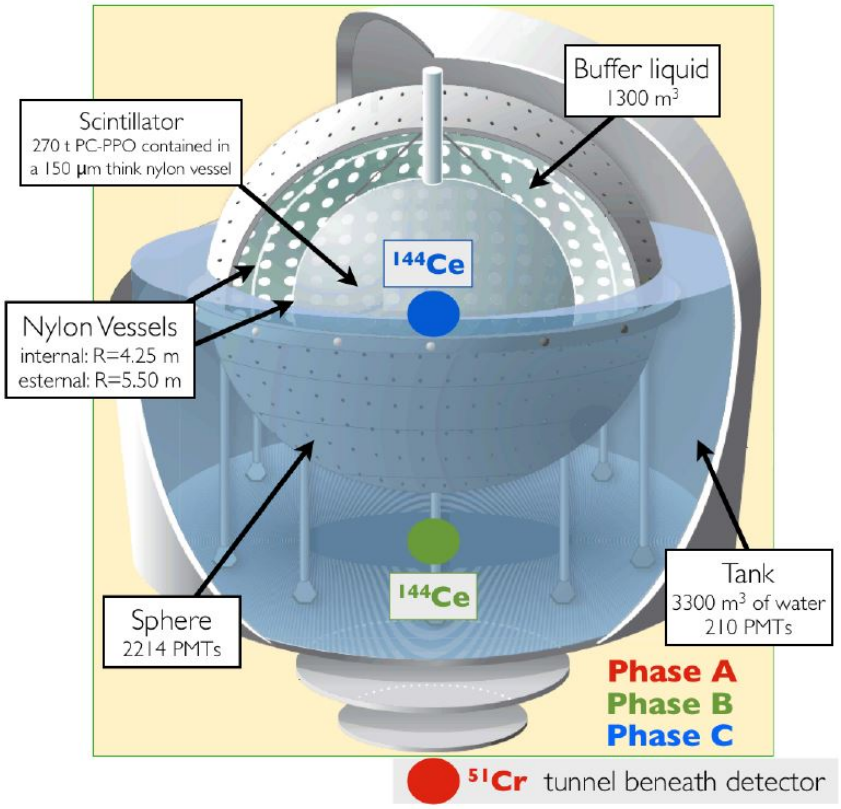

Figure 3.1: The initially planned three phases for the SOX experiment. In Phase A, a neutrino source was planned to be placed in a pit under Borexino. Phase B and C would have deployed a anti-neutrino source in the water tank and later in Phase C, directly inside the center of Borexino. Image credit: [20].

In a last step, Phase C would have deployed a similar cerium source, although less active with 1.5 PBq, directly inside the scintillator volume in Borexinos center.

[1] Detection threshold for IBD is 1.8 MeV.

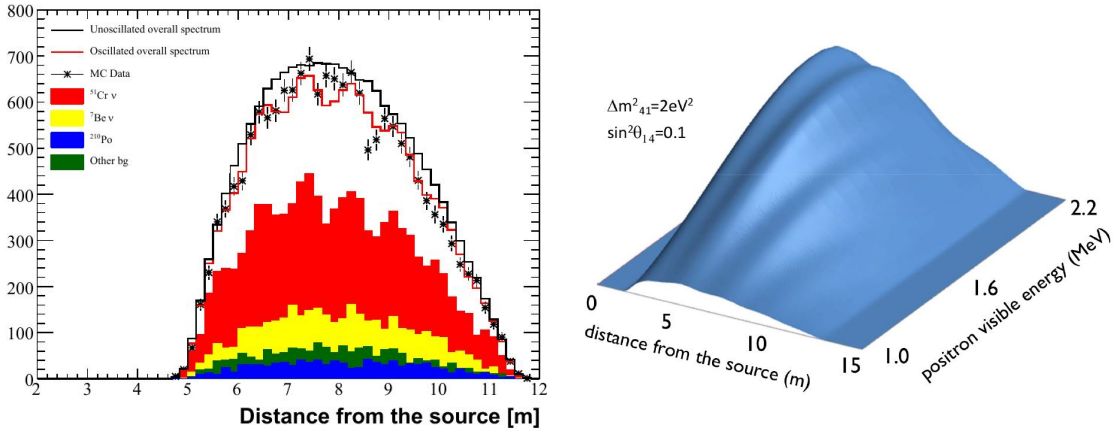

Figure 3.2: On the left: A possible simulated Phase A outcome and the expected spectrum with oscillating and non-oscillating behavior. This Monte Carlo simulation was validated with calibration sources and known backgrounds at the 1% level and corresponds to the ^{51}Cr source, using $\Delta m^2_{41} = 2\,\mathrm{eV}^2$ and $\sin^2(2\Phi_{14}) = 0.3$. The signal, in red for the oscillation case and in black for then non-oscillation, is clearly dominant and would allow reconstruction of squared mass and mixing angle. The right plot shows the wave-like pattern of the cerium source for Phase B as a function of visible energy. Image credit: [20].

It is clear that for Phase B and especially C rigorous steps in terms of radio-purity for the source encapsulations would have been crucial.

The disappearance of the neutrino flux from the sources compared to a no-oscillation case on this small scale could then point to a sterile neutrino. Because Borexino has such a large sensitive volume, combined with the favored values for $\Delta m^2_{41} \approx 1\,\mathrm{eV}^2$ and an neutrino energy of $\approx 1\,\mathrm{MeV}$ the resulting oscillation in the range of a few meters could have been directly observed by Borexino.

$$P(\nu_e \to \nu_e) \approxeq 1 - \sin^2(2\Phi_{14}) \sin^2\left(\frac{1.27\Delta m^2_{41} L[\mathrm{km}]}{E[\mathrm{MeV}]}\right) \tag{3.1}$$

Equation 3.1 shows the already discussed two-flavor oscillation formula from Section 1.4 and shows that for a distance L of approximately 8 m, Borexino could have been able to observe an oscillatory pattern for both the cerium and the chromium source, for the favored Δm^2_{41} region. This potential oscillatory behavior has been simulated via Monte Carlo simulations and can be seen in Figure 3.2. The potential sensitivity for sterile neutrinos concerning the two sources has been evaluated with a Monte Carlo approach, where 2000 Δm^2_{41} and $\sin^2(2\Phi_{14})$ sample pairs had been simulated. For background constraints this simulation assumes 15 weeks of data taking before any source deployment. In case of the ^{51}Cr source an error of 1% for the source activity and the knowledge on the FV was assumed. This error on the source activity was believed to be achievable by developing a well calibrated thermal calorimeter and measure the activity via the thermal power created by the source. Regarding the FV error, Borexino had already shown during its Phase I of solar neutrino data taking that this 1% error would have been realistic. A similar (1.5%) error on source activity knowledge was assumed for the ^{144}Ce source. As the

anti-neutrinos from this source are detected via the IBD and are thus resulting in two correlated signals, a bigger FV could have been used. It was, in fact, proposed and also assumed for this sensitivity simulation to use a sensitive volume with a radius of 5.5 m. To achieve this, the OV would had to be filled with scintillator. In order to account for residual systematic effects an error of 2% was used.
The exclusion plot shown in Figure 3.3 was created assuming a 370 PBq ^{51}Cr source, deployed for 100 days, with a detector duty cycle of 90% and a 2.3 PBq ^{144}Ce-^{144}Pr source with 1.5 years of data taking. The resulting sensitivity would have covered most of the parameter space from the reactor anomaly. The contributions of accidental geo-neutrinos or distant reactor neutrinos were estimated to be less than five events per year.

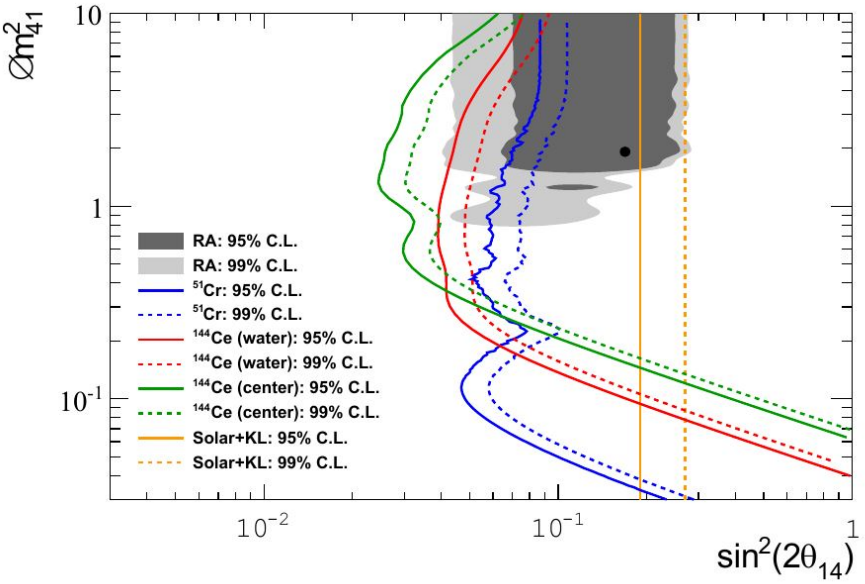

Figure 3.3: The sensitivity for the SOX Phases (A in blue, B in red and C in green) to the parameter space of a light sterile neutrino. The gray area refers to the reactor anomaly (RA) assuming a light sterile neutrino. The yellow line indicates the exclusion from solar neutrinos. Image credit: [20].

After a brief concept phase and the testing of early ^{51}Cr samples obtained from some manufactures, the SOX/Borexino Collaboration decided against the use of a chromium source. Instead, Phase A would be made with the cerium source and Phase B and C would be put on hold. This resulted in a new plan and timetable for SOX and the source delivery, from a nuclear power facility in Russia, was expected for the end of 2018.
This new plan now would have placed a ^{144}Ce-^{144}Pr source with an activity of $4-5$ PBq and $\bar{\nu}_e$ energies from $1.8-3$ MeV for a duration of 1.5 years in the pit under Borexino. This would have translated to a total number of events in the order of 10^4. With only one source and one phase, even though a more active source, stricter limits on source activity and the knowledge of the β-spectrum had to be implemented. Spectral shape measurements for the ^{144}Ce-^{144}Pr source were carried

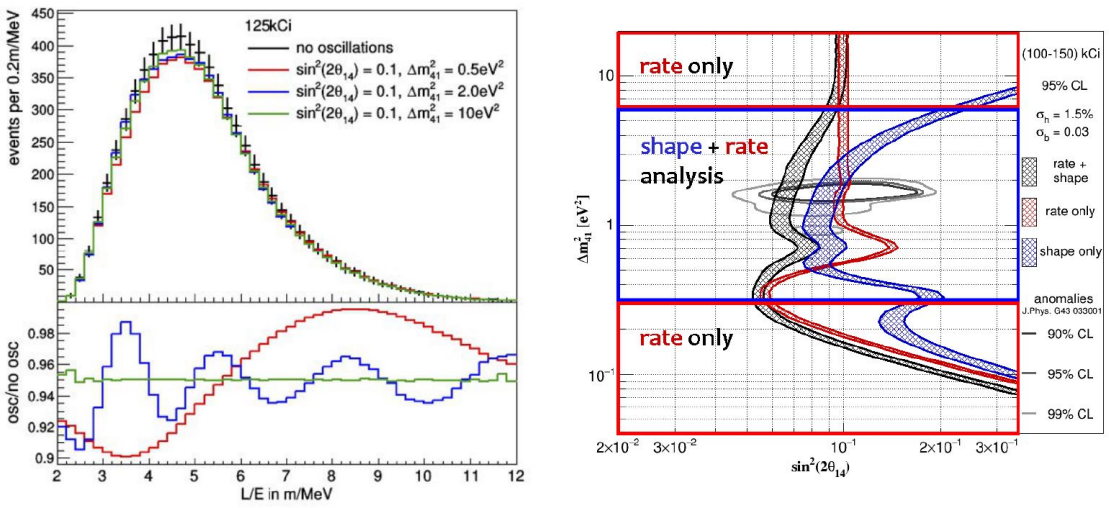

Figure 3.4: Left: The top shows neutrino events for three sterile neutrino parameter sets as well as a non-oscillating signal. The bottom shows the ratios of these parameters in terms of oscillation/no-oscillation.
Right: This plot shows the expected sensitivity to a sterile neutrino including systematic uncertainties of 1.5% on the source activity and an absolute error of 0.03 on the shape factor of the electron spectrum of ^{144}Pr. Image credit: [37]

out, as they directly influence the sensitivity. As already stated, the cerium source enables in addition to the observation of a disappearance (rate) the possibility to observe potential oscillation patterns directly. As seen in Figure 3.4, these depend mainly on Δm^2_{41}. Low squared masses ($\Delta m^2_{41} < 0.2\,\mathrm{eV}^2$) would lead to oscillation lengths wider than Borexino, whilst higher ($\Delta m^2_{41} > 5\,\mathrm{eV}^2$) would be to small to observe with the detector resolution. Squared masses between 0.2 and $5\,\mathrm{eV}^2$ could have been analyzed with shape and rate thus yielding the highest sensitivity.

Unfortunately, in December 2017, the Mayak Production Association, the company charged with the production of the ^{144}Ce-^{144}Pr source, announced to the collaboration their inability to produce a cerium source meeting the requirements in both activity and impurity levels. Without the source, the key element for the SOX experiment, the Collaboration was forced to abandon the SOX project in February 2018 [33].

Before this unfortunate end, progress on building, operating and calibrating a very precise thermal calorimeter was made and will be reported in the next sections after a short explanation on the proposed cerium source, its encapsulation and potential involvement in the Mayak incident (Section 3.2.1).

3.2 Cerium Source

The source is an anti-neutrino emitter consisting of ^{144}Ce, a long lived cerium isotope with a half-life of 285 days and low β-decay energy of $Q = 318\,\mathrm{keV}$ (which is under

the IBD threshold). The praseodymium produced by the ^{144}Ce has a half-life of 17.3 min and two measurable β-decay branches with an end-point energy of 2996 keV (97.9%) and 2301 keV (1.0%), as it can be seen in Figure 3.5. The long half-life of cerium is ideal to have enough time for production and transportation of the source, while the short half-life of praseodymium provides a good number of anti-neutrino events. As already stated, the exact knowledge of the β-spectrum from ^{144}Pr is very

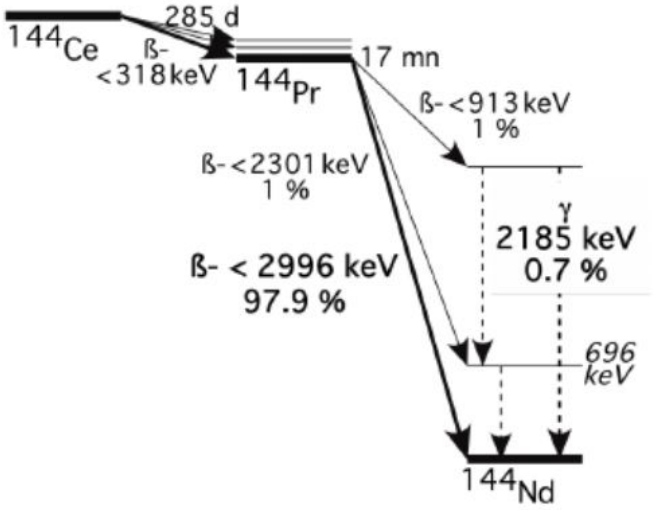

Figure 3.5: Decay branch of ^{144}Ce and ^{144}Pr showing the half-life and β-decay branches until the stable ^{144}Nd. Image credit: [74].

important, more specifically the parameter b from Equation 3.3, as the counting rate $N(E_\nu, L, t)$ is given by:

$$N(E_\nu, L, t) \approx A(t) \times S_\nu(E_\nu, b) \approx \frac{P(t)}{\langle E(b) \rangle} \times S_\nu(E_\nu, b) \tag{3.2}$$

where $A(t)$ is the source activity, which can be expressed via the measured thermal power $P(t)$ and the mean energy per decay $< E(b) >$. $S_\nu(E_\nu, b)$ is the shape of the ^{144}Pr spectrum. The weak finite-size correction $C(Z, W)$, which contributes to the shape $S_\nu(E_\nu, b)$, with the nucleus charge Z and $W = E_e/m_e + 1$ as the total energy of the β^--particle expressed via m_e rest mass units, is typically parameterized as:

$$C(Z, W) = 1 + aW + \frac{b}{W} + c^2 W \tag{3.3}$$

with the parameters a, b, c.
As $P(t)$ can be constrained by calibration of the calorimeter, the b parameter of the source would have been obtained by dedicated β-spectrum measurements of samples of the source material, once it would have arrived.

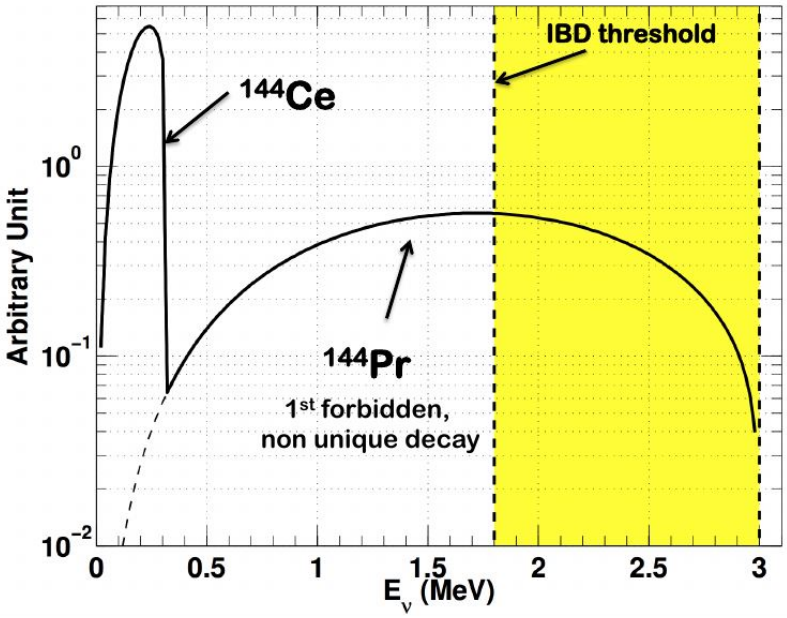

Figure 3.6: Plot showing the $\bar{\nu}_e$ spectrum of ^{144}Ce and ^{144}Pr, with the IBD threshold at 1.8 MeV, shown in yellow. The $\bar{\nu}_e$ from ^{144}Pr are mostly from one branch (97.9%) which has its endpoint at 2.996 MeV. Image from [74].

The ^{144}Ce was extracted from spent nuclear fuel via a chemical purification method, namely the **P**lutonium **U**ranium **R**edox **EX**traction (PUREX) method. PUREX is used to separate the fission products from spent nuclear fuel. The cerium is produced in the order of 5.5% from uranium and 3.7% from plutonium, besides the other actinides and fission products during the nuclear fission. The spent fuel from the Kola Nuclear Power Plant, located in northern Russia was transported to the Mayak facilities. There, in a radiochemical plant, after a cooling period of the fuel, separation of uranium and plutonium from lighter elements via PUREX and then in a next step the extraction of the ^{144}Ce, as well as a first rough activity measurement was performed. Unfortunately these measurements yielded an activity below the requirements for the SOX project as well as not meeting the limits on source purity. After primary encapsulation the source would have been transported to a near radioisotope plant for source manufacturing. Besides from the primary encapsulation and an additional tungsten shielding, the source would have then been loaded into a shielded transport cask. From Mayak it was planned to transport the source by train to St. Petersburg, then load it on a ship to Le Havre in northern France and finally transported it with a truck to the LNGS. With an expected travel time of 10 days for the train, 5 for the shipping and 4 days for the truck, no significant loss in activity were foreseen.

3.2.1 Mayak Incident

In October 2017, a cloud of Ruthenium-106 was detected by monitoring stations all over Europe and reported as a "radioactive" cloud by countless news agencies ([47],

[91], [2] and [108]). With its very low activity[2] combined with the low environmental impact of ruthenium in general, this cloud did not pose any danger, but questions of its possible origin were immediately raised.
^{106}Ru is a radionuclide created as a fission product from nuclear reactors with a half-life of 371.8 days. As no other radioactive contributions were measured, a major incident at a nuclear reactor seemed unlikely. In January 2018, the French institute for nuclear safety published a report on this event and a possible explanation for this ruthenium release. The main aspects of this report [97], its techniques and conclusion are summarized here briefly.

Most of the data used originate from air filters. These air samplers are manually collected after a sampling time of days up to weeks and validated at meteorological laboratories, via gamma spectroscopy. In some stations direct deposits of grass or rain water are additionally collected at regular intervals and probed for potential artificial contamination. As these measurements are more susceptible to mistakes, the report focuses on data collected from the air filters only. Due to the difference in sampling time, these measurements have been corrected and multiple filters combined and averaged per station or operating region. Figure 3.7 shows these corrected and averaged values concerning the ruthenium cloud. With these

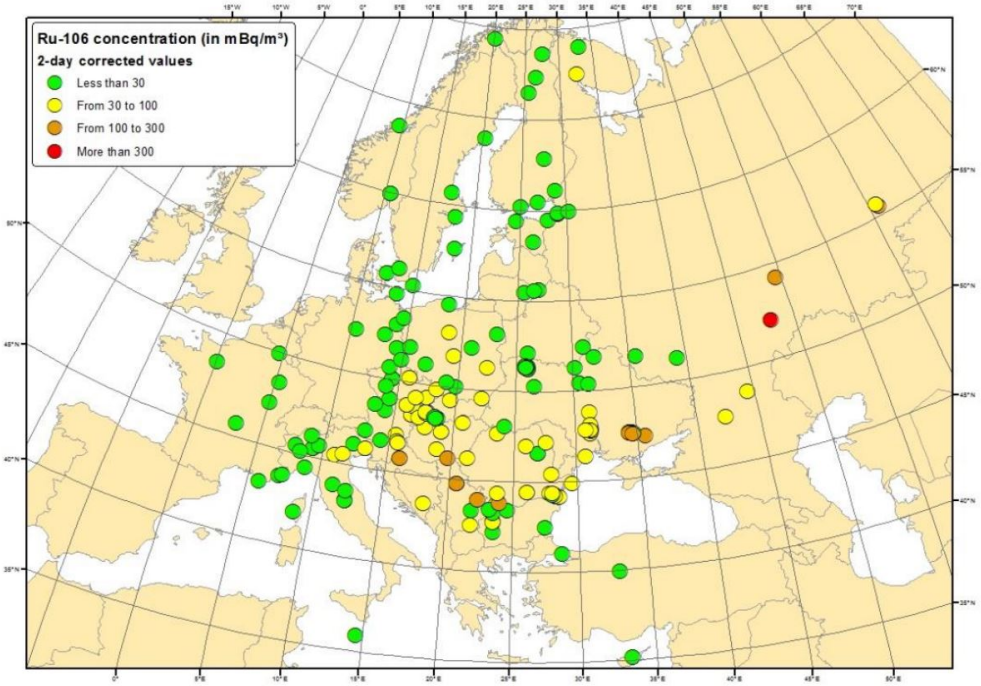

Figure 3.7: This map shows the ruthenium concentration in the atmosphere over the period of detection. These values have been corrected to account for difference in the sampling time of the air filters. Image credit: [97].

measurements and atmospheric dispersion modeling the source of this ruthenium contamination is investigated with a so called inverse modeling method. In order to

[2] a few μBq/ m^3

pinpoint a geographical area with a most likely release of ruthenium, the complete domain is represented and divided in a grid-mesh. In this mesh, each grid area is assumed to harbor a point source and its release of ruthenium is modeled and then checked for agreement with the observation and cloud behavior by projecting the released ^{106}Ru back to the map.
This is achieved by comparing the model predictions $H\sigma$ versus the available data μ, within a cost function $J(\sigma)$, which is then minimized.

$$J(\sigma) = (\mu - H\sigma)^T R^{-1}(\mu - H\sigma) + (\sigma - \sigma_b)^T B^{-1}(\sigma - \sigma_b) \tag{3.4}$$

where $R = E[\epsilon\epsilon^T]$ denotes the error covariance matrix with ϵ related to measurement or modeling errors and $B = E[(\sigma - \sigma_b)(\sigma - \sigma_b)^T]$ as the background error covariance matrix. The matrix H from Equation 3.4 is a Jacobian matrix where the response of the dispersion model to a release of ^{106}Ru is represented in each column. Finally σ_b represents the a priori emission in contrast to the updated source from σ. These techniques and mathematical formalisms regarding the inverse modeling have been developed after the Chernobyl incident and extensively tested and validated in any nuclear incident since then.
The specific domain used in this case ranges from [-10W,70E] and [34N,70N], with a spacial resolution of 2° x 2° leading to 720 potential sources. For a duration of measured activity over 14 days by 161 air sampling stations this resulted in the calculation and analysis of 720x14 distinct atmospheric dispersion simulations, to determine the most likely source position. Figure 3.8 shows the final results in terms of agreement between these simulations and the observed values. The likelihood of the source location drops below 30% outside of Russia and parts of Ukraine. In

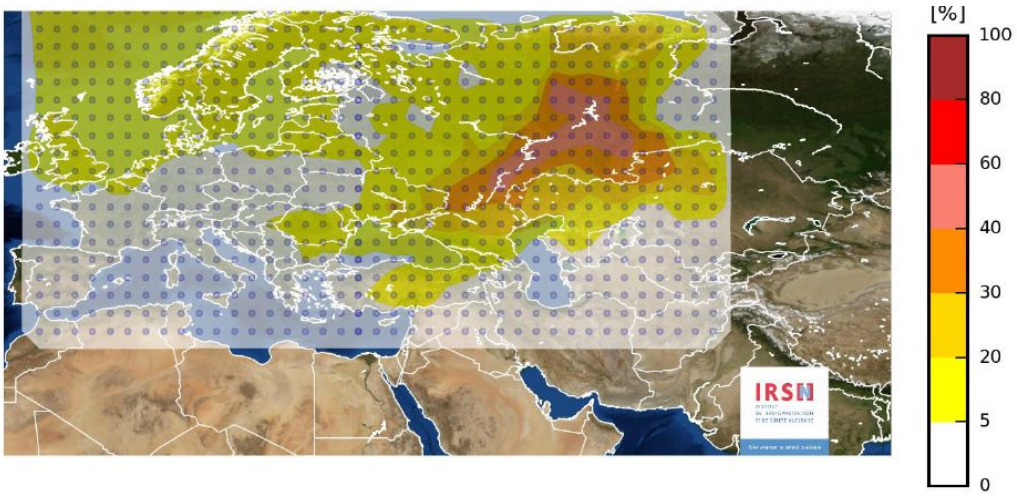

Figure 3.8: The grid overlay on the map, where each dot represents a potential source in the domain. Except for the Ural region in Russia, other geographical regions are very unlikely to be the source for the ruthenium contamination. Image credit: [97].

fact the most likely scenario seems to be a 150 TBq source releasing ^{106}Ru over a duration of not more than 24 h, on the 25th of September in the southern Ural region.

In a next step the report investigated possible scenarios, consistent with the data, in order to identify the origin of this accident. A reactor incident can be excluded, because no other radionuclides besides ruthenium where measured. ^{106}Ru can be used as a medical source in the treatment of some forms of cancer, but such a source would be highly unlikely as the typical medical activities are much lower. To observe the measured ruthenium activity several thousand medical sources would have been needed. Another possibility is the accidental release of ruthenium through a PUREX process. During the separation process of the radionuclides, ruthenium transforms from its solid (RuO_2) to its liquid phase ($RuNO(NO_3)_3$). Above $100° - 120°$C, the gas RuO_4 is produced, which is not stopped by filters, as the are typically designed to filter cesium, strontium and other radionuclide at this point in the process and the escape of ruthenium can usually be monitored and controlled by the temperature. A loss of cooling fluid or other unexpected temperature rise at this point of the PUREX procedure could therefore have been responsible. A similar event occurred in 2001 in the La Hague AREVA fuel reprocessing plant.
The estimated source term calculated with knowledge of the PUREX process and validated at the La Hague incident puts the initial source at several PBq, in agreement with the CeSOX source. In addition to this and the geographical evidence hinting to Mayak, the ratio of ^{106}Ru/^{103}Ru further points to the manufacturing of the SOX source as the cause of this accident. This ratio is only determined by the cooling time (time since last irradiation) and has been detected by the air filters in the ruthenium cloud to be ≈ 4000. A ratio that high excludes cooling times of 7-10 years, which is the typical time for reprocessing and favors a much shorter cooling time of a few years, like the two years of the cerium source.

The conclusion from this report ([97]) is a possible scenario in which an uncontrolled rise in temperature during the PUREX process lead to an ruthenium release during the production of the SOX source in Mayak, leading to the observed cloud as well as the failure in production of the cerium source. As no official statement by any authorities have been made to date regarding this incident, further information/validation or confirmation on what actually happened remains unfortunately unavailable.

3.2.2 Encapsulation

The ^{144}Ce-^{144}Pr source was planned to be encapsulated in multiple layers of shielding to absorb β-radiation, for transportation and to protect against building pressure. The chemical form of the cerium is CeO_2 and cerium and praseodymium differ in terms of valence, which leads to the following reaction via β-decay:

$$4CeO_2 \rightarrow 2Pr_2O_3 + O_2 \tag{3.5}$$

This accumulating oxygen would have lead to a pressure increase inside the source capsule. Although this effect would have only resulted in a pressure increase of approximately 5 bars over the course of two years, it had to be taken into consideration when developing the inner encapsulation.

Another potential risk (as the source is self-heating, with a thermal source power in the range of approximately 1 to 1.5 kW) arose from the possible chemical reduction of Ce at high temperatures:

$$CeO_2 \rightarrow CeO_{2-\epsilon} + \frac{\epsilon}{2}O_2 \tag{3.6}$$

This could have lead to water dissociation and the production of H_2. To account for theses effects, to provide shielding against β-particles, to ensure a low temperature and a homogeneous heat profile as well as to provide pressure resistance, the inner shielding seen in Figure 3.9 was proposed. The CeO_2 is pressed in several copper

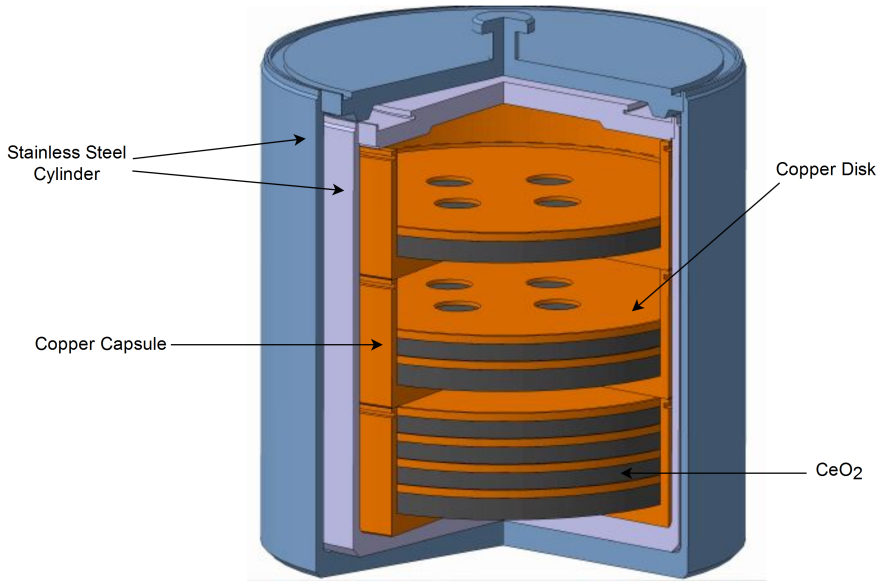

Figure 3.9: This 3D model shows the CeO_2 in its inner shielding. The ^{144}Ce was planned to be pressed into pellets of $2.5 - 3.0\,g/cm^2$, shown in dark grey. These are encased in copper disks of 1 mm thickness, in three copper capsules and surrounded by two stainless steel cylinders. The whole design offers a free volume of $\approx 25\%$ for good heat dissipation. Thermal studies have shown, for a 3.7 to 5.5 PBq source, the thermal power can be of the order of 1.2 to 1.5 kW and temperature of the CeO_2 can be of the order of 500°C and 300°C for outside of the steel cylinders (see Section 4.4). Image based on [74].

disks, stacked in a copper bar structure (containing three copper capsules) and enclosed in two steel cylinders. The cerium pellets (pressed from cerium powder) can generate thermal power in the kW-regime and therefore reach temperature of several hundred degrees, if left uncooled (see Section 4.4), which is why special temperature resistant steel alloy would have been used or with regular steel, the steel cylinders where planned to be treated with Spray-applied Fire-Resistive Materials (SFRM). These SFRMs are usually applied to structural steel beams to protect the material from breaking during a fire or can be applied to all other important steel and metal structures, without interfering with their structural integrity.
Although effectively shielding the β-radiation, this inner encapsulation would not have been sufficient in shielding γ-rays. Exited states of ^{144}Pr produce $1 - 2$ MeV γ's, as can be seen in Figure 3.10. The most notable γ's are at 1380 keV (0.007%),

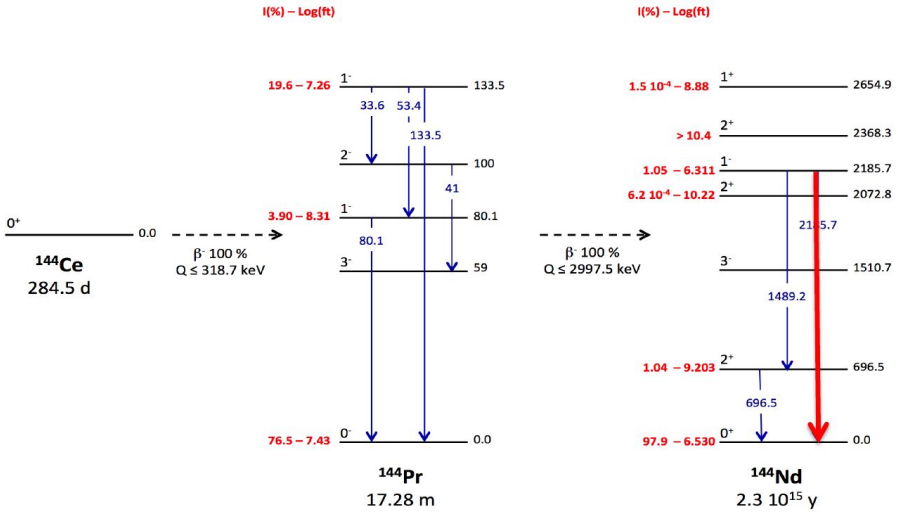

Figure 3.10: This term scheme shows the γ's created from the ^{144}Ce and exited states of ^{144}Pr, especially the most problematic one at 2185 keV, marked in red. Image based on [74].

1489 keV (0.3%) and most importantly at 2185 keV (0.7%). Due to the very high activity of the source these are not negligible, the 2.185 MeV γ's alone result in $2 \cdot 10^{10} \gamma$ per sec for a 3.7 PBq source. To absorb these, the source with the inner encapsulation was planned to be embedded in a high-density tungsten alloy shielding, sealed with a tungsten cap and encased by a steel flange. Figure 3.11 shows the planned full source shielding with its 2 t tungsten alloy main shielding. Special holes enable the deployment of temperature sensors close to the source and the whole setup can be lifted with a crane on steel handles. These handles are mounted via a so called helicoi technology, where drilled threads are filled with a second thread of higher material strength to protect the thread from mechanical damage, and this is especially useful for brittle materials as it is the case with most tungsten alloys.

Besides the shielding against γ-radiation, the outer tungsten encapsulation has additional requirements arising from safety regulations. Due to the transportation through Russia, France and Italy, all safety requirements from the various authorities had to be met and taken into consideration when developing the outer tungsten shielding. These tests include a percussion test, where the shielding is struck heavily with a steel bar, a heat test where a temperature of 800°C is applied for 10 minutes and a drop test in which the tungsten is dropped from 9 m. Besides these, the outer encapsulation had to also pass a leak test, all the while performing its main task in shimming against γ-rays.
The tungsten alloy HWNF50 was developed by a Chinese manufacturer XTC, who succeeded after a first failed attempt to produce a shielding meeting the set requirements. The full shielding provided a thickness of 190 mm of HWNF50 tungsten around the inner steel capsule, with a height of 541 mm and a diameter of 538 mm. Measurements showed a global density of 18.25 ± 0.25 g/cm^3 and a vacuum tightness of 10^{-3} mbar l/s. The finished shielding was used briefly for assembly testing and

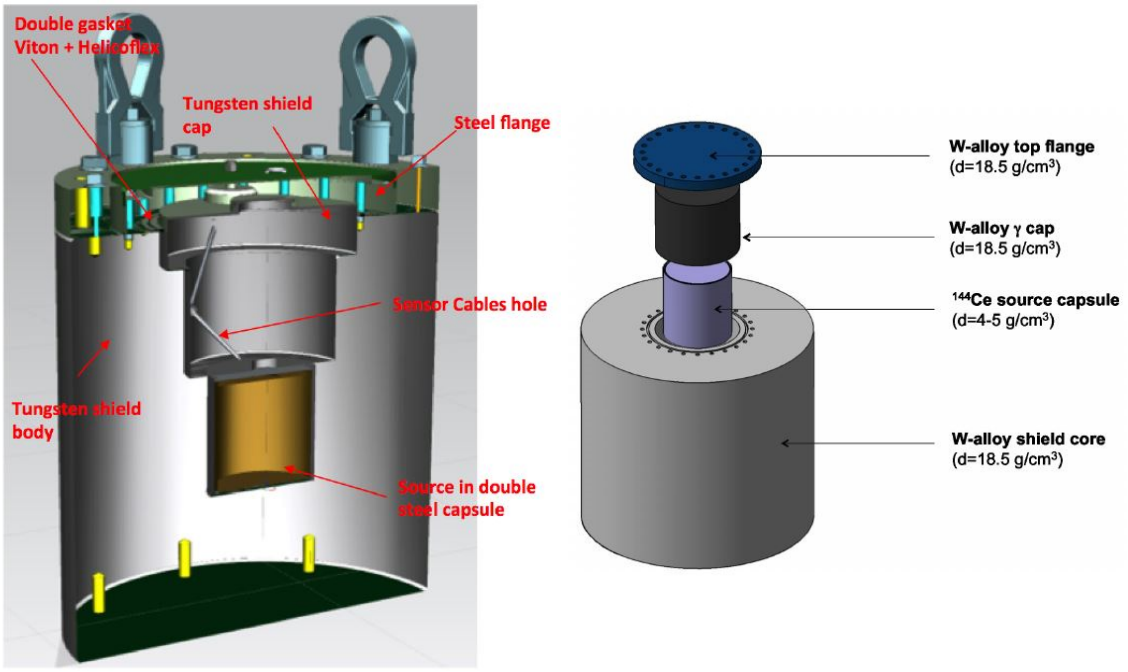

Figure 3.11: These sketches show the source in its full encapsulation which would have been deployed in the calorimeter.
On the right: To place the source capsule in the main shielding, the top of the inner steel encapsulation has a knob on top to enable lifting and inserting. After being placed in the outer tungsten, the source can be sealed by first placing the tungsten cap on top and then screwing the top flange and last the steel flange. This full setup effectively shields against β- and γ- radiation, mechanical hazards and is able to be placed in the calorimeter. In order to lift the heavy, more than 2 t full setup (0.5 m $\times$ 0.5 m), four thick steel handles are located at the top, visible in the left image. Due to the brittleness of the materials involved, the deployment of so called helicoi threads was necessary. In fact all threads on the tungsten shielding (and the aluminum in case of the mockup) use this thread reinforcement technology. The sensor cable holes, foreseen to house a temperature sensor, can be accessed on the top via a 9-Pin vacuum connector on the steel flange. Image based on [74].

could be used already for preliminary tests with the mockup inside the calorimeter, before it was shipped to Mayak.

3.3 The Mockup Source

The mockup system was designed with the goal to enable a high precision calibration of the calorimeter, whilst remaining as close to the potential source and its proposed encapsulation as possible. Therefore the mockup is able to deposit a known amount of thermal power via electrical heaters into a copper cylinder with identical dimensions than the stainless steel capsule used in the cerium source setup and can be mounted fully in the calorimeter with its vacuum tight outer shielding. Besides functioning as a calibration tool, the similarity in terms of geometry and encapsulation, also enabled testing of mounting and assembling procedures as a preparation for the cerium source.
At its core, the mockup consist of several mechanical parts, namely the inner copper body, the aluminum plug, outer aluminum shielding, aluminum ring and stainless steel top flange, all with identical dimensions to the cerium source and its shielding. This means the mockup is virtually identical[3] to the shielding seen in Figure 3.11, besides its innermost parts. These feature an electrical system consisting of the copper conductor heaters, able to provide a thermal heating power of up to 1.5 kW, driven by a precision power supply, and three PT-100 temperature sensors, which are read-out via Digital Multi Meters (DMM). The complete system (mockup and calorimeter) is controlled and monitored by a LabVIEW based setup.
This section will describe these mechanical and electrical components and review the performance of the mockup system, which was a crucial element in the successfully performed calibration of the calorimetric system, discussed in Section 3.4.

3.3.1 Mechanical System

The innermost part of the mockup consists of a 15.3 cm high and 15.4 cm in diameter copper cylinder that houses the electrical heaters. It also differs the most of all the mockup parts in geometrical aspects compared to the proposed cerium encapsulation seen in Figure 3.9. As the main purpose of the mockup is the controlled release of a known amount of heat for calibration purposes, a selected material should enable a fast heat transportation from the cartridge heaters to prevent overheating or cooling and to reliably study the behavior of the system with different thermal powers. It is also mentionable, that during the construction of the mockup, no source design besides the overall dimensions had been finalized. Additionally due to the cabling needed for these heaters, cabling holes are a necessity.

The mockup design therefore consists of an inner copper (E-copper 99%[4]) cylinder, complete with a copper cap/lid with a cabling hole, as can be seen in Figure 3.12. This massive, ≈ 30 kg cylinder was machined in the workshop in Tübingen according

[3] In terms of dimension and geometry; selected materials differ.
[4] Oxygen-free (less than 1%) copper

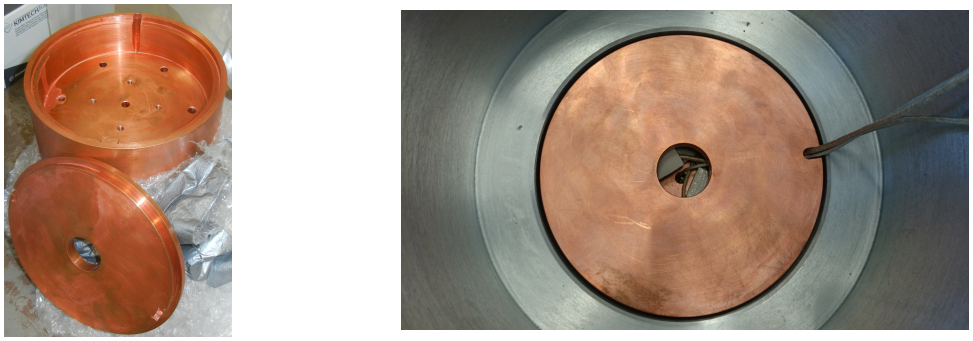

Figure 3.12: The left image shows the copper mockup cylinder and copper lid. The six visible holes are where the cartridge heaters can be inserted, while the hole in the middle is reserved for a temperature sensor. The remaining holes can be used to lift the copper in and out of the shielding. The copper cap has an assembly hole on top and a small gap an the side, where the cabling of the heaters and temperature sensors can be brought through. The right image shows the copper parts inside the aluminum shielding with the deployed heaters and cabling. The cabling is then feed through the aluminum plug and connected to the 9-Pin vacuum connector on the stainless steel.

to a CAD[5] design. It features 6 x Ø6.3 mm holes, 85 mm deep, which end on the bottom of the structure in Ø2 mm and 33 mm deep holes to house the heater heads. To prevent overheating on air, these holes fit the heaters, with just a little room to account for thermal expansion. In fact after a few initial heat ups, the heater heads usually expand and require some force to get them out, which means overall good thermal contact can be safely assumed. The middle hole is reserved for a temperature sensor, the remaining 4 x Ø3.3 mm holes are 11.5 mm deep and threaded so they can be used to screw handles on the copper during assembly. Between the main copper part and the copper cap a space of roughly 30 mm in height is left out for cabling storage, which is fed through all the way to the vacuum connector on top of the stainless steel flange.

This copper cylinder is encapsulated by the aluminum outer shielding, identical to the HWNF50 tungsten outer shielding, except for the material. The aluminum alloy EN AW 2007 (AlCuMgPb) was selected as a feasible alternative, which meets both the requirements arising from machining and is sufficiently similar in terms of thermal properties compared to the tungsten[6]. The same alloy was used for the sealing plug, which differs only slightly when compared to the source encapsulation geometry. This difference is related to cabling, as the heater setup required a bigger hole as just for the temperature sensor foreseen in the source design, enlarging it to 10 mm in diameter. The right picture of Figure 3.12 shows the copper part and cap and also the heater with their cabling inside the aluminum shielding. It can also be seen that there is a gap of a few millimeters between the sides of the copper and the shielding. This bigger cut-out radius on the outer aluminum is intentional to

[5] Computer Aided Design

[6] The thermal conductivity of the used aluminum is 140 $W/(m \cdot K)$ compared to 175 $W/(m \cdot K)$ of tungsten.

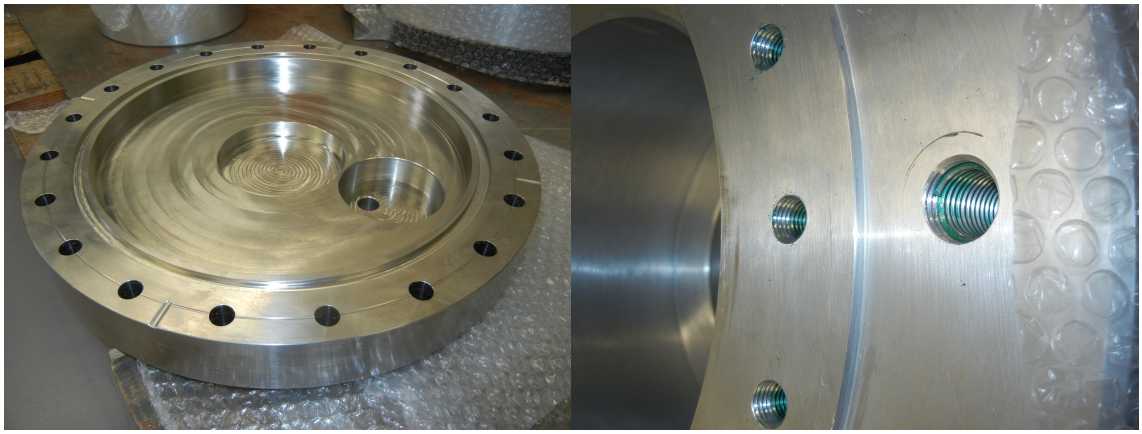

Figure 3.13: The bottom side of the stainless steel flange can be seen on the left image with its recesses for the aluminum plug and Viton O-Ring. On the right image the helicoi can be seen inside the threads on the topside of the aluminum shielding. These (light green) helicois can be inserted into a thread after it is re-cut with a special tool and protect the threads of brittle materials.

leave more space for assembly and thermal expansion, to not get the rather massive copper stuck inside the shielding and risk potential damage. The downside to this necessary safety gap, is a worse thermal contact and this visible air gap has to be taken into account concerning the thermal simulation, discussed in Section 4.3.

To successfully seal the top of the mockup for vacuum tightness, the ring had to be made with a different aluminum alloy, because the EN AW 2007 alloy is to brittle for some delicate machining operations, needed in this case. Therefore EN AW 5083 ($AlMg_{4.5}Mn_{0.7}$) was chosen as a compromise between thermal similarity[7] and mechanical realization. Due to their rather massive size and weight both the aluminum ring and outer shielding were manufactured by Kuppler[8], a company located in Mössingen (Germany) and specialized in the production of metal prototype parts. The stainless steel flange, sealing the whole setup together with the aluminum ring, is virtually identical to the one proposed for the source setup and could be built in-house by the workshop in Tübingen. Figure 3.13 shows the bottom of this steel flange on the left image, with an opening slightly to the right leading to a 9-Pin vacuum connector and a groove where a Viton O-Ring is placed to provide a good enclosure. On the right picture the helicoi can be seen in the threads. Brittle materials like aluminum or tungsten are sometimes prone to break threads when heavy forces are attached. To prevent this the threads had been re-cut and outfitted with helicois to reinforce the threads, which is especially needed for those attached to the handles used for lifting the whole setup. Another useful advantage provided by these helicois is that they minimize the loosening of tiny fragments of material during screwing and unscrewing of parts, which are a real danger to the vacuum pump in the calorimeter setup. Nonetheless after assembly or disassembly, the whole mockup

[7] Thermal conductivity of 121 $W/(m \cdot K)$.
[8] www.kuppler.com

setup has to be thoroughly cleaned before it can enter the calorimeter to achieve a good vacuum (in the order of 10^{-5} mbar).

Figure 3.14 shows a top view of the mockup parts with the aluminum ring, stainless steel plug and vacuum connector during the very first assembly test in Tübingen, done in March/April 2015. There a first heat-up of the system could be performed, before it was shipped to Munich a few weeks later for first tests inside the calorimeter. Besides a widening of the groove on the stainless steel flange for better vacuum sealing, no significant alterations concerning the mechanical parts had to be made. The whole mockup system operated successfully without failure from April 2015 till November 2017.

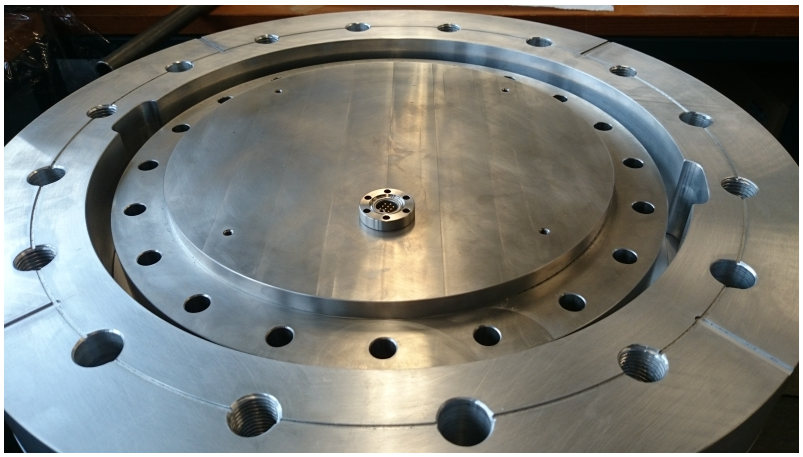

Figure 3.14: This image shows the top of the un-screwed mockup parts on top of the aluminum shielding during the first assembly testing in Tübingen in April 2015.

3.3.2 Electrical System

The core of the electrical mockup system are the electrical cartridge heaters. Six 250 W heaters are aligned in two separate parallel blocks containing three heaters each in series, enabling a total power of up to 1.5 kW. These heaters are operated via a precise power supply, connected via heat resistant cabling and operated via LabVIEW. The current and voltage measurement is acquired via two Digital Multi Meters (DMM) in a PXI-crate (see Section 3.3.2.2). Because the DMMs can't handle such a high current (>4 A), a custom-made current sensor, based on a shunt resistor, enables a voltage measurement instead. In general the heater resistance is temperature dependent, which makes a power regulation based on the voltage and current measurement vital, to either keep a stable set power or to mimic an exponential power decay like it would be the case with the real source. For calibration reasons the mockup system is also able to generate a sinusoid power function. In order to monitor, control and implement safety measures, three temperature sensors are placed inside the mockup. One directly in the middle of the copper cylinder in the center of the heaters, another one on the side of the outer aluminum shielding

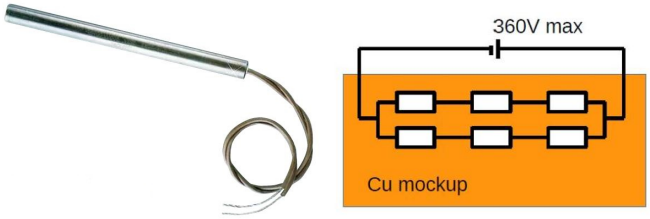

Figure 3.15: The left image shows a single CIR high Watt density cartridge heater, identical to the ones used in the mockup system. On the right, the basic schematic heater setup in the copper mockup can be seen, as there are two parallel blocks of three heaters in series. Each of those heaters is able to provide 250 W at 120 V, which amounts to a total available power of 1.5 kW. Left image based on [89].

and the last one on the top side of the aluminum plug and under the stainless steel flange.

3.3.2.1 Heaters

The CIR-1024/120V high Watt density cartridge heaters from the Omegalux company [88] meet all of the requirements for a mockup heater selection. They were chosen for their high working temperature, reliability, shock and corrosion resistance. Surfaces of these CIR-heaters are blackened and oxidized purposely while manufactured, giving them a higher life expectancy and lower mantle operating temperatures. They are built with an Incoloy 800 mantle material, which is an iron-nickel-chromium alloy, with a copper wiring, enforced by carbon, aluminum and titan. This Incoloy 800 is a high temperature resistant material, enabling safe operation temperatures of up to 750°C.

Figure 3.15 shows such a CIR-heater as well as the heater alignment inside the copper mockup. Two parallel blocks of three heaters, each with 250 W enable a total heating power of 1.5 kW. The heaters are connected and supplied via heat resistant wiring (HTMG-1CU-2620S/C). These single stranded 27% nickel coated copper conductor cables, isolated by Mica Tape insulation with treated glass overbraids, are able to support voltages of up to 600 V and temperatures of up to 450°C.

The maximum allowed operational temperature of a single heater depends on the Watt density (W/in^2) and the thermal contact. This is expressed in Figure 3.16 as the "fit in hole", namely the difference between the maximum hole diameter and the minimum heater outer diameter in inches. In a conservative estimate, a drill hole is between 0.003" and 0.008" over the drill, which results in a fit in hole of $\approx$ 0.0010" to 0.0015". This leads to a maximum operating temperature of e.g 310°C to 430°C for 127 W/in^2. With the thermal simulation model discussed in Chapter 4, maximum temperatures for a 1.2 kW to 1.5 kW power don't exceed 250°C in the copper mockup. Regardless, as a safety precaution, temperatures above 350°C, measured by the inner copper sensor will result in a safety shutdown of the system.

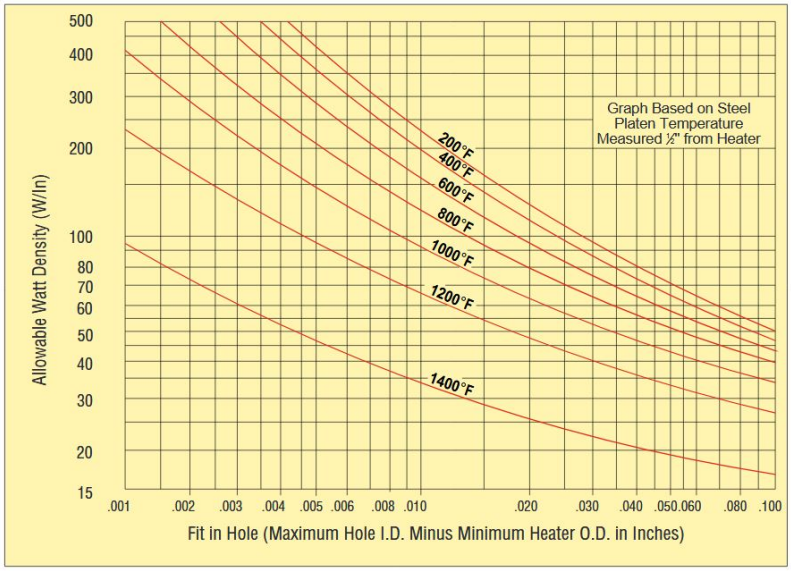

Figure 3.16: This plot from the cartridge heater manual shows the maximum allowed heater operating temperatures, defined by the Watt density and thermal contact. Image from [90].

The resistance of these heaters is in the range of $\approx 80\ \Omega$, but does change linear with temperature. This behavior has been studied by placing the heaters in a thermos flask, with modeling clay and heat the heaters passively by each other [81]. At first the flask was heated up, then let cool down with one active heater. Each time a constant temperature was reached, the active heaters power was decreased. Between 20°C and 60°C, a linear R(T) behavior was observed and fitted with 467990 data points to:

$$\mathrm{R(T)} = 0.0062\frac{\Omega}{^{\circ}\mathrm{C}} \cdot \mathrm{T} + 82.415\,\Omega \tag{3.7}$$

As it can be seen in Equation 3.7, the resistance increase through temperature is very slow, but is still an effect that has to be taken into account for a precise and stable set power.

3.3.2.2 Power Supply and Data Acquisition

An EPS PS8360-1SDT power supply was chosen to operate the mockup heaters. Besides from meeting the stability criteria (0.05% constant voltage stability under load) and providing up to 360 V and 5 A, this power supply has the additional advantage that it can be integrated and operated in a LabVIEW system. As the mockup and the calorimeter are using LabVIEW based data acquisition, this provided an obvious advantage regarding integrability.
To determine the power, keep it stable or implement power functions, a feedback loop was integrated to account for the changes in heater resistance. Two LabVIEW DMMs in a NI PXIe-1073 crate were foreseen for the current and voltage measurement. Aside from these multimeters the crate reads out the three connected PT100 precision temperature sensors via a 4-wire measurement on its internal measurement

card. These sensors are 1/10 DIN normed, which means their error is guaranteed lower than 0.07% over the whole range of interest.
The mentioned changes in the foreseen SOX phases, discussed in Section 3.1 lead to a singular high activity cerium source, over the early years of conceptualizing the experiment. The initial setup for the mockup, with the two DMMs to determine the power, however, was limited to 900 W by the limit on the current measurement set by the DMMs of 3 A, as at this point would have been sufficient to mimic a source of less activity. But in a scenario with a high activity cerium source, the thermal power could have reached 1.2 kW or even up to 1.5 kW. This resulted in a change in the electronic setup and the development of a current sensor with a range of up to 6 A. This current sensor, based on the voltage drop of a temperature stabilized shunt resistor (0.1 Ω), effectively converted the current measurement to a voltage measurement. Therefore the mockup operating capabilities could be expanded to 1.5 kW, without any loss in stability. A schematic of the basic overall mockup electronic and acquisition system can be found in Figure 3.17.

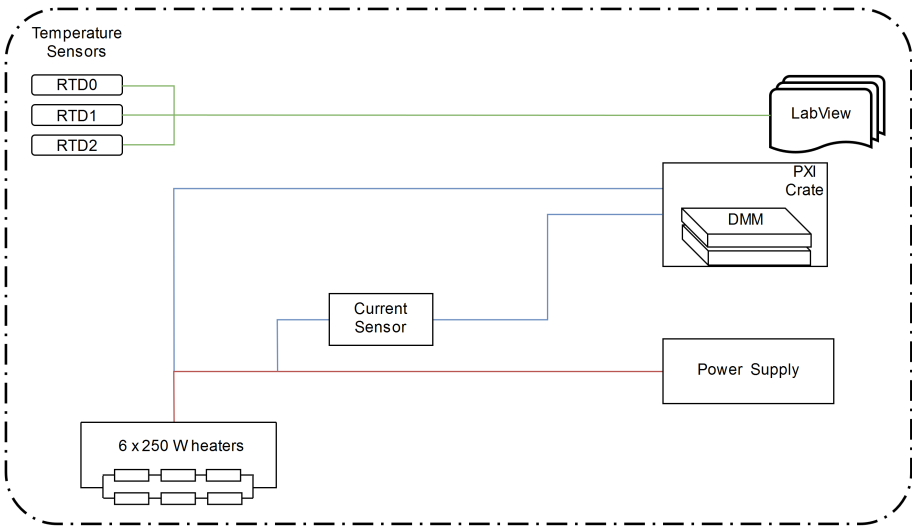

Figure 3.17: This schematic shows the main workings of the mockup electronic setup. The heaters are driven by a EPS PS8360-1SDT power supply. Voltage is measured by a DMM in a PXI-crate and a custom-made current sensor transforms the current to a voltage, which is also measured by a DMM. The voltage measurement is performed as close to the mockup as possible, right after the 9-Pin vacuum connector, while the current measurement is performed directly after the current sensor. Three PT100 temperature sensors are also connected to the PXI-crate. The whole system, including the power supply, is managed and read-out via a LabVIEW script, which had been integrated in the calorimeter LabVIEW control setup.

The resolution of the voltage measurement, done by the PXI-4071 DMM is 10 μV over the range of 0 - 360 V. Measuring of the voltage drop from the shunt resistor is achieved by the PXI-4065 DMM, with a precision of 1 μV between 0 and 5 V, as

the current sensor is designed for a voltage drop of 1 V per 1 A. These two voltage measurements are very precise, which is why the current sensor itself was carefully calibrated with a precision power supply to minimize its impact on the system and was validated to have an error on the current measurement of 0.04%.
The main parts of the current sensor are an Ohmite temperature stable 14FPR-100E-ND shunt resistor, which is especially suited for current sensing applications, a MAX680CPA voltage converter and a AD524 precision instrumentation amplifier. This amplifier is hermetically sealed in a ceramic housing and its initial small voltage offset can be compensated via two potentiometers. Additional capacitors and resistors are placed to smoothen and stabilize the circuit seen in Figure 3.18.

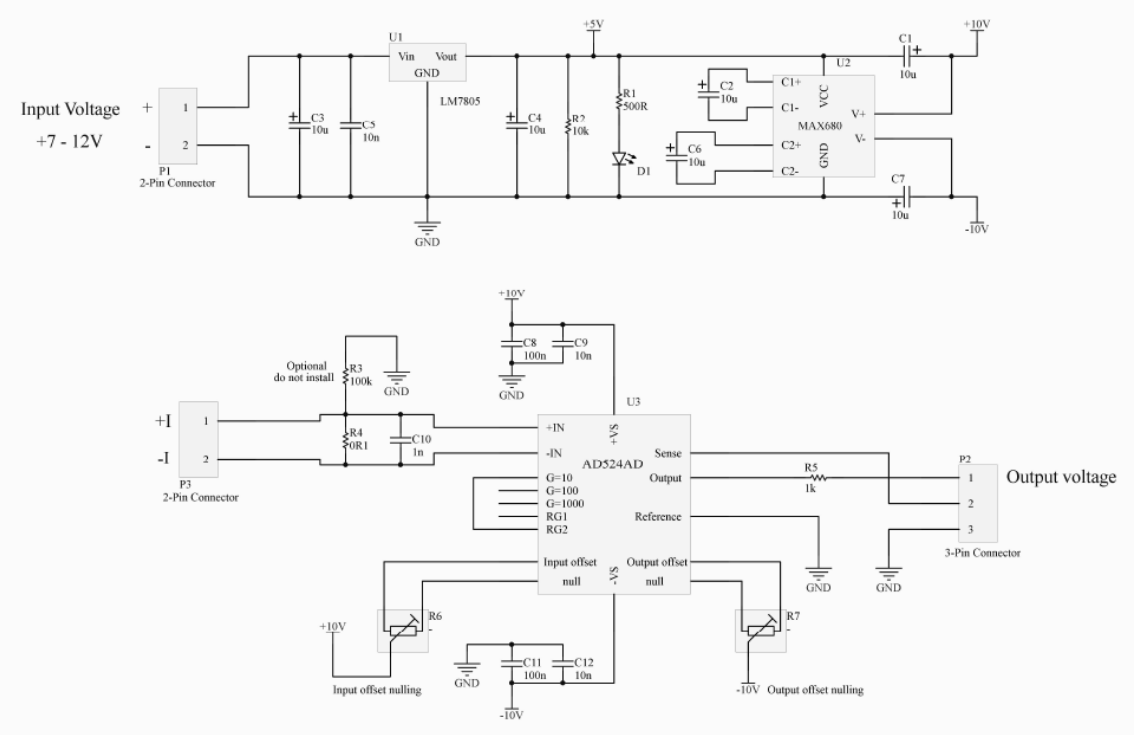

Figure 3.18: This schematic depicts the current sensor, which is a self-stabilizing temperature controlled shunt resistor system. This current sensor has been calibrated for an output of 1 V per A and validated with a 0.04% error.

Extended long time calibration (multiple days uninterrupted) measurements have put the overall accuracy and stability of the whole mockup system at less than 0.01% error for $P > 500\,W$. With its high precision and reliability, the mockup played the key role in calibrating and validating the calorimeter, discussed in the following chapter, to reach the sub 1% error constraint, required for success of the SOX experiment.

3.4 SOX Calorimeter

To determine the source power and therefore the activity and corresponding flux a custom made calorimeter has been devolved for the SOX experiment, thoroughly discussed in a dedicated paper [6] and briefly introduced in this chapter. In a flow based calorimeter the source power is determined via the temperature difference of a heat exchanger fluid (outgoing minus ingoing temperature) in thermal contact with the source. Vital parts of such a measurement are the precise knowledge of the properties of the used fluid and the general heat losses due to convection, friction or radiation. The source power P_s can in principle be stated as:

$$P_s = \dot{m}[h(p, T_{out}) - h(p, T_{in})] + P_l \tag{3.8}$$

where $\dot{m}$ denotes the mass flow and h the specific enthalpy and P_l the accumulated total heat leakage[9], which is typically a negative value. By choosing deionized water the enthalpy function h can be obtained from well documented literature values and is known with good precision. The heat loss can be minimized and controlled by special thermal and radiation insulation, as well as estimated and simulated to account for theses contributions. If both of these, specific enthalpy and heat leakage are known, a measurement of the mass flow and the in and outgoing water temperature determines the source power.
The mass flow $\dot{m}$ is the only value that can be changed and selected and is generally kept relatively low as it has impact on the friction and therefore contributes to the heat loss P_l. This power loss due to friction P_f is expressed by:

$$P_f = \frac{8\dot{m}^3 \lambda L}{\pi^2 D^5 \delta^2} \tag{3.9}$$

with the density δ, the length L and diameter D of the pipes and the friction coefficient λ.
However, the mass flow must be still large enough to prevent a phase transition of the fluid. To ensure this, in the calorimeter the outlet temperature is kept below 70°C. This results in typical mass flows of 3 - 13 g/s for a source power of 1.2 kW.

3.4.1 Calorimeter Design

The calorimeter seen in Figure 3.19 and Figure 3.21 is in principle a stainless steel vacuum chamber of cylindrical shape, divided in a bottom part, holding all the connections for water pumps, sensors and cabling and a removable top bell structure. The complete chamber is 83 cm high and has a diameter of 92 cm and the bottom part and the bell are divided by a 923 mm thick flange, that closes due to the weight of the bell.

A water circuit with 8 mm pipes is interlaced over the vacuum chamber, which enables the thermalization of the chamber to be equal to the inside structures and

[9] Conductive or convective heat losses, e.g the heat loss due to a low vacuum investigated in Section 4.5 and seen in Table 4.4.

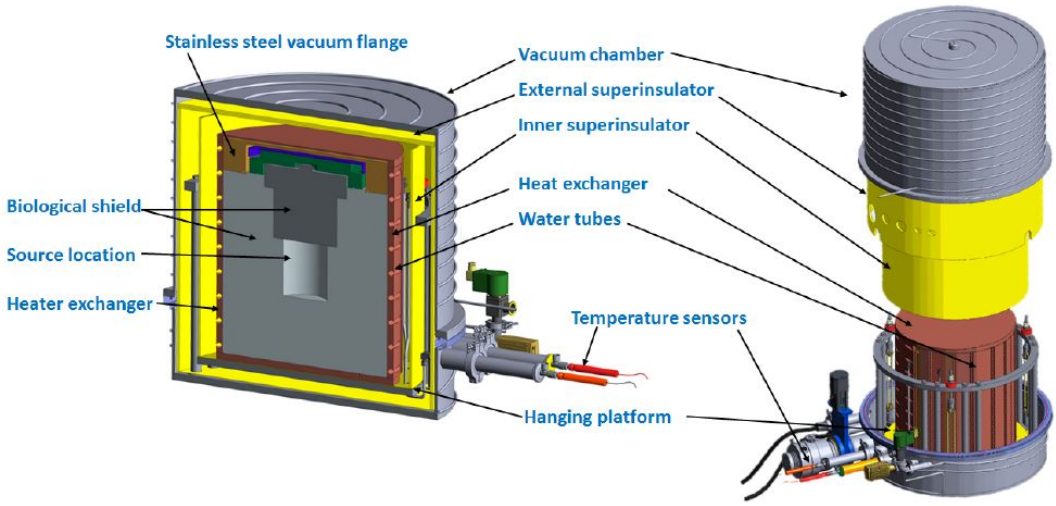

Figure 3.19: These renderings show the main parts of the calorimeter. The outer vacuum chamber is split in two parts and the upper one can be lifted to mount the copper heat exchanger, super-insulator and mockup/Ce-source with their shielding on a hanging Kevlar rope platform. The lower part houses all the necessary connections and tubes for the vacuum and the two water circuits. Image: [6].

thus minimizes conduction, radiation and convection losses.
The mockup (or in principle the source and its shielding) are wrapped by a copper heat exchanger with 6 mm stainless steel tubes for the main water loop. The copper heat exchanger is divided in three parts, each with a tube structure that is connected via VCR fittings. It consists of a bottom and top part of 20 mm thickness as well as a lateral one, which can be tightened with 10 screws on the front and back side to provide better fitting and therefore better thermal contact.

Multiple stages of super-insulators shield against thermal radiation. Coolcat 2N, which is a double-side aluminized mylar with a non-woven polyester spacer material, is placed as a 10-layer foil all around the heat exchanger as well as the support platform and the bottom floor of the vacuum chamber.
To reduce conduction losses, all of the inner structure is placed on a Kevlar rope suspension system. These Kevlar ropes of 0.3 m length each were chosen because the thermal conductivity of Kevlar is only k = 4 W/m K.

As already seen via Equation 3.8 the relevant measurements to determine the source power are the mass flow $\dot{m}$ of the heat exchange fluid and the in and outgoing temperature T_{in} and T_{out}. Figure 3.20 shows the schematic positions of these measurements among other related instrumentation. The $\dot{m}$ measurement is obtained by two Micro Motion Coriolis Elite Sensors positioned at both the start and end of the water flow system, with an accuracy of 0.05% for mass flows of 1.4 - 30 g/s. Similarly placed are two PRT thermometers with a precision of 3 mK, immersed in water in two separate Ertacetal tubes placed at entry and exit points of the water loop. Cooling

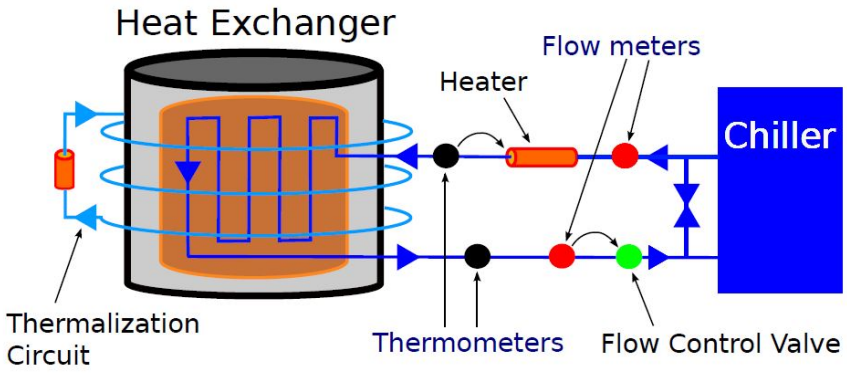

Figure 3.20: A chiller supplies and cooles the main water loop where the flow and temperature is stabilized by feedback loops with a 100 W heater, flow meters, thermometers and a flow control valve. The thermalization loop for the outer chamber is handled separately to not influence the measurement. Image from [6].

and pumping of the water is handled by a chiller[10], which provides a cooling power of 3 kW and supply's water with a temperature of 15°C at 3 bar. To stabilize the important parameters of mass flow and inlet temperature, a proportional Samsung Type 3510-1 valve stabilizes the mass flow with an maximum oscillation around the set point of 0.3%. The temperature is, besides the chiller, additionally stabilized by a 100 W heater, enabling a stability of 0.2°C for inlet temperatures of 13 - 18°C. Both the temperature and mass flow stabilization systems are operated via feedback loops using the data obtained from flow meters and temperature senors.
To minimize losses due to convective heat transfer, a vacuum of at least 10^{-5} mbar is produced by a scroll pump (SCROLLVAC SC 15D) and a turbo pump (TURBOVAC 361). The vacuum pressure is monitored via IONIVAC Combi Transmitter ITR-90 pressure gauges on multiply locations inside the chamber. Because the power calculation is very sensitive to the liquid's properties, a conductivity-meter[11] monitors the purity of the ionized water.

All the mentioned systems and their sensor controls are handled by a CompactRIO NI 9068 system. Designed for real-time measurement this device is connected via Ethernet to a dedicated computer, which runs, operates and monitors the calorimeter and mockup system via a LabVIEW script. Besides various safety measures embedded in this control software, in case of a signal loss and possible uncontrollable heating, a programmable logic shuts down the heater system when a special control signal sent from the CompactRIO is lost.

[10] Huber Unichiller 025T
[11] Swansensor RC U

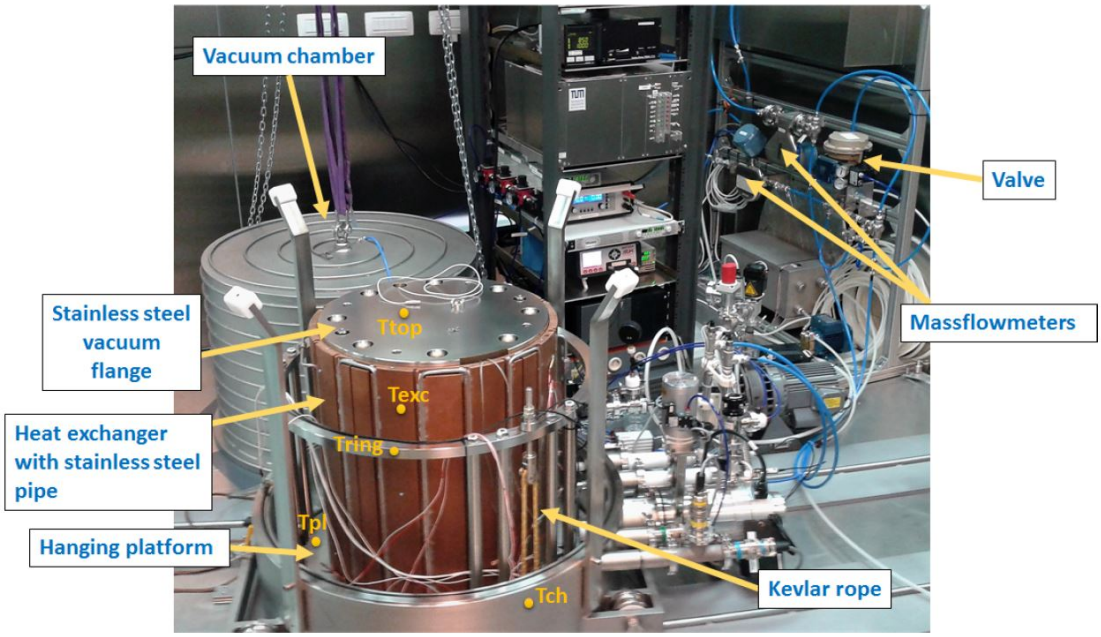

Figure 3.21: A picture of the calorimeter, taken in the clean room of the LNGS laboratory. Here, the vacuum chamber is lifted and seen in the back and the super-insulators and the top copper part are removed, so the mockup in the copper jacket can be seen. The yellow points mark the temperature sensors of several parts for monitoring reasons. Image from [6].

3.4.2 Calibration Results

The first measurements done over the period of one year in the Laboratory of the Technische Universität München (TUM) were dedicated to measure the impact of the potential heat losses and gain understanding on the behavior of the system. During this period, measurements were done with a constant power function, typically between 700 - 1000 W and were compared and accompanied by thermal simulations, discussed in the next chapter (Chapter 4) to study the impact of the heat losses and understand the temperature gradient inside the vacuum chamber.

When a constant power is applied, the system takes approximately 2-3 days of transient time to reach thermal equilibrium. This equilibrium was defined by the differential of the outgoing water temperature T_{out}:

$$T'_{out} = \frac{T_{out}(t+\delta t) - T_{out}(t)}{\delta t} \tag{3.10}$$

with $\delta t = 3\,\mathrm{h}$ and a limit on $|T'_{out}| < 18\,\mathrm{mK/h}$.
In order to estimate the loss due to thermal radiation, both of the super-insulators were removed and compared to regular measurements with different source powers. Although temperature dependent, the overall losses are smaller than 0.6% on the measured power and are of the order of typically 1.5 W.

A blind measurement was used to test the understanding and reconstruction capabilities of the calorimeter and its data analysis. With a mass flow of 5 g/s, the power of the mockup source was set to $P_{set} = 729$ W and measured to be $P_{mes} = 727.9 \pm 1.3$ W, resulting in an error of only 0.2% for measurements with constant power.
As the cerium source would not had constant power, the main goal is to obtain power measurements from an exponentially decaying power source. The mockup system is able to provide such a power function with realistic time scales and the results of such a measurement can be seen in Figure 3.22. The power function was

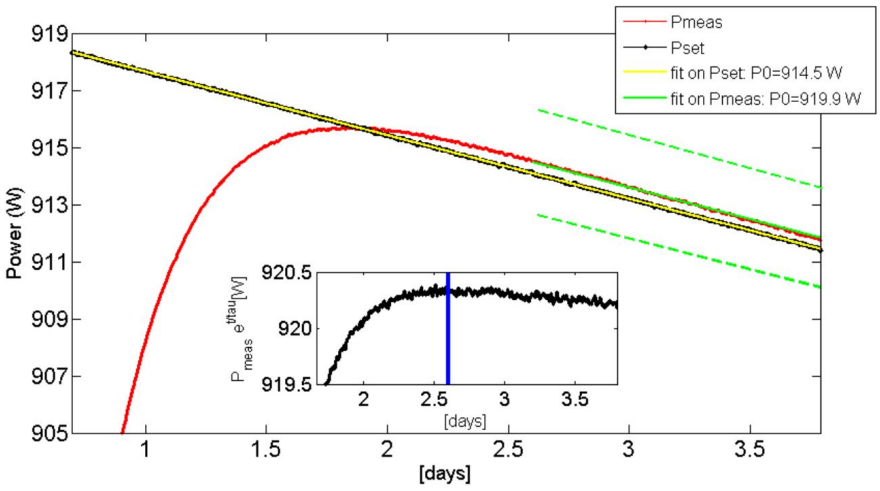

Figure 3.22: Example of a calorimetric measurement with an exponentially decaying mockup power function, seen in black. After a thermalization period of 2.5 days, the measured power, shown in red, closely follows the mockup power. To derive a power measurement, a stability criteria, defined by Equation 3.10, has been used and the system stays well within the 0.2% band error plotted in the green dashed lines. Image from [6].

set to:

$$P(t) = P_0 \cdot e^{-\frac{t}{\tau_{Ce}}} \tag{3.11}$$

with $\tau_{Ce} = 411$ days.

In order to determine the power, the measured power was multiplied by $e^{\frac{t}{\tau_{Ce}}}$, once a stability criteria similar to Equation 3.10 was reached. A difference between the set and measured power of only 0.7 W (for 914 W) has been measured. This results in an error of the order of 0.1%, which includes potential heat losses and the thermal time delay from the heaters to the cooling water. With this precision, the SOX calorimeter was a full success and would have been perfectly able to measure the cerium source at better than 1% level, to meet the requirements on the knowledge of the flux on this anti-neutrino source.

Chapter 4

Thermal Simulation

4.1 Introduction

The following chapter is dedicated to the accompanying thermal simulations of the mockup, cerium source encapsulation and calorimetric systems, developed during this thesis. The goal of these thermal simulations was to contribute in understanding of these systems, to predict thermal timescales and therefore measurement time beforehand, to test possible mechanical adjustments and to provide safety requirements by gaining knowledge on the internal thermal gradient, otherwise inaccessible via temperature sensors.
To achieve this, a framework capable of handling complex geometries and able to connect heat and fluid flow physics was needed and found in the commercial COMSOL Multiphysics software, a state of the art finite element simulation toolkit. With this software, several different simulations during multiple steps in the development phase have been designed and validated, ranging from an early understanding of the mockup heaters to constraining the losses due to convection in the full calorimetric setup. After an introduction of the basic concepts on finite element simulations and the COMSOL Multiphysics framework, these simulations will be introduced and their performance shown as well as their goals and contributions to the overall development discussed.

4.2 The COMSOL Multiphysics Framework

The COMSOL Multiphysics software is a commercial cross-platform interactive simulation tool, which enables the simulation of physical, chemical and mechanical processes expressed by differential equations. COMSOL is already well established in a multitude of studies ([66], [86], [106]) and it consists of a Multiphysics[1] framework, coupled with a graphical interface that enables the user to implement or build a geometry, assign materials, set the relevant physics and solve for the wanted variables. Due to the modular structure, physics modules are treated (and purchased) separately, but can be freely connected to best represent the current physics problems,

[1] A COMSOL term, meaning that it is possible to connect various physics modules.

as for example heat transfer and fluid flow physics, in the case of the simulations performed here. Besides this flexibility, the COMSOL software enables (via its CAD Import Module) to directly import CAD-files for the geometry building, which is a vital requirement when simulating complex and evolving geometries.

COMSOL is based on the Finite Element Analyses (FEA), which is a numerical approach to solve partial differential equations. The principle of this FEA method is to divide a geometry into smaller finite elements. These elements, encased by boundary points, consist of simpler geometries (tetraeders, quaders, etc.) and their physical behavior is therefore easier to model. With the use of linear or polynomial basis functions defined only over such elements and continuity between the elements on the boundary points, this leads to a system of algebraic equations, of which the solutions result in a value for each boundary point and therefore in an approximate description of the system. The actual form of these basis functions is typically given by the problem itself and/or the geometry of a element, in the sense that a three dimensional geometry for example results in a higher polynomial approach than a two dimensional one. Continuity between the boundary points is always mandatory, not only from a standpoint of formalism, but also from a physical, in form of energy release and conservation within solid bodies or movements of objects, which also follows that a geometry can not be disconnected in these types of simulations.
The process of dividing the domain into smaller elements is often referred to as meshing, or mesh generation. Hereby it is not required that all meshes share the same geometrical base objects and it is in fact often better to mix and choose between different geometries depending on the object in question. On one hand it is desirable to generate a very dense mesh and therefore big amount of finite boundary points to improve precision, but this generally results in longer computing times and can sometimes not even yield better results (see Section 4.2.1). Picking the right mesh for a given problem is a vital part in FEA simulations as these equally influence solvability, precision and computing times and it is often a great starting point for optimization and improvement.

After meshing, the linear equation system with its boundary conditions is solved by either a direct or iterative solver, depending on the system (static or time dependent differential equations) and memory or error constraints, as a direct solver approach is more robust, but will result in higher memory usage than a iterative solver. This is an issue that has to be taken into consideration with dense meshes, as e.g. for the full calorimetric simulation seen in Section 4.5, more than 32GB of RAM are required with a direct solver. The iterative solver, on the other hand may require longer computational time and can also be more unstable but can converge on a solution with way less of RAM usage. It is also possible by selecting good start parameters for the iterative solver, to outperform the direct one, if a good knowledge of the system or previous simulations are used as input parameters.
Both, knowledge on the meshing procedure and specific solvers with their configurations settings is often needed to tackle complex simulations, especially when multiple physics frameworks are used as it is the case for the simulations presented in this

chapter. The most relevant techniques, geometry building, meshing and solving in the COMSOL framework, will be discussed shortly as they are used in all of the following thermal models.

4.2.1 Geometry Building, Meshing and Solving in the COMSOL Framework

The use of the COMSOL CAD Import Module enables the import of CAD-files for geometry building, which provides a big advantage over manually drawing a given setup. Nonetheless, this import method needs some adjustments and good judgment on the users end, as it can otherwise lead to unwanted complexity as well as virtually unsolvable simulations. As CAD drawings of parts are designed from an engineering's perspective, features like threads, valves or very fine grooves can hinder meshing of the geometry and therefore a compromise between meshability and setup similarity must often be made.

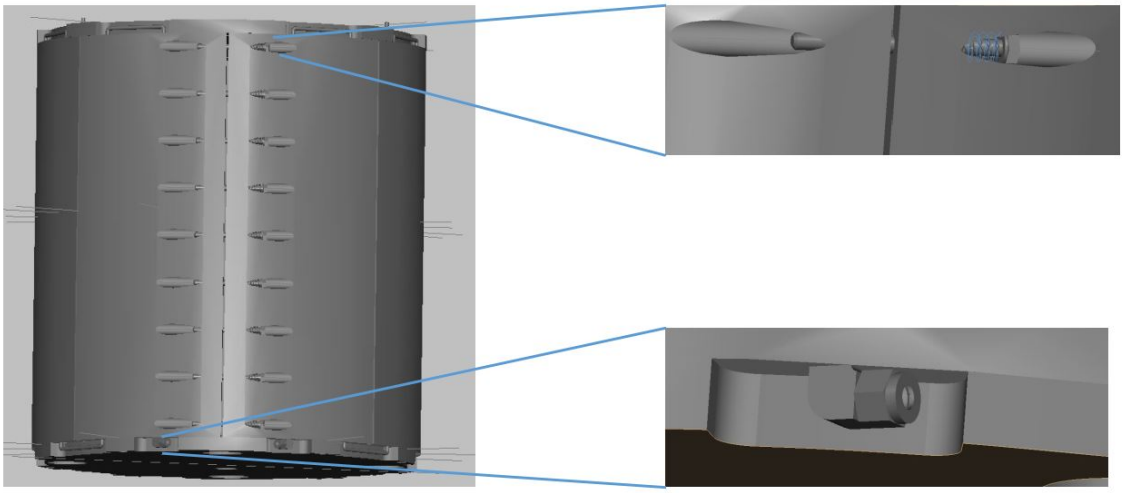

Figure 4.1: Example of removal of features in the thermal simulation. The two features shown on the right, belonging to the copper jacket, namely the threads and valves had to be removed from the CAD-files in order to keep the simulation solvable and meshable. Similar manual adjustments had to be made and threads removed from other parts, while overall though, the simulated geometries had been very close to the original setup and its complexity.

Figure 4.1 shows exemplary two problematic parts, located on the copper jacket outside of the mockup. The valve-pump-structure for the water loop and the screws to seal and tighten the lateral part were removed to prevent meshing issues. By manually removing or adjusting problematic parts, a good and solvable approximation of the mockup-calorimeter geometry could be build, which also remained somewhat flexible due the use of CAD-files versus a manually drawn geometry, in the sense that e.g. a simulation without the top of the copper could be easily achieved by

simply de-selecting the CAD top copper part, instead of building a new geometry. All of the simulations presented in this chapter, have been build with this CAD-files based technique and rather than adding them to COMSOL's own visual geometry representation, a CAD kernel could be used for all graphical purposes.

Because mesh generation affects the direct accuracy of a FEA simulation and not just the computational time, mesh refinement/optimization is needed and worth the effort. After the first steps of geometry adjustments, like those described earlier, a simple starting mesh can be generated. To improve this, one could simply increase the density of the mesh elements. Typically this is not ideal as a homogeneous dense mesh is not suitable for complex geometries and also creates immense computation time. In a 3D simulation, such as those discussed in this chapter, a tetrahedral mesh is characterized by its minimal/maximal element size and the element growth rate. To improve on a given mesh an approach can be to start with a coarse but suitable initial mesh and reduce the minimum element size whilst comparing the resulting solutions. COMSOL provides a Global Adaptive mesh refinement, where an error estimation strategy is used to generate a global mesh of varying element size for a given geometry. Although often a good starting point, this typically results in a usable mesh which often tends to over-mesh edges and small features, sometimes of little to no interest in a given simulation, while selecting bigger elements for regions of interest from a physics perspective. There is the possibility of selecting parts of the geometry only to build a Local Adaptive mesh, but then special care has to be given to the boundary where two locally generated meshes intersect to stay congruent. Even though time consuming, a manual mesh generation can outperform these adaptive meshes and also enable more flexible accuracy requirements to meet the needs of a specific physics question targeted at the simulation. Two partial example meshes from the model discussed in Section 4.3 can be seen in Figure 4.2. All the simulations developed during this thesis were built with manual meshes, often with two distinct sets of meshes, one aimed at fast computation time, used for parameter refinement and debugging and another one aimed at maximum precision, especially around temperature sensors or physical relevant features like the mockup heaters or water circuit.

To generate these meshes mostly tetrahedrals were used but also some cubic elements, in cases where it suited the geometry. These range from 0.1 mm to a maximum element size diameter of 62 mm and result in 34 million domain elements, 42 million boundary elements, and 56 280 edge elements in the full mockup-calorimeter simulation. The right side of Figure 4.2 shows a mesh aimed at maximum accuracy for the inside of the mockup copper part, with its six heaters and sensor located in the middle. Such a mesh is needed for time sensitive studies and to resolve/observe the heat flow from individual heaters inside the copper. On the other hand, in a simulation of longer timescales such a mesh would only increase computation time (because the copper is equally thermalized after a short time), therefore mesh selection additionally to mesh generation is also dependent on the specific goal of a given simulation.

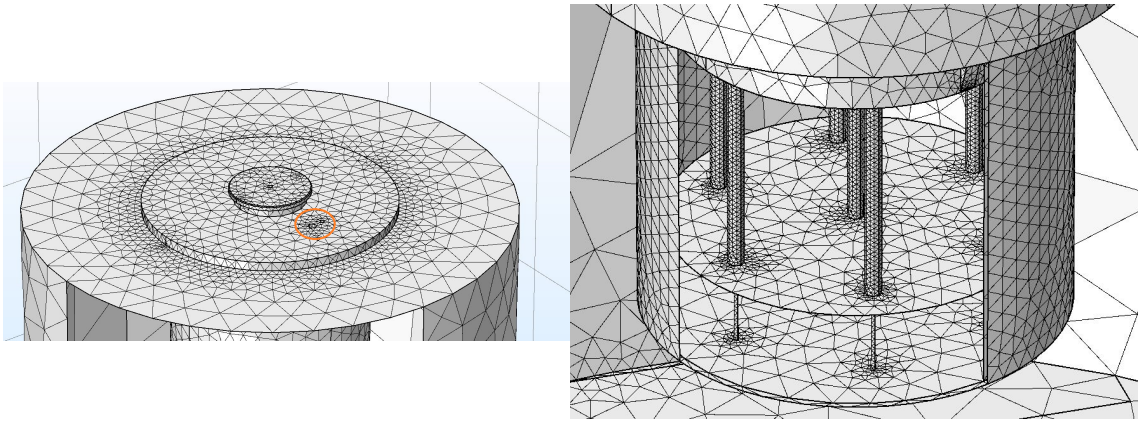

Figure 4.2: Two example meshes from the model discussed in Section 4.3. The left side shows the top of the mockup shielding with the aluminum plug and it can be seen that the mesh is at its densest on the hole used for the temperature sensors on top of the mockup (inside the orange ring), while bigger elements are used for the main outer shielding. The right shows a cut image of a very detailed mesh to resolve the catridge heaters and temperature sensors inside the inner copper domain, to simulate these important parts with the highest accuracy possible.

As already stated when solving a COMSOL simulation the choice of solvers has to be considered. In principle the choice is between a direct or iterative approach and, if multiple physics modules are used, between a coupled or segregated solver. The left side of Figure 4.3 shows the convergence of an iterative solver for a steady state simulation of the model discussed in Section 4.3. With good starting values (typically obtained by previous simulations) an iterative solver converges on the solution within a few minutes and minimal RAM usage, opposed to a direct approach taking roughly double the time with massive RAM requirements. If multiple physics modules are used, the situation gets more complicated. It is possible to couple the physics and look for the solution with direct or iterative approaches or to split them and treat each sequentially using the results of the previous steps. In a complex model such as the one detailed in Section 4.5 two different physics packages and over 10 million degrees of freedom have to be assembled and solved for.

A coupled approach with two direct solvers will in theory always converge on a solution, but the coupled matrices get so big, that it is often not feasible. With a segregated approach this is manageable, but introduces the risk that the simulation will simply not converge. Figure 4.3 shows such a segregated approach for a mockup-calorimeter model, where the green lines represent the fluid flow module and the blue ones the heat transfer module. Depending on the error constraints, this example can be solved with this segregated approach in approximately 30 min on a regular PC or in around 10 hours in a direct approach.

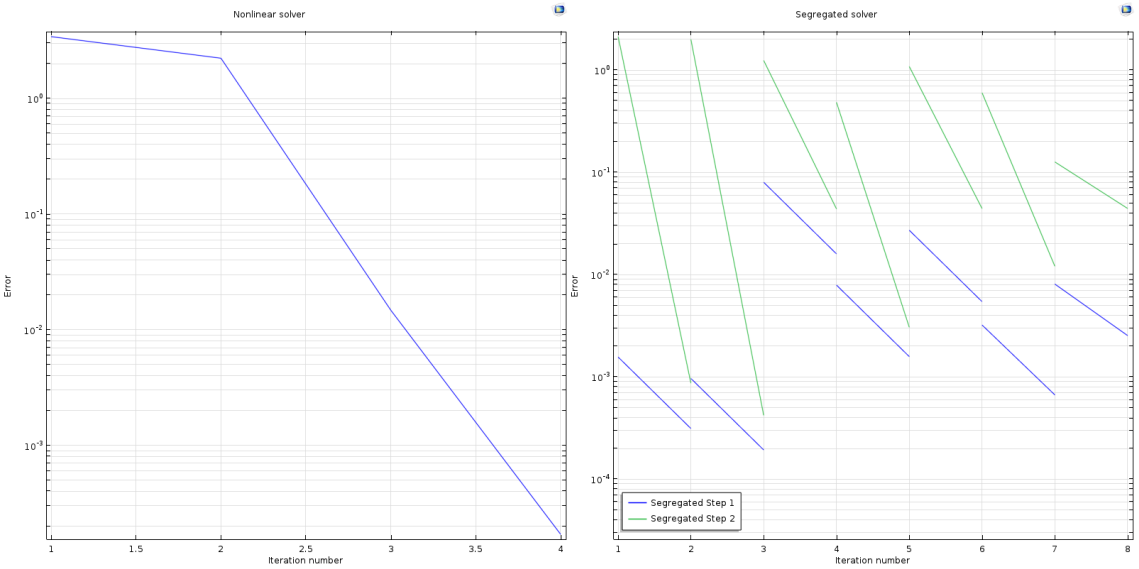

Figure 4.3: Two examples on convergence of solvers in the COMSOL framework. The left example shows an iterative solver chosen for a steady state simulation of the model from Section 4.3, while the right plot corresponds to a segregated solver applied on a time dependent simulation of the full mockup-calorimeter setup, where the fluid flow physics (green) and the heat transfer (blue) are treated sequentially. The error is related to internal error estimates, based on the selected solver, more information can be found in [109].

4.3 Mockup Setup

During the first assembly and testing of the mockup in April 2015 in Tübingen, a first thermal model was developed alongside. The goal of this thermal mockup model was to gain a basic understanding of the system, develop a good knowledge of the cartridge heaters, fix thermal properties of the involved materials, and derive critical temperatures for safety reasons of the yet unknown system.

Figure 4.4: An image of the not yet assembled mockup parts in a laboratory in Tübingen. This setup, without the stainless steel flange and the aluminum ring, was used as the input geometry for a first thermal model of the mockup system.

The hardware setup shown in Figure 4.4 shows a yet to be assembled setup, resting on four metal blocks on top of a steel sheet. The first assembly and test runs were performed with the inner copper part, sealed by the aluminum plug inside the shielding. The stainless steel flange and aluminum ring were not part of these first tests as the threads required for their assembly (with the helicoi) had not been cut at this point. This setup was implemented in a thermal simulation and its geometric representation can be seen in Figure 4.5. The main heat transport mechanism is due to conduction. With a heat source Q and a temperature gradient $q = -k\nabla T$, where k is the thermal conductivity, this leads to the main Equation 4.1 to solve, based on Fourier's law:

$$\rho C_p \frac{\partial T}{\partial t} = \nabla \cdot (k \nabla T) + Q \tag{4.1}$$

with C_p the heat capacity at constant pressure and the density ρ.

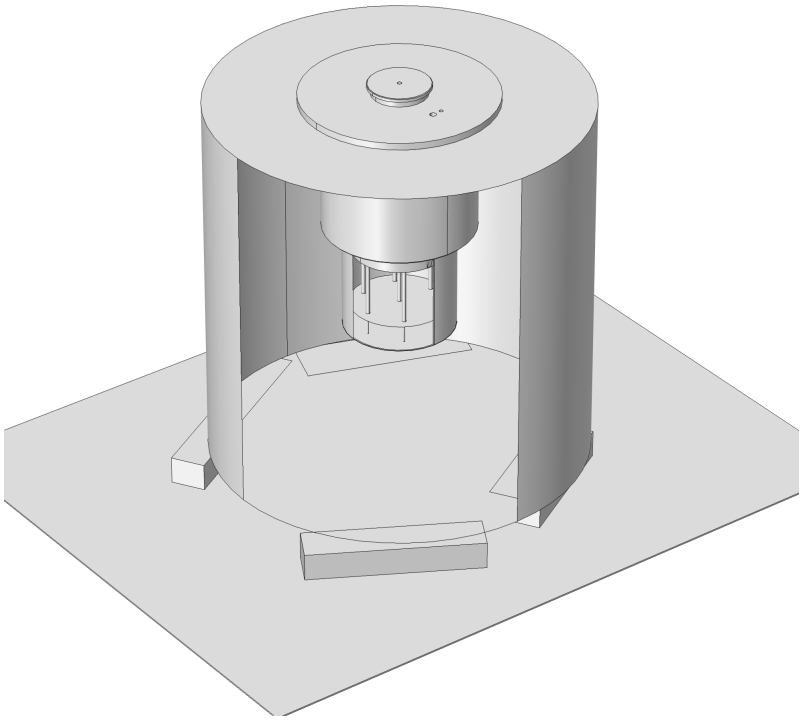

Figure 4.5: The geometric representation of the first Tübingen setup in the COMSOL thermal simulation. The outer shield is cut open to see the cartridge heaters inside the inner copper. The setup itself is resting on four metal blocks and a steel sheet and is sealed in by the aluminum plug which can been seen on top. Three temperature sensors are present, located on the side of the outer shield, the inside of the mockup and on top, in a visible hole on the aluminum plug.

The six cartridge heaters seen in Figure 4.6 are implemented as a domain heat source with an overall heat transfer rate of $Q_0 = \frac{P_0}{V}$, where P_0 can be a fixed value or changed over time. COMSOL enables the import of data from files with the possibility to create functions for physics models out of them. This enables to directly use the measured voltage and current values stored in a data file from a given mockup measurement and to use them as input for P_0, to be as exact as possible to the heat generation in the real setup.

After tuning the thermal model with first measurements and gaining some trust, the model was used to estimate the maximum allowed temperatures for the cartridge heaters based on the discussion in Section 3.3.2.1 and to therefore develop first safety measures. During these simulations air pockets with varying thickness were placed between the copper and the heater heads to determine the possible fit-in-hole for the current setup. However, especially after a few initial heat ups, the best approximation of the system seems to be without air between the heater heads and the copper. An assumption further validated, when assembling the system and observing the heaters being stuck in the holes, due to their thermal expansion.

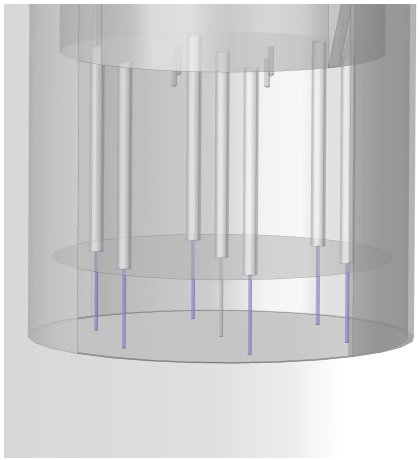

Figure 4.6: The cartridge heaters in the thermal model. The blue selection shows the heater heads, where the thermal power is released in the system via domain heating, which is calculated on the voltage and current applied to the heaters for which real measurements can be used as input.

Other air domains however are present and not negligible, the most obvious one already seen and mentioned in Figure 3.12, is the air on the side between the copper and outer shielding. This was taken into account by a 2.4 mm thick air gap in the thermal model and can be seen in blue on the side of Figure 4.7. The same image shows air pockets in the cabling holes for the heaters, but more importantly on the bottom.

On close inspection, the bottom part of the copper does not rest homogeneously on the aluminum, but is placed rather like a coffee cup on a table, with the most contact on a boundary on the side and the vast majority of the surface not directly touching. To account for this a thin layer of 0.008 mm air is placed under the copper and above the aluminum contact layer, with a direct contact between the two only on the outermost parts of the bottom side. This approach was taken, rather than defining two contact pairs and accounting for surface roughness, as the air model is easier to tune (and motivated by observation) than a potential surface roughness estimate.

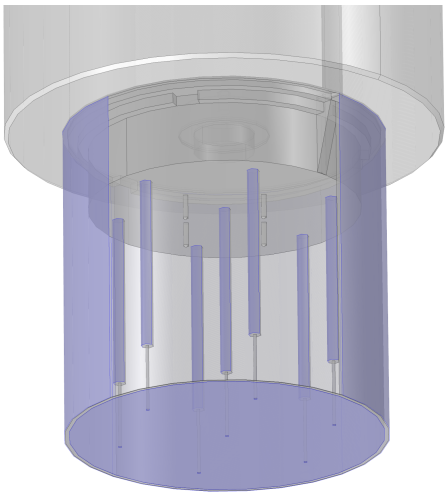

Figure 4.7: The air domains (blue sections) in the simulations. The biggest one is a 2.4 mm thick one on the side. The cabling holes for the heaters and the space between the copper and the lid are additionally filled with air. The most important air boundary is the thin layer of air on the bottom to reduce the surface connection of the copper, to account for a realistic setup with inhomogeneous surfaces.

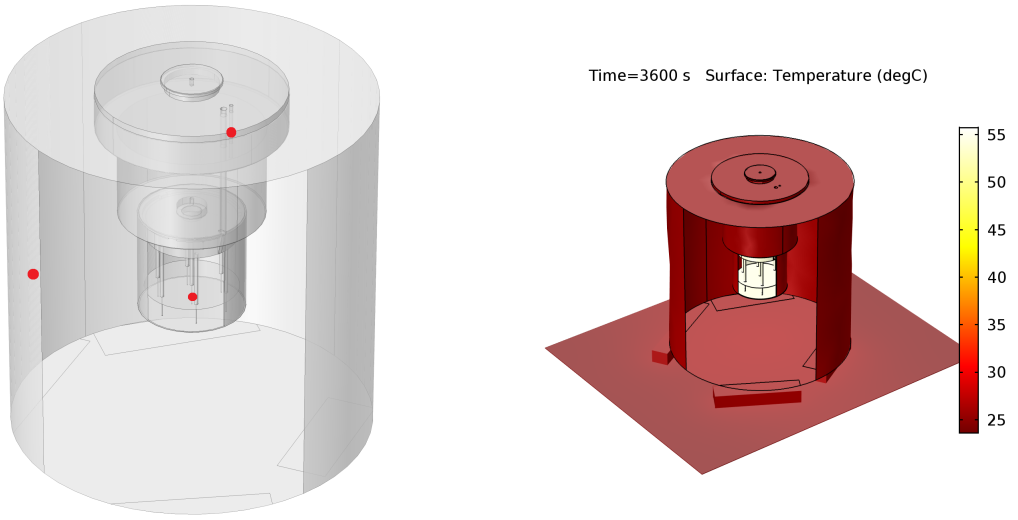

Figure 4.8: This rendering on the left image shows the positions of the temperature sensors, drawn as red dots. These sensors where implemented in the thermal simulation as so called cut points, which are points with a fixed position, whose temperature values are stored separately for each simulation. They can then be plotted and stored to compare them to measurements. The right image shows an example temperature gradient for the system, after being heated with 250 W for 1 h and shows the expected behavior and temperature distribution.

4.3.1 Performance

The thermal model of the Tübingen setup has been calibrated and evaluated with measurements performed over the period of one month. These measurements include heating times from 1 min to 3 h and were performed with up to 500 W. Figure 4.8 shows the temperature sensors present in the setup and the thermal model, as three red dots, which served as the main comparisons points.

Because this early setup had no form of cooling, the 500 W maximal power was chosen as an conservative safety measure. For longer heating times power was reduced in order not to risk damaging the still new mockup setup. With the main thermal properties of the used materials seen in in Table 4.1 the setup was able to describe the system and predict temperature gradients and sensor values over the complete range of measurements performed in the setup. A comparison for a 3 h measurement with 250 W can be seen in Figure 4.9 and Figure 4.10 where the simulation (in green) follows the data (in blue) in all three sensors very closely.

Table 4.1: The list of used materials and their thermal properties as they are used in the mockup thermal model.

	E-Copper	EN AW 2007	EN AW 5083	Steel AISI 4340
ρ [kg/m^3]	8700	2850	2660	7850
C_p [J/(kg · K)]	390	878	899.5	500
k [W/(m · K)]	394	140	121	44.5

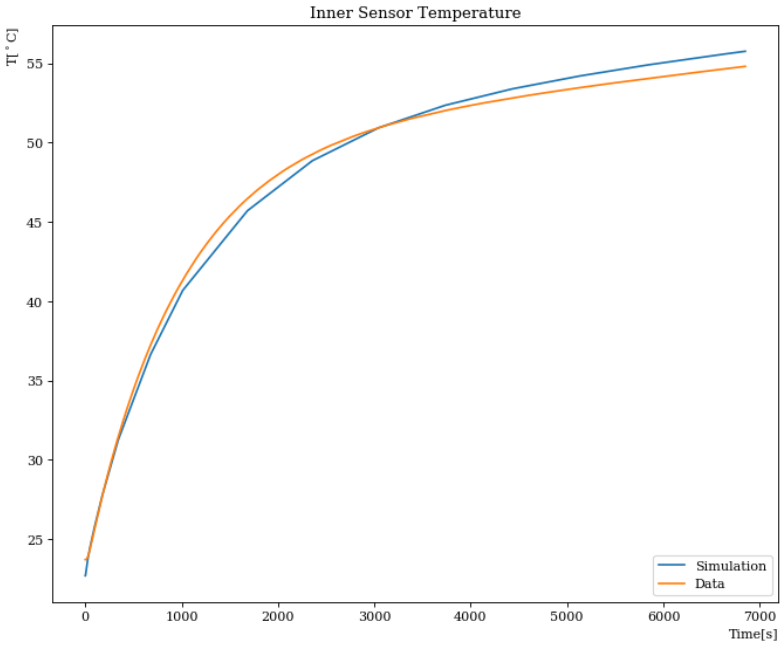

Figure 4.9: Comparison between data, drawn in red, and simulation in blue for a 3 h, 250 W simulation. This image shows results for the inner sensor which is located in the middle between the cartridge heaters in the inner copper part. Error bars for data are not drawn in this plot, as the error on the temperature sensor is $<$0.07% and too small to be seen. There is, however, an error on the set power uncertainty in this early setup of up to 10 W present, due to no control loops being implemented at this stage.

To reach this precision, the temperature of the steel sheet was measured before each run and used as an input parameter as heat losses due to natural convection play only a small role in this temperature regime and time-frame and had not been simulated.

Overall this early thermal model was successful in its goals to predict, reproduce and understand this early mockup setup and was used to develop first safety parameters for the cartridge heaters[2] and fix the thermal parameters of the involved materials, as these parameters are only roughly known from literature and/or sometimes manufacturer information. Additionally this model served as a building block for

[2]Temperatures above 350°C, measured by the inner copper sensor will result in a safety shutdown of the system, to avoid damage to the heaters, see Section 3.3.2.1.

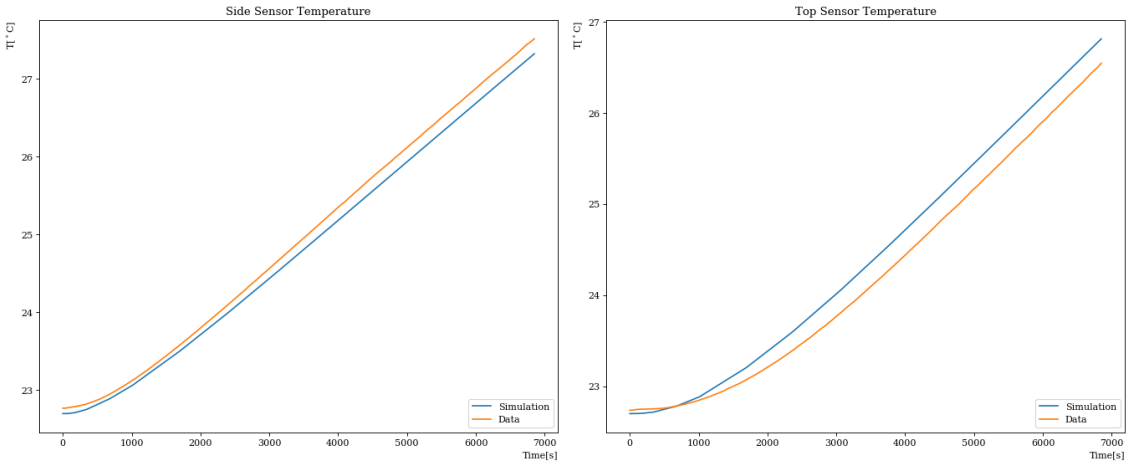

Figure 4.10: Data (red) and simulation (blue) comparison for a 3 h, 250 W simulation, which is shown on the left for the sensor located on the side of the aluminum shielding. The right plot corresponds to the sensor located on the top of the setup in the aluminum plug.

the mockup-calorimeter simulation and the experience and trust gained with it also helped for estimates used in the cerium simulation described in the next chapter, where no data could be used to constrain and verify the model.

Figure 4.11: The geometry of the cerium encapsulation in its inner and outer shielding and sealed with a tungsten flange. The left transparent rendering shows the full encapsulation, while the right shows the inner shielding with three copper caskets analog to the discussion in Section 3.2.2.

4.4 Cerium Source in Shielding

To estimate the expected maximum temperatures of the cerium source and its encapsulation, a thermal model was developed. Besides deriving estimates on the expected surface temperatures, the model should enable to test potential inner encapsulation candidates and investigate potential critical temperatures for involved materials.
As stated in Section 3.2.2, a potential inner encapsulation should provide a homogeneous heat profile, besides the requirements in shielding and pressure resistance. A proposed encapsulation had the cerium in pressed pellets inserted in copper capsules in a double steel cylinder (see Figure 3.9). This inner shielding has been modeled in the thermal simulation, together with its tungsten outer shielding. The outer encapsulation is by design virtually identical to the mockup's outer shielding, so the geometry from the mockup thermal model could be used in part also for the cerium simulation. The inner encapsulation and the setup can be seen in Figure 4.11.

These rendering images show the geometry used for the cerium thermal model, differing from the mockup simulation (besides materials) in the inner encapsulation and the sealing of the cerium setup by a tungsten flange on top of the tungsten outer shielding.

To estimate potential maximal temperatures the copper capsules were heated with 1.5 kW, the theoretical maximum power for the cerium source directly after its production and without specific cooling, besides natural air convection on the surfaces. This air convection was implemented with an external natural convection model. In

this convection model, temperature variations on surfaces cause density differences which result in buoyancy forces, leading to a rising of the hotter air and replacement by colder air layers. This type of natural convection (non-forced, unlike with a fan) is not a very efficient heat transfer mechanism, but is meant to simulate a free standing and not specifically cooled hot and encapsulated cerium source.
Equation 4.2 shows how the convective heat flux is treated in the simulation:

$$q_0 = h(T_{air} - T), \quad h = h_{air}(L, p_A, T_{air}) \tag{4.2}$$

where p_A is the absolute pressure, L the length of the surface which the air is interacting with and h itself is the convective heat transfer coefficient of the process.
The surfaces selected to participate in the external natural convection can be seen in Figure 4.12 in blue, where the sides of the tungsten flange are left out intentionally as their contribution is minimal, but would increase complexity and computational time.

Figure 4.12: This render image shows the surfaces selected for external natural convection. This applies to all surfaces, but due to their minor impact and higher computational needs, smaller surfaces as those on the tungsten flange had been intentionally left out.

Due to the expected high temperatures close to the source, "regular" (304, 304L or 304H) stainless steel can not be used safely. Therefore temperature resistant steel has to be used or high strength austenitic steel which has been treated with Spray-applied Fire-Restive Materials. In the model the use of 321 temperature resistant stainless steel [103] is assumed (and which was initially proposed), which values can be seen together with the other used materials in Table 4.2. A steady state simulation of this model with external natural convection and a total heating power of 1.5 kW was simulated and its results are shown in Figure 4.13. On the left slice image it can be seen, that the copper and the outside of the double steel cylinder have a homogeneous heat profile.

Table 4.2: The materials and their thermal properties as they are used in the cerium source thermal model.

	Copper	Tungsten	321 Stainless Steel
ρ [kg/m^3]	8960	17800	7920
C_p [J/(kg · K)]	385	132	500
k [W/(m · K)]	400	175	16

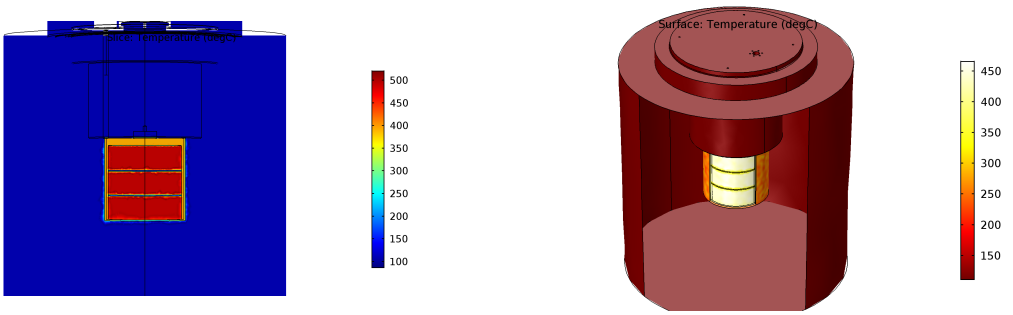

Figure 4.13: A slice and cut 3D-view of a steady state simulation of the cerium thermal model in [°C]. The applied heating power was 1.5 kW and the air temperature used in the external natural convection model was assumed to be 22°C. Temperatures range from 490°C on the copper caskets to 111°C on the tungsten surfaces.

The hottest point in the simulation is found at 490°C at the copper caskets, while the inside of the steel heats up to 390°C, the outside of the steel to 281°C and the outside surface of the tungsten up to 111°C. This outside temperature, although over 100°C warm, would not have been a safety concern. In case of the material used for the inner cylinders, the critical temperature for the 321 stainless steel alloy is at about 800°C, which is higher by a factor of two compared to the hottest simulated point, which meant no critical issues could have been identified in the cerium shielding and no problems foreseen with the selection of 321 stainless steel. Unfortunately no measurements could be taken to evaluate the precision of this thermal cerium source model, although the performance of the, to some degree comparable, mockup model gives these simulations some credibility.

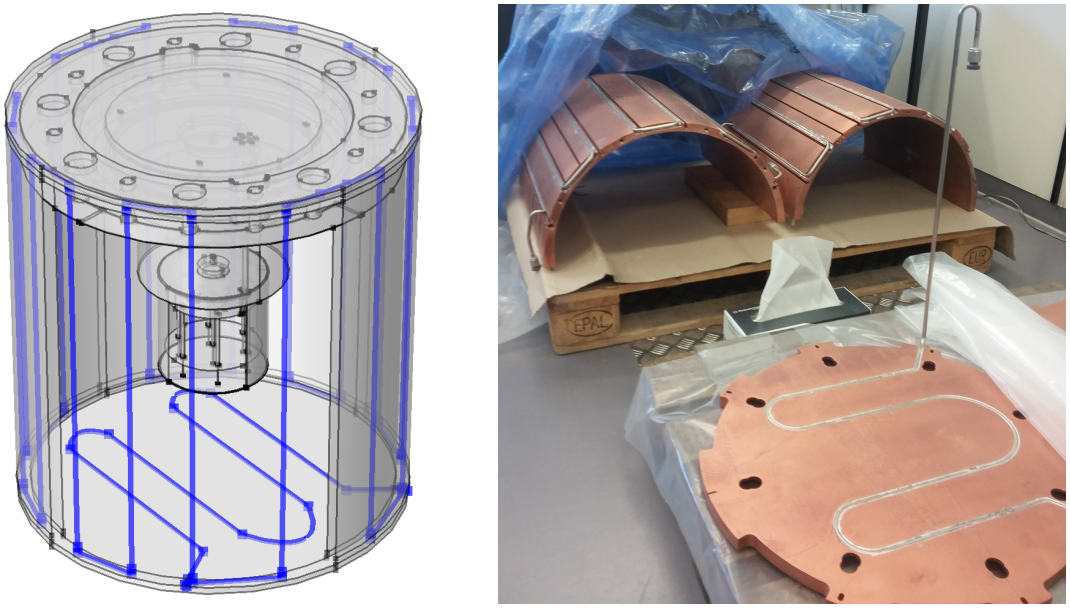

Figure 4.14: The geometry of the mockup-calorimeter simulation and the cooling pipes in the copper heat exchanger. The cooling pipes shown in blue on the left image differ the most from the actual setup. This is due to prevent meshing issues and an optimization strategy relying on 1D-pipes, scaling them after solving. In the right picture the bottom copper part and the copper jacket (in the back) with the cooling pipes can be seen.

4.5 Mockup-Calorimeter Thermal Model

The mockup-calorimeter thermal model was developed to assist during the calibration phase of the calorimetric setup. It enabled to preview potential calibration runs, help in the estimation on heat losses and answer specific safety questions. These included maximal allowed operating temperatures on critical parts and potential dangerous situations, like a bad vacuum or a non moving cooling fluid due to a potential pump failure.

The model's geometry can be seen in Figure 4.14 and includes the complete mockup model, together with the heaters and the full mockup sealing on top. The mockup is then encased with a lateral copper jacket and two copper parts on top and bottom. The cooling pipes in the copper heat exchanger had been altered and rebuilt, for meshing reasons (see Section 4.2.1) but more importantly due to an optimization strategy connected to the Pipe Flow Module. This specific module works on one dimensional edges (lines) only and scales them to 3D geometry when solving fluid flow equations, which meant the cooling pipes had to be redone manually for this module. Besides the heat exchanger and pipes, the rest of the geometry is still CAD-files based as in the previous models, enabling to react to setup changes quite easily in the thermal model. As the cooling water is an integral part of the system it must also be modeled as good as possible in the thermal simulation. In contrast to a conduction-only thermal model, a fluid adds an additional convective contribution. Also, a fluid, especially a fast moving one, produces heat due to viscous effects. The

governing transient heat equation for the temperature field is then given by:

$$\rho A C_p \frac{\partial T}{\partial t} + \rho A C_p \mathbf{u} \cdot \nabla T = \nabla \cdot A k \nabla T + f_d \frac{\rho A}{2 d_h} |\mathbf{u}|^3 + Q + Q_{wall} \tag{4.3}$$

with:

- A the cross-section of the pipe,
- $\mathbf{u}$ the velocity field inside the fluid,
- f_d as the so called Darcy friction factor,
- d_h as the hydraulic parameter connected to the pipe dimensions,
- Q_{wall} the external heat exchange between the wall and the fluid.

In principle, an additional term accounting for pressure drops in the fluid could be added to Equation 4.3, but as the temperature and pressure difference in the case of this model is very low, this was neglected. Heat exchange through the external surrounding surfaces and the fluid are accounted by Q_{wall}, which is expressed as:

$$Q_{\text{wall}} = (hZ)_{\text{eff}} (T_{ext} - T) \tag{4.4}$$

where T_{ext} is the temperature field from the outside surfaces and governed by Equation 4.1 and h the transfer coefficient, with Z as the wall perimeter of the pipe. For a circular pipe, with a single wall $(hZ)_{\text{eff}}$ is approximated as:

$$(hZ)_{\text{eff}} = \frac{2\pi}{\frac{1}{r_{in}} + \frac{1}{r_{out}} + \frac{\ln(\frac{r}{r-1})}{k_{\text{wall}}}} \tag{4.5}$$

with r_{in} and r_{out} as the inner and outer pipe radius. These phenomenological equations are quite common in fluid flow problems and have been well established.

In Figure 4.15 a steady state simulation with a thermal power of 920 W, a cooling water temperature set at 15°C and a mass flow of 5 g/s is shown. The two most important points for verification of the model are the temperature measured inside the copper mockup and the outgoing cooling water temperature. In the 1000 W - 900 W power regime the simulation is able to predict outgoing cooling water temperature on the 3% level and inner sensors values with a precision of 5%. This region was chosen as this power regime is most likely where most measurements with the cerium source would have been taken. Consequently, most calibration runs were performed in this heating power interval. For lower power values the precision drops, as can be seen in Table 4.3. The best agreement can be found at 920 W, as these runs were mostly used to constrain the modules parameters, mainly those connected to heat exchange from the wall.

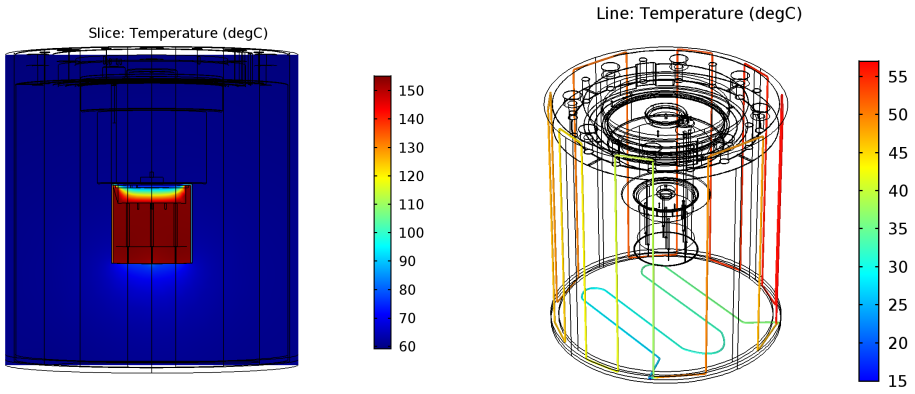

Figure 4.15: The temperature profile for the calorimeter and cooling water for a 920 W steady state simulation in [°C]. The measurement affiliated with this simulation was performed without the copper lid and a mass flow of 5 g/s. This measurement was mainly used in tuning the thermal model and the temperature difference for both the inner copper sensor and outgoing water is at the 1% level.

Table 4.3: The precision of the mockup-calorimeter thermal model, validated at two sensors. While the agreement in the 900 W range is very good, the accuracy decreases to lower power values.

	620 W	700 W	900 W	920 W
Cooling water	9%	8%	3%	1%
Inner copper	27%	11%	5%	1%

Due to the design of the calorimeter, the heat losses by convection, conduction and radiation are small. The radiative losses, anyway very small at this low temperatures are negligible, thanks to the two superinsultors surrounding the outside of the copper jacket, while conduction losses are minimized by the Kevlar rope structure, as discussed in Section 3.4.1. However, in a case where no good vacuum can be achieved or the turbo pump damaged, significant losses due to convection could occur. As this is nearly impossible to measure, the thermal model was used to give an estimate on the expected convective losses.

To achieve this, the external natural convection mechanism, discussed earlier in this chapter, was implemented on the outside surfaces of the copper heat exchanger. In order to minimize the simulations uncertainty on the initial heat gradient, data from a measurement with a corresponding mockup power was used as the simulations initial temperature profile. From this, the convective losses could be estimated by integrating the convective losses over the surfaces for various source powers and vacuum pressure values. The resulting simulated convective heat losses are found in Table 4.4 and are typically in the range of several mW up to a maximum of approximately 1 W, thus confirming that even in a low vacuum state, the calorimeter is still well within its design goals and does not loose its source measurement capabilities.

Table 4.4: The simulated convective losses in a lower vacuum. All of these simulations were obtained with a heat profile from an accompanying measurement on this source power and were performed with a mass flow of 5 g/s.

	500 W	700 W	1000 W
10^{-5} mbar	0.38 W	0.50 W	0.99 W
10^{-3} mbar	0.30 W	0.63 W	1.15 W

Overall the developed thermal models were successful in assisting during the various conception and calibration phases. They also enabled the safe testing of critical parts, maximal temperatures, assisted in material selection, tested possible geometric design proposals and constrained potential convective losses.

This also concludes the work on the mockup and calorimeter systems, which had been started in 2015, beginning with the hardware and mechanical parts development of the mockup and continued in contributions to the electrical systems of the mockup-calorimeter setup and the discussed accompanying thermal models.

The next chapters will move away from the source/calorimeter related subjects and will instead focus on the detector side, more precisely on external γ-particles in Borexino's simulation framework.

Chapter 5

Borexino's Internal and External Background

In previous Borexino solar neutrino measurements, the main background contributions originated from ^{14}C, ^{210}Bi, ^{210}Po among others. Although present, γ-particles from outside the IV were of minor importance. The relevant energy window for solar neutrinos can be seen in Figure 5.1 and extends up to about 1400 keV. Additionally, in the solar analysis a FV of approximately 3 m radius is used, which already excludes most of the external gamma background.

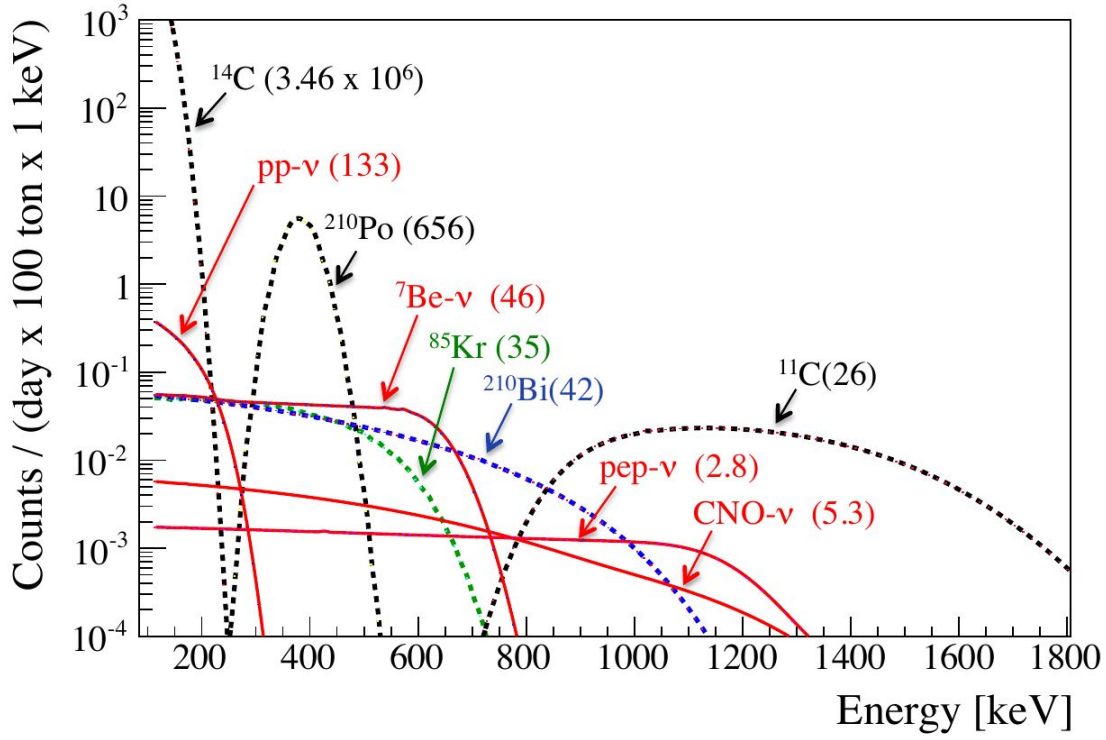

Figure 5.1: The main (calculated) background concerning solar neutrinos in Borexino. This plot corresponds to a FV of approximately 3 m. Image credit: [21].

For the SOX experiment, however, the interesting energy region would have been above those of solar neutrinos (1.8 MeV of up to 3 MeV, see Figure 3.6) and the FV used in the analysis would have been much bigger, thus leading to a higher external background. This chapter will give an overview of the main backgrounds in Borexino, discuss the origin of the external gamma background and briefly introduce an external calibration campaign, performed in 2011, as the data obtained by this campaign was used in the validation of Borexino's framework capabilities, discussed in the next chapter.

5.1 Internal and Muon-induced Background

In Borexino, the detector background is categorized as internal background (including surface background), muon-induced background and the external background. Before focusing on the external background, a brief summary of Borexino's other background contributions is given, analog to [21].

5.1.1 Internal Background

The internal background in Borexino refers to a contamination of radioactive isotopes directly in the scintillator. Table 5.1 shows the contaminating isotopes most relevant for this background. The thorium and uranium contributions are discussed later as those are not specific to the scintillator region and contribute to the external and internal background equally.

Table 5.1: The main background contributors in the scintillating volume of Borexino, besides those originating from the uranium and thorium decay chains. Besides the γ-energy of 1460 keV from ^{40}K (via EC) all other energies are end-point energies. Based on [21].

Isotope	Mean Life	Energy [keV]	Decay	Decay Rate [cpd/100 t]
^{14}C	8.27×10^3 yrs	156	β^-	$(3.46 \pm 0.09)\cdot10^6$
^{85}Kr	14.5 yrs	687	β^-	$30.4 \pm 5.3 \pm 1.5$
^{40}K (89%)	18.5×10^9 yrs	1310	β^-	< 0.42 (95% C.L.)
^{40}K (11%)	18.5×10^9 yrs	1460	EC+γ	< 0.42 (95% C.L.)
^{39}Ar	388 yrs	565	β^-	0.4

The highest contribution originates from ^{14}C. This prominent[1] carbon isotope is chemically identical to ^{12}C and an unremovable component in Borexino's organic

[1] Known for its use in the radiocarbon dating.

scintillator. The relatively low $^{14}C/^{12}C$ ratio, measured to be 10^{-8} g/g in the scintillator used in Borexino is due to the use of petroleum from underground deposits only. As ^{14}C is produced via the interaction of cosmogenic neutrons and nitrogen in Earth's upper atmosphere, a reduction of approximately a million of ^{14}C levels can be achieved by selecting deep and old petroleum locations only. With an endpoint of 156 keV by β-emission, this effectively limits Borexino's low-energy threshold. By selecting a trigger threshold of 50 keV, this results in a rate of 30 Hz. Although ^{14}C is very dominant in the range below 200 keV, the pp- and ^{7}Be-neutrinos have an energy spectrum reaching above the ^{14}C endpoint and can be fitted to keep a high sensitivity for these neutrinos.

The β-emitting ^{85}Kr isotope is another internal background contributor, as its spectrum, with an endpoint of 687 keV, is similar to the electron recoil spectrum of ^{7}Be-neutrinos. Although produced by cosmic rays, most ^{85}Kr in the atmosphere is due to reprocessing of nuclear fuel, nuclear accidents like Chernobyl and Fukushima Daiichi as well as nuclear weapons testing. Because this krypton contamination is introduced by air contact, special measures in the scintillator filling phase of Borexino were taken to reduce or minimize air exposure times. Unfortunately and despite these measures, during the filling procedure small air leaks had been present[2].

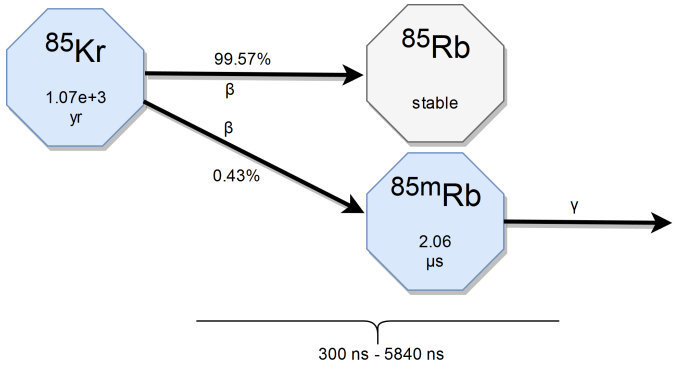

Figure 5.2: Abstract drawing of the β-γ coincidence used to constrain the ^{85}Kr rate. A time window of 300 ns - 5840 ns is used to search for two separate entries of a β- and a γ-event.

Due to the similarity in the β-spectrum to ^{7}Be-neutrinos, a method to identify the ^{85}Kr is based on a β-γ coincidence. ^{85}Kr decays to the stable ^{85}Rb, but there is a another branch (0.43%) that results in an exited rubidium state, which decays via a γ-emission to its ground state, as seen in Figure 5.2. By selecting a suitable time frame and searching for this β-γ coincidence the rate of ^{85}Kr can be constrained to $(30.4 \pm 5.3(\text{stat}) \pm 1.5\ (\text{sys}))$ cpd/100 ton. The systematic error is due to the FV definition and the uncertainty on the β-cut.

[2]During Borexino's scintillator filing and inner vessel assembly the average ^{85}Kr activity was in the range of 1.5 Bq/m^3 and is expected to reach 3 Bq/m^3 in the 2020s [73].

Also introduced due to air leaks during the filling phase, an ^{39}Ar contamination is present in the scintillator region. This argon isotope, which is produced by cosmic rays in the atmosphere, is a β-emitter and has an endpoint at 565 keV. As this ^{39}Ar decays solely by β-decay, the disentangling from the ^{7}Be-neutrino spectrum is very challenging. But under the assumption that ^{39}Ar and ^{85}Kr entered both via an air leak and assuming a 1.4 Bq/m^3 activity for argon in the atmosphere, the ^{85}Kr rate (obtained by the β-γ coincidence) can be used to estimate the argon count rate in the scintillator. This translates to a count rate of 0.4 cpd/100 ton and was deemed low enough to not include it into the spectral fits.

^{40}K is a natural potassium isotope with an abundance of 0.012% and is a source of internal as well as external background. Potassium decays mostly (89%) via β-decay, with an endpoint of 1310 keV. An additional EC to an exited argon state has a branching ratio of about 11% and after its de-excitation emits a γ-particle with an energy of 1460 keV. Unfortunately, this rather prominent mono-energetic γ-line signature is not usable to model the ^{40}K rate as these γs can enter the FV from practically everywhere in the detector (at different energies due to e.g Compton interactions in the buffer). Part of this potassium presence is due to the fact that the wavelength shifter (PPO), which is added with a concentration of 1.5 g/l, is contaminated with ^{40}K. Purification and filtration may have reduced this contamination drastically, however, the efficiency of these methods is not known. Additionally, ^{40}K is naturally present in dust, which means small dust particles can diffuse directly into the scintillating volume and also build dust layers on both the nylon vessels, the vessel end-caps, PMTs and SSS. Therefore, in Borexino's solar analysis ^{40}K is treated as a free parameter and an upper limit, with regards to the pep-neutrino FV (r $<$ 2.8 m, vessel end-caps excluded), was estimated to be 0.42 cpd/100 ton (95% C.L.).

Besides the already mentioned isotopes, additional contributions arise from the ^{238}U, ^{232}Th and ^{222}Rn decay chains, seen in Figure 5.5 and Figure 5.6. The rates of these and some relevant daughter nuclei are displayed in Table 5.2.

Table 5.2: Table of the rates of ^{238}U, ^{222}Rn, ^{232}Th as well as two relevant daughter nuclei. The rates refer to a FV $<$ 3 m. Based on [21].

Isotope	Mean Life	Decay Rate [cpd/100 t]
^{238}U	6.45×10^9 yrs	0.57 ± 0.05
^{222}Rn	5.51 days	1.72 ± 0.06
^{210}Bi	7.23 days	$41.0 \pm 1.5 \pm 2.3$
^{210}Po	200 days	$(0.5 - 0.8) \cdot 10^3$
^{232}Th	1.4×10^{10} yrs	0.13 ± 0.03

In principle the ^{238}U rate could be estimated and monitored by the decay sequence of ^{214}Bi - ^{214}Po via:

$$\begin{aligned} ^{214}\text{Bi} &\rightarrow {}^{214}\text{Po} + e^- + \bar{\nu}_e \\ ^{214}\text{Po} &\rightarrow {}^{210}\text{Pb} + \alpha \end{aligned} \tag{5.1}$$

in secular equilibrium. With the ^{214}Po lifetime of $\tau = 238\,\mu$s a time window for identification is chosen to be between 20 and 944 μs, in the energy range of 180 - 3600 keV for ^{214}Bi, 400 - 1000 keV for ^{214}Po and within a distance of less than 1 m. The identification efficiency of this ^{214}Bi - ^{214}Po coincidence was evaluated by Monte Carlo simulations to be at the 90% percentile. But because ^{222}Rn can enter all parts of the detector via diffusion and is constantly replenished, the assumption of secular equilibrium is not valid. Nonetheless, the monitoring of this ^{214}Bi - ^{214}Po coincidence does still allow for estimates on the detector's ^{222}Rn impurities and an increase after hardware operations, like refilling or calibration campaigns was observed.

Two additional background contributors, ^{210}Bi and ^{210}Po, originate from ^{210}Pb. This lead isotope, with a mean life of 32 yrs, is by itself negligible due to its low endpoint of 63.5 keV, but has a tendency to stick on the nylon vessel surface. As such the daughters of ^{210}Pb are mostly responsible for the vessel surface contamination. ^{210}Bi with its endpoint at 1160 keV has impact throughout the solar neutrino analysis and no clear identification signal besides its spectral shape. But fortunately, ^{210}Bi and also ^{210}Po (α-emission at roughly 5300 keV) are mostly contained on the vessel surface (as seen in Figure 5.3) and their rate is heavily reduced by a FV cut.

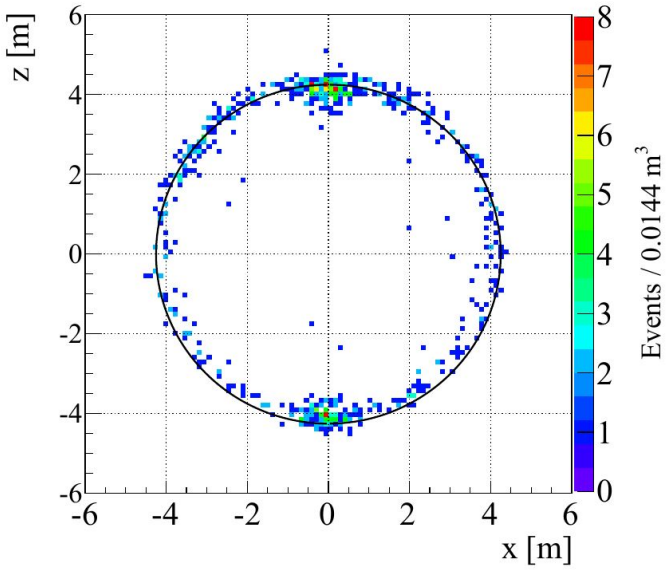

Figure 5.3: A plot showing mostly events due to ^{210}Bi contamination on the inner vessel surface. This x-z distribution, with $|y| < 0.5$ m, shows the energy range of 800 - 900 keV. It can be seen that there are event excesses near the two vessel endcaps in the north and south and also that most events are shifted compared to a spherical vessel, drawn in black. This is due to the vessel deformation, discussed in Section 2.1.3.3. Image credit: [21].

The obtained rate on ^{210}Bi and ^{210}Po seems to be variable and has been observed to increase after a refilling procedure. This makes the count rate of these two isotopes time and FV-cut dependent and has therefore to be evaluated constantly.

Similar to the ^{238}U chain, a ^{212}Bi - ^{212}Po coincidence is used to evaluate the ^{232}Th and

^{222}Rn rates. With a spatial distance of less than 1 m, the time windows is chosen to be between 400 and 1732 ns, while the energy for the first potential event is less than 2000 keV and lays between 900 and 1300 keV for the second one. This allows for an estimate in the total ^{232}Th contamination in the scintillator of $(3.8 \pm 0.8) \cdot 10^{-18}$ g/g at equilibrium.

5.1.2 Muon-induced Background

Although heavily reduced by the rock overburden (with a factor of about 10^{-6}) the muon flux in Borexino is approximately 1.2 muons m^{-2} h^{-1}. These muons are tagged and vetoed by the OD with an efficiency of 99.2%, but can produce cosmogenic isotopes on their track. These isotopes seen in Table 5.3 are suppressed by a 300 ms rejection windows after a tagged muon. If a muon travels directly through the scintillator, the veto efficiency increases to 99.992%. The most problematic muon

Table 5.3: Table of the cosmogenic isotopes in Borexino, detailing mean life, energy and decay. The residual rate refers to the rate after the 300 ms dead time window is applied. Reproduced from [21].

Isotope	Mean Life	Energy [keV]	Decay	Residual Rate [cpd/100 t]
n	255 μs	2230	γ (Capture on ^{1}H)	< 0.005
^{12}N	15.9 ms	17300	β^+	$< 5{\times}10^{-5}$
^{13}B	25.0 ms	13400	β^-, γ	$< 5{\times}10^{-5}$
^{12}B	29.1 ms	13400	β^-	$(7.1 \pm 0.2) \times 10^{-5}$
^{8}He	171.7 ms	10700	β^-, γ, n	0.004 ± 0.002
^{9}C	182.5 ms	16500	β^+	0.020 ± 0.006
^{9}Li	257.2 ms	13600	β^-, γ, n	0.022 ± 0.002
^{8}B	1.11 s	18000	β^+, α	0.21 ± 0.05
^{6}He	1.16 s	3510	β^-	0.31 ± 0.04
^{8}Li	1.21 s	16000	β^-, α	0.31 ± 0.05
^{11}Be	19.9 s	11500	β^-	0.034 ± 0.006
^{10}C	27.8 s	3650	β^+, γ	0.54 ± 0.04
^{7}Be	76.9 days	478	EC, γ	0.36 ± 0.05

induced background is ^{11}C, as 95% of those isotopes are produced via

$$\mu + {}^{12}\mathrm{C} \rightarrow \mu + {}^{11}\mathrm{C} + \mathrm{n} \tag{5.2}$$

and which decays via

$$^{11}\mathrm{C} \rightarrow {}^{11}\mathrm{B} + e^+ + \nu_e \tag{5.3}$$

with a mean lifetime of $\tau = 29.5$ min.

This interaction is resulting in a few tens of ^{11}C nuclei being produced in the scintillator per day. Due to the e^+ annihilation (2×511 keV) and the Q = 960 keV for

the β^+-decay, this impacts the energy of the pep- and CNO-neutrinos. As they are continuously reproduced, these ^{11}C isotopes can not be removed with a dedicated purification of the scintillator. Instead this background is estimated (and later subtracted) via the time coincidence of the tagged muon and capture of the free neutron of $(254 \pm 1.8)\,\mu$s with a 2230 keV γ-particle), combined with a typical pulse-shape identification.

5.2 External Gamma Background

The term external background refers to any contamination outside the IV, able to deposit energy in the scintillating volume. Due to Borexino's buffer layer between the OV and the SSS, only high energetic γ-rays have the potential to penetrate, although at a high suppression (of about several hundred thousand for γ-particles in the range of a few MeV). These γ-rays originate from daughters of the uranium and thorium chains as well as the already mentioned ^{40}K, present on the PMTs and SSS itself. Contrary to the estimates on radiopurity discussed in the internal background section, with only the γ-particle reaching the scintillator and the absence of a marker like the ^{212}Bi - ^{212}Po coincidence, a similar rate estimate on the external uranium and thorium contamination is not possible. In 2001, a dedicated radioactivity measurement [17] was able to obtain data on the present contamination, by measuring selected material samples. The measurements mentioned there were performed on most hardware and electronic components as well as stainless steel and nylon samples with gamma spectrometry, low background scintillation detectors and miniature gas proportional counters. Table 5.4 shows the most significant ones.

Figure 5.4 shows a similar plot than Figure 5.1, but this time with the inclusion of the γ's originating from ^{214}Bi and ^{208}Tl. It can be seen that due to the vessel cut and the lower energy of the solar neutrinos this background is of lower concern and has never received the same amount of attention than the internal contaminations due to its little impact on the solar measurements.

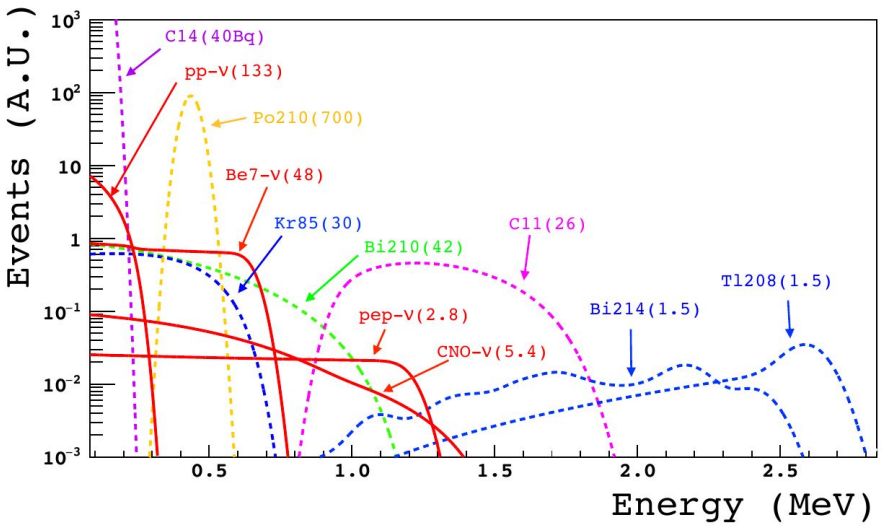

Figure 5.4: The calculated background, with regards to a 3 m FV. Compared to the one shown in Figure 5.1, this includes the energy range of up to 2.8 MeV and the external gamma contributions. The ^{40}K contribution is not considered in this plot. Image credit: [24].

Table 5.4: Contamination measurement values for ^{238}U, ^{232}Th and ^{40}K for important parts of the Borexino detector setup. This selection is based on the measurements performed in [17].

	^{238}U (g/g)	^{232}Th (g/g)	^{40}K (g/g)
PMT inner parts			
Dynodes	$< 2.3 \cdot 10^{-8}$	$(1.1 \pm 0.4) \cdot 10^{-7}$	$< 7.6 \cdot 10^{-6}$
Aluminum for dynode structure	$(9.6 \pm 0.8) \cdot 10^{-8}$	$(2.4 \pm 0.2) \cdot 10^{-7}$	$(9 \pm 2) \cdot 10^{-5}$
PMT glass			
Base Glass	$(4.2 \pm 0.7) \cdot 10^{-8}$	$(1.0 \pm 0.2) \cdot 10^{-7}$	$(7.3 \pm 0.2) \cdot 10^{-3}$
ETL low radiation glass	$(6.6 \pm 1.9) \cdot 10^{-8}$	$(3.2 \pm 0.3) \cdot 10^{-8}$	$(1.6 \pm 0.4) \cdot 10^{-5}$
PMT ancillary parts			
Voltage divider board	$(1.4 \pm 0.5) \cdot 10^{-8}$	$(1.9 \pm 1.0) \cdot 10^{-8}$	$(2.5 \pm 1.2) \cdot 10^{-5}$
Voltage divider complete	$(5.5 \pm 0.3) \cdot 10^{-8}$	$(7.9 \pm 0.6) \cdot 10^{-8}$	$(1.0 \pm 0.1) \cdot 10^{-4}$
Cable and connector			
Neoprene connector boot	$(1.1 \pm 0.3) \cdot 10^{-7}$	$(3.1 \pm 0.7) \cdot 10^{-8}$	$(5.1 \pm 0.8) \cdot 10^{-5}$
Jupiter connector O-ring	$(1.1 \pm 0.3) \cdot 10^{-7}$	$(2.9 \pm 0.9) \cdot 10^{-7}$	$(2.5 \pm 1.1) \cdot 10^{-4}$
Steel samples			
Piping steel	$< 1.1 \cdot 10^{-9}$	$< 2.5 \cdot 10^{-9}$	$< 1.1 \cdot 10^{-6}$
Steel for storage vessel	$(1.4 \pm 0.2) \cdot 10^{-9}$	$(9.3 \pm 6.4) \cdot 10^{-10}$	$< 6 \cdot 10^{-7}$

The values from Table 5.4 show that the most contamination accumulates on the PMTs themselves and especially the PMT glass, as well as on the SSS itself, with the highest contamination arising from the mounting and sealing parts on the SSS and PMTs.

In the uranium and thorium decay chains countless γ-particles are created, but only those above 1 MeV can effectively penetrate the buffer region and are able to deposit energy in the IV. Figure 5.6 and Figure 5.5 show the respective decay chains and mark the elements with γ-lines above 1 MeV, and therefore of interest for the external background, in yellow.

Besides the γ-line at 1460 keV, resulting from the EC-branch of ^{40}K, the most significant γ-rays originate from ^{208}Tl and ^{214}Bi. Here, the most important γ-line is the one from ^{208}Tl, with an energy of 2615 keV, while the two ^{214}Bi-lines are at 1764 keV and 1120 keV.

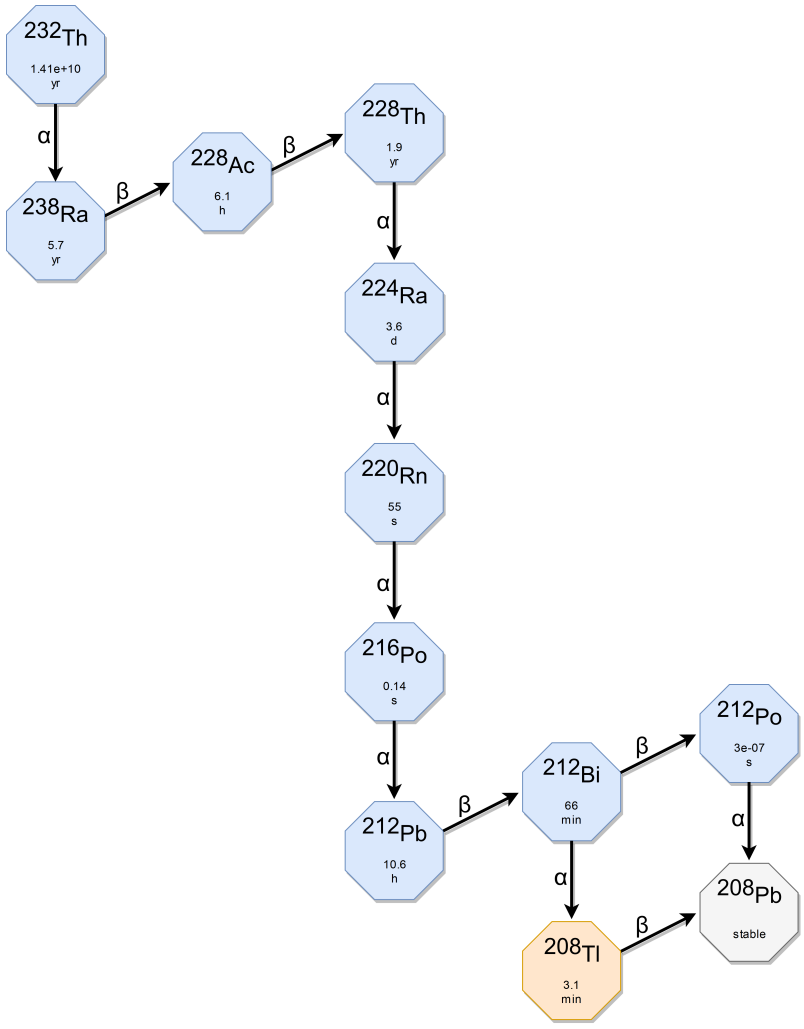

Figure 5.5: The thorium decay chain, reaching from the naturally occurring ^{232}Th to the stable ^{208}Pb, with a total energy release of 42.6 MeV. ^{208}Tl is marked in yellow, which emits a 2615 keV γ-particle with 99% and is most responsible for the external gamma background.

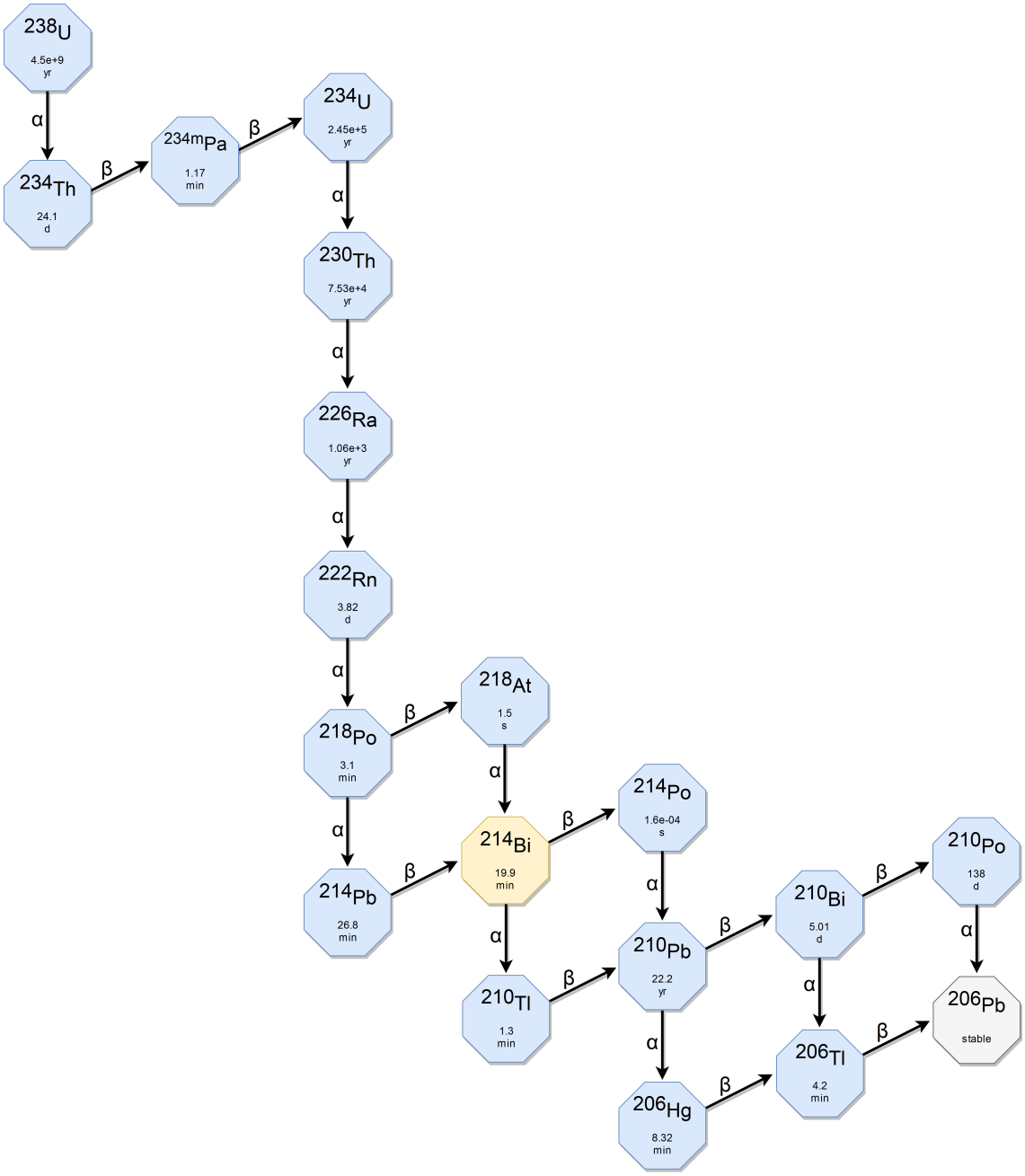

Figure 5.6: The uranium decay chain, reaching from the naturally present ^{238}U to the stable ^{206}Pb, with a total energy release of 51.7 MeV. The yellow marked ^{214}Bi emits a 1120 keV and 1764 keV γ-particle at roughly 15% for both γ's. This decay chain is also responsible for the ^{210}Pb vessel surface contamination, discussed in Section 5.1.1.

5.2.1 External Calibration

A calibration using a radioactive source placed in the buffer of Borexino, enabled the verification of Borexino's framework capability in simulating these external γ-particles. As such the calibration and its source is shortly discussed, analog to [19] and [79], where else the validation is discussed in Section 6.3.

Borexino's external calibration system enables the deployment of a radioactive source capsule in the buffer region in order to investigate the spectral shape and radial dependence of the external gamma background. As the 2.61 MeV line from ^{208}Tl is the most relevant external gamma contribution, a ^{228}Th-source was selected for this calibration.
The deployment of such a calibration source is made possible by a tube system, consisting of fourteen reentrant tubes, which are housed on the SSS. A render image of this tube insertion system can be seen in Figure 5.7.

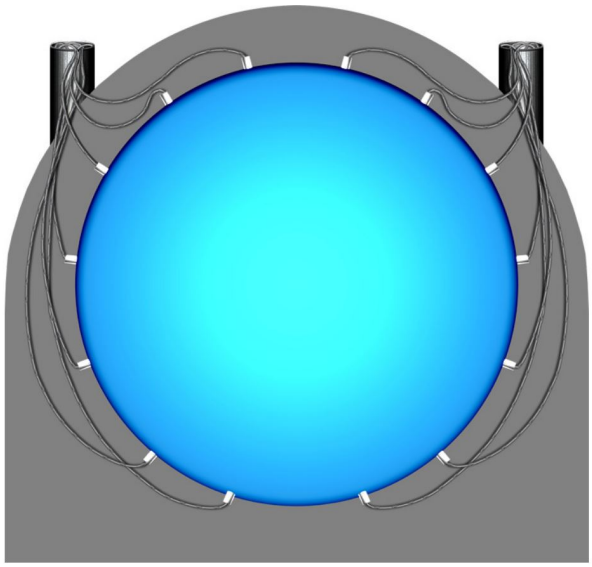

Figure 5.7: A rendering of the external calibration system. A polyethylene tube system, is able to deploy a source capsule silver-soldered to an electricians fish tape, on fourteen different positions. These reachable points inside the buffer layer enable a deployment radius from 6.35 m to 6.85 m from the detectors center. Image credit: [19].

These reentrant tubes reach with flexible polyethylene tubes through the OD to the buffer and can position a source capsule near the PMTs, at roughly 6.35 m to 6.85 m distance from the center of the detector. As seen in Figure 5.7, the tubes are connected from the outside of the ID to two organ pipes on top of Borexino. To withstand the water pressure from the OD, these tubes had been made thick to easily move a source capsule through. Additionally their inside was smoothened to reduce friction and minimize the risk of a stuck capsule inside these tubes. Figure 5.8 shows the source encapsulation, which is a 9 mm stainless steel capsule, formed like a bullet, and is silver-soldered to a electricians fish tape.

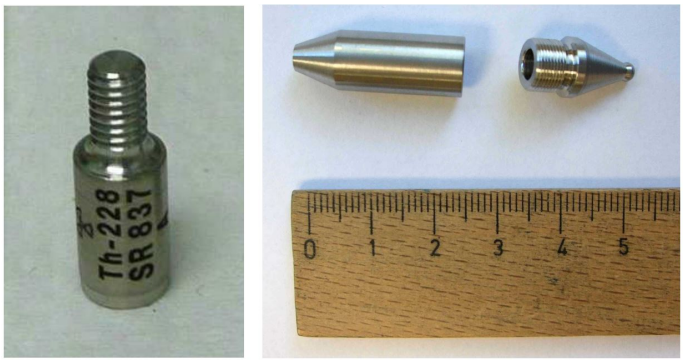

Figure 5.8: The left image depicts the custom made ^{228}Th source, which is a ThO_2 solution embedded in a gold foil. The right image shows the bullet-like stainless steel encapsulation, which is fed through the reentrant tubes. Image credit: [19].

The capsule and the fish tape can then be feed through the tubing to the various positions. The use of this fish tape enables to connect the end of the metallic source with a flange inside the organ pipe, thus allowing a verification on successful source deployment with an accuracy of $\pm$ 3 cm.

Although there are commercial thorium sources with sufficiently high activities (MBq) available, these are typically encapsulated in ceramic materials, which do not adequately prevent the emission of free neutrons. These neutrons are no real issue for Borexino's itself, but since surrounding experiments search for dark matter, strong limitations on the neutron flux had to be imposed. Therefore, a custom thorium source was developed [79], where a converted ThO_2 solution was embedded in a gold foil in order to limit the neutron flux and stored in the stainless steel "bullet" seen in Figure 5.8. The initial measured activity of this source was (541 ± 0.30) MBq on March 1^{st}, 2010.

The first calibration tests were performed in July 2010 over 9 days with a source activity of approximately 4.8 MBq. While this first calibration only covered three source positions, a more thorough second measurement period took place from November to December 2011. This time the ^{228}Th-source, with an activity of about 2.9 MBq, was deployed in ten different positions, as seen in Table 5.5, all with a radius of about 685 cm from the center. During this time a trigger threshold of 120 keV was applied.

Table 5.5: The source positions during the calibration campaign in 2011. The axes refer to Borexino's internal coordinate system, where (0,0,0) marks the detectors center. Table produced from internal documents.

	N1	N2	N3	N4	N5	N6	N7	S3	S5	S7
X [m]	2.63	4.16	5.93	6.53	6.07	4.37	2.55	-6.00	-6.06	-2.21
Y [m]	-0.62	-0.81	-1.44	-1.65	-1.08	-0.80	-0.43	-0.98	1.02	0.27
Z [m]	6.29	5.39	3.11	1.24	-2.99	-5.22	6.34	3.15	-3.03	-6.48

A plot in the *nhits* variable for the N1 source position and a radius of 4.25 m is shown in Figure 5.9. The *nhits* variable is introduced and discussed in Section 2.1.7, while the overall shape of the *nhits* spectra is discussed in Section 6.3.1. Here the impact of the internal contributions (purely qualitatively) on these spectra are briefly discussed, to better explain the slight differences observed in data and simulations at lower energies, which are due to these internal impurities.

From Figure 5.4 it can be understood that the main unwanted contributions originate from ^{14}C and ^{210}Po. The higher trigger threshold reduces the ^{14}C amount, but it can still be seen as part of the first peak below 100 nhits, in Figure 5.10. The second peak, slightly below 200 nhits is from the ^{210}Po impurities. Of course, other contributions discussed in this chapter are all present in this plot as well, but are negligible due to the high source activity (and their relative low contributions).

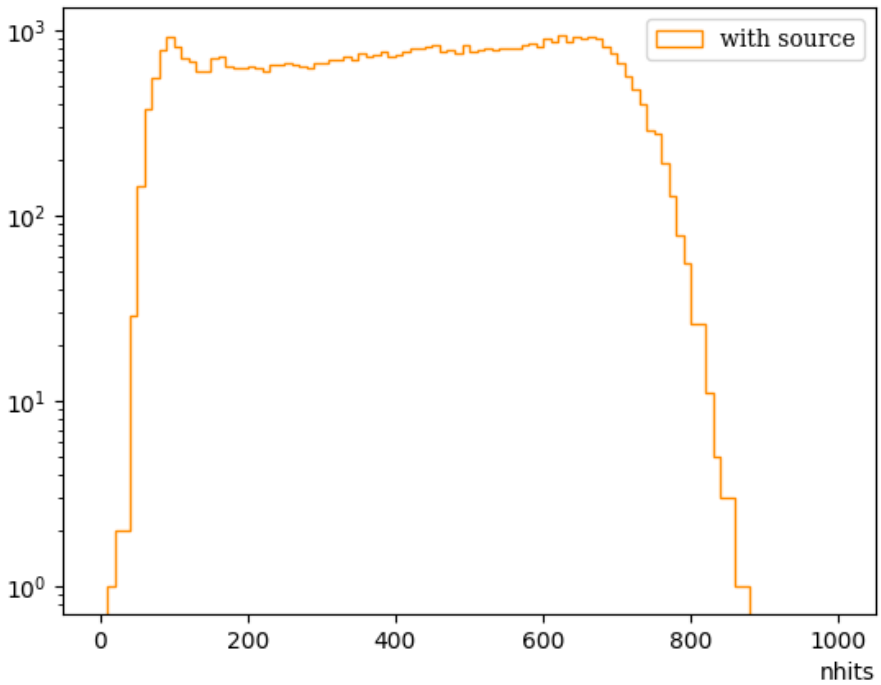

Figure 5.9: The *nhits* spectrum for the N1 source position, plotted on a logarithmic scale and for a radius of 4.25 m. It shows the spectrum from the 2.61 MeV γs (discussed in Section 6.3.1) and internal contributions on the lower ($<$ 300 nhits) part.

The *nhits* spectrum seen in Figure 5.10 depicts a data run from a week before the N1 source measurement. It shows the spectrum expected from Figure 5.4 and features the clear ^{14}C and ^{210}Po peaks and the culminated contributions of other discussed background and solar neutrino (^{7}Be) events.

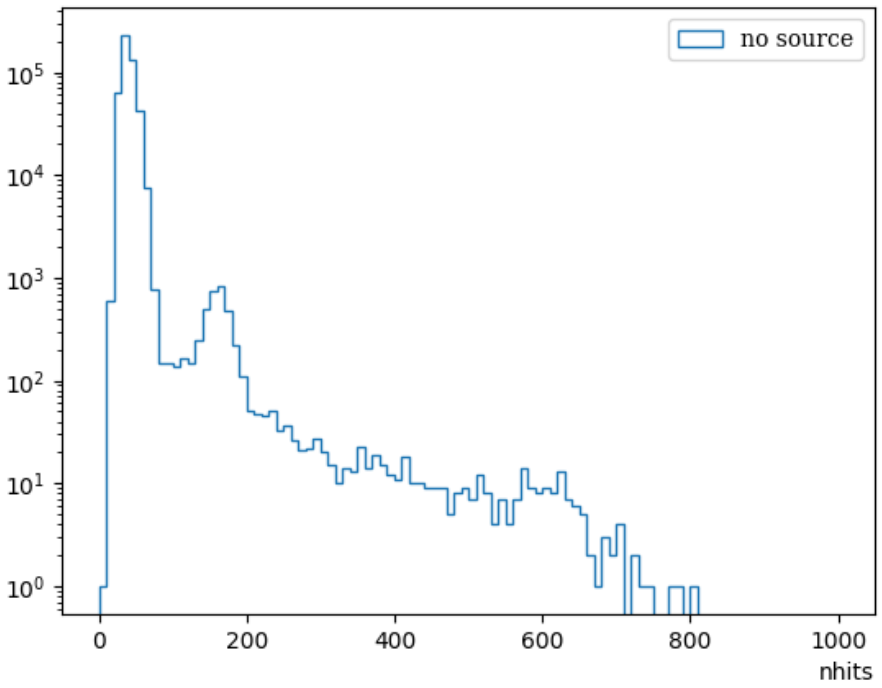

Figure 5.10: A data run from one weak before the external calibration campaign shows the two prominent ^{14}C and ^{210}Po on the left. The rest is composed from (^{7}Be) events and additional background discussed during this chapter, including some external events.

As already stated, the external gamma background is FV cut dependent and barely relevant for a small FV, the internal contributions are presents everywhere in the scintillating volume and therefore not as impacted by a FV cut. The previous plots, as already mentioned, were printed for a radius cut of 4.25 m (full vessel), whereas in Figure 5.11 a radius of 3 m is used.

This radius cut shows that the most notable internal contributions in the source measurements are below 300 nhits and indeed originating from ^{14}C and ^{210}Po. As the simulations performed in the next chapter do not include any other contributions besides the 2.61 MeV γ-line, this lower region can not be used for a comparison due to this unwanted contributions.

Before the simulated spectra can be compared to those from the external calibration campaign, the Borexino's simulation framework and a dedicated approach to enable the simulation of γ-particles in the presence of a high buffer suppression is discussed first in the following chapter.

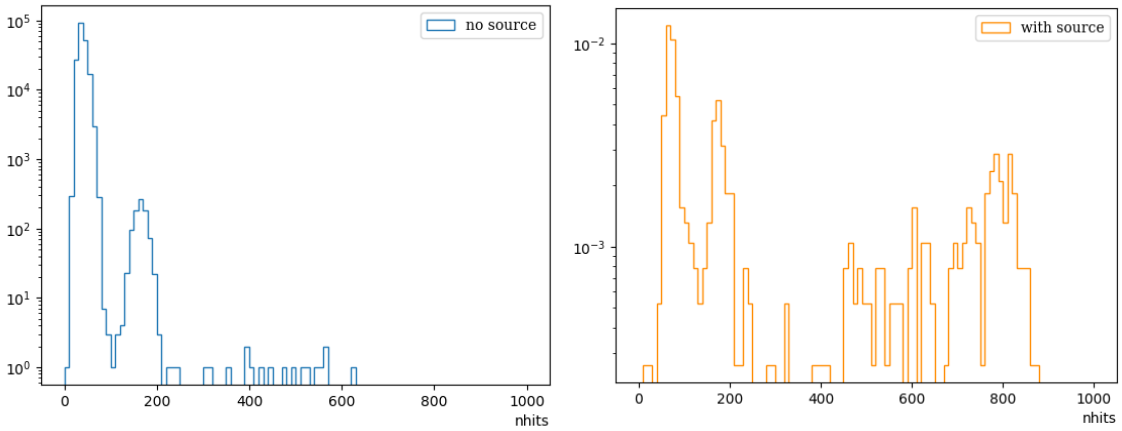

Figure 5.11: A comparison after a radius cut of 3 m for a measurement run one week before the external calibration campaign (shown in blue on the left) and for the N1 source positions (on the right, in dark orange). The peaks originating from the internal background of ^{14}C and ^{210}Po can clearly be identified. Their relative height differs due to the higher trigger threshold, which was 120 keV for the N1 source position, roughly double the threshold applied for the run shown on the left plot. Also this comparison shows that events above 300 nhits are almost exclusively γ-events.

Chapter 6

Gamma Biasing in Borexino's Simulation Framework

To predict detector behavior, better understand data, neutrino signals and background, a dedicated simulation framework was set up alongside the development of Borexino. While some of its original parts date back as far as Borexino's earlier days, the framework itself has been continuously updated and reshaped. This simulation environment, introduced in Section 6.1, consists of Monte Carlo based particle simulations (an extension of *Geant*4) as well as a simulation of Borexino's electronics and trigger systems, and produces the same type (format) of data as real measurements.
As such the simulation framework features a detector geometry as close as possible to the real Borexino setup. This realism is not without consequence when considering the external gamma background discussed in the last chapter (see Section 5.2). In a typical simulation, a single particle would be tracked from its origin, propagated with various physics interactions including the production of secondary particles, until it is absorbed or leaves the relevant world volume. The buffer layer of Borexino reduces the flux of γ-particles (in the MeV range) traveling from the SSS to the IV of a factor of about 10^{-6}. This means that in a simulation, where about 1000 γ-particles should reach the scintillating region, approximately 10^9 photons would have to be simulated. In order to reduce computation time and resources needed enough to make this even possible, a so called biasing approach is part of Borexino's simulation framework. This biasing method itself and how it is intertwined in the simulation environment is discussed in Section 6.2.
With this approach it is possible to handle external γ-particles and produce these simulations in a feasible and statistical relevant manner, thus enabling a comparison with real data. Such a comparison is shown in Section 6.3 where the capabilities of the framework are shown and validated using data from the external calibration campaign, previously introduced.
This chapter then concludes the external background simulations discussion by assembling a combined spectrum of known contributors and estimates their impact with regards to the SOX experiment, as in this case a bigger FV volume and larger energy window would have been required for the analysis.

6.1 Borexino's Simulation Framework

The Borexino simulation framework handles the production of particles, their energy loss while propagating through the detector, the generation of Cherenkov and scintillation photons and the full simulation of the electronics behavior when these photons hit the PMTs. This framework is described and thoroughly discussed in [24], whereas here only a short introduction is given.
The simulation framework can be grouped in three separate packages, namely *g4bx2*, *bx_elec* and *echidna*[1]. The first package, *g4bx2* is an extension of the C++ based Monte Carlo toolkit *Geant4*, adapting the software to the requirements of the Borexino experiment. *Geant4* is well established within and beyond particle physics as a capable particle simulation toolkit [94] and provides the generators to produce a variety of particles and radioactive decays. These generated particles are propagated and tracked through the detector geometry, where interactions with other particles and materials are simulated. With a good representation of the scintillator and buffer properties inside the simulation, the *g4bx2* package generates photons from Cherenkov or scintillation interactions. These resulting photons are also tracked including their interactions with the scintillator and buffer medium as well as the detector materials until they are absorbed or reach one of the PMTs. The PMT response is also a part of the simulation, where the tracked photons hit the PMT's photo-cathode and the individual quantum efficiency of each PMT is taken into account. The generation of scintillation and Cherenkov photons is implemented analogously to the discussion in Section 2.1.3.1.

A very good approximation of Borexino's geometry is crucial to correctly render the particle interactions with the implemented materials. All the impactful detector parts and their geometries are using the geometry building tools provided by *Geant4*. Figure 6.1 shows the rendered detailed Borexino geometry with both nylon vessels, OD, ID, SSS, steel pliers and the PMTs, based on the *g4bx2* geometry model.

To account for the realistic vessel shape, the deformation is set according to a vessel shape fit obtained for each data week. This vessel shape fit determines the IV position by using background events originating from the vessel surface contamination, as briefly described in Section 5.1.1. In the simulation framework this shape is then approximated by a polygonal shape in the r - θ plane. The goodness of this approximation can be set manually and is typically of the oder of 5 cm, as the vessel shape fit itself has an error of several cm [21].

After the photons reach the photo-cathode of the PMTs, the response of the electronics chain is simulated by the *bx_elec* package. During a data taking period all relevant values regarding the PMTs and their connected electronics are stored. These include, but are not limited to, the PMT gains, dark count rate, number of active channels, etc. The dark count rate is superimposed on the signal in the

[1] This analysis-package is the same for simulation as in regular data taking.

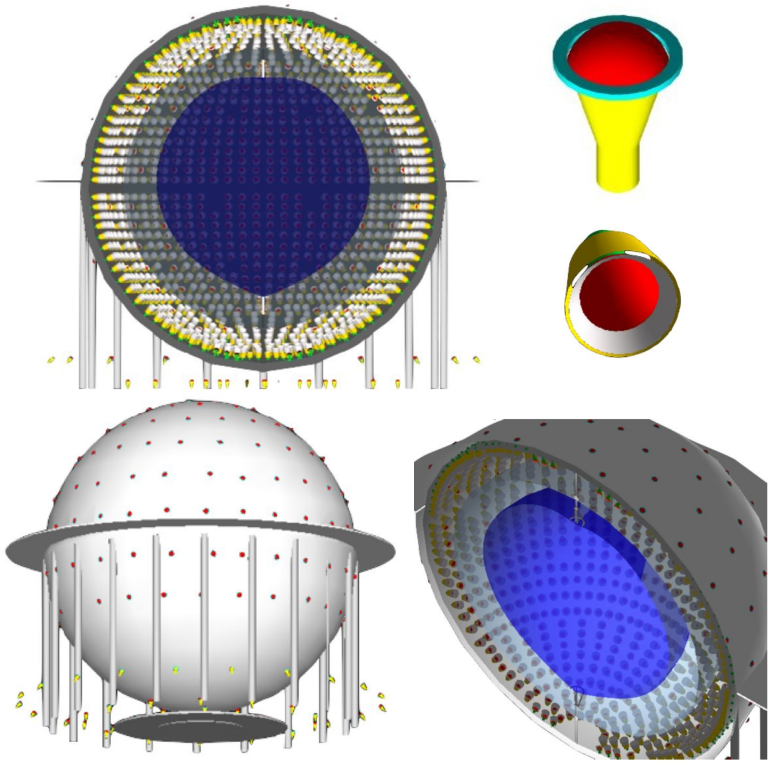

Figure 6.1: These rendered images show the representation of the Borexino geometry in the simulation framework. On the top right, PMTs with and without light cones are shown. These PMTs are modeled with their positions in the detector according to the selected measurement period. The IV, in blue, is created from a vessel shape fit to correctly represent the vessel deformation present in the simulated data taking period. Image based on [24].

simulation according to the values of the complementary measurement run and a dead time window of 140 ns is applied, which is introduced by the digital boards (see Section 2.1.5). The primary events from the *g4bx2* Monte Carlo particle tracking simulation contain no timing information on these events, as there is no absolute time scale in the particle simulation. This time information is introduced during the electronics simulation, where each event receives a time stamp, which is sampled from a distribution generated from real events in the corresponding data taking period. To evaluate the trigger condition, a fixed time window around the events obtained by the particle simulation is assessed. This technique is much faster than searching for a trigger chronologically, but the trigger condition appearance is then correlated to the presence of a simulated event. Although this is no issue for most simulations, in the case of a dedicated trigger efficiency study this approach would not be advisable and a chronological search should be taken instead.

In a final step *echidna* identifies the number of hits on the PMTs and reconstructs the energy and position of the events as detailed in Section 2.1.7. The reconstruction algorithms are exactly identical for both, simulated and real data.

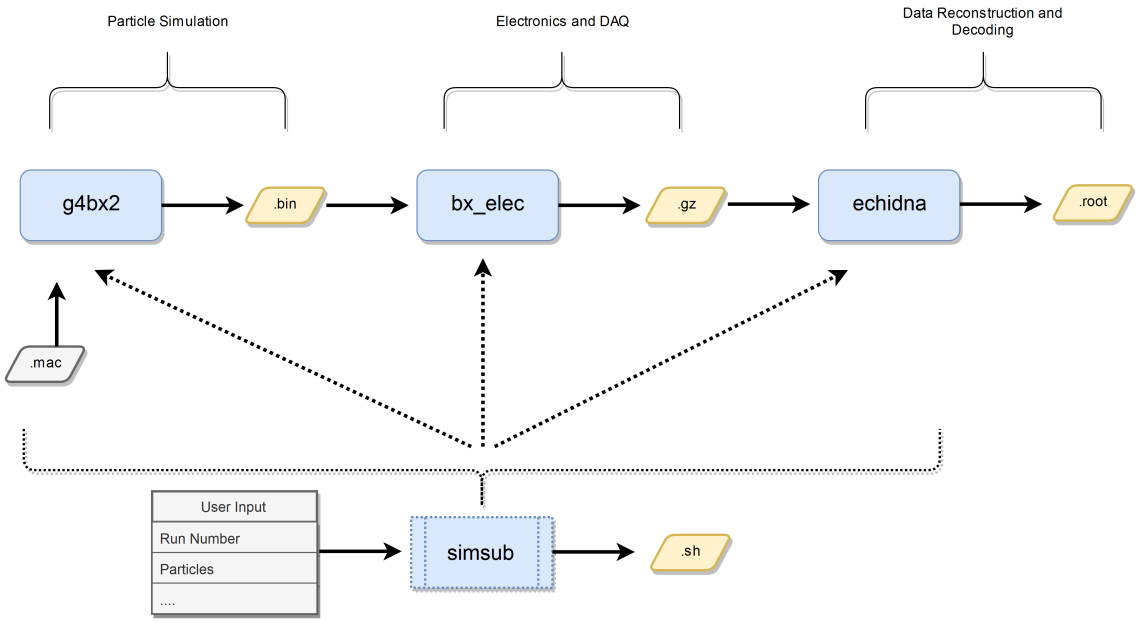

Figure 6.2: This diagram gives an overview on the various parts of the simulation chain. The distinct packages and the simulation and submission script (*simsub*) are drawn in blue, while yellow depicts the output from these packages.

Figure 6.2 illustrates how the Borexino framework operates and details the connections and layers of its structure. The particles and detector configurations among other parameters are set via a *mac*-file as input for the particle simulation *g4bx2*. The output after particle tracking is a binary file, which serves as an input for the electronics simulation. When *bx_elec* finishes, the output is a packed raw data file, identical to the output of a real measurement and a final *root*-file is created by the data decoding and reconstruction package *echidna*. The generation of the *mac*-files (although manually creatable) can be done automatically by a script which also handles the outputs of each simulation and provides the file handling between the distinct packages. Due to their computational requirements these simulations are typically run on clusters and server farms, where they are submitted and worked of in batches. The submission and management depends on the architecture of the individual cluster. For LSF[2] based management platforms the simulation and submission script (*simsub*) can handle the cluster communication and for different architectures only small adjustments are needed. This enables to control and submit simulations with the full Borexino framework relatively easily with a few command line arguments. The most notable features of this framework, besides the biasing approach discussed in the next section, are the adjusted class for scintillation light production, the modeling of positronium and the simulation of individual PMTs based on calibration data, which are detailed in [24].

[2]A Load Sharing Facility (LSF) platform currently owned and licensed by IBM, which is used to manage and submit batch jobs to clusters.

6.2 Biasing Approach

A biasing strategy is available in Borexino's framework to enable the simulation of γ-particles propagating through the large buffer layer, by drastically reducing the computing time needed. Usually a Monte Carlo simulation aims to mimic a real setup as close as possible and if events occur very rarely in a real world example or are heavily suppressed, the simulation will inherit this behavior. As a Monte Carlo simulation draws events at random from a primary distribution reflecting the "real" counterpart, techniques that allow for a preference in rare events, distort the primary event distribution and therefore introduce a bias in the simulation. However, this bias can be corrected for and a gain in simulation speed and efficiency for rare events can be achieved. A short introduction on these biasing principles and the implementation in the Borexino simulation framework is now given.
How these biases are introduced and implemented generally depends on the actual events of interest and the simulation environment at hand, but regarding the simulation toolkit *Geant*4, they can be grouped in two distinct approaches, namely selection or physics based biasing. Physics based biasing refers to interfering with physical properties or processes to speed up the production of events of interest. These include, among others, the changing of cross-sections, forced interactions, the production of secondary particles or decay probabilities. This has of course a direct impact on the physics simulation. The selection based biasing leaves all physical properties and processes untouched, but samples less interesting events or geometry regions less often [59]. For example in a simulation for a particle shower only the particle carrying the most energy would be tracked fully and those under a certain threshold killed, which can speed up computational time tremendously but can not conserve energy.

A geometry based selection on the other hand operates by assigning an importance value to each region, which is higher for regions of interest. Particles traveling towards these regions are preferred and even multiplied with a given probability, while tracks leading to less important areas are killed. This technique is known as geometrical importance sampling [49] and is the technique of choice for passive shielding issues and problems where the exact physical interactions leading to energy loss (Compton scattering for example) are relevant. This is the case for the γ-particles from the external background as their interactions produce the observed scintillation and Cherenkov light and their energy spectrum is important, in order to estimate their impact for the SOX experiment and to select a suitable FV for the analyses.

It is important to note, that the following techniques/approaches discussed (and implemented in the Borexino framework) are not only introduced to speed up the production of the energy spectra's simulation, but rather making them possible in the first place. Due to the high suppression of the buffer layer a brute-force simulation is simply not possible under the current setup. γ-particles originating from the SSS have to travel through roughly 2.5 m of buffer layer, with an attenuation length of approximately 20 cm for 2 MeV γs, this results in a suppression factor of several

hundred thousands. If 10 000 γs should reach the IV, $2.68{\cdot}10^9$ particles are needed. This is absolutely above the scale of the resources available in the regular cluster[3] used for performing Borexino's simulations. In principle this can be done by using the full cluster of a few hundred CPUs for a single dedicated brute-force simulation and therefore halting all other activities, or renting a different high power cluster for a short time, however, this would not help much. To successfully study this background, a single simulation is not sufficient, as there are at least three relevant γ-particles of different energies as well as a dependency on the data-taking period due to the vessel deformation and overall PMT distribution. It is also not possible to start the γs near the IV, e.g. in the middle of the buffer instead the SSS, to reduce the suppression, as this changes the energy spectra due to their Compton interactions. This means that in this specific case where millions of γ-particles have to be simulated repeatedly for different data-taking periods, a biasing approach based on the geometrical importance sampling is the technique of choice.

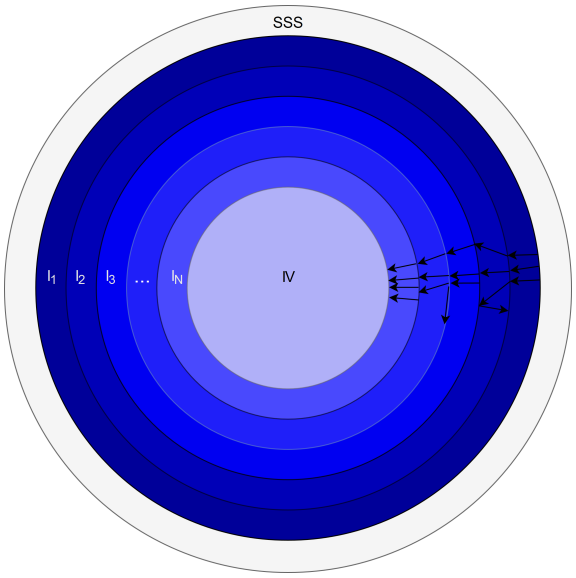

Figure 6.3: Illustration detailing the shell structure of the buffer (blue) in the parallel geometry, where the importance of the shells rises towards the center (IV) and the biased γ-particle simulation takes place.

In terms of implementation this means that a copy of the Borexino geometry is created and the buffer liquid is divided into spherical shells. This parallel geometry, technically referred to as *ghost world* assigns an importance factor (I) to each shell, which is increasing towards the scintillating volume. As Figure 6.3 shows, the outermost shell I_1 is considered of lowest importance, while I_N the last shell before the IV has the highest importance value assigned. Particles moving from a lower to a higher importance shell (towards the IV) can be copied with a probability connected to the assigned importance. The additionally created particle is then tracked from the shell it was artificially created, thus saving calculation time on the previous less

[3]The INFN-CNAF computing grid.

important region[4]. In order to correct for these induced biases, individual weights (w) are assigned to the tracks (particles) depending on the importance values (I_1 - I_N). These weights are later used to revert these artificially induced distortions.

By defining r as $r = \frac{I_{n+1}}{I_n}$, $r > 1$ would mean the track is split to $N = r$ tracks (if r is an integer) at a boundary of two shells. If r is not an integer value $N = \text{int}(\frac{I_{n+1}}{I_n}) + 1$ tracks are created with the probability $p = r$ - int(r). This process is known as particle splitting (or sometimes also referred to as geometry splitting), while in the case of $r < 1$ (moving to a less important shell) the track is killed with the survival probability $p = 1$ - r. This killing of the track is known as Russian Roulette [49].
When a particle travels inside a shell the simulation works as usual[5] as the biasing only copies or kills particles at the shell boundary, depending on their direction of travel. To later account for these additional particles created by the biasing algorithm and reconstruct the radial distribution, each created particle is assigned a weight, which is $w_0 = 1$ for an initially started γ. When particle splitting is applied the new weight is set as $w = \frac{I_n}{I_{n+1}} \times w_0$.

Figure 6.4 shows a simple example for particle splitting and Russian Roulette for two shells, where $I_2 = 2I_1$, analog to the example provided in [49]. In this scenario a particle moving towards the less important region is killed with a probability of 50%, or has its weight doubled in case of survival. If a track is not split on the boundary of I_2/I_1, the particle continues without any influence from the biasing algorithm and would reach (if it is not absorbed inside shell I_2) the "interesting" region with its initial weight of $w_0 = 1$. Each particle splitting therefore reduces

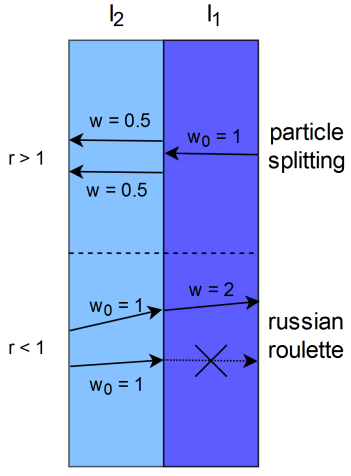

Figure 6.4: The two main principles of the geometrical importance sampling, shows the splitting and killing of the tracks on the boundary of two shells I_1 and I_2, where $I_1 = 2I_1$.

the weight of the resulting particles (or increases it in the case of Russian Roulette) and can span over multiple magnitudes connected to the suppression of the shield-

[4]Instead of starting a new particle from the SSS, as it would be the case in a regular simulation.
[5]Unbiased regular *g4bx*2.

ing. If there is an interaction e.g. via Compton scattering, the biasing algorithm saves the coordinates, deposited energies, secondary particles and the weight of the interacting particle as part of the *BxBiasedEvent* class in a *root*-file. No photons or secondary particles are tracked in this biased simulation. When the biased simulation is done, millions of deposits belonging to γ-tracks are created. A second, (non-biased) simulation then calculates the amount of visible energy (produced photons) for these *BxBiasedEvents*. The last simulation step takes care of photon tracking to the PMTs and recovers the radial shape with the use of the weight distribution to produce the final output. This is achieved by a special generator which finds the maximum value w_{max} from the weight distribution and then draws a value from the weight distribution in the range of (0, w_{max}), effectively not drawing fully random from the primary distribution, but picking weighted[6] and therefore removing the biasing effect of the deposit distribution. From this weight the corresponding deposit from the *BxBiasedEvent* is loaded and the photons are started and tracked. When an event number of e.g. 10 000 is selected, 10 000 draws from the weight distribution are then computed from the initial millions of deposits. It is possible to simply discard deposits which are fully contained in the buffer which do not produce enough light to be seen anyway and only draw from a radius close to the vessel[7]. A typical value for this radius in which the deposits are kept is 4.5 to 5 m from the IV center. With such a selection 10 000 draws will lead to roughly 7500 visible events. This superb efficiency comes at the cost of the event rates, which cannot be recovered in such a simulation approach, but as only the radial and energy shape are of interest, this is not a big downside.

Two parameters are relevant and have to be set and tuned for a γ-particle of a given energy. These parameters are the number of shells (typically 1000) and the value of relative importance of the shells, which assigns each individual importance value I_1 - I_N. In the case of the above two shell example this relative importance value would simply be 2, as this value sets the increase of importance for the shells. However, in the case of Borexino's implementation the values lay typically in the range of 1.03 - 1.04, as seen in Table 6.2.

A good selection of shells depends on the shielding capabilities of the materials and is linked to the relative importance value. A thick shell (or in other words only a few shells as the buffer radius is fixed) would lead to a higher flux reduction and would provide little gain compared to an un-biased simulation[8]. On the other hand, very thin shells create more boundaries where each time splitting or killing has to be evaluated and track weights set. When the generation of deposits is monitored as a function of the radius, in a non-biased simulation most deposits would be fully contained in the buffer above 5 m and it would show an overall exponential decay towards the center (if a high enough amount could be simulated). To successfully bias an external gamma simulation, this exponential decay of deposits has to be tuned

[6] Lower weights are less probable.
[7] Implemented simply via a flag, that the user can set.
[8] Just one shell would simply mean no biasing.

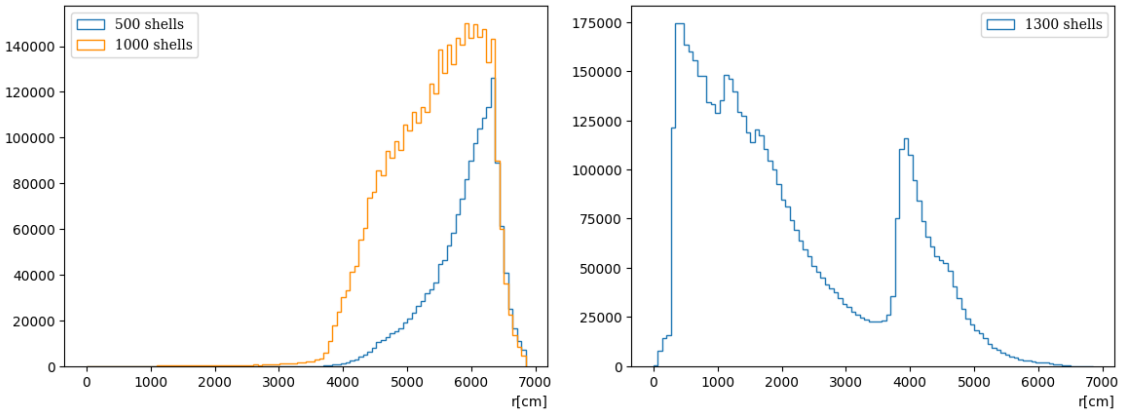

Figure 6.5: A comparison for different shells, with a fixed relative importance value. Each point represents a deposit (*BxBiasedEvent*) along the radius. On the left it can be seen that in the 500 shell example barely any particles reach the IV, while the right plot shows an example for "over-biasing", where the cascade effects towards the center can be seen. The 1000 shell example shows most events contained in the buffer and a more or less flat tail in the IV region. In all of these example an initial 10 000 γs were started.

to be more or less flat (on the lower end towards the IV), otherwise there would be no gain in biasing at all. Of course this influences the primary distribution, but this can be ultimately corrected for by the applied weights as discussed earlier. It can happen, by selecting to many shells and/or a too high relative importance value, that this deposit distribution rises towards the center. This would be some sort of "over-biasing "as more and more particle are copied because the importance value of the shells rises quicker as particles are lost to the shielding. Besides creating an highly un-efficient simulation, these simulations are also highly unstable and prone to collapse a CPU by running out of memory. Figure 6.5 shows a comparison for different amounts of shells, with a fixed relative importance value of 1.032 (for a 2.61 MeV γ). With a low amount of shells $n < 400 - 500$, the shells are so thick that most particles get absorbed in the shells and the low end of the distribution decays exponentially, almost as in a non-biased case. For $n = 500$ shells it can be seen that most events are still contained in the buffer and only a few reach the IV. The $n = 1000$ shell value, is the one used for the biased simulations discussed during this thesis, as most deposits are in the buffer but the lower part towards the IV is more or less flat and creates a stable and sufficient amount of deposits. Higher amounts of shells, e.g $n = 1300$ behave differently, especially at lower radii where they are prone to cascade intro producing more particles than those absorbed, as seen on the right of Figure 6.5.

With the shells set/fixed, the relative importance values are tuned for specific energies, by monitoring the generation of deposits along the radius, similar to the shell selection discussed above. When tuning for a new energy the range of the relative importance value is constrained at the lower part by 1, which means simply no biasing and by (in this specific case discussed here) values over 1.5 as they will run out of memory, similar to when to much shells are created. After a roughly flat

distribution is achieved in the lower end part of the radial deposit distribution, the simulation can already be used. Further tuning now relies on the computing time needed for the generation of deposits in the interesting radius, e.g. $r < 4 - 5\,\mathrm{m}$. As this cluster is composed of a variety of CPUs, to be comparable, it has to be made sure to only run on similar or the same CPUs and take the number of parallel threads running into account. Table 6.1 shows an example of such a tuning, for 1000 shells and a γ-particle energy of 2.61 MeV.

Table 6.1: A tuning example for a fixed γ-particle energy of 2.61 MeV and 1000 shells. I simply refers to the relative importance value. The runtime is adjusted to account for the amount of parallel threads running and a mean value is derived from 20 CPUs, to enable a meaningful comparison in the total amount of deposits generated in a radius of $r < 4.5\,\mathrm{m}$.

I	Deposits	Runtime [s]
1.029	$7.83 \cdot 10^5$	1490
1.030	$1.27 \cdot 10^6$	2872
1.032	$2.74 \cdot 10^6$	3387
1.034	$7.40 \cdot 10^6$	10969
1.039	-	-

While it can be seen that the 1.029 value is rather fast, it creates the least amount of deposits. The 1.030 and 1.032 values are not that much apart in terms of runtime, but the 1.032 has double the amounts of deposits. In the case of 1.034 it has to be stated that although a large amount of deposits are created not all CPUs are able to work with this amount, as only about 1/3 of the CPUs have the power to handle this, while the 1.039 is not able to be computed on any CPU available in the cluster. For this reason the 1.032 relative importance value was chosen for the 2.61 MeV γs. Such a (technical) efficiency discussion is heavily influenced by the cluster/CPU setup available and can certainly deliver different outcomes on another server farm.

It is important to highlight again, that this biasing approach does not interfere with the physical processes or properties of the simulation at any point. The number of shells and relative importance value parameters only impact computational efficiency and times. To illustrate this, Figure 6.6 shows the resulting energy spectra, shown via the *nhits* variable for a fixed number of $n = 1000$ shells but two different relative importance values. These two spectra differ only due to the random seed selection of *g4bx2*, if this seed is forced to a fixed value, both spectra are identical. Practically this means that the amount of optimization does not affect the outcome of these simulations, but only their efficiency. This also means that even though these non-physical parameters are somewhat energy depended, a tuned selection works just fine for energies close to the initial tuning energy[9]. Re-tuning is only needed when this energy range gets bigger or when a high efficiency is specifically desired for a given energy. Such is the case for the external gamma background

[9] Typically up to a few hundred keV.

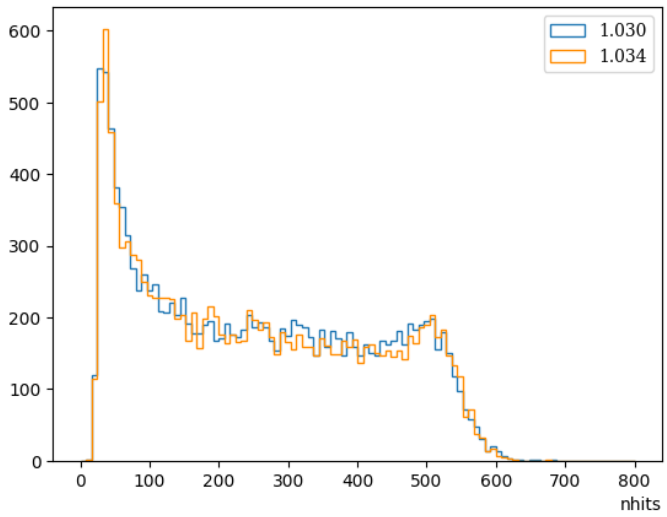

Figure 6.6: An example for the resulting *nhits* spectra for two different relative importance values. The spectra only differ due to the initial seed selection of the Monte Carlo simulation and are besides this identical.

events and thus every γ-particle contributing to the combined spectrum seen in Section 6.4 was specifically tuned to produce this vast amount of data needed. These tuning values can be seen in Table 6.2, where they are listed with their energy and element/isotope of origin.

Table 6.2: The tuned parameters of the relative importance value I and for 1000 shells.

Energy [MeV]	I	Element
1.13	1.037	^{214}Bi
1.46	1.040	^{40}K
1.76	1.0369	^{214}Bi
2.61	1.032	^{208}Tl

A selection of the number of shells and the relative importance value is always needed for each new energy. To produce these biased simulations successfully, a lot of additional work on top of an already functioning simulation framework has to be done. For different particles, besides γs, the process would have to be redone completely and overall event rates, if desired, can not be recovered with such an approach. The choice between a brute-force regular simulation and such a described biasing technique is therefore one, which has to be made on an experiment to experiment basis. Even though *Geant*4 provides these biasing algorithms and functions, it has to be taken into consideration that most work typically involves the combination of biased and non-biased simulations and their overall integration in a larger, potentially un-flexible existing simulation framework.

To summarize, in a biased simulation the *g*4*bx*2 package is run three times as its

tasks are split. As it is illustrated in Figure 6.7, the first step (1) takes care of the γ-particles biasing and the assigning of the weights. Each interaction is stored as a *BxBiasedEvent* but not further computed as only the biased γs are propagated and treated according to the discussed geometrical importance sampling approach in the parallel geometry (*ghost world*). With the weights and all generated deposits as an input, *g4bx2* calculates the secondary particles as well as the scintillation and Cherenkov photons (2). In a last step (3) a weighted draw from the deposits is performed and the photons are properly simulated and tracked until they reach the PMTs and the rest of the simulation chain is run.

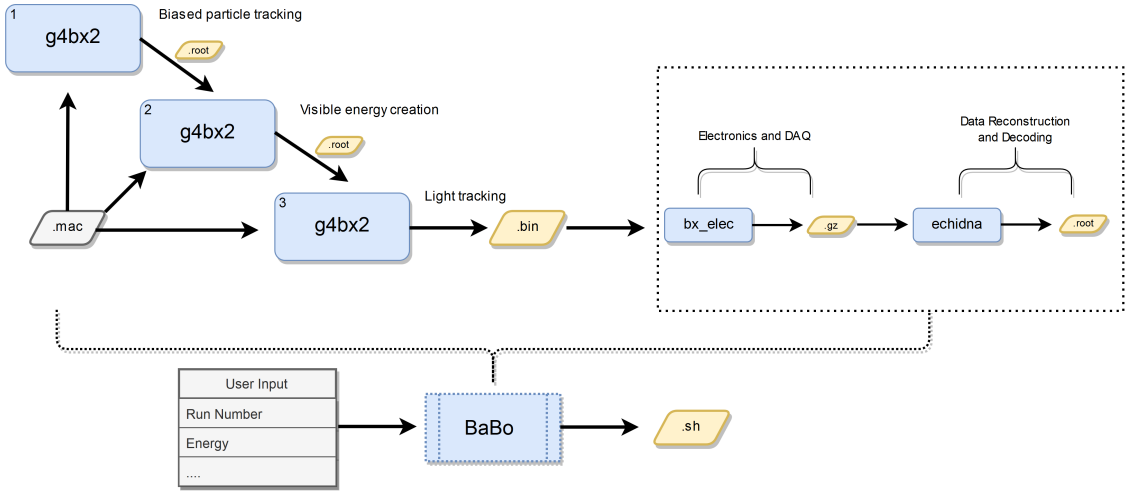

Figure 6.7: A flow diagram illustrating the steps in a biased simulation. The particles simulation is split in three parts, where first a biased γ-simulation is performed, then the visible energy based on the interactions of the the γ-particles is calculated, followed by the production and tracking of scintillation and Cherenkov photons.

All of these steps and the complete biased simulation including the server/cluster submission and communication is handled by the **B**iasing **A**pproach for **Bo**rexino (*BaBo*) script, developed during this thesis. This script enables to run biased simulations of the most relevant external γ-particles, which can be generated directly as particles or originate via their respective decays. When a γ-particle of a given energy is selected by the user, it is assigned a relative importance value, based on the nearest energy tuning point. Among other operating modes, the *BaBo* script features a dedicated tuning mode, to enable the convenient inclusion of new energies, based on the tuning steps discussed earlier. It is capable of submitting biased simulation in batches (of typically 20 parallel jobs) and can run only a biased simulation, or run the full simulation framework chain, or recover previously biased simulations by using the *root*-file containing the *BxBiasedEvents* as an input. Furthermore it features an automated cleanup mode, where the biased deposits can be deleted after a successful run of the full simulation chain to free up space (as these can take up to several GB per biased simulation) and is able to merge multiple simulations of the same energy together. All biased simulations discussed in the scope of this thesis were simulated with the discussed approach and *BaBo* script.

6.3 Validation

To evaluate the capabilities of the Borexino framework combined with the biasing approach, the external calibration campaign discussed in Section 5.2.1 was used to compare the data from the N1, N2, N3, N4, S3 and S7 source positions with simulation results. These six out of the ten positions were selected as they already provide a good selection to study the different positions without the need to generate all the data needed for the full ten locations. The external calibration campaign deployed a ^{228}Th-source, which produces the 2.61 MeV γs from the ^{208}Tl decay (shown in Figure 5.5). Therefore a tuned 2.61 MeV γ energy, with the parameters shown in Table 6.2, was used to generate the biased simulations.
The source locations are illustrated in Figure 6.8, while their exact positions are given in Table 5.5. As stated earlier, the energy spectrum is important to estimate the impact of this background in the SOX energy window and the radial spectrum is needed to select a FV for the analysis with a good compromise between scintillating volume and external background as the radius is increased compared to previous analysis. Therefore the agreement in the energy spectrum (between data and simulation) whilst following overall detector behavior is validated in this chapter.

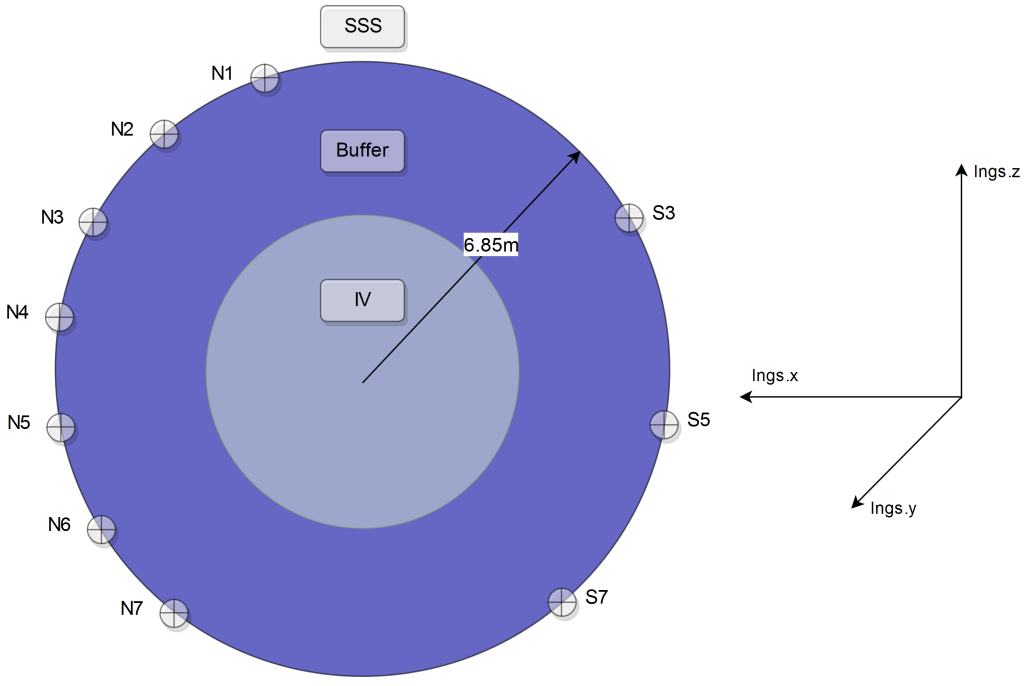

Figure 6.8: Illustration showing the source locations during the 2011 external calibration campaign and Borexino's internal coordinate system. With a dedicated tube system, the source capsule was deployed in ten positions. The radial distance had been 6.85 m in all locations and their number refers to their relative height with respect to the ground (with "1" being the top).

First the simulated shape of the resulting energy spectrum, exemplary for the N2 source position, is discussed (Figure 6.9), followed by a comparison of the data and

simulated energy spectra. The overall good agreement of such an energy spectrum is plotted in Figure 6.10. In Section 6.3.2 the radial event distribution is evaluated and compared by fitting the x, y, and z coordinates separately for data and simulation to compare the radial event distribution.

6.3.1 Energy Spectra

The overall shape of the *nhits* spectrum, seen in Figure 6.9 for the N2 source positions, shows three distinct features. From left to right, first on the low end of the *nhits* spectrum there is a peak, which morphs at around 100 nhits to a flat continuum and then shows another peak between 700 - 800 nhits. In the 2 MeV γ-ray energy range Compton scattering is dominant for practically all absorber materials. As the γs travel from the SSS through the buffer they undergo multiple[10] Compton scatterings and form the, in the following called, "effective Compton edge" seen at around 750 nhits. The position of this effective Compton edge is moving depending on the source position, due to the deformed vessel. This means a difference in buffer travel distance therefore changes the amount of Compton scattering depending on the source position. After the Compton continuum the peak on the low end of the spectrum is due to the photoelectric effect as the energy of the γs has now been lowered enough due to the scatterings. However, because the γs arrive at different low energies this is not a sharp peak but is rather smeared out.

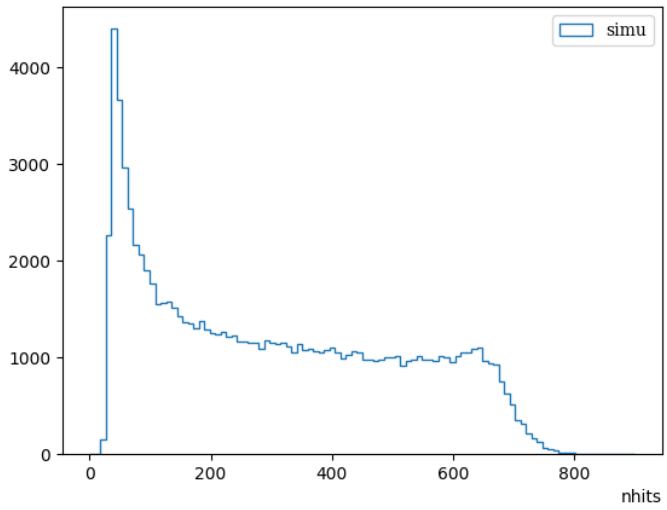

Figure 6.9: Simulation for the N2 source location without any radius cuts. The *nhits* spectrum shows (from left to right) a photoelectric peak, a Compton continuum and an effective Compton edge. When a radius cut is applied, the effective Compton edge shifts to lower *nhits*.

The effective Compton edge was used as the comparison tool to validate the agreement between simulation and data of the various source positions, by means of a

[10] As opposed to a "normal" Compton edge.

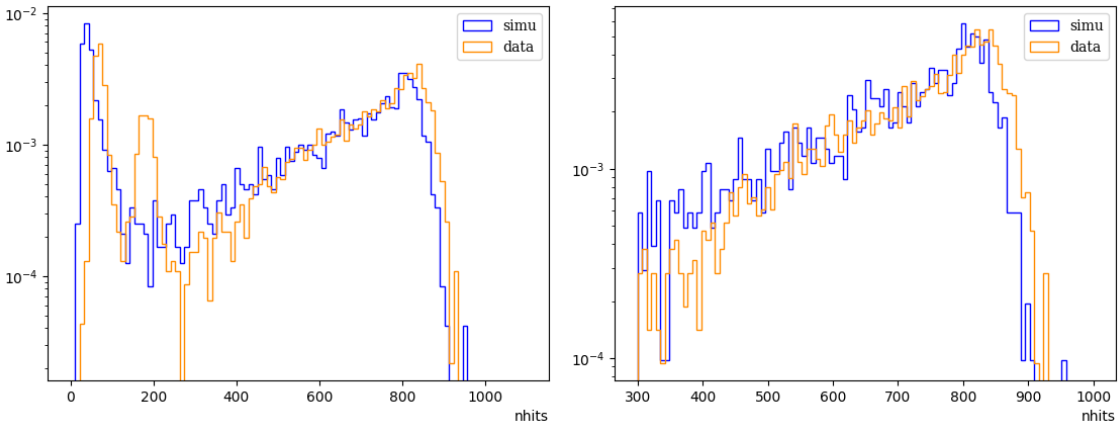

Figure 6.10: On the left image, a comparison for the complete *nhits* range is shown. The most obvious deviation is the additional peak at about 180 nhits (which is due to mostly ^{210}Po events, see Section 5.2.1 and Figure 5.1), in the data spectrum. The right plot shows the spectra above 300 nhits, to exclude these events. Both spectra, in this case for N2 location, are very similar except for a small shift in *nhits*. To also reduce additional events from the vessel surface contamination, a radius cut of 3.5 m was used. The spectra are plotted on a logarithmic scale, both are normalized and only single cluster events are considered.

Gaussian fit around this distinct peak. The photo-peak although present in data was not used for a comparison due to it being convoluted with internal contaminations, discussed in Section 5.2.1. Because the biased simulation contains only the events created by the 2.61 MeV γs, in order to ensure a meaningful comparison, the additional contaminations not originating from the thorium source have to be filtered out from the data. Even though the data is dominated by the 2.61 MeV γs due to the high source activity (of about 2.9 MBq), two unwanted contaminations are still present in the data. One being the internal contamination (Section 5.1.1) at low energies ($<$ 300 nhits) and the second one comes from the vessel surface contamination (seen in Figure 5.3). The Gaussian fits of the effective Compton edge were therefore performed for a vessel radius cut of 3.5 m to exclude surface contamination events and in a *nhits* interval ranging from 300 to 1000 nhits, as it is illustrated in Figure 6.10. Additionally, to further reduce unwanted contaminations, only single cluster events have been considered. As discussed in Section 2.1.7, the clustering algorithm can identify two events close together, like those originating from a fast ^{212}Bi-^{212}Po decay (see Figure 2.16 and Section 5.1.1 for more information on the clustering and this fast decay coincidence). This results, in the data being filtered to contain only single cluster events, which further assists in the comparison of the γ energy spectra. Also, the trigger condition present in the data runs was applied to all simulations.

The results of these fits are summarized in Table 6.3, where the means of the Gaussian fits are compared for data and simulation. The lower shift observed in the previous N2 example is seen as a systematic shift to lower *nhits* in all positions,

also the effective Compton edge seems to be slightly more Gaussian shaped and prominent in the data than it is in the simulation. This behavior seems to originate from a steeper decline in the data from the effective Compton edge to the Compton continuum, which seems to be slightly more flat in the simulation (and is responsible for the marginally larger errors of the means of the Gaussian fits in the simulation).

Table 6.3: The means of the Gaussian fits for data and simulation. The simulation contained half the events of data for all source locations.

Position	Data [nhits]	Simulation [nhits]
N1	826 ± 4.12	791 ± 3.46
N2	830 ± 1.64	793 ± 4.97
N3	824 ± 1.47	782 ± 2.58
N4	820 ± 1.22	776 ± 3.80
S3	821 ± 2.32	787 ± 3.21
S7	754 ± 1.78	743 ± 1.15

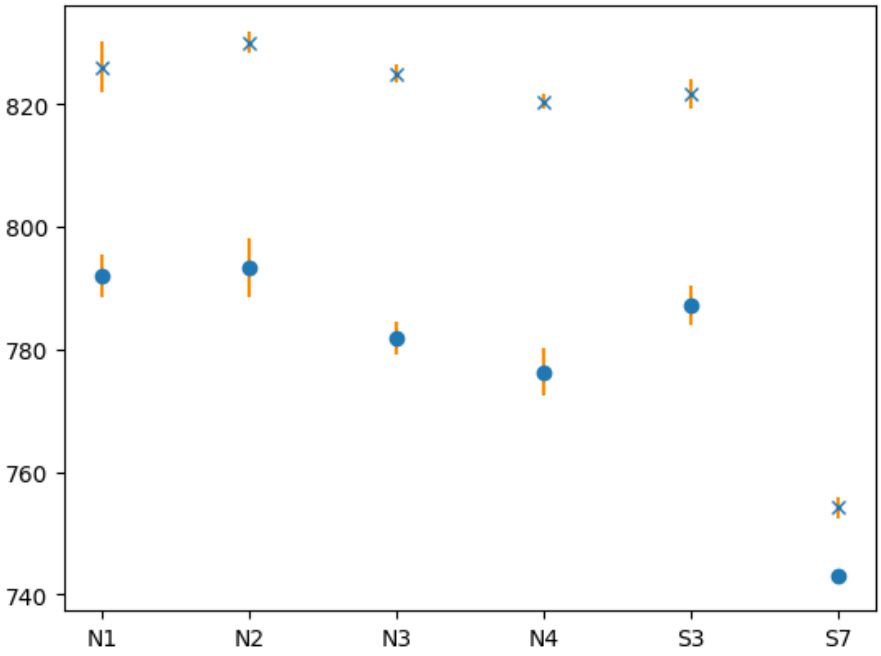

Figure 6.11: The effective Compton edge position per source location, obtained by comparing the means of Gaussian fits performed for data (plotted as X) and for simulation (dots).

Several observations can be made:

- First: The overall source position dependence of the effective Compton edge is mimicked by the simulation, which implies that the vessel deformation is sufficiently well simulated as this effective edge position is dependent on the

distance traveled through the buffer layer.

- Second: A shift to lower *nhits* values is present in the simulation, ranging roughly from 11 up to 44 nhits between data and simulation, meaning that the simulation overall sees less light than the data (34 nhits on average). This relatively small effect may be caused by a smaller number (or a different distribution) of life-PMTs in the simulation. Although this behavior should be corrected for, because the PMT distribution is automatically selected from the corresponding data run, a small deviation seems still to be present[11]. In principle this could be investigated by manually adjusting the PMT distribution, unfortunately recovering of the initial PMT data is not possible anymore. Furthermore conventional (un-biased) simulations show already a discrepancy of several percent [24] in the *nhits* variable between data and simulation. As this issue is present in most simulations and most certainly not related to biasing, this shift has not been further investigated, especially since the energy spectra themselves show the same features and the effective Compton edge's behavior per source location in the simulation follows the data.

- Third: In the S7 source position the effective Compton edge is at its lowest value in data and simulation alike. This is to be expected, as the light collection ranges roughly from +8% slightly towards the top (but still close to the center) to -20% in the bottom of the detector [3]. The S7 location is not completely at the bottom so the loss of approximately 10% for data compared to the N3 position (which is located more or less on the equatorial plane) and the approximately 5% in the simulation seem reasonable.

The successful simulation of the energy spectra enables to estimate the amount of external gammas arriving for a given energy (*nhits*). This could have already assisted in background understanding or a potential energy cut for the SOX analysis. Next the radial spectrum is investigated to validate the capabilities of the framework and to help in selecting a FV which could have been suitable for the SOX experiment.

[11] The effects of the PMT distribution on the *nhits* has been discussed in Section 2.1.7.

6.3.2 Radial Spectra

To evaluate the agreement of the radial spectra between data and simulation a comparison in the x, y and z coordinate was performed, since Borexino uses an internal Cartesian coordinate system. The expected behavior for a point-like external γ-source is of course an overall exponential radial behavior, but in this internal Cartesian coordinate system (and no source location being aligned with any coordinate axis), this results in a somewhat Gaussian shape. Figure 6.12 shows an example for the N3 source positions and its resulting shape in x and y coordinates.

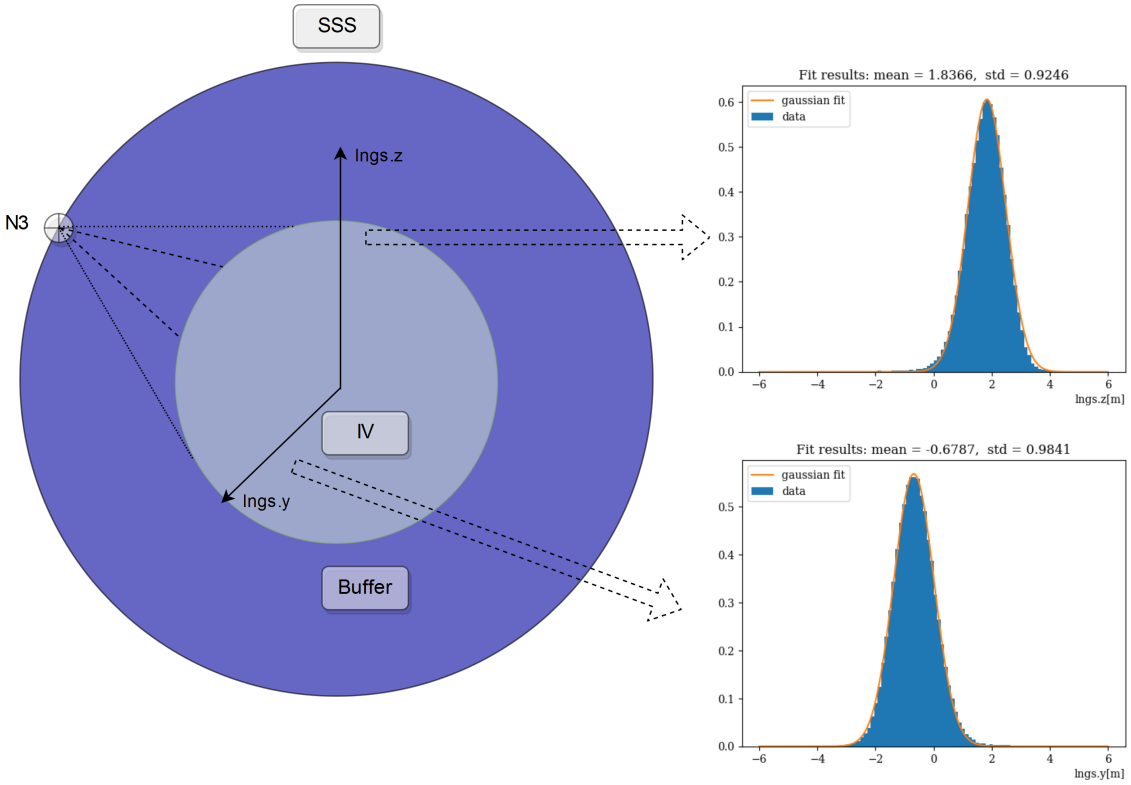

Figure 6.12: An example of the N3 source position and the resulting shape of the x and y coordinate. A point-like source leads to roughly Gaussian shaped data, due to Borexino's Cartesian coordinate system.

From Figure 6.12 it becomes clear that a plot in the y-z-plane for this N3 position results in a ring-like behavior, where most events point towards the source location. The roughly heart-like shape of the IV as well as the x-axis for the N3 source position is shown in Figure 6.13 and resembles more the expected radial behavior, with some Gaussian features showing due to the axis projection. All source positions follow this behavior of two roughly Gaussian-like axis projections and one slightly more exponential one.

The radius itself is not expected to be a pure exponential for two reasons. One being events close to the vessel can get reconstructed outside of the vessel by the

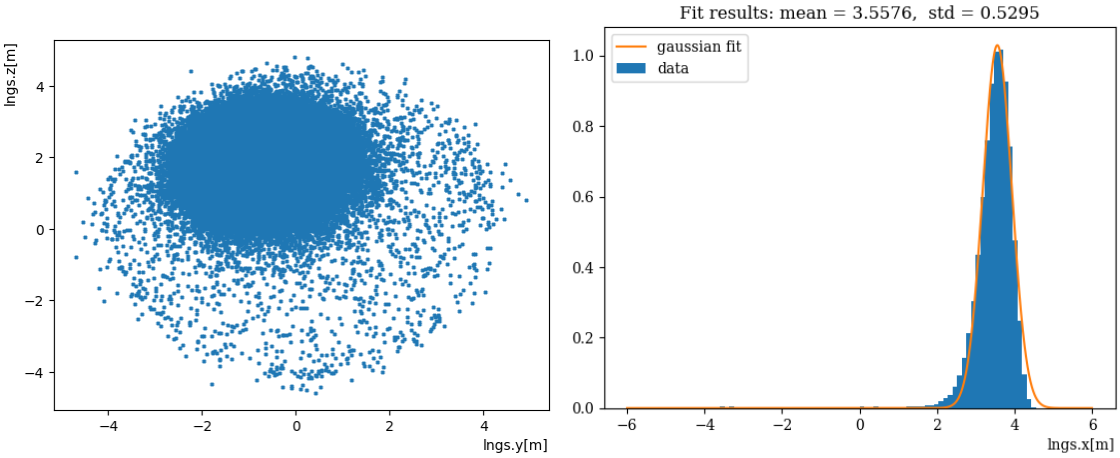

Figure 6.13: The left plot shows the y-z-plane of the N3 source location and the x-axis is shown on the right.

position reconstruction algorithm (see Section 2.1.7), which has an error of approximately 10 cm in this energy range even close to the IV's center and is certainly getting worse towards higher radii [26]. The other reason is related to the vessel leak, discussed in Section 2.1.3.3, which resulted in scintillator spilling in the buffer. With the high source activity of the calibration source discussed in Section 5.2.1, this is a visible effect and one Borexino's simulation framework does not take into account. This buffer-scintillator is not equally distributed but is more present in the equatorial region (and towards the south), as can be seen in Figure 6.14, where the S3 and N4 locations are drawn. To minimize this scintillating buffer effect, a radius cut of 4.25 m was used. With this radius cut an exemplary comparison for

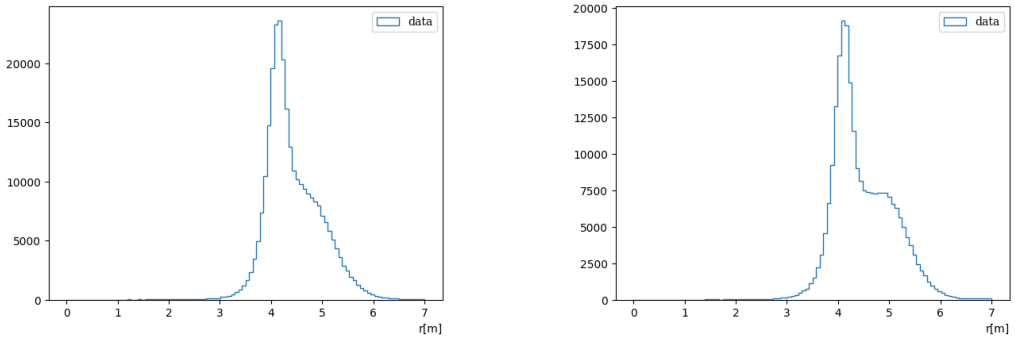

(a) S3 **(b)** N4

Figure 6.14: These two radial plots of the S3 and N4 source positions show the impact of the scintillator in the buffer. The vessel ends at around 4.25 m and only a few events, which are very close to the vessel or get reconstructed outside of it should be seen. Instead there are events fully contained in the buffer, which should produce almost no light and therefore be invisible, but are highly visible due to the scintillator present after the vessel leak. This behavior is also very position dependent, as the produced shapes are different for each source position.

the N3 source position between data in all coordinates and the radius is shown in Figure 6.15. These show a good agreement and to quantify this, all of the spectra were fit with a Gaussian and compared via their mean position in each axis. The results of this mean comparison is summarized in Table 6.4, while all the fits can be found in the attachment in Chapter 7.

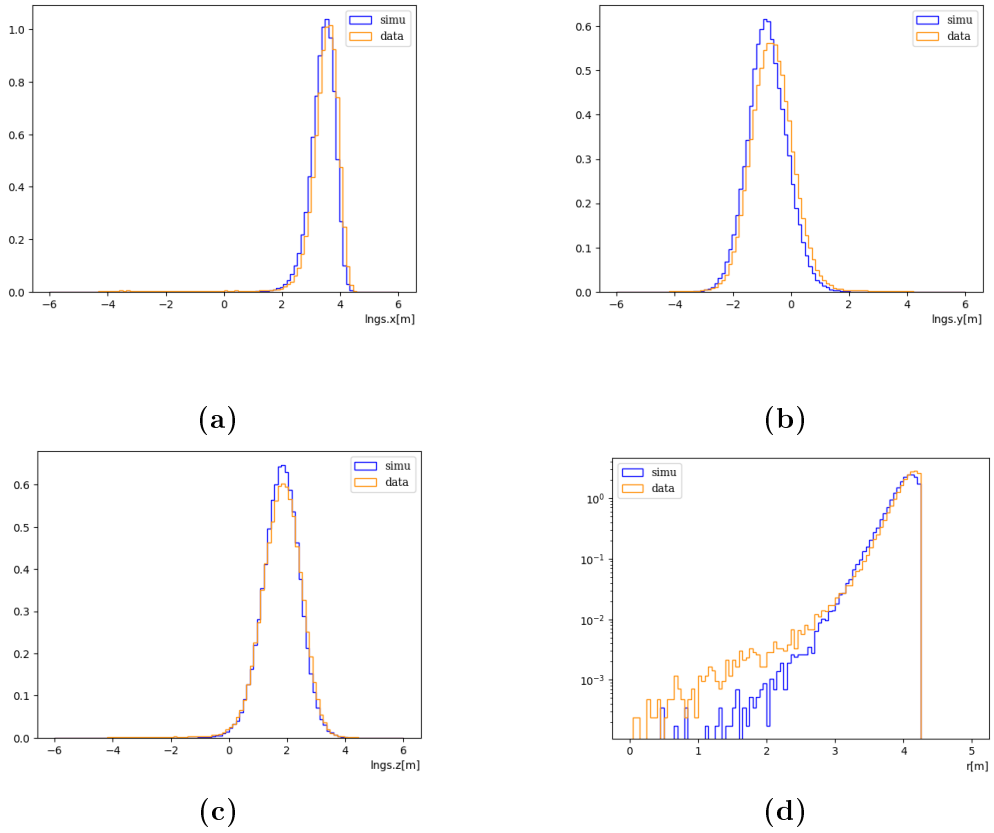

Figure 6.15: A comparison for the N3 source location between data and simulation. It can be seen that the simulation follows the shape in all three coordinates (a to c) to a good degree. The resulting radius (d) deviates only below 3 m due to the internal contaminations, already discussed in Section 5.2.1. Higher radii, above the 4.25 m radius cut are not compared due to the impact of the scintillator in the buffer. The most interesting region is the one above the solar FV (of roughly $r = 3$ m) and below the vessel end at 4.25 m as there a potential FV for SOX would have been selected and the simulation shows a good agreement with the data in this radius interval.

Table 6.4: This table details the means of the Gaussian fits performed for data and simulation for each coordinate and source position.

	Data [m]	Simulation [m]
N1		
X	1.56 ± 0.003	1.54 ± 0.004
Y	-0.29 ± 0.002	-0.32 ± 0.003
Z	3.82 ± 0.006	3.77 ± 0.006
N2		
X	2.53 ± 0.003	2.38 ± 0.003
Y	-0.44 ± 0.001	-0.46 ± 0.002
Z	3.22 ± 0.006	3.25 ± 0.006
N3		
X	3.56 ± 0.005	3.45 ± 0.006
Y	-0.68 ± 0.002	-0.84 ± 0.004
Z	1.84 ± 0.003	1.81 ± 0.003
N4		
X	3.90 ± 0.003	3.71 ± 0.005
Y	-0.74 ± 0.002	-0.98 ± 0.002
Z	0.57 ± 0.002	0.78 ± 0.002
S3		
X	-3.56 ± 0.005	-3.48 ± 0.006
Y	0.60 ± 0.002	0.59 ± 0.002
Z	1.83 ± 0.003	1.83 ± 0.002
S7		
X	-1.21 ± 0.002	-1.09 ± 0.002
Y	0.68 ± 0.003	0.15 ± 0.003
Z	-3.54 ± 0.004	-3.61 ± 0.005

Simply to visualize the discrepancy between data and simulation, for each source location the differences of the means of the Gaussian fits per coordinate (Δx, Δy, Δz) were combined to $d = \sqrt{\Delta x^2 + \Delta y^2 + \Delta z^2}$ and are shown in Figure 6.16. The overall agreement seems to worsen towards the southern region (with the exception of the S3 position). This could be connected to the discussed potential deviations in the PMT distribution in Section 6.3.1. But since non of these issues are part of the biasing approach or specific to γ-particles and the overall detector behavior in terms of the radial event distribution (except from the scintillating buffer) is approximated to a good degree, these deviations were not investigated further.

This validation has shown that the Borexino framework with the biasing approach is capable of simulating γ-events successfully, even in the prescience of a high sup-

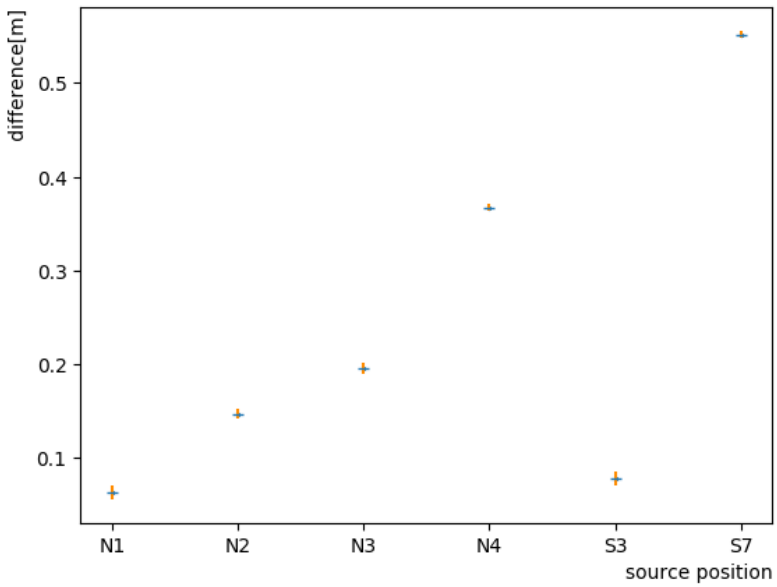

Figure 6.16: The means of the Gaussian fits have been compared in terms of their distance $d = \sqrt{\Delta x^2 + \Delta y^2 + \Delta z^2}$ and the difference in distance for each source position is plotted in blue. The small yellow lines show the errors for $r > 0$, calculated via Gaussian error propagation. It can be seen, that the agreement worsens towards the south of the detector (except for the S3 location).

pression. The resulting energy spectra and radial event distributions differ due to internal events which are not considered in the simulations and show a systematic shift in the *nhits* variable, but result in the same shapes and are able to account for the vessel shape deformation.

To expand on the external gamma background analyses additional γ-contributers are added, such as ^{214}Bi and ^{40}K and their spectra combined with ^{208}Tl. This serves simply a proof of concept on how this could have influenced the selection of a SOX FV and helped in overall external background reduction.

6.4 Radial Profile of the External Background

As discussed in Section 5.2, the most significant contributions of the external gamma background arise from ^{214}Bi, from the uranium decay chain (Figure 5.6), ^{208}Tl, from the thorium decay chain (Figure 5.5) and the natural occurring ^{40}K. To disentangle background from neutrino events, a background subtraction of these contributors would have had to be performed. Due to the energy of these neutrinos being in the range of 1.8 to 3 MeV (Figure 3.6), external gamma background would have been the most significant background (as can be seen by Figure 5.4, with ^{11}C being the only internal contributor in this energy range). Combining all of the relevant external gammas to one single gamma background spectrum would allow to estimate this contribution for a given energy range (useful for background subtraction in the

analyses) and by investigating their radial distribution could have helped in selecting a FV for the SOX experiment.

In principle a FV in the SOX case would be preferably as big as possible to provide the best sensitivity as discussed in Section 3.1 (even plans to fill the buffer partially with scintillator to enlarge the sensitive volume were discussed). However, a bigger FV would imply also a bigger impact from the external background. To investigate this background and prepare the detector for the SOX experiment, a dedicated calibration campaign was planned before the arrival of the source. In this campaign a new measurement with radioactive sources would have been performed, this time also including ^{40}K among others. Due to the cancellation of the SOX experiment this calibration was never done. Therefore the following steps on how to derive a combined external gamma spectrum are purely a proof of concept and have only some validation for the 2.6 MeV γ-line from ^{208}Tl.
Without such a calibration campaign to estimate/constrain the activities and fluxes of the gamma contributors, the last radioactivity measurement (performed in 2001) was used. The measurement discussed in Table 5.4 gives g/g contaminations of the PMTs for potassium, uranium and thorium. With these values and the PMT's combined mass of 2×10^3 kg, the conversion factors in Table 6.5 are used to derive an activity estimate for ^{214}Bi, ^{208}Tl and ^{40}K[12]. By then only considering γ-particles above 1 MeV with a non-negligible emission probability (seen in Table 6.6), the combined spectrum is assembled.

Table 6.5: The conversion factors for uranium, thorium and potassium [17].

	Conversion factor
^{40}K	10^{-9} g/g = 31 μBq/kg
^{232}Th	10^{-9} g/g = 4.06 mBq/kg
^{238}U	10^{-9} g/g = 12.35 mBq/kg

Table 6.6: The emission probability for γ-particles above 1 MeV. Based on [70].

Energy [MeV]	Origin	Emission Probability
1.13	^{214}Bi	14.92%
1.46	^{40}K	11%
1.76	^{214}Bi	15.3%
2.61	^{208}Tl	99.75%

The spectrum seen in Figure 6.17 combines four γ-particles originating from ^{214}Bi, ^{208}Tl and ^{40}K to one combined spectrum, drawn on a logarithmic scale in the *nhits* variable without any radial cuts. The features of these γ-spectra were already discussed in Section 6.3.2. No internal contributions or surface events were simulated

[12] If secular equilibrium is assumed.

and the γ-particles are started uniformly from the PMTs on the SSS (at a distance of 6.85 m). In Figure 6.18 this resulting combined spectrum is shown for a radius

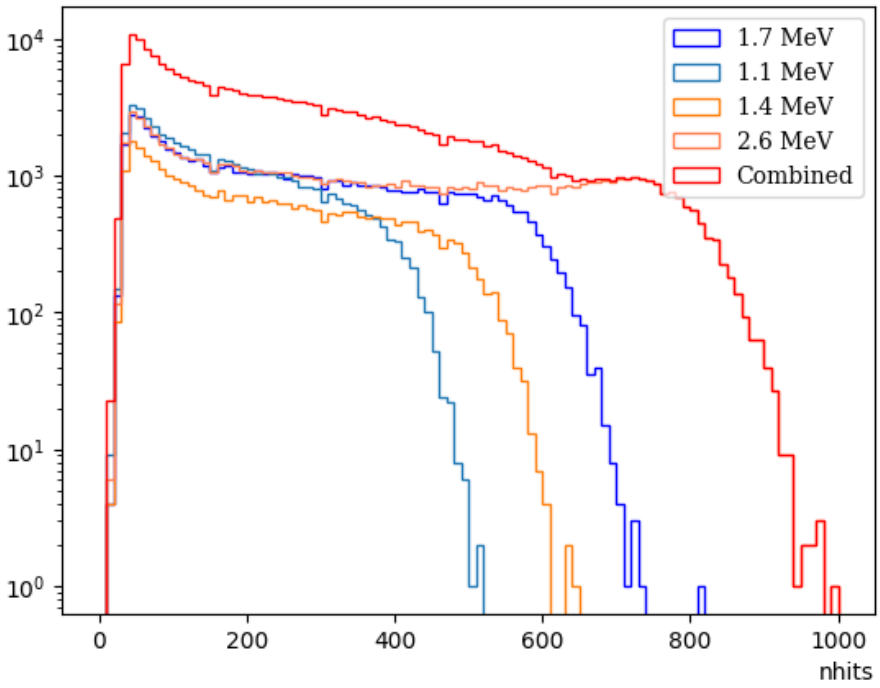

Figure 6.17: The *nhits* spectra of the four γ-particles originating from ^{214}Bi, ^{208}Tl and ^{40}K plotted on a logarithmic scale and without any radius cut. The red line represents the combined external γ-spectrum used in this analysis.

cut of 4.25 m (in arbitrary units) and grouped in three areas. The left part (area 1) shows all the combined photo-peaks from the various γ-lines, while the middle (area 2) shows a Compton scatter continuum combined with the effective Compton edges of all but the 2.61 MeV γ. Its remaining effective Compton edge populates the interval to the right (area 3). The radial behavior of this combined spectrum is investigated in the radius interval of 4.25 m to 2.5 m, where the number of γ-events per area is calculated, the results can be found in Table 6.7.

In most solar neutrino measurements Borexino has applied a trigger threshold of at least 25-30 nhits (Section 2.1.5). With SOX's higher energy window (compared to solar neutrinos), even in a conservative estimate, events below 150 nhits can safely be excluded. With only considering area 2&3 an exponential function is fitted to describe their radial behavior.

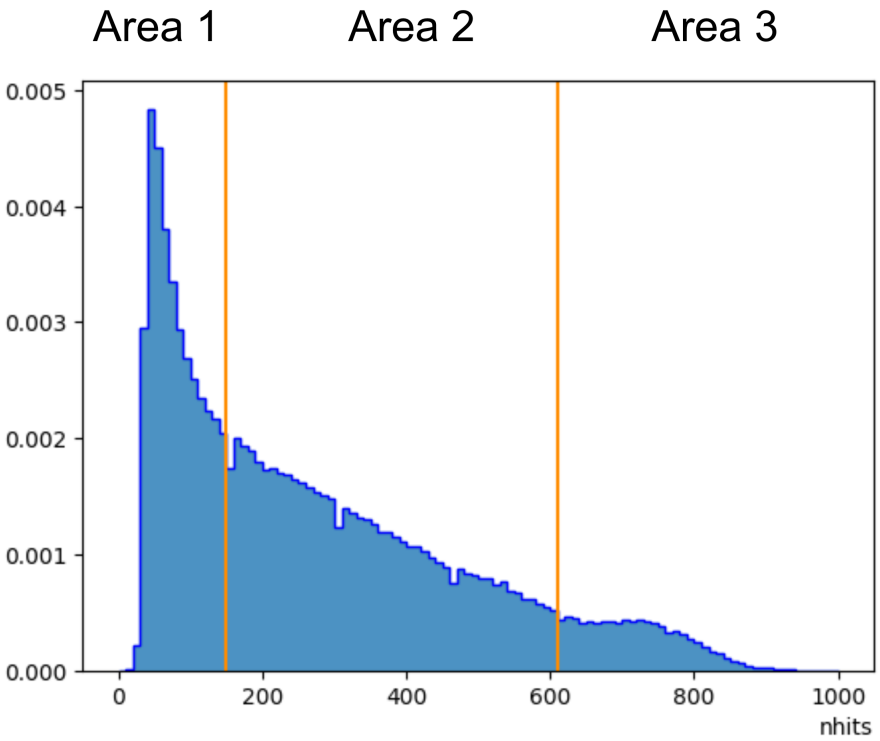

Figure 6.18: The combined γ-spectrum in the *nhits* variable for a radius cut of r = 4.25 m. The dark orange lines separate three areas, with the combined photo-peak on the left, the Compton continuum of various lines in the middle and the effective Compton edge from the 2.61 MeV line on the right.

Table 6.7: The amount of events per area for a given radius.

Radius [m]	Area 1	Area 2	Area 3	Total
4.25	28826	61791	13854	104471
4.15	21970	44276	11087	77333
4.0	13843	24959	7468	46270
3.9	10016	16578	5500	32094
3.8	7152	10615	3980	21747
3.7	5187	6575	2760	14522
3.6	3731	3887	1864	9482
3.5	2753	2170	1262	6185
3.3	1609	646	529	2784
3.0	828	96	156	1080
2.5	376	3	22	401

For a FV selection the gain in additional sensitive volume[13] has to be made with regards to the additional background. This gain in sensitive volume versus additional external background is plotted in Figure 6.19 purely for visualization. For

[13] And therefore an overall potential increase in sensitivity.

this example discussed here, it can be seen that an FV cut for a radius of about 3.9 m to 4.0 m already suppresses the external background events by a factor of 2, while only reducing the sensitive volume from 250 kg/m^3 to 200 kg/m^3.

The important ingredient for a FV selection would have been the understanding of the external background on the basis of a given energy window used in the analysis and the expected background rates of the known contributors gained by a calibration campaign [14]. Due to the end of the SOX project, this remains a proof of concept and only serves to give some ideas on how these external gamma simulations would have been fit into the analysis of the SOX experiment.

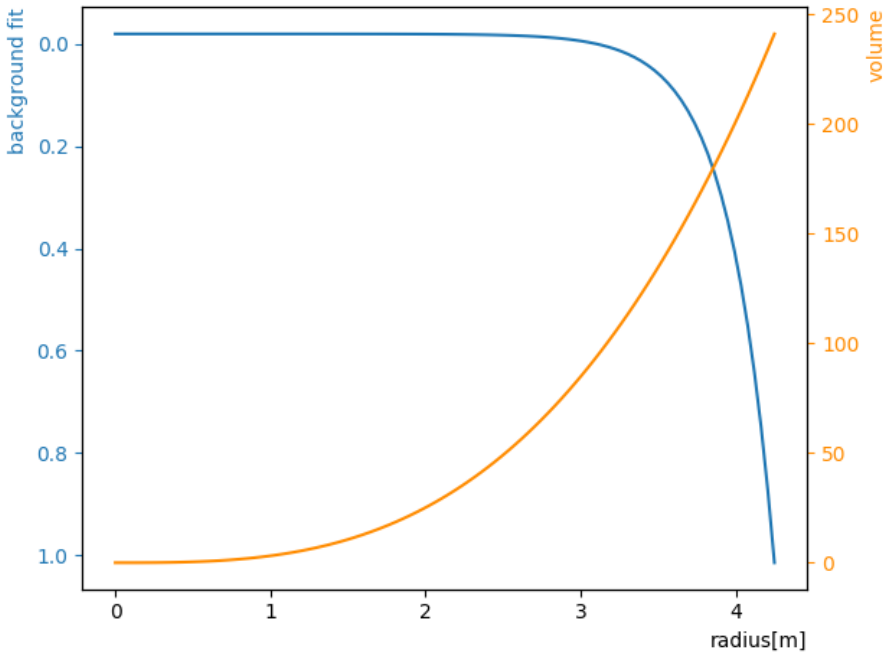

Figure 6.19: Plot comparing the external background to the scintillating volume. By fitting the combined events from area 1&2 along the radius, the exponential background fit drawn in blue is derived. On this scale it is normalized to the maximum event at 4.25 m. The scintillating volume, in kg/m^3 is drawn in dark yellow and both are compared to the radius.

[14] At the very least, recent limits could have been obtained.

6.5 Summary

In conclusion the Borexino framework together with the biasing approach is able to simulate the main external gamma contributors, whilst accounting for the vessel shape and these simulations are performed with a high efficiency.
The biasing technique, discussed during this chapter, enables the simulation of γ-events, otherwise impossible within the current computing capabilities of the cluster used for Borexino's simulation and analysis. To validate these simulations a comparison with the 2011 external calibration campaign was performed, where the resulting *nhits* (energy) and radial distributions were compared. Such a comparison is an overall test for Borexino's simulation framework and not for the biasing technique as such, due to the lack of regular (unbiased) simulations. This, within the general precision of the simulation framework's good agreement, is by itself already an achievement for the capabilities of this framework. The *BaBo* script, developed during this thesis, does not only integrate the biasing in the overall framework, it also enables to expand to different γ energies rather convenient. The simulation of a combined spectrum consisting of four γs of different energy in the previous chapter is possible thanks to this feature.

Additional work was done in simulating millions of γs in order to develop a new vessel shape fit. Because these γ-spectra are dependent on the vessel shape, this could in turn be used to reconstruct the vessel shape of future measurement periods by combining external gamma data with events from the vessel surface. To tune this vessel shape fit, γs originating from thallium and potassium were simulated for different vessel shapes. This work was not completed as the work on the new vessel shape fit method ended together with the SOX experiment.

Due to the technical aspects and principles being similar to those of other experiments (high buffer suppression, external radioactive contaminations and not unlimited computational resources), this approach and the experiences derived from it may still prove useful beyond the scope of the canceled SOX experiment.

Chapter 7

Results and Outlook

Regardless of the cancellation of the SOX experiment, a fully functioning and precise calorimeter was successfully developed by the SOX collaboration. During this thesis, contributions in the calibration of this calorimeter were made. On the hardware side, these contributions culminated in the mockup source and its integration in the calorimetric setup, including dedicated software and electronics development. During the development phase of the calorimeter and mockup, additional assistance was given in the form of thermal simulations able to predict expected temperatures and perform tests for safety concerns and material studies.

This thermal model, created with the COMSOL Multiphysics software, was able to model the system and successfully mirror observed temperatures at measurement sensors. The two most relevant temperatures being the outgoing cooling water temperature and the innermost copper sensor inside the mockup. Table 7.1 shows a comparison of the model with measurements for an energy range of 620 W to 920 W. As the expected operating range was in the 900 W regime, an overall precision of around 5% could be achieved.

Table 7.1: The precision of the mockup-calorimeter thermal model.

	620 W	700 W	900 W	920 W
Cooling water	9%	8%	3%	1%
Inner copper	27%	11%	5%	1%

Additionally, the thermal simulation was able to simulate the expected heat losses due to convection in a lower vacuum (10^{-5} to 10^{-3} mbar, see Table 7.2) and perform a safety study for the proposed 321 stainless steel alloy. This low vacuum could occur due to a turbo pump failure and was also used in order to provide an estimate to constrain the systematic loss due to convection in the range of a up to 1 W. The 321 stainless steel alloy was planned to be used for the inner cylinders holding the cerium source and the hottest point for a 1.5 kW source without specific cooling was found to be at around 490°C, which is well beyond the critical temperature of 800°C for this heat resistant stainless steel alloy.

Table 7.2: The simulated convective losses in a lower vacuum. All of these simulations were obtained with a heat profile from an accompanying measurement on this source power.

	500 W	700 W	1000 W
10^{-5} mbar	0.38 W	0.50 W	0.99 W
10^{-3} mbar	0.30 W	0.63 W	1.15 W

Due to the different energy window and FV potentially used for the SOX project, external gamma background was expected to play a bigger role than in previous solar analyses. Investigating this background and performing dedicated simulations was the focus during the second half of this thesis. An already existing biasing approach, to enable the simulation of these γs by drastically reducing computation time, was expanded and integrated into Borexino's simulation framework via a dedicated master script (*BaBo*), with the possibility to create and further widen these external gamma simulations, with minimal user interaction necessary and high computational efficiency.

To validate the capabilities of this approach combined with the Borexino simulation framework, the data from the 2011 calibration campaign was compared to the simulated source positions. This analysis investigated the radial distributions and the effective Compton edge of the 2.61 MeV γ-spectrum from thallium-208. Figure 7.1 shows the agreement between simulation and the calibration data.

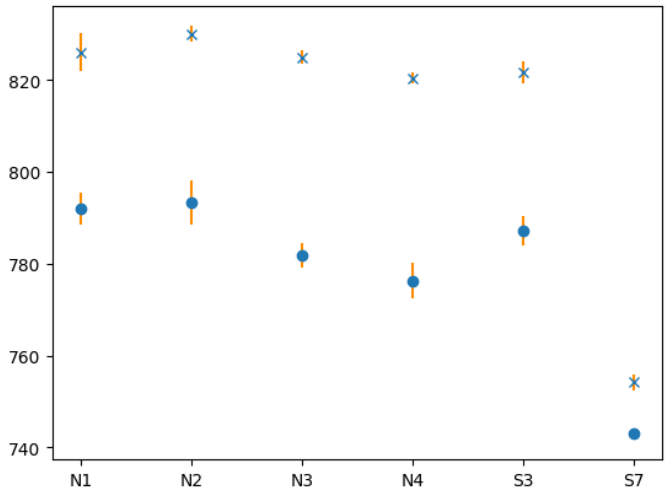

Figure 7.1: The effective Compton edge position per source location, obtained by comparing the means of Gaussian fits performed for data (plotted as X) and for simulation (dots).

In a second step, a combined spectrum of known gamma contributors was build and its impact on different radii tested, in order to serve as a proof of concept and illustrate on how these external gamma simulations could have assisted in the selection of a suitable FV for SOX.

The end of the SOX experiment does not mark the end in the search for sterile neutrinos or in the push towards resolving recent experimental anomalies. Quite the contrary as a multitude of running and planned experiments aim to provide new data on short baseline neutrino oscillations, such as DANSS [38], STEREO [40] and SoLiD [80], to name only a few. They are truly needed as the situation has gotten even more confusing, compared to the state presented in Section 1.5 during the time of writing of this thesis. New data from the MiniBooNE experiment claimed a new excess of electron neutrinos suggesting a fourth neutrino [84] and the Neutrino-4 experiment [104] suggests also an additional sterile neutrino, but with best fit parameters in tension to other experiments. Not only were the outcomes of these two recent publications received critically by the community [71], but they are also in violation to the limits obtained from the IceCube experiments [68],[51].

As it stands now, the mysteries around these anomalies are still not revealed. A look at the grand picture suggests that even with an additional sterile neutrino, not all of these deviations can be explained fully [78]. This could mean an overall rethinking of neutrino oscillations as we know it might become necessary, potentially including a new neutrino flavor. The exiting conclusion at this point is that Pauli's original ghost particle still refuses to give up all its secrets, at least for the moment.

Attachment

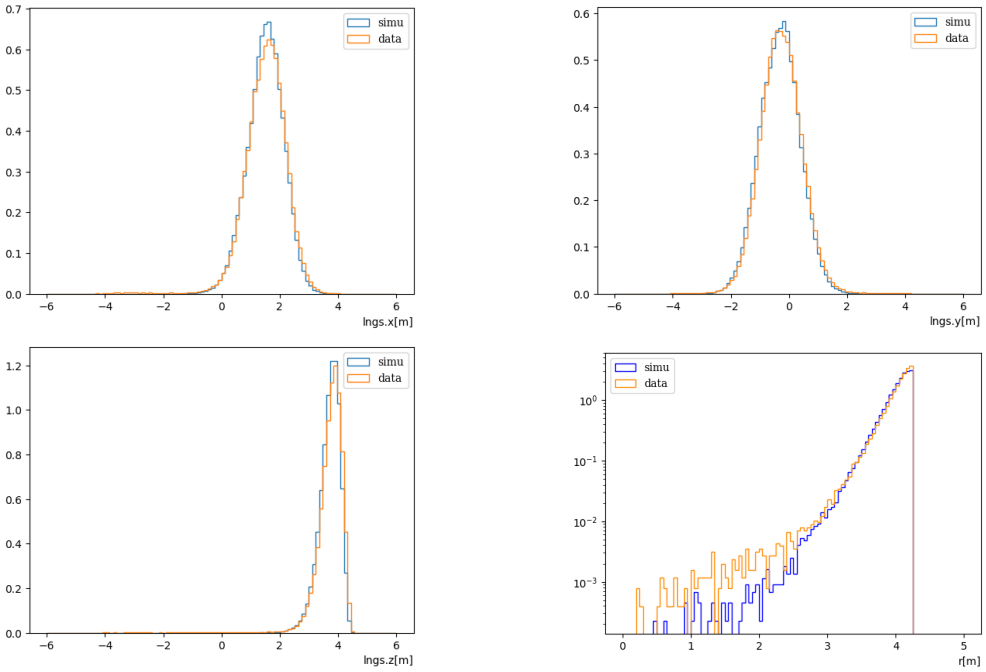

Figure 7.2: N1 comparison

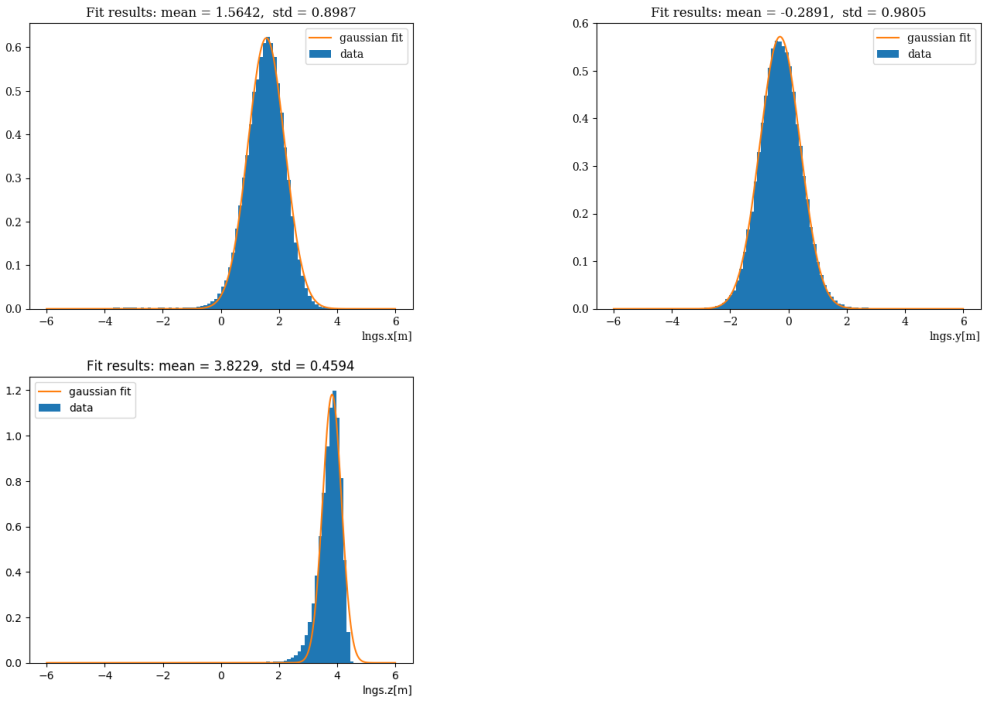

Figure 7.3: N1 data fits

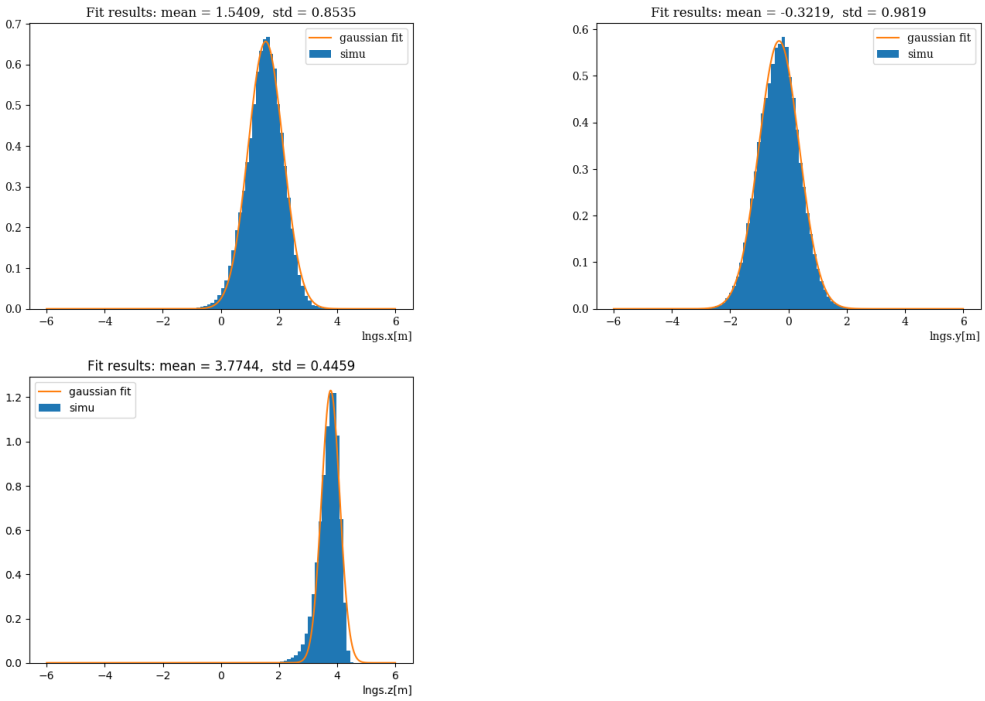

Figure 7.4: N1 simulation fits

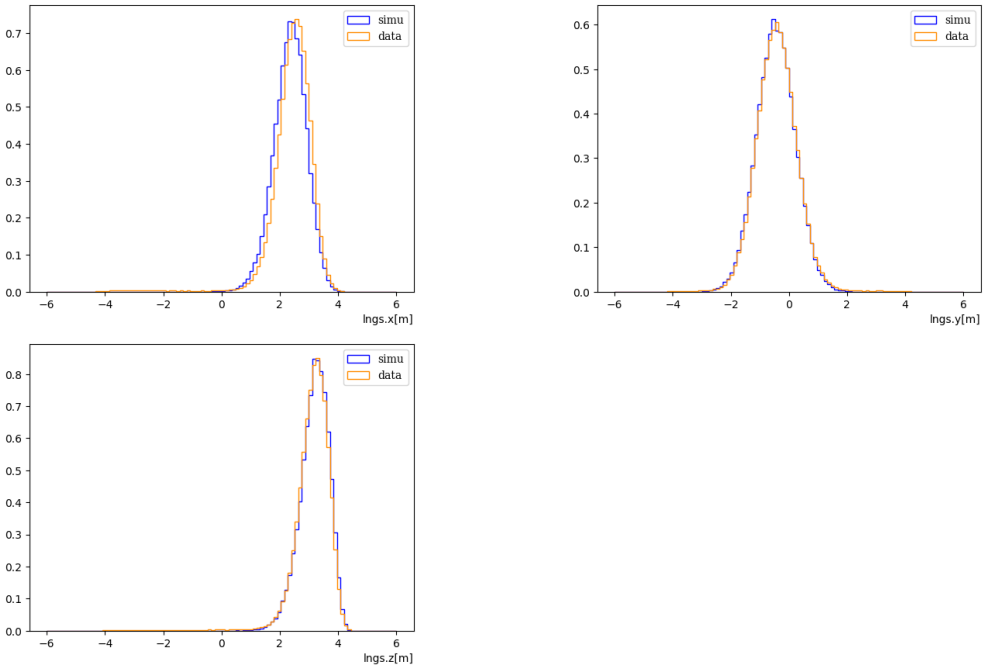

Figure 7.5: N2 comparison

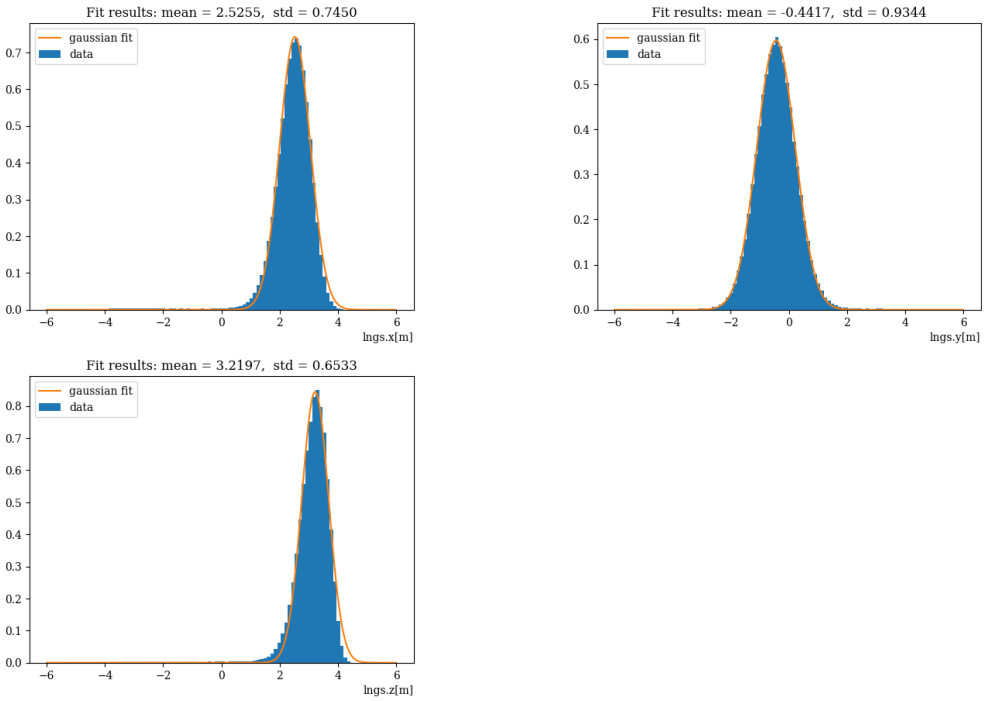

Figure 7.6: N2 data fits

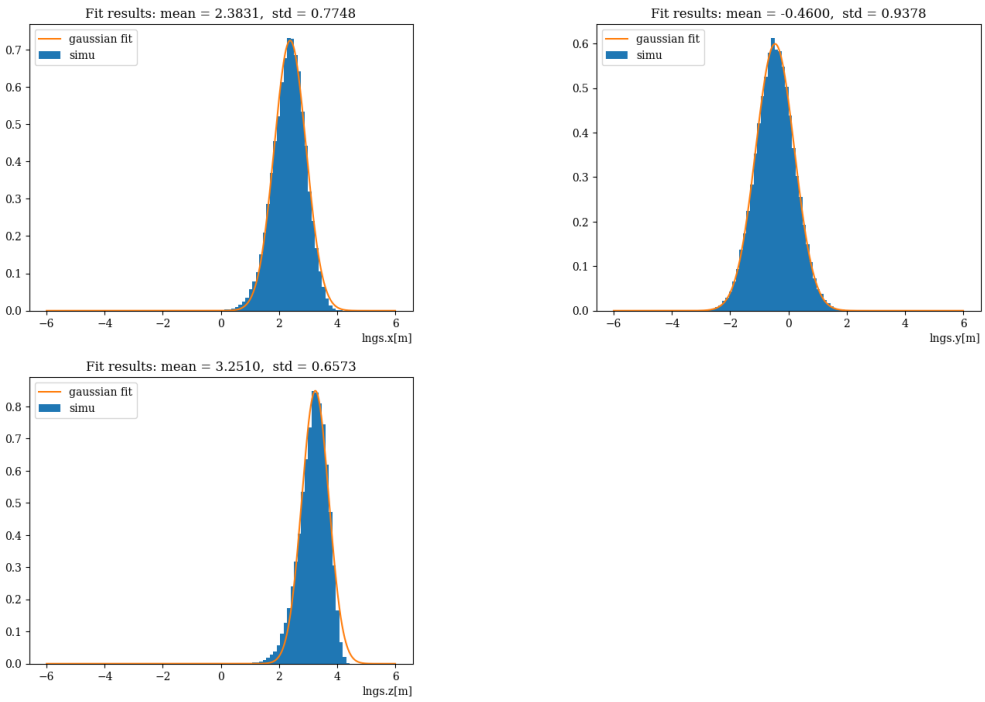

Figure 7.7: N2 simulation fits

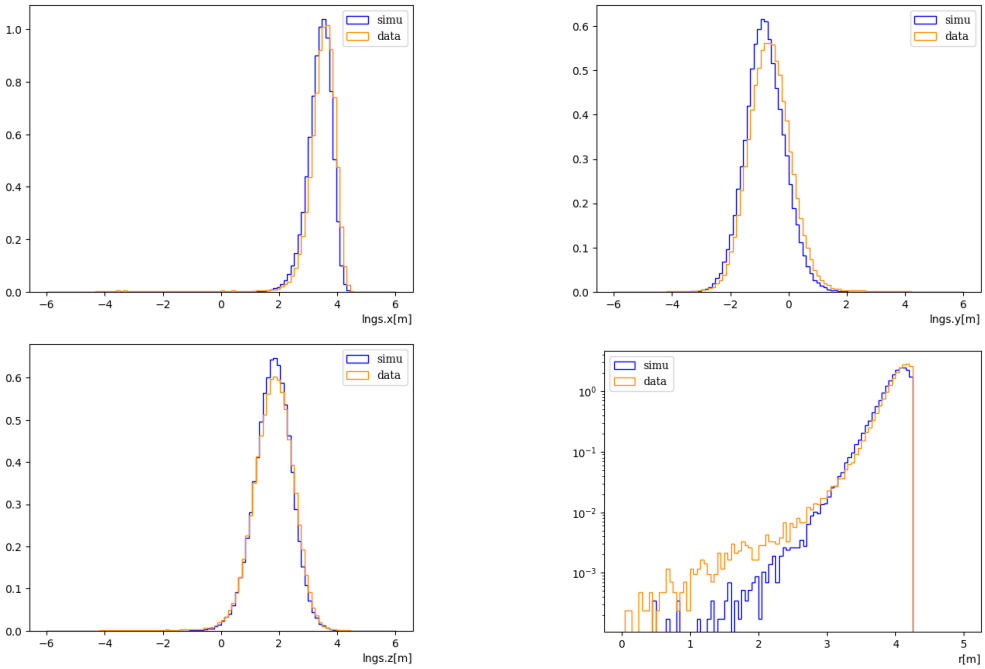

Figure 7.8: N3 comparison

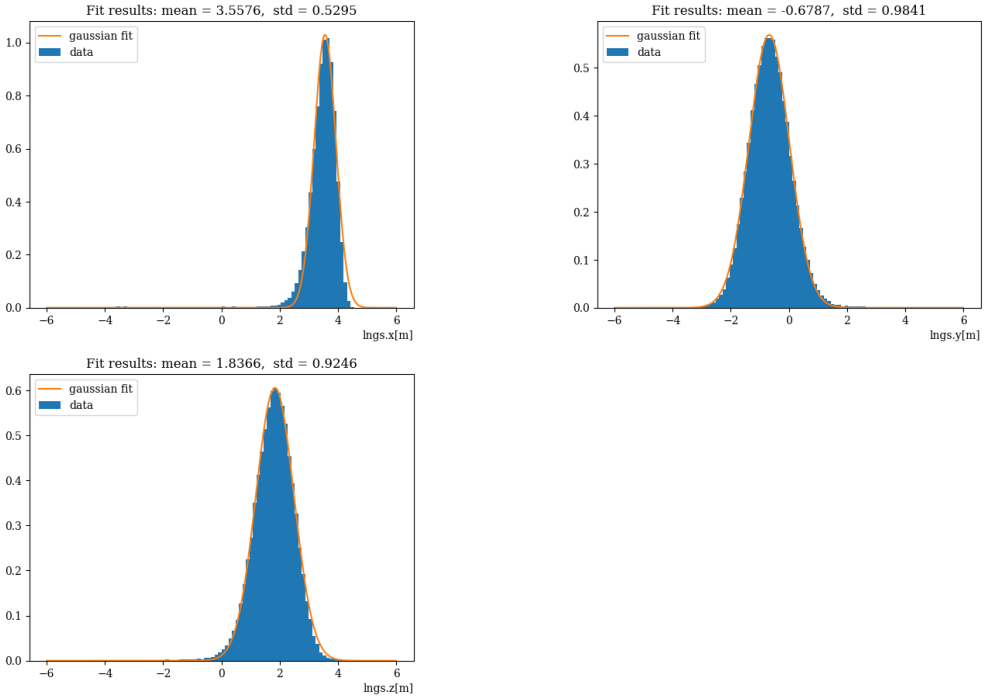

Figure 7.9: N3 data fits

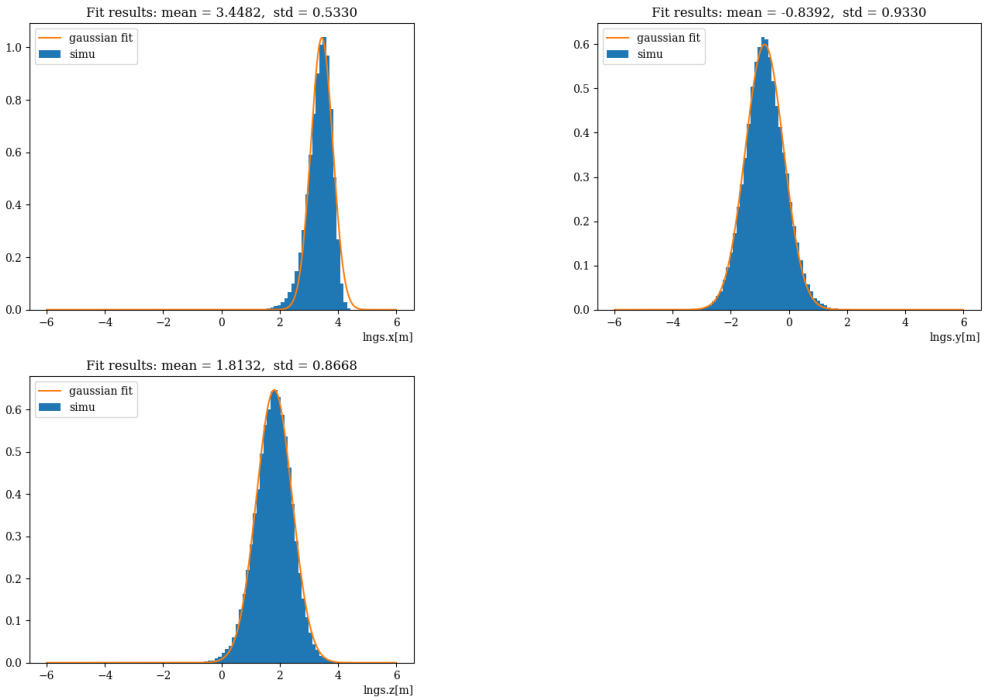

Figure 7.10: N3 simulation fits

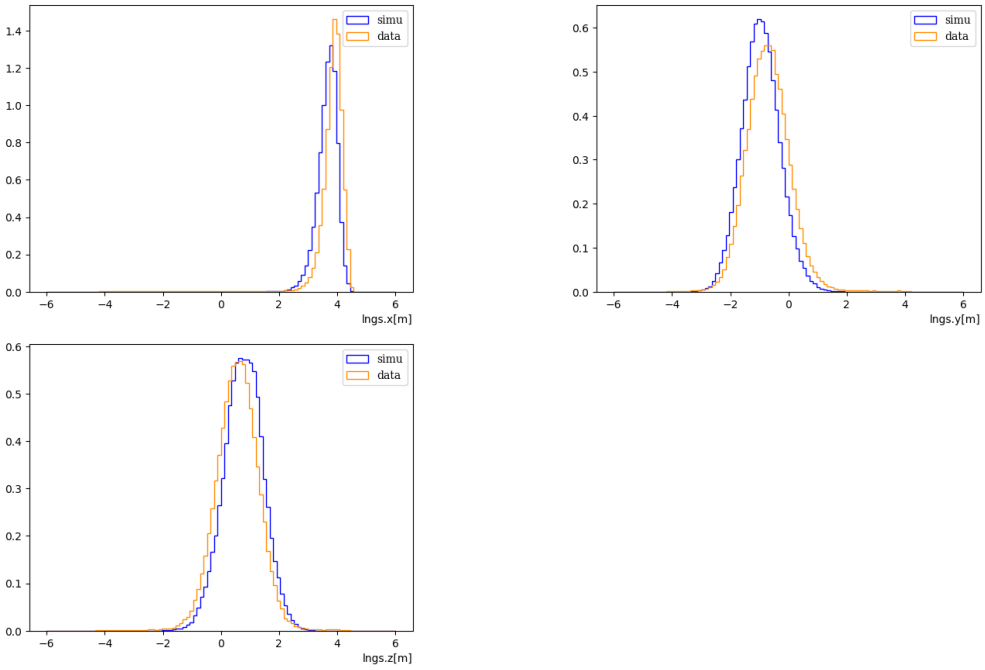

Figure 7.11: N4 comparison

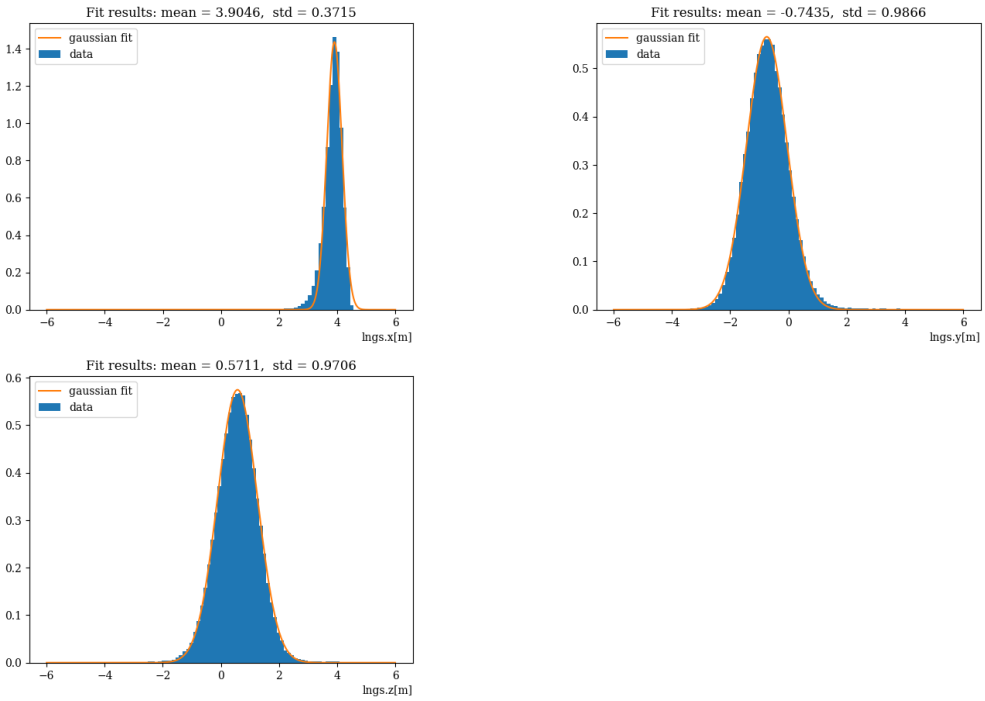

Figure 7.12: N4 data fits

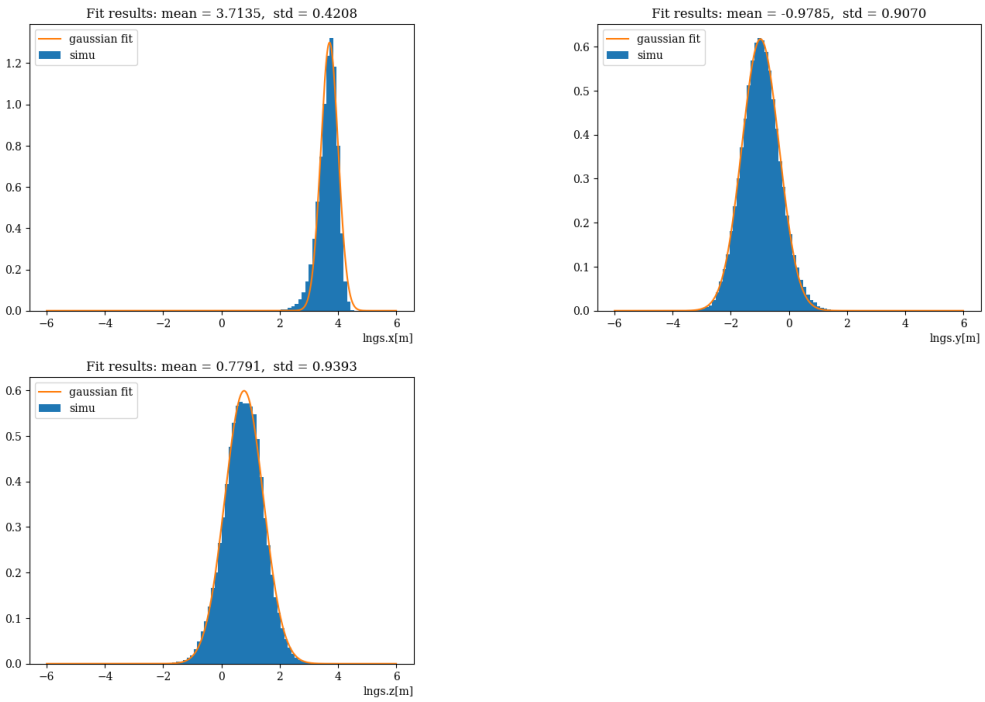

Figure 7.13: N4 simulation fits

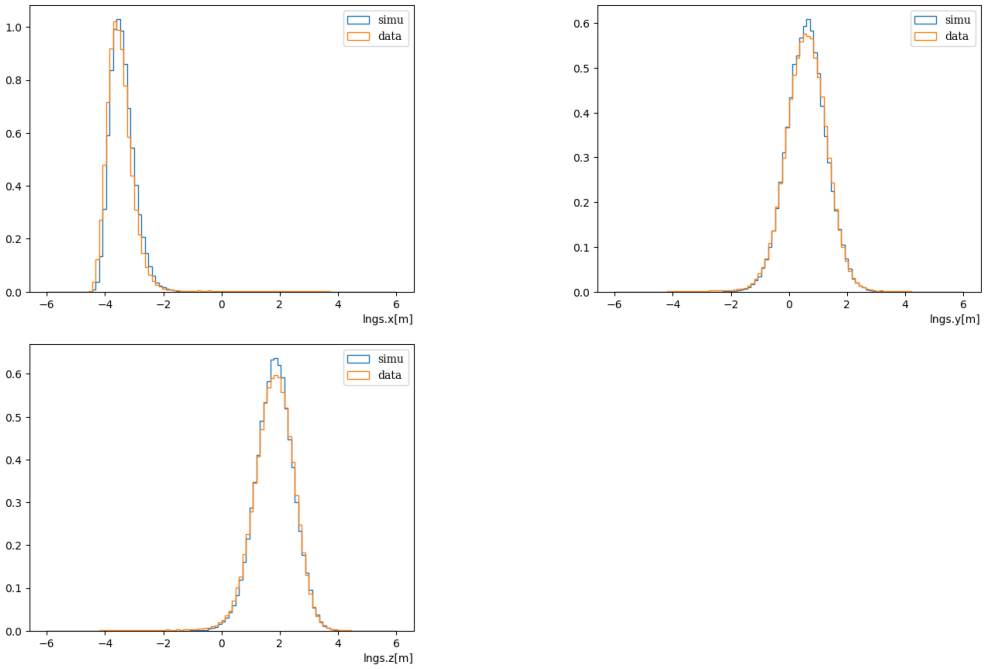

Figure 7.14: S3 comparison

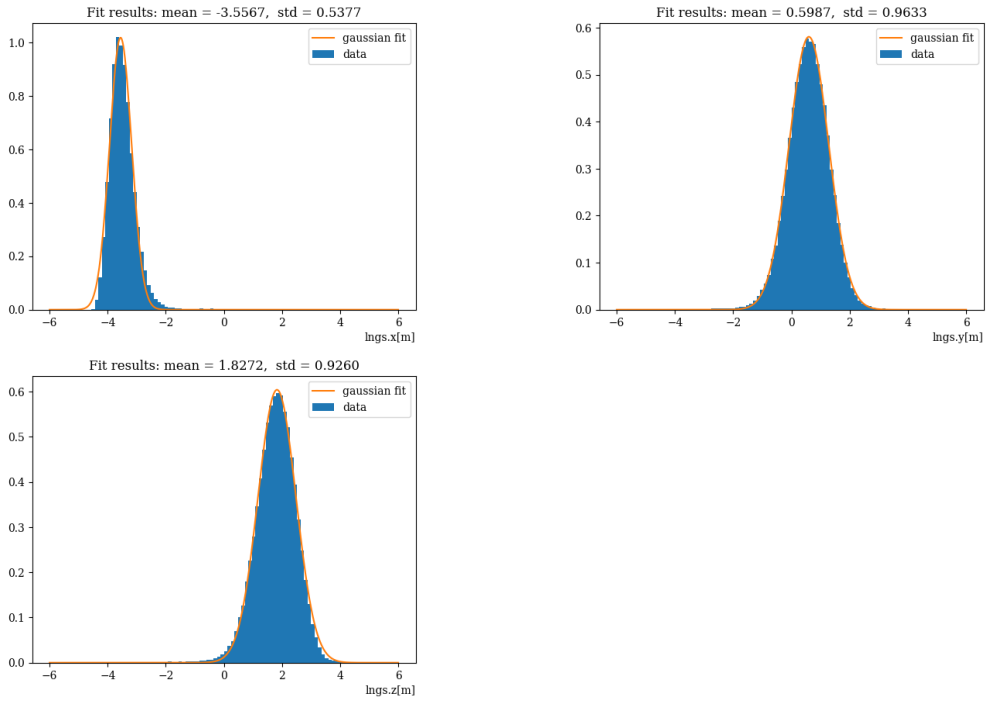

Figure 7.15: S3 data fits

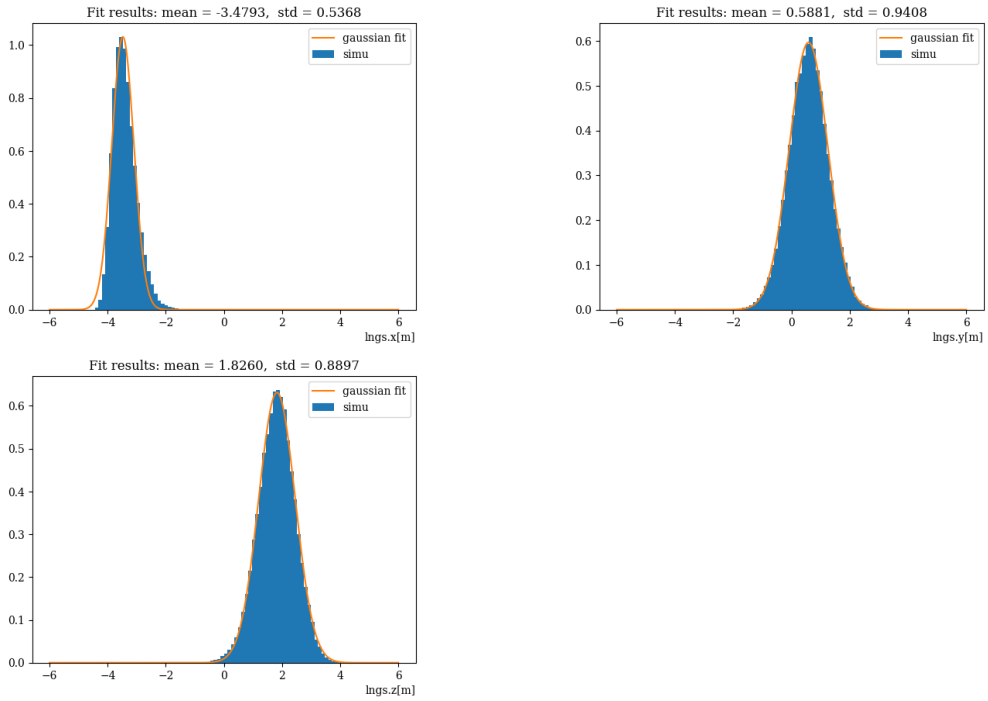

Figure 7.16: S3 simulation fits

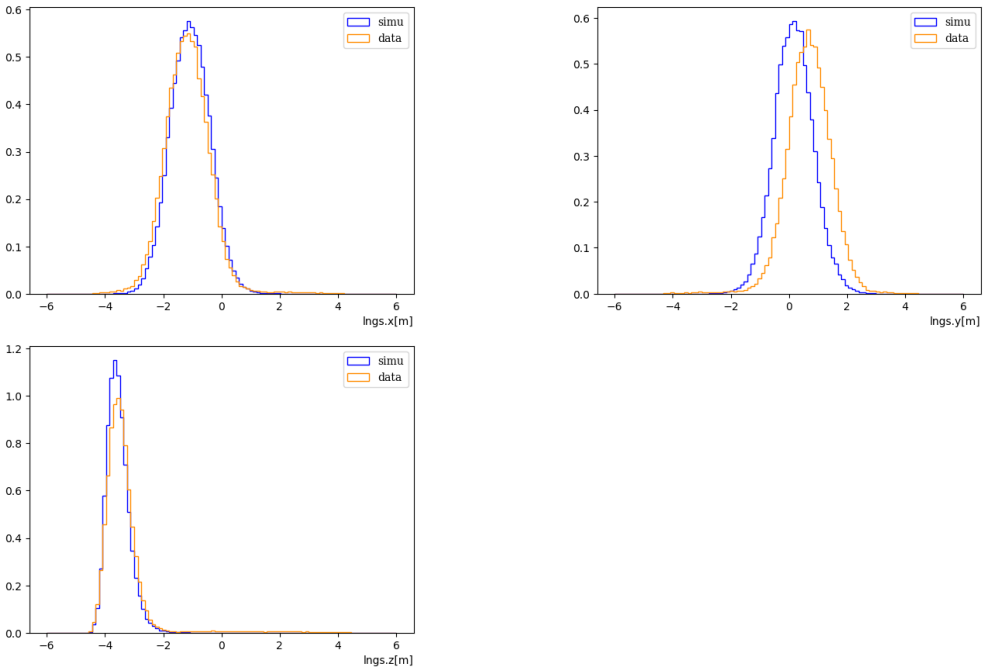

Figure 7.17: S7 comparison

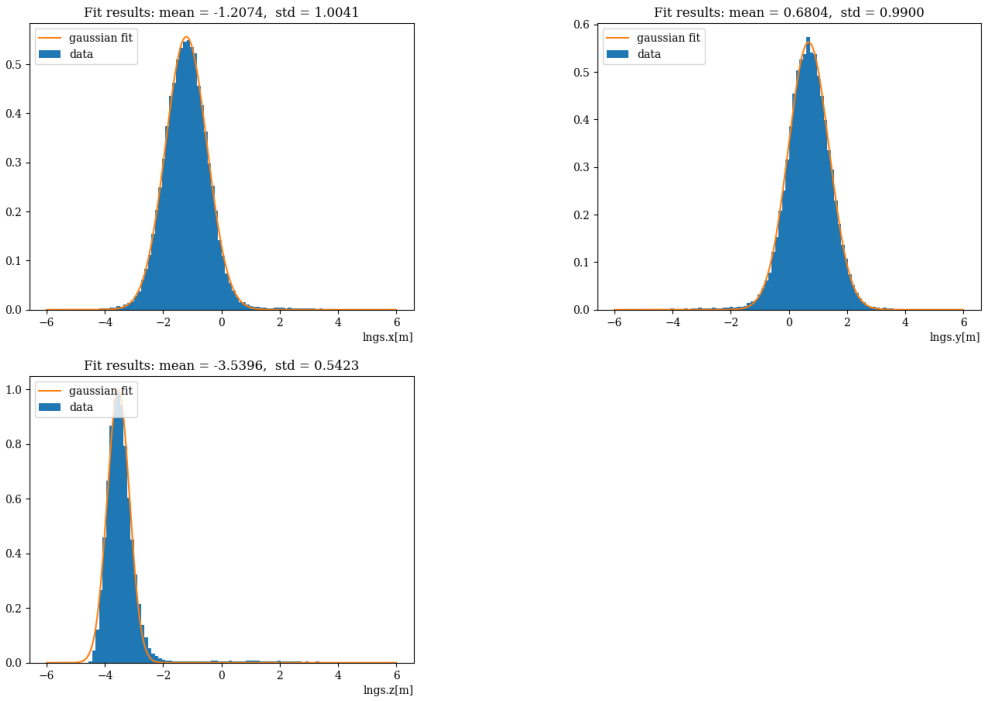

Figure 7.18: S7 data fits

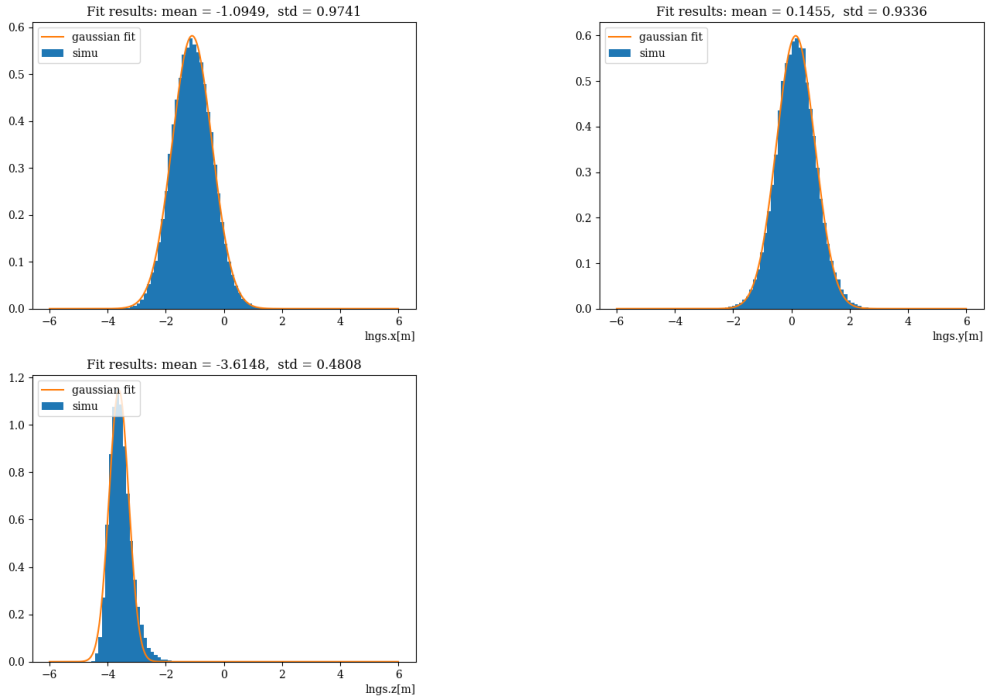

Figure 7.19: S7 simulation fits

List of Figures

List of Tables

Bibliography

[1] K. N. et all Abazajian. Light Sterile Neutrinos: A White Paper. *ArXiv e-prints*, April 2012. 11

[2] Nuclear 'accident' sends radioactive pollution over Europe. *Radioactive Cloud Europe*, (accessed August 22, 2018). URL https://www.telegraph.co.uk/news/2017/11/10/harmless-radioactive-cloud-europe-may-have-come-nuclear-accident/. 49

[3] M. Agostini et al. Improved measurement of 8B solar neutrinos with 1.5 kt y of Borexino exposure. 2017. 38, 120

[4] A. et al. Aguilar. Evidence for Neutrino Oscillations from the Observation of Electron Anti-neutrinos in a Muon Anti-Neutrino Beam. Phys. Rev. D, 64 (11):112007, December 2001. doi: 10.1103/PhysRevD.64.112007. 14, 15

[5] M. H. for the KSK Collaboration Ahn. Measurement of neutrino oscillation by the k2k experiment. *Phys. Rev. D*, 74:072003, Oct 2006. doi: 10.1103/PhysRevD.74.072003. URL https://link.aps.org/doi/10.1103/PhysRevD.74.072003. 8

[6] K. Altenmüller et al. A calorimeter for the precise determination of the activity of the 144 ce- 144 pr anti-neutrino source in the sox experiment. *Journal of Instrumentation*, 13:P09008–P09008, 09 2018. doi: 10.1088/1748-0221/13/09/P09008. 63, 64, 65, 66, 67

[7] F. P. An, Q. An, J. Z. Bai, A. B. Balantekin, H. R. Band, W. Beriguete, M. Bishai, S. Blyth, R. L. Brown, G. F. Cao, and et al. Improved measurement of electron antineutrino disappearance at Daya Bay. *Chinese Physics C*, 37 (1):011001, January 2013. doi: 10.1088/1674-1137/37/1/011001. 8

[8] H. Back et al. Borexino calibrations: Hardware, methods, and results. *Journal of Instrumentation*, 7:P10018, 10 2012. doi: 10.1088/1748-0221/7/10/P10018. 35

[9] John N. Bahcall, Neta A. Bahcall, and Giora Shaviv. Present status of the theoretical predictions for the ^{37}Cl solar-neutrino experiment. *Phys. Rev. Lett.*, 20:1209–1212, May 1968. doi: 10.1103/PhysRevLett.20.1209. URL https://link.aps.org/doi/10.1103/PhysRevLett.20.1209. 7

[10] John N. Bahcall, Marc Kamionkowski, and Alberto Sirlin. Solar neutrinos: Radiative corrections in neutrino-electron scattering experiments. *Phys. Rev. D*, 51:6146–6158, Jun 1995. doi: 10.1103/PhysRevD.51.6146. URL https://link.aps.org/doi/10.1103/PhysRevD.51.6146. 20

[11] A. Bellerive, J. R. Klein, A. B. McDonald, A. J. Noble, and A. W. P. Poon. The Sudbury Neutrino Observatory. *Nuclear Physics B*, 908:30–51, July 2016. doi: 10.1016/j.nuclphysb.2016.04.035. 8

[12] G. Bellini, L. Ludhova, G. Ranucci, and F. L. Villante. Neutrino oscillations. *ArXiv e-prints*, October 2013. 8

[13] S. Bilenky. Neutrino oscillations: From a historical perspective to the present status. *Nuclear Physics B*, 908:2–13, July 2016. doi: 10.1016/j.nuclphysb.2016.01.025. 8

[14] J.B. Birks. *The Theory and Practice of Scintillation Counting*. International series of monographs on electronics and instrumentation. Pergamon Press, 1964. URL https://books.google.de/books?id=02MMogEACAAJ. 22

[15] A. et al. Bolshakova. Revisiting the LSND anomaly. I. Impact of new data. Phys. Rev. D, 85(9):092008, May 2012. doi: 10.1103/PhysRevD.85.092008. 14

[16] A. et al. Bolshakova. Revisiting the LSND anomaly. II. Critique of the data analysis. Phys. Rev. D, 85(9):092009, May 2012. doi: 10.1103/PhysRevD.85.092009. 14

[17] BOREXINO Collaboration. Measurements of extremely low radioactivity levels in BOREXINO. *Astroparticle Physics*, 18:1–25, August 2002. 95, 96, 126

[18] BOREXINO Collaboration. The Borexino detector at the Laboratori Nazionali del Gran Sasso. *Nuclear Instruments and Methods in Physics Research A*, 600:568–593, March 2009. doi: 10.1016/j.nima.2008.11.076. 17, 19, 20, 22, 23, 28, 29, 30, 33, 34

[19] Borexino collaboration. Borexino calibrations: Hardware, Methods, and Results. *ArXiv e-prints*, July 2012. 99, 100

[20] Borexino Collaboration. SOX: Short distance neutrino Oscillations with BoreXino. *ArXiv e-prints*, April 2013. 16, 42, 43, 44, 45

[21] Borexino Collaboration. Final results of Borexino Phase-I on low energy solar neutrino spectroscopy. *ArXiv e-prints*, August 2013. 8, 17, 21, 23, 30, 31, 36, 88, 89, 91, 92, 93, 105

[22] BOREXINO Collaboration. Spectroscopy of geo-neutrinos from 2056 days of Borexino data. *ArXiv e-prints*, June 2015. 40

[23] BOREXINO Collaboration. The Main Results of the Borexino Experiment. *ArXiv e-prints*, May 2016. 36, 39, 41

[24] BOREXINO Collaboration. The Monte Carlo simulation of the Borexino detector. *Astroparticle Physics*, 97:136–159, January 2018. doi: 10.1016/j.astropartphys.2017.10.003. 24, 95, 105, 106, 107, 120

[25] L. M. Brown. The idea of the neutrino. *Physics Today*, 31:23–28, September 1978. doi: 10.1063/1.2995181. 4

[26] Alessio Caminata. *Internal documents, private conversations*. 35, 122

[27] J. Chadwick. Possible Existence of a Neutron. Nature, 129:312, February 1932. doi: 10.1038/129312a0. 5

[28] G. et al. Cheng. Dual baseline search for muon antineutrino disappearance. Phys. Rev. D, 86(5):052009, September 2012. doi: 10.1103/PhysRevD.86.052009. 14

[29] Borexino Collaboration. Limiting neutrino magnetic moments with borexino phase-ii solar neutrino data. *Physical Review D*, 96, 11 2017. doi: 10.1103/PhysRevD.96.091103. 40

[30] Borexino Collaboration. Modulations of the cosmic muon signal in ten years of borexino data. *To be puplished - JCAP*, 2019. 40

[31] Borexino Collaboration. *Borexino SSS fully filled with water (viewed from camera 4)*, 21.12.2006 (accessed April 08, 2018). URL http://borex.lngs.infn.it/pictures/Borexino/SSS_H2O_full-c7.jpg. 25

[32] Borexino Collaboration. *A view of the Borexino vessels (gas) inflated.*, 21.12.2006 (accessed April 08, 2018). URL http://borex.lngs.infn.it/pictures/Borexino/inflated_vessels-1082.jpg. 25

[33] Borexino / SOX Collaboration. *Press release detailing the end of the SOX experiment*, 1.2.2018 (accessed April 25, 2018). URL https://www.lngs.infn.it/en/news/nota-stampa-esperimento-sox. 42, 46

[34] Double Chooz Collaboration. Improved measurements of the neutrino mixing angle θ_{13} with the Double Chooz detector. *Journal of High Energy Physics*, 10:86, October 2014. doi: 10.1007/JHEP10(2014)086. 8

[35] MiniBooNE Collaboration. Event excess in the miniboone search for $\overline{\nu}_\mu \rightarrow \overline{\nu}_e$ oscillations. *Phys. Rev. Lett.*, 105:181801, Oct 2010. doi: 10.1103/PhysRevLett.105.181801. URL https://link.aps.org/doi/10.1103/PhysRevLett.105.181801. 15

[36] RENO Collaboration. Observation of reactor electron antineutrinos disappearance in the reno experiment. *Phys. Rev. Lett.*, 108:191802, May 2012. doi: 10.1103/PhysRevLett.108.191802. URL https://link.aps.org/doi/10.1103/PhysRevLett.108.191802. 8

[37] SOX Collaboration. Cesox: An experimental test of the sterile neutrino hypothesis with borexino. *Journal of Physics: Conference Series*, 934(1):012003, 2017. URL http://stacks.iop.org/1742-6596/934/i=1/a=012003. 46

[38] The DANSS Collaboration. Search for sterile neutrinos at the DANSS experiment. *Physics Letters B*, 787:56–63, December 2018. doi: 10.1016/j.physletb.2018.10.038. 133

[39] The Daya Bay collaboration. Evolution of the Reactor Antineutrino Flux and Spectrum at Daya Bay. *Physical Review Letters*, 118(25):251801, June 2017. doi: 10.1103/PhysRevLett.118.251801. 15

[40] The STEREO Collaboration. The STEREO Experiment. *Journal of Instrumentation*, 13:P07009, July 2018. doi: 10.1088/1748-0221/13/07/P07009. 133

[41] J. M. Conrad and M. H. Shaevitz. Sterile Neutrinos: An Introduction to Experiments. *ArXiv e-prints*, September 2016. 14

[42] C. L. Cowan, Jr., F. Reines, F. B. Harrison, H. W. Kruse, and A. D. McGuire. Detection of the Free Neutrino: A Confirmation. *Science*, 124:103–104, July 1956. doi: 10.1126/science.124.3212.103. 6

[43] G. Danby, J-M. Gaillard, K. Goulianos, L. M. Lederman, N. Mistry, M. Schwartz, and J. Steinberger. Observation of high-energy neutrino reactions and the existence of two kinds of neutrinos. *Phys. Rev. Lett.*, 9:36–44, Jul 1962. doi: 10.1103/PhysRevLett.9.36. URL https://link.aps.org/doi/10.1103/PhysRevLett.9.36. 7

[44] R. Davis. Nobel Lecture: A half-century with solar neutrinos. *Rev. Mod. Phys.*, 75:985–994, 2003. doi: 10.1103/RevModPhys.75.985. 7

[45] Raymond Davis, Jr., Don S. Harmer, and Kenneth C. Hoffman. Search for neutrinos from the sun. *Phys. Rev. Lett.*, 20:1205–1209, 1968. doi: 10.1103/PhysRevLett.20.1205. 7

[46] P. F. de Salas, D. V. Forero, C. A. Ternes, M. Tortola, and J. W. F. Valle. Status of neutrino oscillations 2017. *ArXiv e-prints*, August 2017. 8, 12

[47] Deutschlandfunk. *Ruthenium-Wolke ueber Europa*. 48

[48] DONUT Collaboration. Observation of tau neutrino interactions. *Physics Letters B*, 504:218–224, April 2001. doi: 10.1016/S0370-2693(01)00307-0. 8

[49] M. Dressel. Geometrical importance sampling in Geant4: from design to verification. December 2003. 108, 110

[50] C. D. Ellis and W. A. Wooster. The average energy of disintegration of radium e. *Proceedings of the Royal Society of London A: Mathematical, Physical and Engineering Sciences*, 117(776):109–123, 1927. ISSN 0950-1207. doi: 10.1098/rspa.1927.0168. URL http://rspa.royalsocietypublishing.org/content/117/776/109. 4

[51] A. Esmaili and H. Nunokawa. On the robustness of IceCube's bound on sterile neutrinos in the presence of non-standard interactions. *ArXiv e-prints*, October 2018. 133

[52] Adamson et al. Measurement of the Neutrino Mass Splitting and Flavor Mixing by MINOS. *Physical Review Letters*, 106(18):181801, May 2011. doi: 10.1103/PhysRevLett.106.181801. 8

[53] Beringer et al. Review of particle physics. *Phys. Rev. D*, 86:010001, Jul 2012. doi: 10.1103/PhysRevD.86.010001. URL https://link.aps.org/doi/10.1103/PhysRevD.86.010001. 11

[54] E. Fermi. Versuch einer Theorie der β-Strahlen. I. *Zeitschrift fur Physik*, 88: 161–177, March 1934. doi: 10.1007/BF01351864. 6

[55] E. Fermi. Tentativo di una Teoria Dei Raggi β. *Il Nuovo Cimento*, 11:1–19, January 1934. doi: 10.1007/BF02959820. 6

[56] J. A. Formaggio and J. Barrett. Resolving the reactor neutrino anomaly with the KATRIN neutrino experiment. *Physics Letters B*, 706:68–71, November 2011. doi: 10.1016/j.physletb.2011.10.069. 11

[57] S. J. et al. Freedman. A new detector for solar neutrino. *Nuclear Physics B Proceedings Supplements*, 23:159–169, July 1991. doi: 10.1016/0920-5632(91)90044-F. 17

[58] Y. et al. Fukuda. Evidence for Oscillation of Atmospheric Neutrinos. *Physical Review Letters*, 81:1562–1567, August 1998. doi: 10.1103/PhysRevLett.81.1562. 7

[59] Geant4 lecture. *Geant4 - Additional Capabilities*, (accessed November 6, 2018). URL https://www.ge.infn.it/geant4/training/portland/additionalCapabilities.pdf. 108

[60] M. Goldhaber, L. Grodzins, and A. W. Sunyar. Helicity of neutrinos. *Phys. Rev.*, 109:1015–1017, Feb 1958. doi: 10.1103/PhysRev.109.1015. URL https://link.aps.org/doi/10.1103/PhysRev.109.1015. 7

[61] M. C. Gonzalez-Garcia, M. Maltoni, and T. Schwetz. Updated fit to three neutrino mixing: status of leptonic CP violation. *Journal of High Energy Physics*, 11:52, November 2014. doi: 10.1007/JHEP11(2014)052. 11

[62] W. et al. Hampel. GALLEX solar neutrino observations: results for GALLEX IV. *Physics Letters B*, 447:127–133, February 1999. doi: 10.1016/S0370-2693(98)01579-2. 7

[63] W. C. Haxton, R. G. Hamish Robertson, and A. M. Serenelli. Solar Neutrinos: Status and Prospects. ARA&A, 51:21–61, August 2013. doi: 10.1146/annurev-astro-081811-125539. 38

[64] K. S. et al. Hirata. Observation of ^{8}B solar neutrinos in the kamiokande-ii detector. *Phys. Rev. Lett.*, 63:16–19, Jul 1989. doi: 10.1103/PhysRevLett.63.16. URL https://link.aps.org/doi/10.1103/PhysRevLett.63.16. 7

[65] P. Huber. Determination of antineutrino spectra from nuclear reactors. Phys. Rev. C, 84(2):024617, August 2011. doi: 10.1103/PhysRevC.84.024617. 15

[66] T. Huebner, U. Martens, J. Walowski, M. Münzenberg, A. Thomas, G. Reiss, and T. Kuschel. Thermal conductivity of thin insulating films determined by tunnel magneto-Seebeck effect measurements and finite-element modeling. *Journal of Physics D Applied Physics*, 51(22):224006, June 2018. doi: 10.1088/1361-6463/aabfb3. 68

[67] IceCube Collaboration, M. G. Aartsen, M. Ackermann, J. Adams, J. A. Aguilar, M. Ahlers, M. Ahrens, I. A. Samarai, D. Altmann, K. Andeen, and et al. Neutrinos and Cosmic Rays Observed by IceCube. *ArXiv e-prints*, January 2017. 8

[68] IceCube Collaboration, M. G. Aartsen, M. Ackermann, J. Adams, J. A. Aguilar, M. Ahlers, M. Ahrens, I. A. Samarai, D. Altmann, K. Andeen, and et al. Search for sterile neutrino mixing using three years of IceCube DeepCore data. *ArXiv e-prints*, February 2017. 133

[69] K. Ichimura and for the KamLAND Collaboration. Recent Results from KamLAND. *ArXiv e-prints*, October 2008. 8

[70] National Nuclear Data Center (NNDC) in Brookhaven National Laboratory. *NuDat 2*, (accessed December 21, 2018). URL https://www.nndc.bnl.gov/nudat2/chartNuc.jsp. 126

[71] J. R. Jordan, Y. Kahn, G. Krnjaic, M. Moschella, and J. Spitz. Severe Constraints on New Physics Explanations of the MiniBooNE Excess. *ArXiv e-prints*, October 2018. 133

[72] J. Kopp, P. A. N. Machado, M. Maltoni, and T. Schwetz. Sterile neutrino oscillations: the global picture. *Journal of High Energy Physics*, 5:50, May 2013. doi: 10.1007/JHEP05(2013)050. 13

[73] A. T. Korsakov and E. G. Tertyshnik. Krypton-85 in the atmosphere. *ArXiv e-prints*, July 2013. 90

[74] Thierry Lassere. *Internal document*. 47, 48, 52, 53, 54

[75] LNGS. *The LNGS Laboratory*, (accessed April 08, 2018). URL https://www.lngs.infn.it/images/About/lngs_FA.jpg. 18

[76] LNGS. *The LNGS Laboratory Underground*, (accessed April 08, 2018). URL https://www.lngs.infn.it/images/photogallery/mappa_lngs_en.jpg. 18

[77] Z. Maki, M. Nakagawa, and S. Sakata. Remarks on the Unified Model of Elementary Particles. *Progress of Theoretical Physics*, 28:870–880, November 1962. doi: 10.1143/PTP.28.870. 8

[78] Michele Maltoni. Sterile Neutrinos the Global Picture, Jun 2018. 133

[79] W. Maneschg, L. Baudis, R. Dressler, K. Eberhardt, R. Eichler, H. Keller, R. Lackner, B. Praast, R. Santorelli, J. Schreiner, M. Tarka, B. Wiegel, and A. Zimbal. Production and characterization of a custom-made 228th source with reduced neutron source strength for the borexino experiment. *Nuclear Instruments and Methods in Physics Research Section A: Accelerators, Spectrometers, Detectors and Associated Equipment*, 680:161 – 167, 2012. ISSN 0168-9002. doi: https://doi.org/10.1016/j.nima.2012.04.019. URL http://www.sciencedirect.com/science/article/pii/S0168900212003749. 99, 100

[80] L. Manzanillas. Status of the SoLid experiment: Search for sterile neutrinos at the SCK·CEN BR2 reactor. *ArXiv e-prints*, October 2017. 133

[81] Johann Martyn. *Internal documents - Resistance Measurement of Cartridge Heaters*. 60

[82] L. Meitner and W. Orthmann. *Zeitschrifft f. Physik*, Band 60:143, 1930. 4

[83] G. Mention, M. Fechner, T. Lasserre, T. A. Mueller, D. Lhuillier, M. Cribier, and A. Letourneau. Reactor antineutrino anomaly. Phys. Rev. D, 83(7): 073006, April 2011. doi: 10.1103/PhysRevD.83.073006. 15, 16

[84] MiniBooNE Collaboration. Significant Excess of ElectronLike Events in the MiniBooNE Short-Baseline Neutrino Experiment. *ArXiv e-prints*, May 2018. 133

[85] T. A. Mueller, D. Lhuillier, M. Fallot, A. Letourneau, S. Cormon, M. Fechner, L. Giot, T. Lasserre, J. Martino, G. Mention, A. Porta, and F. Yermia. Improved predictions of reactor antineutrino spectra. Phys. Rev. C, 83(5): 054615, May 2011. doi: 10.1103/PhysRevC.83.054615. 15

[86] D. Niraula and V. Karpov. Comprehensive numerical modeling of filamentary RRAM devices including voltage ramp-rate and cycle-to-cycle variations. *ArXiv e-prints*, June 2018. 68

[87] K. A. Olive et al. Review of Particle Physics. *Chin. Phys.*, C38:090001, 2014. doi: 10.1088/1674-1137/38/9/090001. 24

[88] Omega. *Heizpatronen mit hoher Leistungsdichte und Nenndurchmesser 6,3 mm*, (accessed August 22, 2018). URL https://www.omega.de/pptst/CIR_14.html. 59

[89] Omegalux. *Catridge Heater CIR-14*, (accessed June 14, 2018). URL https://www.omega.com/heaters/pdf/CIR_14.pdf. 59

[90] Omegalux. *Catridge Heater Info*, (accessed June 14, 2018). URL https://www.omega.com/heaters/pdf/cartridge_heater_info.pdf. 60

[91] Spiegel Online. *Ruthenium-Wolke ueber Europa*, (accessed August 22, 2018). URL https://tinyurl.com/ybadmp3d. 49

[92] M. Pallavicini. Solar Neutrinos. *ArXiv e-prints*, October 2009. 39

[93] Wolfgang Pauli. *Pauli Letter 1930*, 1930 (accessed February 27, 2018). URL http://microboone-docdb.fnal.gov/cgi-bin/RetrieveFile?docid=953;filename=pauli%20letter1930.pdf. 5

[94] M. G. Pia, T. Basaglia, Z. W. Bell, and P. V. Dressendorfer. Geant4 in Scientific Literature. *ArXiv e-prints*, December 2009. 105

[95] A. Pocar et al. Solar Neutrino Physics with Borexino. 2018. 37, 41

[96] B. Pontecorvo. Mesonium and anti-mesonium. *Sov. Phys. JETP*, 6:429, 1957. [Zh. Eksp. Teor. Fiz.33,549(1957)]. 8

[97] Radioprotection and Nuclear Safety Institute (IRSN). *Report on the IRSNs investigations following the widespread detection of 106-Ruthenium in Europe early October 2017*, January 2018 (accessed May 14, 2018). URL http://www.irsn.fr/FR/Actualites_presse/Actualites/Documents/IRSN_Report-on-IRSN-investigations-of-Ru-106-in-Europe-in-october-2017.pdf. 49, 50, 51

[98] F. Reines. The neutrino: From poltergeist to particle. *Rev. Mod. Phys.*, 68: 317–327, 1996. doi: 10.1103/RevModPhys.68.317. 6

[99] F. Reines and C. L. Cowan. The Neutrino. Nature, 178:446–449, September 1956. doi: 10.1038/178446a0. 6

[100] A. G. et al. Riess. A 2.4% Determination of the Local Value of the Hubble Constant. ApJ, 826:56, July 2016. doi: 10.3847/0004-637X/826/1/56. 11

[101] Sebastian Rottenanger. *Private conversation.* 26, 27

[102] SAGE Collaboration. Solar neutrino flux measurements by the Soviet-American gallium experiment (SAGE) for half the 22-year solar cycle. *Soviet Journal of Experimental and Theoretical Physics*, 95:181–193, August 2002. doi: 10.1134/1.1506424. 7

[103] sandmayersteel. *Alloy321-SpecSheet*, (accessed August 12, 2018). URL https://www.sandmeyersteel.com/images/Alloy321-SpecSheet.pdf. 82

[104] A. P. Serebrov, R. M. Samoilov, V. G. Ivochkin, A. K. Fomin, A. O. Polyushkin, V. G. Zinoviev, P. V. Neustroev, V. L. Golovtsov, A. V. Chernyj, O. M. Zherebtsov, M. E. Chaikovskii, V. P. Martemyanov, V. G. Tarasenkov, V. I. Aleshin, A. L. Petelin, A. L. Izhutov, A. A. Tuzov, S. A. Sazontov,

M. O. Gromov, V. V. Afanasiev, M. E. Zaytsev, A. A. Gerasimov, and D. K. Ryazanov. The first observation of effect of oscillation in Neutrino-4 experiment on search for sterile neutrino. *ArXiv e-prints*, September 2018. 133

[105] A. M. Serenelli, W. C. Haxton, and C. Peña-Garay. Solar Models with Accretion. I. Application to the Solar Abundance Problem. ApJ, 743:24, December 2011. doi: 10.1088/0004-637X/743/1/24. 38

[106] B. Shen, T. A. Coombs, and F. Grilli. Investigation of AC Loss in HTS Cross-Conductor Cables for Electrical Power Transmission. *ArXiv e-prints*, July 2018. 68

[107] M. Spurio. Results from the ANTARES neutrino telescope. In *European Physical Journal Web of Conferences*, volume 116 of *European Physical Journal Web of Conferences*, page 11006, April 2016. doi: 10.1051/epjconf/201611611006. 8

[108] NY Times. *Radioactive Cloud Europe*, (accessed August 22, 2018). URL https://www.nytimes.com/2017/11/15/world/europe/radioactive-cloud-europe.html. 49

[109] Walter Frei. *Improving Convergence of Multiphysics Problems* , (accessed December 12 , 2018). URL https://www.comsol.com/blogs/improving-convergence-multiphysics-problems/. 73

[110] C. S. Wu, E. Ambler, R. W. Hayward, D. D. Hoppes, and R. P. Hudson. Experimental test of parity conservation in beta decay. *Phys. Rev.*, 105:1413–1415, Feb 1957. doi: 10.1103/PhysRev.105.1413. URL https://link.aps.org/doi/10.1103/PhysRev.105.1413. 7

Acknowledgment/Danksagung

Am Ende dieser Arbeit möchte ich all den Personen meinen Dank aussprechen, ohne deren Zutun diese Dissertation nicht möglich gewesen und die damit verbundene Zeit sicherlich um einiges ärmer gewesen wäre.
Zunächst natürlich Professor Tobias Lachenmaier dem ich für die Ermöglichung dieser Arbeit, seine Betreuung und Expertise, für eine immer offene Tür und sein Interesse an dieser Arbeit, für seine sehr hilfreichen Korrekturen und nicht zuletzt für die Schaffung einer stets interessanten und durchweg angenehmen Arbeitsatmosphäre danken möchte. Danke auch für alle fachfernen Diskussionen, spontanen Ablenkungsbesuche im Büro und die gemeinsamen Ausflüge in Italien, auch wenn wir die "eine" Pizzeria nie gefunden haben.
Professor Josef Jochum, für stets gute Ratschläge in physikalischen, wie auch anderen Belangen und für Physikfragestellungen aus längst vergessener Zeit.
Professor Michael Wurm, dessen Übersicht der relevanten Physik gepaart mit Borexinos Eigenheiten von großer Unterstützung waren und der sich immer Zeit für Fragen genommen hat.
I want to thank the whole Borexino Collaboration, for their warm welcome and especially Alessio Caminata, who was a huge help during the years and a big inspiration with his great insights in Monte Carlo simulations and his unrivaled knowledge of the Borexino framework, even though he eats his pizza with pineapples. Lazlo Papp, with his technical knowledge and practical approach to complex issues, who was a tremendous help during the mockup assembly.
Danke an alle Mitglieder der Arbeitsgruppe, für nette Kaffeerunden und eine generell wirklich gute Zeit mit vielen neuen Freundschaften. Danke an die Werkstatt und vor allem aber danke für alles ans Büro. Danke an den Druckbeauftragen Alex Tieztschi, Danke an den Kaffee-Enabler Axel Müller und Danke an den Regionalliga Berater David J. Blum und an die Bürokollegen ehrenhalber, Sebastian Rottenanger, den Inkasso-Andi und Tobias Jammer.
Allerherzlichsten Dank meiner Mutter, meiner Schwester, meinem Schwager und meinen Neffen. Danke für eure Liebe und Unterstützung! Danke dir Oma und danke Papa - ich vermiss euch und hätte euch diese Arbeit gerne gezeigt.
Pure love an meine Brüder, Schwestern und Freunde. Ihr seid glücklicherweise so zahlreich und ihr wisst genau wer gemeint ist, sodass ich verbleiben kann mit:
I thank the beat Kalipayan Bieberbrüder Dudeinc4life Knochenmühle forever #strengthmafia